

THESE DE DOCTORAT
DE L'UNIVERSITE DE SCIENCES ET TECHNOLOGIES USTL LILLE 1

Présentée par
Davide COSTA

Pour obtenir le grade de
DOCTEUR

Domaine :
Sciences de la Matière, du Rayonnement et de l'Environnement
UFR de PHYSIQUE

Sujet de la thèse :
MODELLING THE THERMAL AGEING EVOLUTION OF FE-CR ALLOYS USING A
LATTICE KINETIC MONTE CARLO APPROACH BASED ON DFT CALCULATIONS

Thèse soutenue à Villeneuve d'Ascq le 19 juillet 2012 devant le jury composé de :

Marc Hou	Professeur à l'Université Libre de Bruxelles	Président et Rapporteur
Nils Sandberg	Docteur	Rapporteur
Cristelle Pareige	Maître de conférence à l'Université de Rouen	Examinatrice
Gilles Adjanor	Docteur	Encadrant
Christophe Domain	Docteur	Encadrant
Pär Olsson	Docteur	Encadrant
Charlotte Becquart	Professeur à l'ENSCL	Directrice de thèse
Alexandre Legris	Professeur à l'USTL	Directeur de thèse

ACKNOWLEDGMENTS:

I would like to express my sincere gratitude to my supervisors who closely followed my work throughout this PhD project. Prof. Charlotte Becquart – my PhD director –, Dr. Gilles Adjanor, Dr. Pär Olsson, and Dr. Christophe Domain all contributed to this thesis with different and complementary roles. Each of them enriched my vision of the scientific research by sharing with me his experience and competence in the different topics related to my work. I'm particularly grateful to Dr. Gilles Adjanor which has been daily involved in my work by his useful advices and original suggestions always characterised by a pedagogical purpose.

I wish also thank Dr. Sebastien Sallet, Prof. Philippe Pareige and associate professor Cristelle Pareige for attending my PhD progress meetings during which they were able to help me with useful commentaries on my work. In particular, I am very grateful to associate professor Cristelle Pareige for the period I spent in Rouen University; she shared with me her knowledge of the phase transformations phenomena in solids and she taught me the post-processing techniques that I used for the analysis of thermally aged Fe-Cr structures.

I am grateful to Mr. Christophe Varé, head of the MMC department in EDF R&D and, particularly, to Dr. Jean-Paul Massoud and Dr. Olivier Doupond, former and current head of Metallurgy group where I did my research over the past three years. I also thank Prof. Alexandre Legris, head of the UMET in Lille University, for accepting to co-direct my PhD.

I am also grateful to Prof. Alexandre Legris, associate professor Cristelle Pareige, Prof. Marc Hou and Dr. Nils Sandberg for accepting to being part of my PhD thesis committee.

A PhD is a human as well as scientific experience. These last three years would not have been as rich without the presence of all the other young researchers of the lab. My warmest thanks go to Dr. Raoul Ngayam-Happy, Dr. Karim Sebbari, M. Jean-Baptiste Piochaud, M. Gustavo Do Amaral, and M. Jean-Baptiste Baudouin which shared with me the early stages of our scientific career.

Finally, I wish to extend my heartfelt thanks to all the people that encouraged me all along my PhD: I think to my family, my closest friends and Carlotta.

SUMMARY:

INTRODUCTION.....	6
1. THE Fe-Cr ALLOY: A MODEL FOR FERRITIC STEELS.....	12
1.1 Ferritic Steels.....	12
1.2 The Fe-Cr binary alloy	16
1.2.1 The Fe-Cr phase diagram	17
1.2.2 Theoretical results regarding chromium solubility in iron at low concentrations	22
1.2.3 Thermodynamics of phase coexistence and the case of Fe-Cr	24
1.2.3.1 Early stages of nucleation mechanism:.....	25
1.2.3.2 Precipitates growth	30
1.2.3.3 Early stages of spinodal decomposition:.....	31
1.2.3.4 Late stages: coarsening regime:	33
1.2.3.5 Experimental observation and simulation of the Fe-Cr phase separation:.....	35
1.2.4 Magnetic properties of Fe-Cr alloy.....	37
2. SIMULATION METHODS.....	40
2.1 Cohesive models: DFT & EAM potentials	41
2.1.1 Density Functional Theory	41
2.1.1.1 Hohenberg and Kohn theorems	43
2.1.1.2 Kohn-Sham equations.....	45
2.1.1.3 The Local Density Approximation (LDA) and Generalised gradient Approximation (GGA) approximations for the exchange-correlation functional	48
2.1.1.4 Kohn-Sham wavefunction development and description of the electron-ion interaction (pseudopotentials and the Projector Augmented Wave (PAW) method).....	49
2.1.1.5 The Fe-Cr thermodynamics: first principle calculations of Fe-Cr mixing enthalpy	54
2.1.2 Embedded Atom Method based potentials for Fe-Cr alloys.....	57
2.1.2.1 The Two Band Model.....	58
2.1.2.2 The concentration dependent model	59
2.1.2.3 Fe-Cr alloy phase diagram and mixing enthalpy obtained with the EAM Fe-Cr potentials	60
2.2 Ground state energy calculation: the DFT and the EAM-2BM cohesive model.....	64
2.2.1 Chromium-chromium and chromium-vacancy interaction.....	64
2.2.2 Vacancy formation energy.....	67
2.2.3 Substitutional chromium atoms local magnetic moments	68
2.3 Vacancy migration energy calculations	71
2.3.1 The Nudged Elastic Band (NEB) method	72
2.3.2 The Drag Method (DM)	76
3. VACANCY MIGRATION ENERGY DEPENDENCE ON LOCAL CHEMICAL ENVIRONMENT	81
3.1 DFT study of the LAE dependence of the vacancy migration barriers.....	82

3.1.1	Migration barriers dependence on the chromium content in 1 st and 2 nd nearest neighbour sites of the migrating atom	83
3.1.2	Migration barriers dependence on the position of the environmental chromium along the migration path.....	91
3.1.3	Influence of the saddle point and the final configuration environment	93
3.2	EAM-2BM-GB potential.....	101
4.	SIMULATION OF THE THERMAL AGEING OF Fe-Cr BINARY ALLOYS	107
4.1	Atomistic Kinetic Monte Carlo (AKMC). The residence time algorithm.....	108
4.2	Parameterisation of the AKMC simulations of the Fe-Cr thermal ageing	112
4.2.1	Final Initial State Energy approximation.....	113
4.2.2	Parameterisation <i>via</i> the EAM-2BM-GB potential. Vacancy migration energy dependence on the LAE configuration (up to second nearest neighbour shell)	126
4.3	AKMC simulations of Fe-20 at.%Cr and Fe-25 at.%Cr thermal ageing.....	129
4.3.1	Local vacancy environment evolution during thermal ageing.....	131
4.3.2	Time scaling	134
4.3.3	Identification of the chromium rich precipitates	136
4.3.4	Box size effects.....	138
4.3.5	Time evolution of the precipitate size in Fe-20 at.%Cr and Fe-25 at.%Cr alloys	140
	CONCLUSIONS.....	151
	ANNEX 1: LOCAL ATOMIC ENVIRONMENT SITES NOMENCLATURE.....	157
	ANNEX 2: VACANCY MIGRATION ENERGIES FOR ALL SADDLE POINT CONFIGURATIONS.....	159
	ANNEX 3: VACANCY MIGRATION ENERGIES FOR DIFFERENT CONFIGURATIONS OF THE LOCAL ATOMIC ENVIRONMENT.....	169
	BIBLIOGRAPHY	180

ABBREVIATION LIST:

2BM: Two Band Model

AT: Migrating Atom

CDM: Concentration-Dependent Model

CI: Climbing Image

CPA: Coherent Potential Approximation

DFT: Density Functional Theory

DM: Drag Method

EAM: Embedded Atom Method

EMTO: Exact Muffin Tin Orbitals

FISE: Final Initial State Energy

GGA: Generalised Gradient Approximation

KMC: Kinetic Monte Carlo

LAE: Local Atomic Environment

LDA: Local Density Approximation

LMM: Local Magnetic Moment

LSDA: Local Spin Density Approximation

LSW: Lifshitz-Slyozov- Wagner

MMC: Metropolis Monte Carlo

NEB: Nudged Elastic Band

nn: nearest neighbours

PAW: Projector Augmented Wave

SQS: Special Quasi-random Structures

TAP: Tomographic Atom Probe

USPP: Ultra Soft Pseudo-Potentials

V: Vacancy

INTRODUCTION

The world production of nuclear energy has risen significantly in last decades: from 203 TW·h in 1973 to 2731 TW·h in 2008, indeed the percentage of primary energy produced from nuclear fuel increased from 0.9% to 5.8% in this period [IEA2010]. In December 31 2009, there were 437 operating reactors in the world, 55 under construction and 61 whose the construction had been planned [IAEA2010]. In a context where the growing energy demand must be satisfied together with the reduction of greenhouse gas emissions, the use of nuclear power plants represents an important aspect of an energy supply strategy based on the diversification of the energy production technology, especially considering the fact that renewable energies are not yet able to represent a unique alternative to fossil fuels. In this context, it is imperative to ensure the reliability of nuclear reactors during operation and in preparation for the possible extension of their lifetime. Moreover, it is necessary to develop technologies to ensure the safety and the economic viability of nuclear energy production technologies that are still under study (future generation fission reactors and fusion reactors). In both cases, one of the most important tasks is the study and the development of the materials used in environments characterised by extreme conditions: exposure to neutron radiation, high temperatures or presence of a corrosive medium [Zinkle2009, Mansur2004, Was2007, Murty2008, Yvon2009]. France represents an emblematic case among the countries producing nuclear energy: 58 PWRs (Pressurised Water Reactors) operates in France, providing about 75% of the electric power generation. Through its major energy supplier – EDF – it also faces both the problem of extending the service life of reactors in operation [LeDelliou1994, Bonnet1990, Gendrot1999] and the development of new production technologies. EDF is directly involved in the research concerning the materials for nuclear application in next generation reactors as a partner of the European research program GETMAT (Generation IV and Transmutation Materials) and in both current and future generation reactors, as leading partner of the material ageing institute (MAI). The MAI is an international research centre founded and financed by EDF, the Tokyo Electric Power Company (TEPCO), the Kansai Electric Power Company (KEPCO) and the US Electric Power Research Institute (EPRI). The research presented in this thesis work has been achieved in the framework of EDF R&D and the GETMAT project and has been founded by the MAI.

One of the main factors which limits the lifetime of nuclear power plants and may compromise the safety of reactors operation is the degradation of structural materials, especially the vessel steels and primary circuit steels. The vessel contains the reactor core and the primary circuit contains the coolant which carries a few radioactive elements coming from the corrosion of activated primary components or from the partial activation of the coolant itself by absorption of neutrons from the core. For these reasons, the good performance of these two components is a fundamental issue; particularly the reactor vessel which cannot be replaced so that its lifetime limits that of the entire plant. The vessel and primary circuit materials are exposed to physical and chemical conditions that can cause alteration of their mechanical properties. As stated above, the main sources of degradation of structural materials are radiation damage, thermal ageing, and corrosion (concerning the damage caused by corrosion, one can refer, for example, to review article [Fry2002]).

Radiation damage is due to collisions between the neutrons from nuclear reactions occurring in the reactor core and the nuclei of the structural materials. During a period of forty years of operation, the internal components of a light water reactor can be exposed to a fast neutron flux ($E \geq 1$ MeV) up to about 10^{22} n/cm² for a PWR and 10^{23} n/cm² for a boiling water reactor. Such doses of neutron radiation – corresponding to 7 dpa (displacement per atom¹) and 70 dpa, respectively – induce the formation of defects in the crystal lattice of structure of steels [Zinkle2009]. The primary damage induced by neutrons irradiation consists in the formation of point defects: high energy neutrons can knock the lattice atoms, the latter are consequently displaced from their equilibrium position and vacancy-self interstitial atom pairs (*i.e.* Frenkel pairs) can be formed. Vacancy and interstitial atoms are likely to diffuse through the lattice, their mobility being enhanced by the high operating temperature of the reactor. Migrating point defects can combine to form point defects clusters which can give rise to two dimensional defects such as interstitial loops or voids. These defects induce the hardening and the embrittlement of the steel. Vacancies combining in clusters also create voids which are responsible for the swelling phenomenon (this latter issue concerns, particularly, the inner components of the vessel, *i.e.* "internals"). In addition, some of the elements present in the structural materials can absorb neutrons from the core and be consequently activated becoming α emitters. This causes the introduction of helium atoms in the crystal which can diffuse and penetrate into vacancy voids increasing the swelling phenomenon [Gelles2000].

¹ A damage level of 1 dpa corresponds to a "stable" displacement of every atom from its lattice site [Zinkle2009].

Thermal ageing is the microstructural transformation that occurs in materials exposed to relatively high temperatures for long periods when their initial state does not correspond to thermodynamic equilibrium at these temperatures. The operating temperature of materials constituting the vessel or the primary circuit of PWRs is about 300 °C, whereas the materials constituting the containment chambers of nuclear fusion reactors can reach temperatures of 1000 °C.

The present work focuses on the degradation of the structural materials in nuclear power plants by thermal ageing, and, in particular, on the ageing kinetics of the ferritic phase of Fe-Cr based steels. The understanding of the thermal ageing mechanism and a deep knowledge of the material response to a prolonged exposure to operation conditions is a very important issue, both to guarantee the safety of operating nuclear reactors and to guide the structural materials design for future generation reactors.

Concerning the reliability and the service maintenance of the operating nuclear power plants, one fundamental aspect is related to some components of the primary cooling circuit and, particularly, the cast elbows. The cast elbows in French PWRs are made of austenitic-ferritic stainless steel. The austenitic-ferritic stainless steels are alloys containing chromium (~20 wt.%), nickel (~10 wt.%), silicon (~1 wt.%), and sometimes molybdenum (~2.5 wt.%). The austenitic phase has a face centred cubic (fcc) structure while the ferritic phase has a body centred cubic (bcc) structure. This material is historically known as being sensitive to thermal ageing at service temperatures which has an embrittling effect on the alloy [LeDellou1994, Gendrot1999]. The embrittling effect of the thermal ageing is nowadays recognised as a consequence of the chromium precipitation in the ferritic phase. High chromium ferritic steels undergo α - α' phase separation (where α and α' are the iron-rich phase and the chromium-rich phase respectively) if the chromium content exceeds ~9 at.% in the region of temperatures important for their application in the nuclear industry (> 600 K). The latter issue also refers to chromium-rich ferritic-martensitic steels which are considered leading candidates for structural materials for future generation IV fission reactors and fusion reactors [Zinkle2009, Klueh207] because of the high resistance of such alloys to corrosion and radiation damage.

The thermal ageing consists in the evolution of the alloy microstructure. If one neglects the primary radiation damage, which induces the formation of interstitial defects, the microstructure evolution can be considered as being driven by a vacancy diffusion mechanism. The experimental observation of the thermal ageing in chromium-rich ferritic or austenitic-ferritic steels can be achieved *via* the analysis of the microstructure of samples

thermally aged at a given temperature. The most evident drawback of the experimental approach is the fact that experiments are time-consuming since they require the samples to be thermally aged for several years in order to observe the microstructure evolution. In such a context the development of reliable models at the atomic scale and their implementation through numerical simulations represent complementary approaches to the experimental investigation. Atomic-scale theoretical models are likely to help interpret the experimental data and to understand the microscopic mechanism which drives the kinetics of the thermal ageing. Furthermore, the numerical simulations can represent precious predictive tools: in the case of stochastic simulations such as atomistic kinetic Monte Carlo (AKMC) simulations, and considering the current computer's performances, the evolution of an atomic structure (containing up to some thousands of atoms) exposed at a given temperature for some hundreds of hours can be simulated with a computational time of few hours.

The aim of this work is to contribute to the recent modelling effort [Malerba2008, Dudarev2009, Terentyev2011] that is increasingly representing an essential aspect of the research on ferritic and ferritic-martensitic alloys for nuclear power industry. The main goals of the present work are, on the one hand, the achievement of a better understanding of the atomic-scale mechanisms which drive the microstructure evolution *via* the vacancy diffusion and, on the other hand, to exploit such knowledge to parameterise an AKMC approach for the simulation of the thermal ageing of the ferritic steels. The parameterisation of an AKMC simulation is based on the knowledge of the vacancy migration energy towards an occupied lattice site. In principle, this quantity depends both on the atomic species which exchanges its position with the vacancy and on the chemical environment where the vacancy diffusion occurs. The parameterisation of the AKMC simulations should reflect such dependence in order to be realistic and physically consistent.

In order to develop such modelling, we considered a chemically simplified system. The ferritic phase of stainless steels is described as a chromium-rich Fe-Cr binary alloy with bcc structure. Thus we theoretically investigated the vacancy migration energy dependence on the local chemical environment (up to the second nearest neighbour shell of the vacancy-migrating atom pair) in an Fe-Cr alloy. Such an investigation requires the cohesive energy of the system to be computed for several atomic configurations and to introduce a method for computing the vacancy migration energy. The first task has been achieved both in the framework of density functional theory (DFT) and using an Fe-Cr semi-empirical potential based on the embedded atom method (EAM). Concerning the vacancy migration energy, it has been computed with the nudged elastic band method within the density functional theory

and with the drag method within the EAM cohesive model. On the basis of our study of the vacancy migration energy dependence on the local atomic environment, we developed two types of parameterisation for the AKMC simulations. The first is based on the computation of the vacancy migration barriers with the EAM potential for all the possible configurations of the vacancy local atomic environment by the drag method. The second type of parameterisations has been obtained by introducing an approximate expression for the vacancy migration energy depending on both the species of the atom which migrates towards the vacancy and the local atomic environment. Such formulas have been obtained as successive improvements of the existing final initial state energy (FISE) approach. Our improvements consisted in introducing a more explicit dependence of the vacancy migration energy on the local environment deduced from DFT results. Our estimations of the vacancy migration energy performed with the interatomic potential or with the approximate expressions we introduced have been validated by comparison with full DFT calculations for several configurations of the vacancy local atomic environment. Finally, we compared some available experimental observations or theoretical previsions of the Fe-Cr thermal ageing kinetics with the description we obtained with the AKMC simulations parameterised with the different approaches we proposed.

This manuscript is organised as follows. In chapter 1 we will introduce the Fe-Cr system as a model for ferritic stainless steels. In particular, we will present the state of the art knowledge of its phase diagram as well as some still open questions related to this issue. We will then present the models describing the phase separation thermodynamics and kinetics of the binary alloys and we will show that such models should be particularly simple to apply to the Fe-Cr system. Finally we will show that, although the Fe-Cr system is a simplified model for the description of the ferritic stainless steels as well as for the validation of the models describing the phase separation in binary alloys, its complexity is raised by its very peculiar magnetic properties which, as it will be further illustrated in chapter 3, have an influence both on the thermodynamics and the kinetics of decomposition.

In chapter 2, we will present the methods we used for computing the cohesive energy of the Fe-Cr structures: namely the DFT and the EAM potential. We will also present a bibliographic study which allowed us to choose, within the existing EAM Fe-Cr potentials, the one which better describes the thermodynamics of Fe-Cr system with respect to the available DFT previsions and experimental data. Thus we will illustrate some DFT and EAM preliminary calculations which we performed to characterise some properties of the system we are dealing with (vacancy formation energy, chromium-chromium and vacancy-chromium

formation energy in an iron matrix) as well as some DFT calculations characterising the local magnetic properties of different solute chromium configurations in the iron matrix. Finally we will introduce the methods we used for computing the vacancy migration energy both in the framework of DFT (nudged elastic band method) and EAM potential (drag method) as well as the calculations we made to optimise the parameters related to these methods.

Chapter 3 will concern our study of the vacancy migration energy dependence on the local chemical environment both with the DFT and the EAM Fe-Cr potential. In this study we investigated the vacancy migration energy dependence on the chromium content in the local environment and the specific influence of the chromium content in different group of sites of the first and the second nearest neighbour shells of the vacancy-migrating atom pair. We will also characterise the delicate relation between the vacancy migration energy and the variation of the energy of the system which follows a vacancy jump. Moreover, we will illustrate our conclusions about the relation between the vacancy migration energy dependence on the local environment and the chromium-chromium and the chromium-vacancy interactions as well as the variation of the local magnetic moments of the migrating atom and its environment during the migration process. Thus, considering the DFT results as reference values, we studied the capability of the EAM Fe-Cr potential to reproduce such results.

Finally, in chapter 4, we will briefly present the theoretical basis of the AKMC method as well as the approaches we proposed for the parameterisation. In particular, we will discuss the origin of the FISE approximation and our improvement to this approximation to ensure a better description of the effect of the atomic environment on the vacancy migration energy. We will then present our AKMC simulations of the Fe-20 at.%Cr and Fe-25 at.%Cr alloys. In order to compare the results of the AKMC simulations based on the different parameterisations with experimental data, we will introduce the approaches we considered for the estimation of the time dependence of the size of the chromium-rich precipitates and the implementation of the scaling procedure of the AKMC simulated time to the real ageing time. Finally we will discuss the comparison between the results we obtained with the AKMC simulations and the experimental observation, on the one hand, and previsions based on theoretical models, on the other hand.

1. THE Fe-Cr ALLOY: A MODEL FOR FERRITIC STEELS

In this chapter, we will briefly discuss the importance of ferritic steels in operating nuclear reactors and the reasons why they are promising candidates to be employed as structural materials for future generation nuclear power plants. We will then introduce the Fe-Cr system as a model for the study of the ferritic phase of stainless steels. The Fe-Cr binary system represents a simplification with respect to the stainless steels on the chemical point of view, it also represents an apparently simple physical system for the validation of theoretical models describing the phase separation in binary alloys. Nevertheless, despite some simplifications, the Fe-Cr binary alloy still carries some peculiarities which considerably increase the difficulties related to its theoretical modelling. Such difficulties concern the still open issue of the Fe-Cr binary alloy phase boundaries at low temperatures and its very particular magnetic properties (in the next chapter it will be shown how these two aspects are closely related).

1.1 Ferritic Steels

Among the components of the primary circuit of PWRs, a particular attention is devoted to the austenitic-ferritic cast stainless steel elbows. These components are indeed submitted to intense mechanical stress in operating conditions and austenitic-ferritic stainless steels are long-time known to undergo embrittlement due to thermal ageing at temperatures of the order of the reactor operating ones [LeDelliou1994, Gendrot1999] (the temperature of the primary circuit austenitic-ferritic components can vary from 285° C to 323° C, depending on their distance from the reactor core [NOVY2009b]). The study of the behaviour of these materials during reactor operations requires, in particular, an understanding of the mechanisms of thermal ageing of the ferritic phase. Furthermore, ferritic steels are good structural materials candidates for both future generation nuclear fission reactors and fusion reactors prototypes [Kohyama1996, Hishinuma1998, Garner2000, Klueh207] because of their better response – as compared to austenitic steels – to radiation damage and, particularly, for their resistance to radiation induced swelling [Little1979, Gelles1982, Porollo1998, Konobeev2006]. We reproduce in figure 1-Ch1, measures – reported by Yvon and Carré

[Yvon2009] – of the hoop deformation (deformation orthogonal to both the radius and the rotation axis in rotationally symmetric samples) on different irradiated austenitic and ferritic-martensitic steels. The ferritic steels have an iron-based body-centred cubic crystal structure (bcc). They are characterised by low carbon content (< 0.2 wt.%) and a chromium content between 10 wt.% and 30 wt.% (12 wt.% chromium makes the alloy resistant to oxidation) to which other alloying elements (*e.g.* Mo, Nb, Ti, Si, V) can be added in different concentrations to improve their mechanical or chemical properties [Baïlon2007]. In short, the main effects of these alloying elements and their concentration range in commercial steels are the following: molybdenum is added (up to 4.5 wt.%) to improve high temperature strength and hardness, niobium (up to 1.5 wt.%) improves the strength of the alloys for high temperature service, titanium (up to 1 wt.%) minimises intergranular corrosion, silicon (up to 1 wt.%) is a deoxidising agent used during the melting of the steels and, at the same time, improves the strength and the elasticity, vanadium is added (up to 0.3 wt.%) to increase hardness, strength, creep resistance and impact resistance. In ferritic steels for nuclear applications, high activation solutes such as molybdenum and niobium are replaced with tungsten and vanadium. In ODS (Oxide Disperse Steels) - designed to improve the resistance of steel at high temperatures (above 800 K) – chromium concentrations can reach higher values (up to 14 wt.%) [Auger2011].

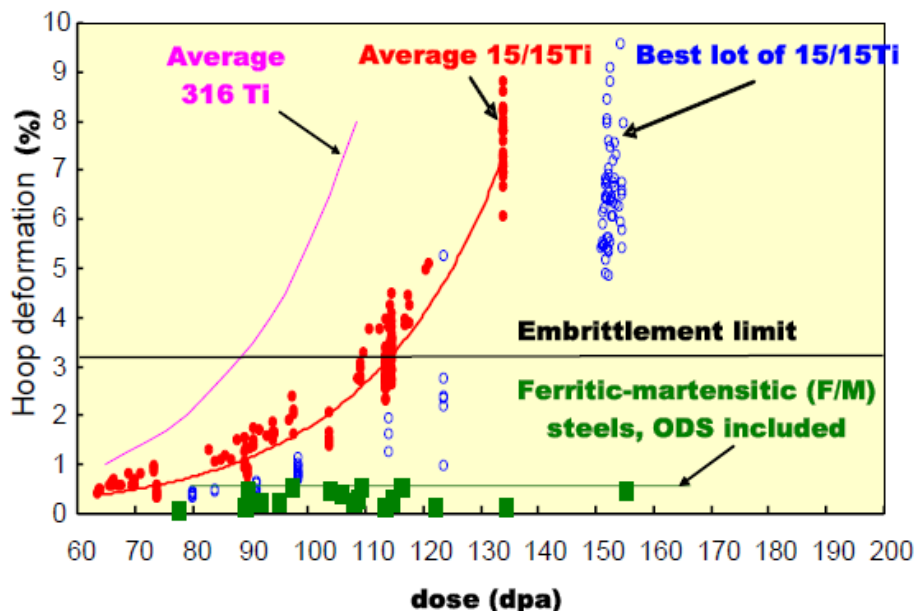


Figure 1-Ch1 Hoop test performed on irradiated austenitic and ferritic-martensitic steels. The figure is from Yvon and Carré [Yvon2009].

Oxidation resistance is a fundamental characteristic for primary circuit and reactor core materials. When one considers other degradation mechanisms such as hardening and embrittlement, the ferritic stainless steels exhibit a non-monotonic behaviour depending on chromium concentration. As a consequence, the optimal composition of steels for structural components of future generation reactors is still under investigation. From a macroscopic point of view, the radiation induced hardening of Fe-Cr steels increases with the chromium content [Matijasevic2008]. The study of the effects of chromium content in Fe-Cr binary alloys shows that the presence of a small amount of chromium (from 0.1 at.%) in an iron matrix promotes the formation of interstitial dislocation loops under neutrons and electrons irradiation [Okada1999]. Arakawa *et al.* [Arakawa2004] showed that chromium contributes to stabilise the interstitial loops: in a ferritic alloy containing 9 wt.% of chromium, dislocation loops are stable up to 820 K, whereas they disappear in pure iron above 620 K. Furthermore, the presence of chromium as an alloying element prevents the formation of voids created by irradiation [Porollo1998, Konobeev2006] thus diminishing the swelling phenomenon. A very significant effect which shows the non-monotonic properties of ferritic steels is the evolution of the ductile-to-brittle transition temperature (DBTT) and the shift of the ductile-to-brittle transition temperature (Δ DBTT) with the chromium content. Figure 2-Ch1 indicates that both the DBTT and Δ DBTT are minimal for a chromium concentration of 9 wt.% [Kohyama1996, Hishinuma1998].

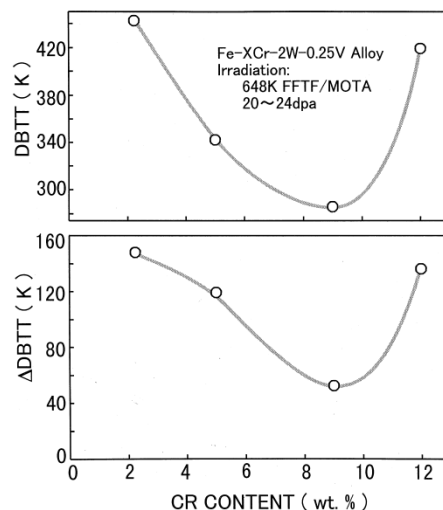


Figure 2-Ch1 Ductile to brittle transition temperature and ductile to brittle transition temperature shift for different chromium contents in Fe-xCr-2W-0,25V alloy. The figure is from Hishinuma *et al.* [Hishinuma1998].

It is well known that ferritic steels with high chromium content undergo embrittlement when they are subjected to temperatures of about 475° C for a long period [Tisinai1957,

Grobner1973, LeDellou1994, Lo2009]. This embrittlement is now recognised as being the result of the formation of chromium rich precipitates (α' phase) during the thermal ageing [Lo2009]. The interaction between the dislocations and the precipitates is responsible for the hardening and the embrittlement of the alloy. Indeed the chromium rich clusters act as pinning centers and the α' phase precipitates hinders dislocation motion [Baïlon2007, Bonny2009a, Lo2009, Soriano-Vargas2010, Malerba2008]. The latter aspect concerns not only the ferritic steels, but also the austenitic-ferritic steels in which the formation of precipitates of chromium may occur in the ferritic phase. The decomposition of a ferritic stainless steel in a chromium-rich phase (phase α') and an iron-rich phase (phase α) can occur by nucleation and growth or by spinodal decomposition. The first mechanism occurs if the second derivative of the free energy with respect to the chromium concentration is positive, the second if it is negative. The latter case means that the initial state which is a quenched solid solution is unstable and no thermodynamic barrier must be crossed for the decomposition to occur [Binder2001]. The precipitation mechanism (spinodal decomposition or nucleation and growth) depends on chromium concentration and temperature. It is often considered that the nucleation and growth unmixing mechanism leads to the formation of isolated α' precipitates whereas the spinodal decomposition occurs throughout the whole volume of the alloy and leads to the formation of interconnected α and α' domains. In reality, interconnected features in the microstructure cannot be seen as a signature of spinodal decomposition. Indeed, in concentrated alloys, where the number density of precipitates of the second phase is large, the spacing between the solute-rich clusters can be small enough to allow for interconnectivity. Thus, the interconnectivity of the microstructure in the late stages of the decomposition can be attributed to other mechanisms such as the coalescence of neighbouring particles or the coarsening of elastically favourable oriented precipitates [Wagner2001] (we remind that the coalescence is a phenomenon that consists in the merging of close precipitates which gives rise to a single bigger precipitate whereas the coarsening is the dissolution of small precipitates in favour of the growth of larger precipitates). The position of the spinodal limit remains controversial. In his early study on stainless steels thermal ageing, Gröbner [Grobner1973] observed, by transmission electron microscope, the formation of a chromium-rich phase in Fe-Cr alloys aged at 316 °C, 371 °C, 427 °C, 482 °C, and 538 °C and concluded that chromium precipitation occurs *via* the formation of isolated chromium-rich precipitates for a chromium concentration lower than 18 wt.%. Miller *et al.* observed, in the case of an Fe-45 at.%Cr-5 at.%Ni, that the morphology of the domains seems to depend on temperature. In particular, between 400 °C and 500 °C, the two phases form an interconnected network

whereas for temperatures above 550 °C α' phase forms as isolated precipitates [Miller1996]. More recently Hättestrand *et al.* [Hättestrand2009] observed by transmission electron microscopy that the chromium-rich α' phase may form in the ferrite phase of a duplex stainless steel Fe-25 wt.%Cr-7 wt.%Ni-4 wt.%Mo either via the formation of isolated precipitates or the formation of two interconnected phases. According to Hättestrand and co-workers, the unmixing mechanism depends on both the ageing temperature and whether the material is cold-worked or not (cold-work rendering the formation of an interconnected structure more likely).

1.2 The Fe-Cr binary alloy

The Fe-Cr binary alloy is considered as the reference model for ferritic stainless steels, in particular it allows characterising the effect of the chromium on the properties of the alloy regardless of the presence of other solutes. The Fe-Cr system is therefore the subject of extensive studies, both theoretical and experimental.

In this section, we will present the main topics on which Fe-Cr system studies focus. First, we will discuss the computation of the Fe-Cr phase diagram, particularly in the low temperature region. In this context, one of the most important issues is the definition of the boundary of the Fe-Cr miscibility gap and, in particular, the localisation of the chromium solubility limit in iron for temperatures approaching zero Kelvin.

Secondly, we will discuss the phase separation mechanism that occurs when the Fe-Cr alloy is quenched in the miscibility gap of the phase diagram. The main theoretical approaches exploited to describe the Fe-Cr phase separation will be presented together with some of the experimental observations related to this aspect.

Finally, we will describe the magnetic properties of pure iron, pure chromium, and their influence on the resulting Fe-Cr magnetic configuration.

Pure iron and pure chromium have the same ground state structure, very close lattice parameter, and similar electronic structure. These characteristics should render the Fe-Cr system a quite simple model for binary alloy. They should allow to employ simple approaches, such as the regular solution model, for the study of the solid solution, and simplify the thermodynamic related to the phase separation (as it will be discussed in the subsection devoted to the unmixing mechanisms). Nevertheless, the magnetism of Fe-Cr system proves to be a major difficulty in studying the properties of the alloy. Indeed, we will

show, in the following chapters, that magnetism has a significant influence, not only on the thermodynamics of the alloy, but also on the kinetic aspect.

1.2.1 The Fe-Cr phase diagram

An essential information for understanding the microstructural evolution of an alloy is its equilibrium phase diagram. Concerning the binary alloy Fe-Cr, Xiong *et al.* have recently calculated the phase diagram using the CALPHAD method [Xiong2011]. The CALPHAD method consists in introducing, for the different phases, an expression of the free energy containing a given number of parameters and to adjust such parameters in order to fit a set of experimentally observed equilibrium thermodynamic properties. In the case of the phase diagram for the Fe-Cr binary alloy, the free energy expression is usually based on the ideal solution model improved by adding terms accounting for the excess properties.

The experimental results Xiong *et al.* used as thermodynamic database to calculate the phase diagram of Fe-Cr are listed and discussed in reference [Xiong2010], the phase diagram they obtained [Xiong2011] is illustrated in figure 3-Ch1. The phases boundaries differ from those previously calculated by Andersson and Sundman [Andersson1987] and are in better agreement with available experimental results [Xiong2010, Xiong2011].

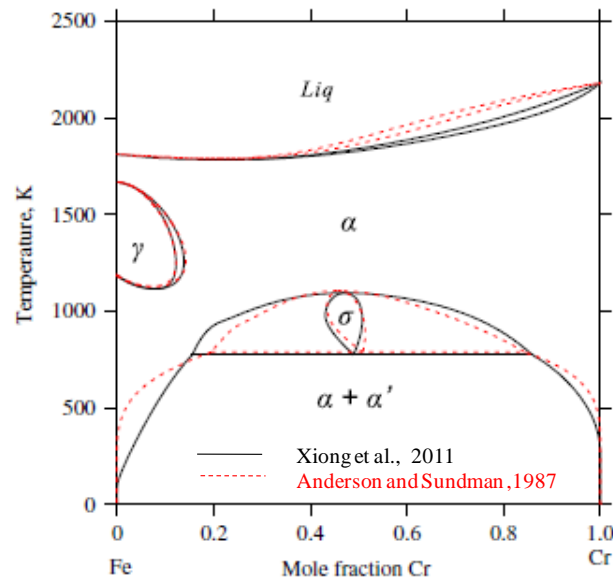


Figure 3-Ch1 Comparison between the equilibrium phase diagram of the Fe-Cr binary alloy calculated by Xiong *et al.* [Xiong2011] and the one calculated by Andersson and Sundman [Andersson1987]. The figure is from Xiong *et al.* [Xiong2011].

The Fe-Cr phase diagram exhibits different solid phases: α , α' , γ or σ , depending on the temperature and the chromium concentration. The Fe-Cr phase diagram is characterized by a large miscibility gap where phase separation occurs between an Fe-rich phase (namely, the α phase) and a Cr-rich phase (namely, the α' phase). Both the α phase and the α' phase have a body centered cubic (bcc) structure. (. Xiong and co-workers used the same parameterisation as Andersson and Sundman [Andersson1987] for the free energy of pure chromium, whereas, for pure iron, they used the parameterisation proposed later on by Chen and Sundman [Chen2001]. This choice allows a description of pure iron in better agreement with the experimental data available at low temperatures. The γ phase has a face-centred cubic (fcc) structure. The σ phase is an intermetallic compound whose unit cell contains 30 atoms and is defined by the space group P42/mmm (a description of this space group can be found, for example, in reference [DeNault2007]) and has an embrittling effect on the alloy. Because of its extremely slow formation kinetics, the σ phase is rarely observed [Joubert2008]. To describe this phase, Xiong *et al.* used the thermodynamic modelling proposed by Joubert [Joubert2008] and fitted it to the experimental data presented in reference [Xiong2010]. They located the lower limit of its zone of formation at 774 K for a chromium concentration of 48.9 at.% and the upper limit at 1093 K for a chromium concentration of 47.1 at.%.

One of the most remarkable features of the Fe-Cr phase diagram is the existence of a large miscibility gap (see figure 3-Ch1) within which the α phase and α' phase are likely to form. The position of the miscibility gap and, particularly, the position of the solubility limit in the iron-rich zone of the phase diagram are still topics under investigation, especially in the very low temperatures zone for which experimental data are missing. At very low temperatures, because of the very slow kinetics, the thermodynamic equilibrium cannot be reached in a time interval suitable for the experiments; therefore it is impossible to obtain experimental data in this area. As a consequence, the phase boundaries at low temperatures are usually extrapolated from experimental data obtained for higher temperatures. One of the first observations suggesting the existence of an Fe-Cr ordered solid solution for low chromium concentration has been the measure, by Mirebeau and Parette [Mirebeau1984], of short range order (SRO) parameter introduced by Cowley [Cowley1950]. The SRO parameter $\alpha_n(x)$ in a solid solution $\text{Fe}_{1-x}\text{Cr}_x$ is defined as follows:

$$\alpha_i(x) = 1 - \frac{p_i^{\text{Cr-Fe}}}{1-x}, \quad (1)$$

where x is the chromium concentration and $P_1^{\text{Cr-Fe}}$ is the conditional probability to find an iron atom in the i^{th} coordination sphere around a chromium atom. $\alpha_i(x)$ equals zero if $P_1^{\text{Cr-Fe}} = 1 - x$ (*i.e.* if the probability corresponds to the iron content and there is no preference for the chromium atoms to be surrounded by iron or chromium atoms, in which case the alloy behaves like an ideal solution). A positive value of $\alpha_i(x)$ indicates a clustering tendency of chromium atoms whereas a negative value of $\alpha_i(x)$ suggests the tendency towards the formation of ordered structures.

In 1984 Mirebeau and Parette [Mirebeau1984] measured by neutron scattering, the SRO parameter of samples of various chromium contents ($\text{Fe}_{0.85}\text{Cr}_{0.15}$, $\text{Fe}_{0.9}\text{Cr}_{0.1}$ and $\text{Fe}_{0.95}\text{Cr}_{0.05}$). They observed that the SRO parameter is negative when the chromium concentration is 5 at.%, positive when the chromium concentration reaches 15 at.% and very close to zero when the chromium concentration is 10 at.%. As stated above, the sign change - from negative to positive - of the Cowley SRO order parameter identifies the transition from the tendency of chromium atoms to repel each other to the tendency of chromium atoms to be surrounded by atoms of the same type. This phenomenon is often interpreted as the evolution from an ordered structure to the formation of solute-rich domains. It is important to notice that Mirebeau *et al.*, in their experience of 1984, measured the SRO only in the first four neighbour shells of the atoms. More recently, Mirebeau and Parette [Mirebeau2010] reproduced similar measures using an optimised experimental procedure (the signal to noise ratio was incremented by a factor 12). They also considered a greater number of chromium concentration values. Figure 4-Ch1, from reference [Mirebeau2010], shows the evolution of the quantity α_{12} with chromium content. The SRO α_{12} is the weighted (with respect to the coordination number) average between the value of the SRO associated with the first and second neighbour shells and is expressed by the following formula:

$$\alpha_{ij} = \frac{(z_i \alpha_i + z_j \alpha_j)}{(z_i + z_j)} \quad (2)$$

where $z_{i(j)}$ and $\alpha_{i(j)}$ are, respectively, the coordination number and the SRO associated with the i^{th} or j^{th} neighbour shells.

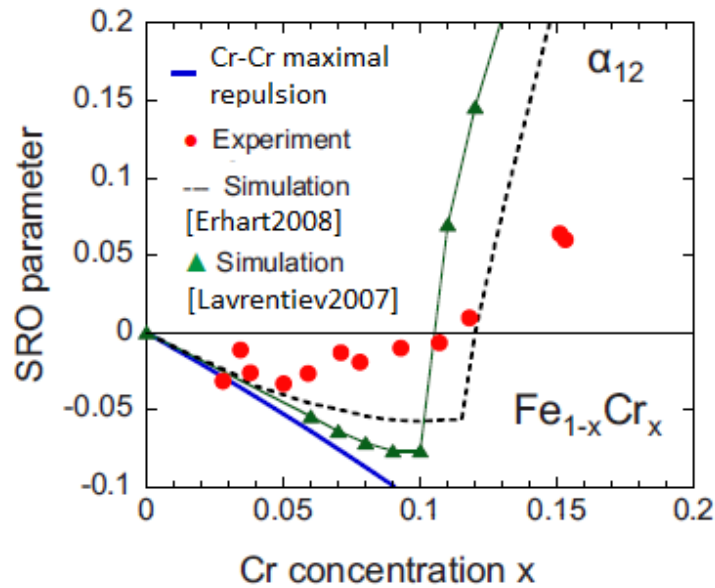


Figure 4-Ch1 α_{12} as a function of the chromium concentration measured by Mirebeau and Parette compared with predictions based on Monte Carlo simulation by Erhart *et al.* [Erhart2008] and Lavrentiev *et al.* [Lavrentiev2007]. The blue line corresponds to maximal repulsion between chromium atoms. The figure is from [Mirebeau2010].

Mirebeau and Parette's results [Mirebeau2010] have been compared with the theoretical predictions of Erhart *et al.* [Erhart2008] and Lavrentiev *et al.* [Lavrentiev2007], who performed Metropolis Monte Carlo (MMC) simulations in the semi-grand canonical ensemble. In order to obtain the energies associated with the different structures, Erhart *et al.* used the Fe-Cr embedded atom method (EAM) cohesive model introduced by Caro *et al.* [Caro2005], whereas Lavrentiev *et al.* used the cluster expansion (CE) method [Sanchez1984]. Lavrentiev *et al.* simulations have been performed on a rigid lattice whereas in Erhart *et al.* the atoms positions were relaxed by molecular dynamics between each MMC step.

In a very recent publication [Dubiel2011], Dubiel and Cieslak measured by Mössbauer spectroscopy the SRO in binary Fe-Cr alloys with chromium concentrations up to 25 at.%. They too observed a sign change, from negative to positive, for α_1 and a sign change, from positive to negative, for α_2 and showed that the chromium concentration value for which the sign change of α_1 and α_2 occurs depends on the metallurgical process employed to prepare the samples. Furthermore, they did not observe the sign change of α_{12} , which, according to their results, was negative whatever the chromium content for samples obtained by cold-rolling and positive for samples annealed at 800° C for 4 hours and quenched in liquid nitrogen. All samples considered by Mirebeau and Parette were shaped into cylinders, after an homogenisation at 800° C, they were heated at 520° C, gradually cooled down to 430° C and,

after few hours, quenched in water. These results indicate thus that the degree of decomposition or ordering strongly depends on samples' metallurgical history.

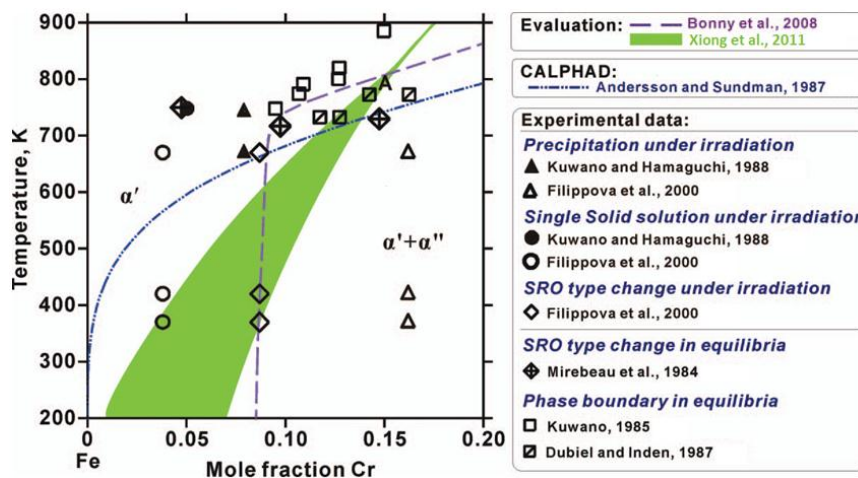


Figure 5-Ch1 Chromium solubility limit in iron obtained by Andersson and Sundman [Andersson1987] compared with extrapolations from Bonny *et al.* [Bonny2008] and Xiong *et al.* [Xiong2010] based on a series of experimental results. Experimental data are from references [Kuwano1985, Dubiel1987, Kuwano1988, Filippova2000]. The figure is from Xiong *et al.* [Xiong2010].

Figure 5-Ch1 shows a temperature-concentration phase diagram where the chromium solubility limit in iron was extrapolated by Bonny *et al.* in a review article [Bonny2008] and Xiong *et al.* [Xiong2010] on the basis of a series of experimental measurements. Bonny *et al.*'s and Xiong *et al.*'s conclusions are compared with the solubility limit predicted by the Fe-Cr phase diagram proposed by Andersson and Sundman [Andersson1987]. Recent results of Bergner *et al.* [Bergner2009, Heintze2011] are missing in figure 5-Ch1 and should be mentioned. These results have been obtained by small angle neutron scattering observation of neutron-irradiated Fe-Cr alloy at 300° C with different chromium concentrations and allowed the authors to locate the chromium solubility limit at 8.5at.%. Figure 4-Ch1 shows that Xiong and co-workers, unlike Bonny *et al.*, do not draw a precisely defined solubility limit, but rather span it on a concentration range that becomes larger as temperature decreases because of the increasing uncertainty. The reason for this uncertainty is due, on the one hand, to the fact that experimental data miss as temperature decreases and, to the other hand, to the fact that most of the experimental results considered by Xiong *et al.* and Bonny *et al.* refers to observations made under irradiation. Bonny *et al.* consider that the only effect of irradiation is to enhance the atoms diffusion and accelerate the ordering or phase separation kinetics [Bonny2008]. Xiong *et al.* disagree strongly and point the fact that no experimental

observation supports this hypothesis [Xiong2010]. Indeed irradiation may alter the structure of an ordered phase [Abromeit2000] or induce solute precipitation by coupling between defect fluxes and atoms and, in general, does not allow samples to reach thermal equilibrium but only stationary conditions [Martin1984]. This implies that the points represented in figure 5-Ch1 obtained from observations on irradiated samples do not necessarily capture the alloy at thermodynamic equilibrium. Therefore, the extrapolation of the equilibrium phase diagram from these points requires some care.

1.2.2 Theoretical results regarding chromium solubility in iron at low concentrations

The existence of a range of chromium concentrations for which the Fe-Cr mixture forms a thermodynamically stable solid solution (not necessarily ordered) at low temperatures was essentially suggested by theoretical predictions. One of the first remarkable results was obtained by Hennion who calculated, by the generalised perturbation method, the interaction potential of chromium-chromium pairs in a ferromagnetic iron matrix [Hennion1983]. At zero Kelvin the potential obtained by Hennion is negative when the chromium concentration is lower than 25 at.% and positive for greater chromium concentrations. Hennion results thus indicate that solutes atoms in an Fe-Cr alloy tend to maximise their distance (ordering tendency) or to form aggregates (unmixing tendency) if their concentration is lower or higher than 25 at.% respectively. One year later, the observations of Mirebeau *et al.* [Mirebeau1984, Mirebeau2010] showed that the chromium concentration limit, which separates the ordering tendency from the unmixing tendency is much smaller than the one proposed by Hennion.

The existence of a chromium concentration domain (at zero Kelvin) in which introducing substitutional chromium atoms in Fe-Cr is energetically favourable has been predicted by many theoretical calculations based on the tight binding method or on the density functional theory (DFT)² [Geng2003, Jiang2004, Olsson2003, Olsson2005b, Olsson2006, Klaver2006, Nguyen-Manh2008a, Nguyen-Manh2007, Ruban2008, Paxton2008, Nguyen-Manh2008b, Nguyen-Manh2009, Korzhavyi2009]. One of the fundamental aspects that have been explored by these techniques is the evolution of the mixing enthalpy with chromium concentration as it is the quantity which determines the solubility limit at zero Kelvin. Olsson

² In the next chapter, we will introduce the density functional theory and its most common approximations. We will then present its most interesting findings about the Fe-Cr system and their theoretical implications.

et al. were among the first ones to show - by *ab initio* calculations within the DFT and taking into account the magnetic properties of the alloy – that the Cr-Fe mixing enthalpy is negative up to a chromium concentration of 6 at.% and positive for higher concentrations [Olsson2003]. Figure 6-Ch1 shows Olsson *et al.* results.

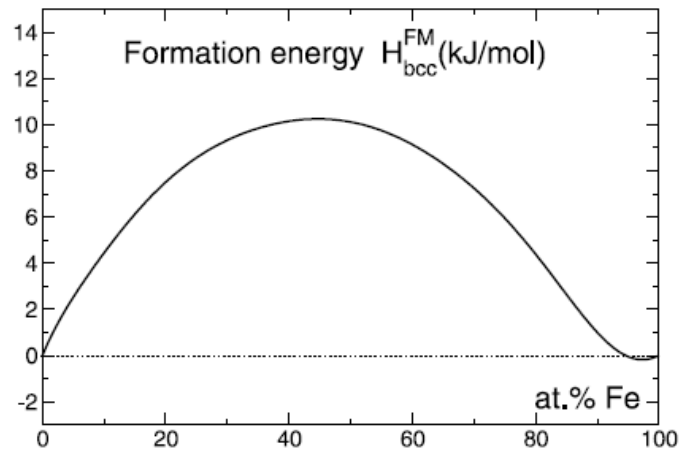


Figure 6-Ch1 Fe-Cr mixing enthalpy as a function of chromium concentration obtained by DFT calculations. The figure is from Olsson *et al.* [Olsson2003].

Several other publications presenting DFT calculations of the Fe-Cr mixing enthalpy qualitatively confirmed Olsson *et al.* results.

Note that ordinary *ab initio* techniques provide the energy of the ground state ($T = 0$ K) of an assembly of atoms, ignoring the influence of temperature. The effects of temperature on the solubility limit can be partially addressed and studied by Monte Carlo simulation in semi-grand canonical ensemble.

Since the publication of Olsson *et al.* *ab initio* results [Olsson2003], several studies whose goal was to develop an empirical model for the cohesive energy of the Fe-Cr system have been published. Empirical models are required to dispose of a predictive tool computationally more efficient than the DFT and able to provide a description of the Fe-Cr system consistent with DFT predictions. In such a context, semi-empirical many-body EAM (embedded atom method) potentials [Caro2005, Olsson2005a, Bonny2011a] and models based on cluster expansion [Sanchez1984, Lavrentiev2009, Lavrentiev2010] have been proposed. These models have been reviewed in a paper by Bonny *et al.* [Bonny2009b]. In the next chapter, we will present the empirical cohesive models we have chosen to perform our atomistic Kinetic Monte-Carlo simulations.

1.2.3 Thermodynamics of phase coexistence and the case of Fe-Cr

Up to this point we focused our attention on the chromium solubility limit in iron. As previously stated, within a set of chromium concentration and temperatures which define the miscibility gap, the Fe-Cr alloy undergoes phase separation through the formation of an iron-rich phase (α phase) and a chromium-rich phase (α' phase). The decomposition of a supersaturated alloy into two distinct phases α and α' usually occurs at constant temperature and pressure. The system reaches the equilibrium when its free enthalpy G is minimised. In a binary alloy at constant temperature, pressure and solute concentration, the equilibrium between the two phases α and α' is achieved when elements chemical potentials in the two different phases are equal:

$$\mu_i^\alpha = \mu_i^{\alpha'} \quad (3)$$

where i stands for the atomic species (either Fe or Cr in the present case). Equation (3) can be written in terms of the free energy derivative with respect to the number of particle of a given species in each phase:

$$\left(\frac{\partial G^\alpha}{\partial n_i}\right)_{T,P,n_j} = \left(\frac{\partial G^{\alpha'}}{\partial n_i}\right)_{T,P,n_j} . \quad (4)$$

The miscibility gap of the binary alloy can be divided in a metastable region and an unstable region according with the sign of the second derivative of the free energy with respect to the solute concentration. $\frac{\partial^2 G}{\partial c^2} > 0$ corresponds to the metastable region whereas $\frac{\partial^2 G}{\partial c^2} < 0$ corresponds to the unstable region of the solid solution. As stated in the previous section, if the alloy is quenched in the metastable region of the miscibility gap phase separation occurs *via* a nucleation and growth mechanism, if the alloy is quenched in the unstable region phase separation occurs *via* a spinodal decomposition. The nucleation mechanism is initiated by sufficiently large and localised thermal composition fluctuations which lead to the formation of stable solute-rich precipitates. It is a thermally activated process. The spinodal decomposition mechanism occurs when the system is unstable with respect to non-localised composition fluctuations of small amplitude, thus it is initiated by means of spontaneous formation and growth of composition fluctuations [Wagner2001].

The reduction of free energy which follows the phase separation is the driving force ΔG of the transformation. The driving force is the sum of two contributions. The first contribution, ΔG_{ch} (chemical driving force), promotes the unmixing process and accounts for the reduction of the free energy due to the precipitation of the α' phase from the supersaturated solid solution. The second contribution, ΔG_{el} , accounts for a reduction of the driving force associated to the increase of the elastic strain energy taking place during the phase separation. In the case of homophase fluctuations, ΔG_{el} is due to the variation of the lattice parameter with composition and depends thus strongly on the difference between the elements atomic radii. In the case of heterophase fluctuations, the nucleation activation energy barrier mainly depends on the matrix/precipitates interface formation energy. Coherent interfaces are energetically more favourable. As a result, the precipitates are usually coherent during the first stages of a phase separation. ΔG_{el} is the energy cost required for the matrix and the precipitates to be coherent and it is due to the mismatch between the lattice parameter of the matrix and the one of the precipitating phase. The iron and the chromium lattice parameters are very close ($a_0(\text{Fe}) = 2.86 \text{ \AA}$, $a_0(\text{Cr}) = 2.88 \text{ \AA}$ [Kittel1996]), and so are their atomic radius. As a consequence, in the case of the Fe-Cr phase separation, the driving force should be dominated by the chemical contribution.

In the following part of this subsection we will briefly present the main features of the theoretical models which describe the phase separation mechanism for a binary alloy. We will first focus on the models accounting for the early stages of the phase separation (nucleation or spinodal decomposition) and then on the description of the late stages (growth and coarsening).

1.2.3.1 Early stages of nucleation mechanism:

Two main approaches exist for the description of the nucleation mechanism: the classical and the non-classical nucleation model. In both models, the precipitate is considered as interacting only with the matrix and the precipitate-precipitate interaction is neglected. In the classical nucleation model (see, for example, [Wagner2001]) the nuclei of the precipitating phase (α' phase) are considered as spherical droplets whose composition remains constant during the precipitation and who have bulk properties. Furthermore, the matrix/precipitate interface is considered as being sharp. The variation of the free energy induced by the formation of a coherent precipitate with radius R can be written as:

$$\Delta G(R) = (\Delta g_{\text{ch}} + \Delta g_{\text{el}}) \frac{4\pi}{3} R^3 + 4\pi R^2 \sigma_{\alpha\alpha'} \quad (5)$$

where $(\Delta g_{\text{ch}} + \Delta g_{\text{el}})$ is the driving force per unit volume (including both the chemical and the elastic contribution) and $\sigma_{\alpha\alpha'}$ is the formation energy per unit surface of the α/α' interface. The first term exhibits a R^3 dependence and accounts for the free energy gain due to the formation of the solute droplets; it represents a negative contribution to the free energy. The second term depends on R^2 and accounts for the energy cost (it is a positive contribution to the free energy) due to the formation of the α/α' interfaces. The positive quadratic term in equation (5) dominates when the droplet radius is lower than a critical value. When the droplet radius is higher than the critical value, the negative cubic term becomes dominant. $\Delta G(R)$ passes thus through a positive maximum corresponding to a critical radius R^* whose expression is:

$$R^* = \frac{2\sigma_{\alpha\alpha'}}{-(\Delta g_{\text{ch}} + \Delta g_{\text{el}})}. \quad (6)$$

Only precipitates with radius higher than the critical value will grow continuously. Hence, a localised composition fluctuation will become a stable nucleus only if it overcomes a nucleation energy barrier given by:

$$\Delta G^* = \Delta G(R^*) = \frac{16\pi\sigma_{\alpha\alpha'}}{3(\Delta g_{\text{ch}} + \Delta g_{\text{el}})^2}. \quad (7)$$

The precipitates size can increase *via* the condensation of solute atoms on the precipitates and decrease *via* the evaporation of solute atoms from the precipitates. It should be noted that, because of the stochastic nature of these processes, it is not impossible that a solute cluster with radius slightly higher than R^* dissolves again in the matrix.

As stated above, in the classical nucleation model, the composition of the precipitates is assumed to be homogeneous and the matrix/precipitates interface is sharp. In the non-classical nucleation theory, developed by Cahn and Hilliard [Cahn1958, Cahn1959a, Cahn1959b], the precipitates/matrix interface is considered to be diffuse because the solid solution, in its metastable state, is considered to contain homophase composition fluctuations with diffuse interfaces and a composition of the precipitates which varies throughout the

solute clusters. Therefore, in the non-classical nucleation model, a critical fluctuation must be characterised by its spatial extension and its spatial composition. The volume and the surface of the precipitates cannot be treated anymore as separate contribution to the free energy change of the system due to the phase separation. In order to develop their formalism, Cahn and Hilliard considered a coarse grained free energy depending on the local (evaluated in a sample volume dV) composition and composition gradient. They expressed the homogeneous solution free energy (ore equivalent free enthalpy) as:

$$F_0 = \int_V f(c_0) dV, \quad (8)$$

and the inhomogeneous solution free energy as:

$$F = \int_V f(c) + K^*(\nabla c)^2 dV, \quad (9)$$

where c_0 is the homogeneous solution composition and c is equal to the mean composition $c(\mathbf{r})$ within a volume dV located at position \mathbf{r} in the inhomogeneous solution and f is the free energy par unit volume. Equation (9) is obtained by assuming the free energy to be a function of the local concentration and its derivatives. They expanded the free energy in a Taylor series about the free energy per molecule of a solution with uniform composition and truncated the development to second order terms. Furthermore they considered the system to have cubic symmetry. The latter assumption introduces some constraints on the free energy spatial dependence because of the symmetry of the crystal (*i.e.* the free energy must be invariant to the sign change of each coordinate and to fourfold rotation about each axis). As can be seen in equation (9), the coarse-grained free energy of the inhomogeneous system depends on the gradient of the composition *via* the term $K^*(\nabla c)^2$ where K^* is the free energy gradient coefficient [Cahn1958]. The coarse-graining methodology requires the number of atoms within each volume element to be sufficiently large so that $c(\mathbf{r})$ and $f(c)$ can be introduced as continuous functions (*i.e.* functions which do not exhibit too sharp variations between adjacent volume elements). On the other hand the volume element must be sufficiently small in order to avoid phase separation to occur within dV .

In the framework of Cahn and Hilliard approach, the free energy change due to the evolution of the system from homogeneous to inhomogeneous (*i.e.* due to the phase separation process) is:

$$\Delta F = (F - F_0) = \int_V [f(c) - f(c_0) + K^*(\nabla c)^2] dV. \quad (10)$$

The non-classical nucleation model provides a continuous description of the precipitates and does not require the matrix/precipitates interface to be sharp. It is based on the assumption that the free energy $f(c)$ varies slowly with the composition and requires the precipitating phase to be coherent with the matrix. If the lattice parameter changes with the composition, introducing a coherency strain, an elastic term has to be introduced in equation (10) which then becomes:

$$\Delta F = (F - F_0) = \int_V [f(c) - f(c_0) + K^*(\nabla c)^2 + \eta^2 Y (c - c_0)^2] dV, \quad (11)$$

where $\eta = \left(\frac{1}{a_0}\right) \left(\frac{\partial a}{\partial c}\right)$ accounts for the change of the lattice parameter (a_0 being the lattice parameter of the homogeneous solid solution with composition c_0) and Y is a combination of elastic constants. It depends on the crystallographic direction of the composition modulation (the details on the derivation of the elastic energy term can be found, for example, in reference [Cahn1961]). As previously stated, the Fe-Cr system represents a rather simple case since pure iron and pure chromium have the same crystallographic structure and very similar lattice parameters. This fact allows the elastic term to be neglected in first approximation. If one neglects the free energy increase due to the coherency strain, a formal analogy can be established between equation (11) and equation (5), the latter describing the free energy change associated to the formation of solute droplets in the framework of classical nucleation model. Indeed, the positive contribution of the gradient energy $K^*(\nabla c)^2$ in equation (11), similarly to the interfacial term $4\pi R^2 \sigma_{\alpha\alpha'}$ in equation (5), can be regarded as the equivalent of an energy barrier opposing the nucleation. Such energy barrier can be overcome by the gain in chemical free energy when the composition difference between the fluctuation and the homogeneous solid solution is large enough. It must be emphasised the fact that the analogy between the $K^*(\nabla c)^2$ term in equation (11) with an interface energy term is more than simply formal. Indeed the composition gradient is non-zero only at the matrix/precipitate energy.

Cahn and Hilliard have shown [Cahn1959b] that, in the case of an isotropic system, the composition profile $c(r)$ of a critical nucleus (r being the distance from the centre of the fluctuation) can be obtained by integrating the following equation:

$$2K^* \frac{d^2c}{dr^2} + 4 \frac{K^*}{r} \frac{dc}{dr} = \left. \frac{\partial f}{\partial c} \right|_c - \left. \frac{\partial f}{\partial c} \right|_{c_0} \quad (12)$$

and considering the following boundary conditions:

$$\frac{dc}{dr} = 0 \text{ if } \begin{cases} r \approx 0 \\ r \rightarrow \infty \end{cases}. \quad (13)$$

The energy barrier that must be overcome for the critical nucleus to form in the homogeneous solid solution is:

$$\Delta F^* = 4\pi \int_0^\infty \left(f(c) - f(c_0) + K^* \left(\frac{dc}{dr} \right)^2 \right) r^2 dr. \quad (14)$$

The classical nucleation model is supposed to apply in weakly supersaturated solid solutions [Wagner2001]. As the supersaturation increases the matrix/precipitate interface becomes more and more diffuse and the non-classical nucleation model becomes more appropriated to describe the phase separation. Moreover, it should be noted that, when the supersaturation increases, the nucleus density in the matrix rises because of the increasing nucleation rate. As a consequence, the non-interacting precipitates approximation becomes less appropriate. It is clear that phase separation in supersaturated alloys represents a very complex scenario because of the breakdown of the simple classical nucleation theory on the one hand and the non-interacting precipitates approximation on the other hand. In this context it is very important to define a reliable criterion for the applicability of the simple classical nucleation theory. Cahn and Hilliard introduced such a criterion [Cahn1959b] by suggesting that the classical nucleation theory can be used for the modelling of the binary solid solutions phase separation if the following condition is fulfilled:

$$l^2 \frac{4\pi\sigma_{\alpha\alpha'}}{75k_B T} \ll 1. \quad (15)$$

Equation (15) simply states that the width of the diffuse interface l must be much smaller than the core of the nucleus where the composition is constant.

1.2.3.2 Precipitates growth

Regardless of the nucleation mechanism (classical or non-classical), once stable nuclei are formed, they might be embedded in a still supersaturated matrix. Chemical potential difference between the supersaturated matrix and the precipitates can be seen as a kinetic driving force promoting precipitates growth. Two different phenomena are involved in the growth mechanism: the diffusion of solute atoms through the matrix and the diffusion of the solute atoms through the precipitates' interface. The slowest process determines the growth rate. As the matrix becomes more and more depleted from solute atoms, the driving force is progressively reduced and solute diffusion through the bulk becomes slower and starts to drive the growth rate [Wagner2001]. Zener showed [Zener1949] that the precipitates radius grows with time as $t^{1/2}$. In this model, he considered that all the precipitates in the matrix were non-interacting spheres of the same size, that the solute concentration near the precipitates was equal to the equilibrium concentration of the α phase, and that the composition of the matrix far from the precipitates was equal to that of the homogeneous solution composition. Finally, he assumed that the diffusion coefficient in the matrix did not depend on the matrix composition. Zener's precipitates growth law can be written as:

$$R(t) = \left(2 \frac{c_0 - c_{\alpha}^{\text{eq}}}{c_{\alpha'}^{\text{pr}} - c_{\alpha}^{\text{eq}}} \right)^{\frac{1}{2}} (Dt)^{\frac{1}{2}} \quad (16)$$

where c_0 is the homogeneous solution composition, c_{α}^{eq} is the equilibrium composition of the α phase, $c_{\alpha'}^{\text{pr}}$ is the equilibrium composition of the α' precipitates and D is the diffusion coefficient in the matrix. It should be noted that one of the roughest approximation introduced by Zener consists in considering that the solute concentration near the matrix/precipitate curved interface of the precipitates is equal to the equilibrium concentration of the α phase. This hypothesis completely neglects the Gibbs-Thomson effect which corresponds to the fact that the solute concentration near the matrix/precipitate interface depends on the curvature of the interface. The relation can be written as follows:

$$c_R(R) = c_{\alpha}^{\text{eq}} \exp\left(\frac{2\sigma_{\alpha\alpha'} V_{\alpha'}}{k_B T R}\right) \quad (17)$$

where R is the radius of the α' precipitate, $V_{\alpha'}$ is the volume of the precipitate and $\sigma_{\alpha\alpha'}$ is the formation energy of the α/α' interface. Not considering the Gibbs-Thomson effect and assuming that all the precipitates have the same size are indeed closely related since the Gibbs-Thomson effect depend on the precipitates radius. It should be noted that Perez and Deschamps, in a recent work [Perez2003], used the classical nucleation and growth theory to model the carbide precipitation in low carbon steels. For the growth stage, they used the Zener's approach that they modified to take into account the Gibbs-Thomson effect and the fact that nucleation can occur during the growth stage. Perez and Deschamps successfully compared their results with experimentally obtained Time-Temperature-Transformation diagram.

1.2.3.3 Early stages of spinodal decomposition:

If a homogeneous supersaturated alloy is quenched in the unstable region of the phase diagram (where $\frac{\partial^2 F}{\partial c^2} < 0$), the phase separation can occur through the spinodal decomposition mechanism. The first theoretical description of the spinodal decomposition in binary alloys [Cahn1961, Cahn1965] is based on the Cahn and Hilliard continuum description of the free energy (the formalism is the same as the one used for the formulation of the non-classical nucleation theory). If one considers equation (10), the difference $f(c) - f(c_0)$ can be written as a Taylor development of the free energy about the free energy calculated for the homogeneous solution of composition c_0 :

$$f(c) - f(c_0) = (c - c_0) \frac{\partial f}{\partial c} + \frac{1}{2} (c - c_0)^2 \frac{\partial^2 f}{\partial c^2}. \quad (18)$$

Since $\int (c - c_0) dV = 0$, equation (10) then becomes:

$$\Delta F = (F - F_0) = \int_V \left[\frac{1}{2} (c - c_0)^2 \frac{\partial^2 f}{\partial c^2} + K^* (\nabla c)^2 + \eta^2 Y (c - c_0)^2 \right] dV. \quad (19)$$

If one considers sinusoidal concentration fluctuations, $c - c_0 = A \cos \beta x$, the subsequent variation of the free energy of the system is:

$$\frac{\Delta F}{V} = \frac{A^2}{4} \left(\frac{\partial^2 f}{\partial c^2} + 2K^* \beta^2 + \eta^2 Y \right). \quad (20)$$

If $\frac{\Delta F}{V}$ is negative, the solution is unstable with respect to the fluctuation of wavelength $\frac{2\pi}{\beta}$. The right hand side of equation (20) is quadratic on the amplitude of the fluctuation so the stability of the solution does not depend on the amplitude. The coefficient K^* has to be positive, otherwise the solution would be unstable also outside of the spinodal region. As a consequence, for $\frac{\partial^2 f}{\partial c^2} > 0$, the solution is stable with respect to sinusoidal fluctuations of all wavelengths. If $\frac{\partial^2 f}{\partial c^2} < 0$, the solution is unstable with respect to sinusoidal fluctuations of wavelengths greater than a critical value:

$$\lambda_c = \frac{2\pi}{\beta_c} = \left[-\frac{8\pi^2 K^*}{\frac{\partial^2 f}{\partial c^2} + \eta^2 Y} \right]^{\frac{1}{2}}. \quad (21)$$

It must be emphasised the fact that the $\eta^2 Y$ term in equation (20), representing the elastic energy term due to the coherency strain, tends to stabilise the solid solution with respect to the composition fluctuations. Indeed, the energy cost necessary to respect the coherency constraint partially compensates the chemical free energy gain associated to the phase separation. The chemical spinodal line, separating the metastable region from the unstable region in a binary phase diagram, only accounts for the chemical contribution to the free energy. When one considers the elastic energy contribution to the free energy, the spinodal region is reduced by the stabilising effect of the coherency strain. In this case, a new spinodal line, the coherent spinodal, must be defined as the boundary between the zone where unmixing occurs through the nucleation mechanism and the zone where spinodal decomposition is observed. This issue can be neglected in the case of the Fe-Cr systems because of the small difference between the pure chromium and pure iron lattice parameters.

Up to this point, we have described the thermodynamic aspect of the spinodal decomposition. A description of the kinetic evolution of the microstructure of a binary alloy A-B during the phase separation has been proposed by Cahn [Cahn1961, Cahn1965] by solving for the fluxes J_i the following equation:

$$J_B = -J_A = M\nabla(\mu_A - \mu_B), \quad (22)$$

where M is defined by Cahn [Cahn1965] as the ratio of diffusional flux to the gradient in chemical potential. The $\mu_A - \mu_B$ term can be obtained as the functional derivative of the free energy $F = [f(c) + K^*(\nabla c)^2 + \eta^2 Y(c - c_0)^2]$ with respect to the concentration of species A in one of the two phases:

$$\mu_A - \mu_B = \frac{\delta F}{\delta c_A}. \quad (23)$$

Finally, the well known Cahn-Hilliard equation can be obtained by considering Fick's second law, $-\nabla \cdot \mathbf{J} = \frac{\partial c(\mathbf{r}, t)}{\partial t}$, which is the continuity condition accounting for the conservation of the average solute concentration in the volume of the alloy, and considering only the linear functions of the composition. This corresponds to consider only the early stages of the phase separation. One obtains thus:

$$\frac{\partial c(\mathbf{r}, t)}{\partial t} = M \left(\frac{\partial^2 F}{\partial c^2} + 2\eta^2 Y \right) \nabla^2 c(\mathbf{r}, t) - 2MK^* \nabla^4 c(\mathbf{r}, t). \quad (24)$$

Equation (24) determines the spatial and time dependence of the concentration fluctuation $c(\mathbf{r}, t)$, thus any random statistical fluctuation is considered during the phase separation. This drawback of the Cahn-Hilliard theory has been removed by Cook [Cook1970] who introduced a Gaussian noise term in the right hand side of equation (24).

As a final remark on the spinodal decomposition mechanism, it must be emphasised that, as by Cahn *et al.* [Cahn1959b, Cahn1961], there is no sudden transition from the nucleation mechanism and spinodal decomposition: the nucleation mechanism approaches spinodal decomposition continuously with the increase of the supersaturation.

1.2.3.4 Late stages: coarsening regime:

The simple model of diffusional growth presented in equation 16 is based on the assumption that the precipitates are isolated and thus non-interacting particles, with uniform size. Moreover, as previously stated, it completely neglects the Gibbs-Thomson effect (equation 17). Such a model does not realistically describe the precipitates evolution beyond their nucleation stage. The main reason for that is the fact that, after the nucleation stage, the precipitates size distribution can be quite broad. According to the Gibbs-Thomson equation

(equation 17) the solubility near a small particle with a large surface to volume ratio is higher than near larger precipitates. As a consequence, the growth rate of a precipitate does depend on its size and hypothesis on which equation (16) is based brakes down. Because of the release of excess interfacial energy, larger precipitates will grow. On the other hand, small precipitates will dissolve. This process is called coarsening or Ostwald ripening and generally leads to the reduction of the precipitates number density. The coarsening of randomly dispersed precipitates is a very complex problem of multiparticle diffusion. The first theoretical description of the coarsening regime is the classical theory proposed by Lifshitz, Slyozov and Wagner (LSW) [Lifshitz1959]. The LSW theory of coarsening is based on the computation of the precipitates growth rate by taking into account the time evolution of the precipitate size distribution $\varphi(R, t)$. Lifshitz *et al.* computed the time evolution of the precipitates size distribution which satisfies the continuity equation:

$$\frac{\partial \varphi}{\partial t} + \frac{\partial}{\partial R} \left[\varphi \frac{\partial R}{\partial t} \right] = 0. \quad (25)$$

By introducing the precipitate size dependence in Zener's growth rate model, Lifshitz *et al.* had been able to take thus into account the Gibbs-Thomson effect. Using the following assumptions:

1. The thermodynamics of both α and α' can be described by a dilute solution model; and the linearised version of the Gibbs-Thomson equation can be considered.
2. The precipitate volume fraction $F_v = \frac{4\pi}{3} \bar{R}^3 N_v$ (where N_v is the precipitate number density) is close to zero and the particles only interact with an infinite matrix.
3. The decomposition is almost completed and the supersaturation is close to zero.

Lifshitz *et al.* derived the time evolution of the mean precipitate radius $\bar{R}(t)$ and of the precipitates number density $N_v(t)$ that, in the asymptotic limit ($\Delta c \rightarrow 0$, where Δc is the supersaturation), can be written as follows:

$$\bar{R}^3(t) = \frac{8D\sigma_{\alpha\alpha'}c_{\alpha'}^{eq}V_{\alpha'}}{9k_B T} t = K_R^{LSW} t \quad (26)$$

$$N_v(t) = \frac{3F_v}{4\pi K_R^{LSW}} t^{-1} = K_N^{LSW} t^{-1}. \quad (27)$$

Since the LSW theory of coarsening is based on the assumption that the precipitate volume fraction is close to zero, it should not apply to the description of the late stages of the phase separation by spinodal decomposition because the latter mechanism is expected to occur for high solute concentrations. Attempts to extend the LSW theory of coarsening to systems characterised by high precipitate volume fraction have been unsuccessful [Binder2001]. Nevertheless, experimental observations [Novy2009a] and atomistic kinetic Monte Carlo simulations [Huse1986, Pareige2011] have shown that the time exponent predicted by the LSW growth law still holds in systems with high solute concentrations.

1.2.3.5 Experimental observation and simulation of the Fe-Cr phase separation:

As previously mentioned, Xiong *et al.* [Xiong2010] presented a series of experimental results concerning the characterisation of the unmixing regime in binary Fe-Cr alloys. They showed the difficulty to accurately locate the spinodal curve, *i.e.* the boundary between nucleation-growth and spinodal regimes.

The experiences presented by Xiong *et al.* were mainly based on microstructure observations by small angle neutron scattering, Mössbauer spectroscopy, atom probe and transmission electron microscopy and were performed at temperatures between 673 and 823 K. One of the reasons of the difficulty of locating the spinodal curve is that, as explained previously, the morphology of the unmixed structure cannot be considered as a fully reliable signature of the decomposition mechanism. Several studies concerning the evolution of the microstructure of the Fe-Cr alloy were recently published. From an experimental point of view, the tomographic atom probe is particularly suitable for such studies since it allows to obtain three dimensional reconstructions of the atomic positions [Danoix2000]. A series of articles have been recently published presenting comparative studies of the Fe-Cr microstructure evolution observed by tomographic atom probe and simulated by kinetic Monte-Carlo (KMC) and/or obtained by numerical solutions of the Cahn-Hilliard-Cook

equation [Miller1995, Hyde1995a, Hyde1995b]. Miller *et al.* Hyde *et al.* considered alloys containing from 17 to 45 at.%Cr aged at 773 K during 500 hours. They observed the formation of isolated chromium precipitates together with some interconnected regions for a chromium content of 24 at.% and an interconnected structure from a chromium content of 32 at.%. As a consequence they proposed that the spinodal line should lie between 24 and 32 at.%Cr at 773 K, considering that the interconnected regions observed in alloy containing 24 at.% of chromium can be due to coarsening. More recent observations of Fe-Cr alloys by atom probe tomography [Novy2009a, Pareige2011] investigated the microstructure evolution during thermal ageing at 773 K of Fe-20 at.%Cr and Fe-25 at.%Cr. Novy and co-workers observed the formation of isolated precipitates in the Fe-20 at.%Cr alloy aged at 773 K - in agreement with previous observations of Bley [Bley1992] by small angle neutron scattering – whereas Pareige *et al.* observed interconnected structures in the Fe-25 at.%Cr alloy that they considered as the consequence of spinodal decomposition. Comparing their experimental results with those of KMC simulations, Pareige *et al.* [Pareige2011] found that the average width of the chromium-rich domains obtained from the simulations were about four times smaller than the values observed experimentally. Both Novy *et al.* [Novy2009a] and Pareige *et al.* [Pareige2011] showed that, despite the elevated matrix supersaturation, the time dependence of chromium-rich precipitates growth rate is described by the LSW coarsening theory in the late stages of the phase separation. KMC simulations have been largely used to investigate the separation phase mechanisms of the Fe-Cr system [Olsson2005a, Wallenius2007, Bonny2009c, Castin2010, Castin2011]. Bonny *et al.* and Castin *et al.* performed simulations of the thermal ageing of Fe-20 at.%Cr at different temperatures, and compared in particular the results they obtained at 773 K with those of Novy *et al.* [Novy2009a]. They obtained some success in reproducing the time dependence of the precipitates radius growth but quite unsatisfactory results about the comparison of the precipitate size. Olsson *et al.* [Olsson2005a], and Wallenius *et al.* [Wallerenius2007] performed KMC simulations of the thermal ageing of Fe-10 at.%Cr and Fe-32 at.%Cr at 704 K. They observed the formation of isolated chromium-rich precipitates in Fe-10 at.%Cr and interconnected chromium-rich and iron-rich domains in Fe-32 at.%Cr. Their conclusions are that for the low Cr content, the Fe-Cr system underwent phase separation by means of nucleation and growth whereas in the other alloy spinodal decomposition occurred. Regarding the interconnected structure observed in the Fe-32 at.%Cr, it could simply result from a coarsening process since the authors did not provide any other argument to prove that the decomposition regime they observed was indeed spinodal decomposition.

1.2.4 Magnetic properties of Fe-Cr alloy

As previously mentioned, the understanding (and modelling) of Fe-Cr alloys behaviour would seem somehow not to be a too complex task, as pure iron and pure chromium have the same crystallographic structure and very close lattice parameters in the temperature and concentration range pertinent with the service conditions in nuclear power plants. Nevertheless, the Fe-Cr binary alloy presents very complex and interesting properties because of magnetism. Pure iron is ferromagnetic, its Curie temperature is 1043 K [Xiong2010]. Pure chromium magnetic properties are more complex as below 311 K (Néel temperature), the local magnetic moments associated to each atom are oriented along an incommensurate spin density wave (SDW) [Fawcett1988]. The first observations by neutron diffraction suggesting the existence of this phenomenon were published by Corliss *et al.* in 1959 [Corliss1959]. In 1962, Overhauser [Overhauser1962] showed that the magnetic configuration of the ground state of an ideal electron gas is a spin wave. DFT ground state calculations for pure chromium are not able to reproduce the incommensurate SDW magnetic configuration; they predict a ground state which, from the magnetic point of view, is characterised by a commensurate antiferromagnetic arrangement whose the period equals the lattice parameter [Hafner2001, Hafner2002]. However, the impact of this drawback is rather marginal when the calculation of the cohesive energy of crystalline structures is addressed since the energy difference between the commensurate antiferromagnetic configuration and the incommensurate SDW magnetic configuration is very small: its order of magnitude is 10^{-3} eV [Hafner2001, Hafner2002, Soularior2010]. Concerning the magnetic properties of Fe-Cr system, the importance of the existence of an incommensurate spin density wave in chromium at low temperatures (below its Néel temperature) is limited to chromium-based alloys containing a very small percentage of iron. Indeed, Tsunoda drew a magnetic phase diagram of Fe-Cr alloy based on the available experimental observations [Tsunoda1994] which shows that, below the Néel temperature, above an iron concentration of 1.5 at.%, the Fe-Cr system is antiferromagnetic with a period equal to the lattice parameter (AF₀ in figure 7-Ch4). A very small amount of iron in chromium is enough to destroy the incommensurate spin density wave configuration. Figure 7-Ch1 shows the phase diagram proposed by Tsunoda: for very low iron contents (<1.5 at.%), the local magnetic moments of the atoms in the structure are oriented along a longitudinal (L-SDW) or transverse (T-SDW) spin density wave depending

on the temperature. When the iron concentration lies between 1.5 at.% and about 2 at.%, the L-SDW phase is completely removed whereas the T-SDW phase can only be observed within a small temperature range. Finally, when chromium content exceeds 2 at.%, the system exhibits a commensurate antiferromagnetic configuration with a period equal to the lattice parameter (AF_0 in figure 7-Ch4) at temperatures below 250 K and is paramagnetic at higher temperatures. The research of materials for the nuclear industry focuses on iron-based alloys whose service temperature is above the chromium Neel temperature; as a consequence, in the context of this work, it is very reasonable to consider that the magnetic ground state of chromium corresponds to a commensurate antiferromagnetic configuration.

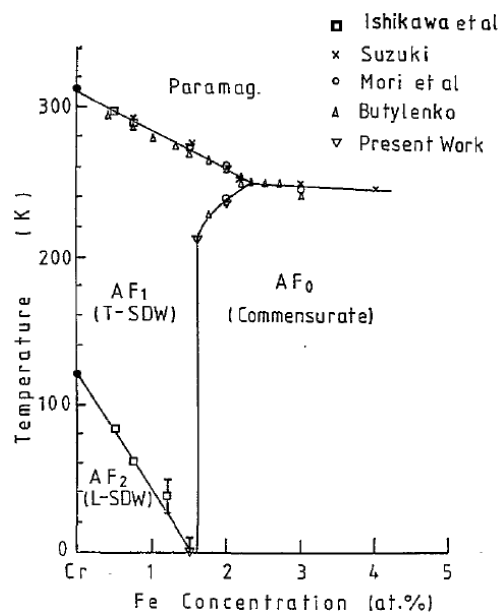


Figure 7-Ch1 Magnetic phase diagram of Cr-Fe alloy. The figure is from Tsunoda *et al.* [Tsunoda1994]

In the following of this manuscript we will show that the magnetic interactions between the iron atoms constituting the matrix and solute chromium atoms is a fundamental issue when one is interested in the thermodynamic and kinetic properties of the Fe-Cr alloy. It is therefore necessary to consider, as a starting point for the study of Fe-Cr, some experimental and theoretical results illustrating the effects that introducing chromium atoms in an iron matrix has on the arrangement of the local magnetic moments of the atoms. Aldred performed magnetisation measurements on iron-based alloys with a chromium content between 2 and 70 at.% and showed that the chromium atoms magnetic moments tend to be oriented in opposite direction with respect to the iron atoms of the matrix and that their absolute value decreases when the chromium concentration increases [Aldred1976a]. This result has been confirmed by observations, using neutron scattering, of Aldred *et al.* and

Kajzar *et al.* [Aldred1976b, Kajzar1980] and, more recently, by the DFT calculations of Klaver *et al.* [Klaver2006] and Nguyen-Manh *et al.* [Nguyen-Manh2009]. The DFT calculations showed the link between the reduction of the local magnetic moment absolute value of the chromium atoms and the increase in the chromium local concentration. Indeed, when chromium concentration increases, magnetic frustration rises as the result of the competition between the tendency of the chromium atoms to orient their magnetic moments in antiparallel direction with respect to those of the surrounding iron atoms and in an antiferromagnetic configuration with respect to the chromium atoms.

In this chapter, we discussed the importance of ferritic steels in the context of operating nuclear reactors and the reasons why they are leading candidates for structural materials in future generation nuclear power plants. We then presented the Fe-Cr binary alloy as a simplified system for the modelling of the ferritic phase of stainless steels. We discussed recent researches concerning the Fe-Cr phase diagram and, in particular, the still open issue concerning the phase boundaries at low temperatures. We briefly outlined the theoretical models describing the thermodynamics of phase coexistence in a binary alloy quenched in the miscibility gap and discussed the reason why the Fe-Cr alloy represents a simple system for the validation of such models. We then discussed the fact that, even if the Fe-Cr binary alloy is a simplified system with respect to ferritic stainless steels, especially for studying the time evolution of the microstructure at a given temperature, it still carries some difficulties that are mainly due to its very particular magnetic properties.

2. SIMULATION METHODS

In chapter 2, we will introduce the theoretical methods that we exploited in order to investigate some properties of the Fe-Cr system: from the cohesive energy associated to a given configuration to the migration energy of a vacancy introduced in the structure. The latter being a fundamental issue for our further investigation of the kinetic properties of the Fe-Cr binary alloy.

In section 2.1, we will describe the theoretical foundations of the two cohesive models (*i.e.* the density functional theory and the embedded atom method interatomic potentials) which we used to compute the ground state energy associated to a given Fe-Cr structure. In the case of the embedded atom method approach, we will briefly describe the Fe-Cr interatomic potentials available in the literature and we will present some arguments leading to the choice of the more appropriate one for describing the Fe-Cr system.

In section 2.2, we will present and discuss some preliminary calculations performed within the density functional theory and the embedded atom method. First, we will compare the density functional theory and the Fe-Cr embedded atom method potential results about the chromium-chromium and the chromium-vacancy binding energy as well as the vacancy formation energy in pure iron and pure chromium. Second, we will use the density functional theory to sketch out some magnetic properties of substitutional chromium atom in a pure iron matrix.

In section 2.3, the methods we will use for computing the vacancy migration energy within both the density functional theory and the embedded atom method will be introduced; some tests that we performed in order to optimise the parameters pertinent to these techniques will be illustrated.

2.1 Cohesive models: DFT & EAM potentials

One of the basic tasks necessary to build a thermodynamic and kinetic description of a crystal – a binary alloy in our case – is to estimate the underlying energies of the system. From a thermodynamic point of view, it is important, for example, to determine the configuration of the system which minimises the cohesive energy. On the other hand, to investigate the evolution of the system, the potential energy associated to a particular configuration is the essential starting point to determine the minimal energy path for a given transition to occur.

From a quantum mechanical point of view, computing the energy of a crystal corresponds to computing the eigenvalues of the Hamiltonian operator, which implies solving the Schrödinger equation:

$$\hat{H}\Psi = E\Psi \quad (1)$$

where \hat{H} is the Hamiltonian operator, Ψ is the many-body wavefunction and E is the energy.

The time-independent Schrödinger equation describing N interacting particles is exactly solvable, under some assumptions (*e.g.* the potential generated by each interacting particle has a spherical symmetry), only for $N \leq 2$. If $N > 2$, an approximated approach is necessary to solve the so called quantum many-body problem. "*Ab initio*" methods are a class of techniques whose aim is to provide an approximate solution for the quantum many-body problem. It should be emphasised that, despite the denomination "*ab initio*" – which is related to the fact that these techniques requires the number of atoms and their species as the only initial data to solve the Schrödinger equation –, these techniques rely on a certain number of approximations.

2.1.1 Density Functional Theory

A widely exploited "*ab initio*" approach in solid state physics is Density Functional Theory (DFT). DFT allows to compute the ground state energy associated to a many-electron time-independent Hamiltonian.

The Hamiltonian operator describing an ensemble of interacting atoms can be written as:

$$\hat{H} = -\frac{\hbar}{2m_e} \sum_i \nabla_i^2 - \sum_I \frac{\hbar}{2M_I} \nabla_I^2 + \frac{1}{2} \sum_{i \neq j} \frac{e^2}{|\mathbf{r}_i - \mathbf{r}_j|} + \frac{1}{2} \sum_{I \neq J} \frac{Z_I Z_J}{|\mathbf{R}_I - \mathbf{R}_J|} - \sum_{i,I} \frac{e Z_I}{|\mathbf{r}_i - \mathbf{R}_I|} \quad (2)$$

where \hbar is the reduced Plank's constant, m_e , e and \mathbf{r}_i are the electron mass, electric charge and position, M_I , Z_I are the mass and the electric charge of a nucleus at position \mathbf{R}_I , ∇_i and ∇_I are the nabla operators acting on the electrons wavefunctions and the nuclei wavefunctions respectively.

The Schrödinger equation associated to Hamiltonian (2) is:

$$\hat{H}\Psi(\mathbf{r}_i, \mathbf{R}_I) = E\Psi(\mathbf{r}_i, \mathbf{R}_I) \quad (3)$$

The first approximation which is introduced in DFT is the Born-Oppenheimer approximation. It assumes that, because of the mass difference between the nuclei and the electrons (the nucleus mass is at least three orders of magnitude higher than the electron mass), electrons can be considered as moving in the potential generated by fixed nuclei. As a consequence of the Born-Oppenheimer approximation, the Hamiltonian of the system can be written as a many-electron Hamiltonian containing a term representing the external potential generated by the nuclei:

$$\hat{H}_e = \hat{T}_e + \hat{V}_{\text{int}} + \hat{V}_{\text{ext}} \quad (4)$$

where \hat{T}_e is the electrons kinetic operator, \hat{V}_{int} is the electron-electron interaction operator and \hat{V}_{ext} is the operator accounting for the electrons' interaction with the external potential generated by the nuclei. To describe the Hamiltonian for the whole system (the electrons plus the nuclei) the nucleus-nucleus interaction operator \hat{V}_{n-n} should also be taken into account. Despite the simplification of nuclei contribution to the Hamiltonian of the system by means of the Born-Oppenheimer approximation, the many-body problem holds and the solution of the Schrödinger equation remains a hard task. One of the main features of the way DFT provides an approximate solution of the many-body problem consists in reformulating the problem by considering the electron charge density as the main variable instead of the wavefunction. A complete description of DFT is given, for example, in reference [Martin2004].

DFT is conceptually based on the Thomas-Fermi model (for a complete description of the model see, for example, [Parr1989]) which represents the first attempt (in the 1920's) to

express the total energy of an ensemble of atoms as a functional of the electron density. The Thomas-Fermi model is based on the assumption that the electrons are uniformly distributed in the six dimensional phase space and that they obey the Fermi-Dirac distribution. Starting from these considerations, Thomas and Fermi introduced an expression of the electrons kinetic energy as a functional of electron density and derived a total energy functional by adding two terms accounting for the nucleus-electron and electron-electron electrostatic interactions. Finally, they assumed that the real ground-state electron density is the one which minimise the total energy functional. Forty years later, Hohenberg and Kohn demonstrated this latter assumption and proved that the many-body quantum problem can be rigorously formulated considering the many-electron density instead of the many-electron wave function. The Thomas-Fermi model turned out to be an oversimplified version of modern DFT.

2.1.1.1 Hohenberg and Kohn theorems

The Hohenberg and Kohn theorems [Hohenberg1964] represent the theoretical basis for the formulation of DFT. They prove that the many-body problem can be formulated in terms of electron density rather than many-electron wavefunction. If the many-electron wavefunction is normalised, then the electron density is:

$$n(\mathbf{r}) = \frac{\langle \Psi | \hat{n}(\mathbf{r}) | \Psi \rangle}{\langle \Psi | \Psi \rangle} = N \int \Psi^*(\mathbf{r}, \mathbf{r}_2, \dots, \mathbf{r}_N) \Psi(\mathbf{r}, \mathbf{r}_2, \dots, \mathbf{r}_N) d\mathbf{r}_2 \dots d\mathbf{r}_N \quad (5)$$

where $\hat{n}(\mathbf{r}) = \sum_{i=1}^N \delta(\mathbf{r} - \mathbf{r}_i)$ is the density operator, N is the number of particles and \mathbf{r}_i are the position vectors associated to each particle. The first Hohenberg and Kohn theorem states that for all systems of interacting particles in an external potential V_{ext} , the external potential V_{ext} is determined up to an additive constant by the knowledge of the ground state electron density $n(\mathbf{r})_0$. The second Hohenberg and Kohn theorem states that the energy of the many-electron system can be defined as a functional $E_{\text{HK}}[n]$ of the density $n(\mathbf{r})$ regardless of the choice of V_{ext} :

$$E_{\text{HK}}[n] = T_{\text{HK}}[n] + E_{\text{int}}[n] + \int V_{\text{ext}}(\mathbf{r})n(\mathbf{r})d\mathbf{r} + V_{n-n} \quad (6)$$

and that the absolute minimum of the functional $E_{\text{HK}}[n]$ corresponds to the energy ground state of the system and the electron density $n(\mathbf{r})$ which minimise $E_{\text{HK}}[n]$ is the ground state

electron density $n_0(\mathbf{r})$. The Hohenberg and Kohn theorems have two fundamental consequences:

- 1) The Hamiltonian operator of a many-electron system can be expressed as a functional of the electron density.
- 2) A variational approach for computing the energy ground state can be exploited when the many-electron problem is formulated in term of electron density.

Simple demonstrations of the Hohenberg and Kohn theorems can be found in references [Parr1989] and [Martin2004]. It should be noticed that Hohenberg and Kohn theorems also hold when the spin degree of freedom of each electron is taken into account. In the latter case the electron density depends not only on position but also on a spin variable:

$$n(\mathbf{r}) = n(\mathbf{r}, \uparrow) + n(\mathbf{r}, \downarrow) \quad (7)$$

and the energy of the system will depend both on electron density and spin density:

$$E = E_{\text{HK}}[n, s] \quad (8)$$

where the spin density can be written as:

$$s(\mathbf{r}) = n(\mathbf{r}, \uparrow) - n(\mathbf{r}, \downarrow). \quad (9)$$

The many-body problem can be formulated exactly in terms of the electron density which is a function depending on a position vector \mathbf{r} and, possibly, a spin degree of freedom rather than the more complex and more abstract many-body wavefunction. However, the Hohenberg and Kohn theorems do not provide a solution of the many-body Schrödinger equation.

2.1.1.2 Kohn-Sham equations

It was thanks to the work of Kohn and Sham [Kohn1965] that DFT became an exploitable approach for ground state energy calculations. The Kohn and Sham method allows solving the many-body problem in the framework of Hohenberg and Kohn theorems and provides the energy and the wavefunction of the ground state of an N-electrons system.

The Kohn and Sham achievement basically consists in replacing the N-body problem by N single body problems. In the Kohn and Sham picture, each electron is described with a single particle time-independent Schrödinger equation where the potential accounts for all exchange-correlation and Coulomb interactions due to the presence of all other electrons. The consistency of this point of view relies on the following assumption: the electron density of the ground state of N interacting particles can be expressed as the electron density of the ground state of N non-interacting particles which experience an external potential. The non-interacting particle system can be described with a Hamiltonian with a kinetic part represented by the usual operator $-\frac{1}{2}\nabla^2$ and a potential $V_{\text{eff}}^\sigma(\mathbf{r})$ which acts on an electron at position \mathbf{r} with spin σ and accounts for exchange-correlation effects. The Kohn-Sham effective Hamiltonian is:

$$\hat{H}_{\text{KS}}^\sigma = -\frac{1}{2}\nabla^2 + \hat{V}_{\text{eff}}^\sigma(\mathbf{r}). \quad (10)$$

Once the $\psi_i^\sigma(\mathbf{r})$ one-electron eigenfunctions associated to the Kohn-Sham Hamiltonian $\hat{H}_{\text{KS}}^\sigma$ has been computed, the electron density of the real system can be obtained by:

$$n(\mathbf{r}) = \sum_\sigma n(\mathbf{r}, \sigma) = \sum_\sigma \sum_{i=1}^{N^\sigma} |\psi_i^\sigma(\mathbf{r})|^2. \quad (11)$$

The expectation value of the kinetic energy of the system is given by the average of the kinetic operator:

$$T_{\text{KS}} = -\frac{1}{2} \sum_\sigma \sum_{i=1}^{N^\sigma} \langle \psi_i^\sigma | \nabla^2 | \psi_i^\sigma \rangle = -\frac{1}{2} \sum_\sigma \sum_{i=1}^{N^\sigma} \int d^3r |\nabla^2 \psi_i^\sigma(\mathbf{r})|^2 \quad (12)$$

while the Coulomb energy due to electron-electron interaction can be written as:

$$E_C[n] = \frac{1}{2} \int d\mathbf{r} d\mathbf{r}' \frac{n(\mathbf{r})n(\mathbf{r}')}{|\mathbf{r}-\mathbf{r}'|}. \quad (13)$$

Thus, the total Kohn-Sham energy can be written as an electron density functional:

$$E_{KS}[n] = T_{KS}[n] + \int d\mathbf{r} V_{\text{ext}}(\mathbf{r})n(\mathbf{r}) + E_C[n] + E_{n-n} + E_{xc}[n], \quad (14)$$

where $E_{xc}[n]$ carries all exchange-correlation effects. Energy $E_{xc}[n]$ can be defined from Hohenberg and Kohn functional (equation 6):

$$E_{xc}[n] = T_{HK} + E_{\text{int}} - (T_{KS}[n] + E_C[n]) = \langle \hat{T}_{HK} \rangle - T_{KS}[n] + \langle \hat{V}_{\text{int}} \rangle - E_C[n]. \quad (15)$$

In this scheme $E_{xc}[n]$ is the difference between the energy of the N interacting electron system and the fictitious N uncoupled electrons system. From this point of view, $E_{xc}[n]$ accounts for the difference between the kinetic energy of non interacting electrons (fictitious system) and the kinetic energy of interacting electrons (real system) and the difference between the total interaction energy of the electrons and the Coulomb contribution. In order to find the ground state energy associated to the Kohn-Sham Hamiltonian, the variational method can be used to find the minimum of $E_{KS}[n]$ functional with respect to the wavefunction. This approach leads to the following variational equation:

$$\frac{\delta E_{KS}}{\delta \psi_i^{\sigma*}(\mathbf{r})} = \frac{\delta T_{KS}}{\delta \psi_i^{\sigma*}(\mathbf{r})} + \left[\frac{\delta E_{\text{ext}}}{\delta n(\mathbf{r},\sigma)} + \frac{\delta E_C}{\delta n(\mathbf{r},\sigma)} \frac{\delta E_{xc}}{\delta n(\mathbf{r},\sigma)} \right] \frac{\delta n(\mathbf{r},\sigma)}{\delta \psi_i^{\sigma*}(\mathbf{r})} = 0. \quad (16)$$

By considering the following relations:

$$\frac{\delta T_{KS}}{\delta \psi_i^{\sigma*}(\mathbf{r})} = -\frac{1}{2} \nabla^2 \psi_i^\sigma(\mathbf{r}) \quad (17)$$

$$\frac{\delta n(\mathbf{r},\sigma)}{\delta \psi_i^{\sigma*}(\mathbf{r})} = \psi_i^\sigma(\mathbf{r}) \quad (18)$$

and wavefunction orthonormalisation constraints $\langle \psi_i^\sigma | \psi_j^{\sigma'} \rangle = \delta_{ij} \delta_{\sigma\sigma'}$, equation (16) leads, *via* the Lagrange multiplier method, to the Kohn-Sham equations [Martin2004]:

$$(\hat{H}_{\text{KS}}^\sigma - \varepsilon_i^\sigma) \psi_i^\sigma(\mathbf{r}) = 0 \quad (19)$$

where the Kohn-Sham Hamiltonian $\hat{H}_{\text{KS}}^\sigma$ is

$$\hat{H}_{\text{KS}}^\sigma = -\frac{1}{2}\nabla^2 + \underbrace{\frac{\delta E_{\text{ext}}}{\delta n(\mathbf{r},\sigma)} + \frac{\delta E_{\text{C}}}{\delta n(\mathbf{r},\sigma)} + \frac{\delta E_{\text{xc}}}{\delta n(\mathbf{r},\sigma)}}_{\hat{V}_{\text{KS}}^\sigma}. \quad (20)$$

The Kohn-Sham equations are iteratively solved with a self-consistent approach: a trial electron density is used to compute the Kohn-Sham Hamiltonian operator, the Hamiltonian operator is diagonalised and the one-electron wavefunctions are calculated. Self-consistency is achieved *via* the computation of the electron density of the N-electron system from equation (11). Once the electron density obtained, the total energy of the system is computed as:

$$E = \sum_\sigma \left(\sum_{i=1}^{N^\sigma} \varepsilon_i - \frac{1}{2} \int d\mathbf{r} d\mathbf{r}' \frac{n(\mathbf{r},\sigma)n(\mathbf{r}',\sigma)}{|\mathbf{r}-\mathbf{r}'|} + E_{\text{xc}}[n] - \int d\mathbf{r} V_{\text{xc}} n(\mathbf{r},\sigma) \right) \quad (21)$$

where

$$V_{\text{xc}} = \frac{\delta E_{\text{xc}}}{\delta n(\mathbf{r},\sigma)} \text{ and}$$

$\sum_\sigma \sum_{i=1}^{N^\sigma} \varepsilon_i = \sum_\sigma \sum_{i=1}^{N^\sigma} \left\langle \psi_i^\sigma \left| -\frac{1}{2}\nabla^2 + \hat{V}_{\text{KS}}^\sigma \right| \psi_i^\sigma \right\rangle = T_{\text{KS}}[n] + \int d\mathbf{r} V_{\text{KS}} n(\mathbf{r},\sigma)$. The nuclei of the structure are then relaxed by computing the interatomic forces from equation (21) *via* the Hellmann-Feynman theorem [Parr1989].

The form of equations (19) does not depend on the choice of the functional E_{xc} , thus the Kohn-Sham approach to the solution of the N-body problem is rigorously exact up to this point.

2.1.1.3 The Local Density Approximation (LDA) and Generalised gradient Approximation (GGA) approximations for the exchange-correlation functional

The first approximation which is introduced to solve the Kohn-Sham equations concerns the functional form of the exchange-correlation energy $E_{xc}[n]$ from which the exchange-correlation potential is obtained as the functional derivative with respect to the electron density: $V_{xc} = \frac{\delta E_{xc}[n]}{\delta n(\mathbf{r},\sigma)}$. Kohn and Sham proposed [Kohn1965] to express $E_{xc}[n]$ as a local functional of the electron density (Local Density Approximation) with the following form:

$$E_{xc}^{LDA}[n] = \int d\mathbf{r} n(\mathbf{r}) \varepsilon_{xc}[n(\mathbf{r})] \quad (21)$$

where $\varepsilon_{xc}[n(\mathbf{r})]$ is the exchange-correlation energy per particle. Within the LDA approach, the exchange–correlation energy is chosen as being equal to the one of a homogeneous electron gas with density $n(\mathbf{r})$. LDA can be extended to local spin density approximation (LSDA) if spin degree of freedom is taken into account. Neglecting spin-orbit coupling, the electron density can be written as a function of the position and a spin variable:

$$n(\mathbf{r}) = n(\mathbf{r}, \uparrow) + n(\mathbf{r}, \downarrow). \quad (22)$$

thus, the exchange-correlation energy in LSDA framework is:

$$E_{xc}^{LSDA}[n^\uparrow, n^\downarrow] = \int d\mathbf{r} n(\mathbf{r}) \varepsilon_{xc}[n(\mathbf{r}, \uparrow), n(\mathbf{r}, \downarrow)]. \quad (23)$$

Equation (23) holds in the case of collinear spins (the spin quantification direction is the same for all particles) but LSDA can be further generalised to the case of non-collinear spin. Even if LDA and LSDA seem to be quite rough approximations, they provide a satisfactory description of many systems. However, they are less accurate for the study of transition metals, in particular LSDA fails to capture the ground state of iron. Indeed LSDA provides slightly lower ground state energy for the non-magnetic hexagonal close packed (hcp) iron than for ferromagnetic iron [Burke2007]. The improvement of the LSDA approximation is the generalised gradient approximation (GGA) which consists in introducing

a non-local dependence of exchange-correlation energy on electron density. In the GGA framework, a dependence on the gradient of the electron density is introduced in the E_{xc} functional, thus the exchange-correlation energy is:

$$E_{xc}^{GGA}[n^\uparrow, n^\downarrow] = \int d\mathbf{r} n(\mathbf{r}) \varepsilon_{xc}[n(\mathbf{r}, \uparrow), n(\mathbf{r}, \downarrow), \nabla n(\mathbf{r}, \uparrow), \nabla n(\mathbf{r}, \downarrow)]. \quad (24)$$

While LDA and LSDA are uniquely defined, different parameterisations exist for the implementation of GGA. The most widely used parameterisations of GGA are those introduced by Perdew, Wang (PW91) [Perdew1991, Perdew1992] and by Perdew, Burke and Ernzerhof [Perdew1996]. The GGA predicts the experimentally observed ferromagnetic bcc phase for the ground state of iron [Domain2001, Postnikov2003]. In all DFT calculation which will be presented and discussed in this work the GGA approach has been used with PW91 parameterisation of Perdew and Wang.

2.1.1.4 Kohn-Sham wavefunction development and description of the electron-ion interaction (pseudopotentials and the Projector Augmented Wave (PAW) method)

Beyond the choice of the functional form of the exchange-correlation energy, the Kohn-Sham method for the solution of the N-body problem requires a further approximation effort which concerns the representation of the one-electron wavefunctions and the description of the ion-electron interactions.

In periodic crystalline structures, the potential generated by the ions is symmetric under discrete translations and so is the Hamiltonian of the system. As a consequence, the Bloch theorem (see [Bloch1928] for the original paper, or [Ashcroft1976]) is verified and one-electron wavefunctions obey the Bloch condition:

$$\psi_{\mathbf{k}}(\mathbf{r} + \mathbf{T}) = e^{i\mathbf{k}\cdot\mathbf{T}} \psi_{\mathbf{k}}(\mathbf{r}) \quad (25)$$

where \mathbf{k} is the Bloch wave vector and \mathbf{T} is the lattice translation vector. If the Kohn-Sham Hamiltonian eigenfunctions and eigenvalues computation is performed in reciprocal the space, then the translational symmetry will apply to one-electron energy eigenvalues, so that:

$$\varepsilon_{\mathbf{k}+\mathbf{K}} = \varepsilon_{\mathbf{k}} \quad (26)$$

where \mathbf{K} is a reciprocal lattice vector. From equations (25) and (26) follow that all the properties of the whole crystal can be obtained by solving the Kohn-Sham equation in the first Brillouin zone. In order to implement the numerical solution of the Kohn-Sham equations, the one-electron wavefunction must be developed on a finite dimension basis set. The choice of the basis set is done together with some approximations concerning the way the ion-electron interaction potential is described and taken into account. Plane waves can be used as basis set to develop the one-electron wavefunctions. In this case, the wavefunctions are expressed as follows:

$$\psi_i(\mathbf{r}) = \sum_{\mathbf{K}} c_{i,\mathbf{K}} e^{i(\mathbf{k}+\mathbf{K})\cdot\mathbf{r}}. \quad (27)$$

To be numerically tractable, the plane waves development must be truncated to an appropriate value of \mathbf{K} which allows a good description of the wavefunctions with low numerical cost. This can be achieved for slowly varying wavefunctions as the ones of valence electrons are. However, in the core region, wavefunctions have a rapidly oscillating behaviour and a very large number of plane waves must be included in the expansion in order to guarantee the convergence towards the real wavefunction. A widely exploited procedure to deal with this issue consists in defining a distance r_c from the ions which represents the limit between the core region ($r < r_c$) and the valence region ($r > r_c$). Core electrons are considered as "frozen" in the core region. The valence electrons experience a potential which is smoothed in the core region with respect to the $\frac{Z}{r}$ potential (where Z is the atomic number of the ions and r is the distance from the ions) because of the screening effect due to the core electrons. The real wavefunction $\psi_i^{\text{real}}(r)$ is then replaced with a smoothed pseudo-wavefunction $\psi_i^{\text{PS}}(r)$ which is an eigenfunction of a Kohn-Sham equation where the external potential has been replaced with the pseudopotential. The following constraints must be satisfied:

1. Real and pseudo valence eigenvalues agree for a given atomic configuration.
2. Real wavefunction $\psi_i^{\text{real}}(r)$ and pseudo-wavefunction $\psi_i^{\text{PS}}(r)$ are identical for $r > r_c$.

3. The total charge of each pseudo-wavefunction equals the charge of the real wavefunction in core region (norm-conservation condition):

$$\int_0^{r_c} r^2 |\psi_i^{\text{PS}}(r)|^2 dr = \int_0^{r_c} r^2 |\psi_i^{\text{real}}(r)|^2 dr.$$

The method described above is the norm-conserving pseudopotentials approach [Hamann1979]. 3d transition metals are characterised by strongly varying atomic orbitals. In such context the norm-conservation is a strong constraint which requires large plane waves basis set to be fulfilled. In the Ultrasoft pseudopotential approach (USPP), introduced by Vanderbilt [Vanderbilt1990], the norm-conservation condition is relaxed. As a consequence a more efficient smoothing of the wavefunctions in core region is possible and the wavefunctions can be expanded on a smaller basis set with respect to the case of norm-conserving pseudopotentials. One drawback is that the USPP approach can lead to a bad estimation of the electron density in the core region [Martin2004]. Another approach describing the electron-ion interactions is the projector augmented wave (PAW) method [Blöchl1994]. In principle, the PAW method is an all-electron approach which allows a more accurate description of the core region and valence region with respect to pseudopotential methods. In the PAW method, core electron wavefunctions are expanded in terms of atomic orbitals. Concerning the description of the valence electrons, the PAW technique consists in introducing a linear transformation \mathcal{T} which maps a set of smooth auxiliary wavefunctions $\tilde{\psi}(\mathbf{r})$, suitable for a plane wave expansion, onto real wavefunctions $\psi(\mathbf{r})$:

$$\psi(\mathbf{r}) = \mathcal{T}\tilde{\psi}(\mathbf{r}). \quad (28)$$

The variation principle can be applied to auxiliary wavefunctions to find the ground state of the system and the real wavefunctions can be retrieved *via* the transformation \mathcal{T} . \mathcal{T} is defined as:

$$\mathcal{T} = 1 + \sum_{\mathbf{R}} S_{\mathbf{R}} \quad (29)$$

where 1 is the identity operator and $S_{\mathbf{R}}$ is the difference between the real and the auxiliary wavefunctions at site \mathbf{R} . Operator $S_{\mathbf{R}}$ vanishes beyond a distance r_c defined as being the limit of the core region. In the core region (*i.e.* where $|\mathbf{r} - \mathbf{R}| < r_c$), valence electron

wavefunctions can be expanded in terms of auxiliary partial waves defined in the framework of quantum scattering theory. Hence, in the core region corresponding to each site, the real wavefunctions of the valence electrons can be written as:

$$\psi(\mathbf{r}) = \sum_i c_i \phi_i(\mathbf{r}) \quad (30)$$

for $|\mathbf{r} - \mathbf{R}_R| < r_{c,R}$ where \mathbf{R}_R stands for the position vector of site R (r_c also depends on atomic site because different atomic species can be included in the structure). The index i in equation (30) runs on all atomic sites and on quantum numbers which identify the partial waves. Since the valence electron wavefunctions must be orthogonal with respect to core electrons wavefunctions, the partial waves $\phi_i(\mathbf{r})$ must be chosen orthogonal to the atomic orbitals which are employed as basis set for the expansion of the core electron wavefunctions. For each partial wavefunction, an auxiliary partial wavefunction can be introduced and auxiliary real wavefunctions can be expanded on an auxiliary partial wavefunction set:

$$\tilde{\psi}(\mathbf{r}) = \sum_i \tilde{c}_i \tilde{\phi}_i(\mathbf{r}). \quad (31)$$

The expansion coefficients \tilde{c}_i are obtained from the scalar product $\langle \tilde{p}_i | \tilde{\psi} \rangle$ where $\langle \tilde{p}_i |$ is the dual vector of state $|\tilde{\phi}_i\rangle$.

Thus, the local (local refers to the core region corresponding to a single atomic site) action of S_R operator on valence electron auxiliary wavefunctions can be defined by its action on the auxiliary partial wave states (partial waves are the position representation of partial wave states):

$$S_R |\tilde{\phi}_i\rangle = |\phi_i\rangle - |\tilde{\phi}_i\rangle, \quad (32)$$

where $|\phi_i\rangle$ and $|\tilde{\phi}_i\rangle$ are the partial wave states for the real wavefunctions and the auxiliary wavefunctions respectively. The action of S_R on an auxiliary state will be:

$$S_R |\tilde{\psi}\rangle = \sum_i S_R |\tilde{\phi}_i\rangle \langle \tilde{p}_i | \tilde{\psi} \rangle = \sum_i (|\phi_i\rangle - |\tilde{\phi}_i\rangle) \langle \tilde{p}_i | \tilde{\psi} \rangle. \quad (33)$$

Operator \mathcal{T} can then be written as:

$$\mathcal{T} = 1 + \sum_i (|\phi_i\rangle - |\tilde{\phi}_i\rangle) \langle \tilde{p}_i |, \quad (34)$$

$$\text{and } |\psi\rangle = |\tilde{\psi}\rangle + \sum_i (|\phi_i\rangle - |\tilde{\phi}_i\rangle) \langle \tilde{p}_i | \tilde{\psi}\rangle.$$

The USPP and the PAW are very similar approaches except for the fact that PAW provides a more accurate description of the core region than USPP does. Many properties of materials, such as bond length or bulk modulus, are described with equal accuracy by USPP and PAW but this is not the case for magnetic properties such as magnetisation energy or atomic local magnetic moment for which PAW approach is more reliable than USPP approach [Kresse1999]. In the particular case of Fe or Cr structures, Olsson *et al.* have shown that experimental measurement of local magnetic moment is better reproduced with the PAW method than with the USPP approach [Olsson2007].

In this work, all DFT calculations have been performed using the Vienna *Ab initio* Simulation Package (VASP) [Kresse1996a, Kresse1996b] implemented with the projector augmented wave method [Blöchl1994] in the general gradient approximation (PAW-GGA) with the Perdew and Wang parameterisation (PW91) for the exchange correlation energy functional [Perdew1991, Perdew1992]. The Brillouin zone sampling has been done using the Monkhorst-Pack scheme [Monkhorst1976]. We performed spin-polarised calculations within the collinear approach: all spin variables are oriented along the same direction. The Vosko *et al.* correction on the interpolation of the correlation energy [Vosko1980] has been systematically taken into account. In all our calculations, the iron matrix has been initially placed in its ground state ferromagnetic configuration with local magnetic moment (LMM) of $2.1 \mu_B$, close to the experimentally observed value of $2.22 \mu_B$ [Kittel1996]. Chromium atoms have been introduced in the system by replacing iron atoms. Following Klaver *et al.* DFT calculations [Klaver2006] the initial LMM of isolated chromium atoms have been oriented anti-ferromagnetically with respect to the matrix iron atoms. When two or more chromium atoms are close to each other in the matrix, their LMM are oriented ferromagnetically, if they are second nearest neighbours (2nn) and anti-ferromagnetically, if they are first nearest neighbours (1nn). Unless otherwise specified, all along this work, we performed the DFT computation of the ground state energy associated to a given structure under the following conditions. We considered a simulation box containing 250 atoms. The initial absolute value of the chromium magnetic moment has been set to $0.6 \mu_B$, according to the experimental

value of the amplitude of the spin-density wave observed in pure chromium structures [Fawcett1988]. The cut-off energy has been set at 300 eV. The first Brillouin zone has been sampled with a mesh of $2 \times 2 \times 2$ k-points in reciprocal space. Both the cut-off energy and the k-point mesh have been chosen in order to guarantee the energy convergence to within 0.06 meV per atom. The theoretical equilibrium lattice parameter of pure iron has been used ($a_0 = 2.831 \text{ \AA}$) [Olsson2007] and the structure have been relaxed by keeping constant the volume of the supercell. The DFT computed Fe-Cr lattice parameter is constant and equals the pure iron lattice parameter in the range of chromium concentrations that we considered in this work [Olsson2006]. Moreover, since both the pure iron and the pure chromium exhibit a bcc structure with very similar lattice parameter, the chromium-rich precipitates that form during the thermal ageing of an Fe-Cr alloy in the miscibility gap are coherent with the matrix. Consequently, performing constant volume calculations (*i.e.* introducing a constraint on the lattice parameter) is a physically reasonable approach.

2.1.1.5 The Fe-Cr thermodynamics: first principle calculations of Fe-Cr mixing enthalpy

One of the most important features of DFT calculations consists in the fact they provide insight in properties of materials at zero Kelvin. Very low temperature equilibrium properties cannot be observed experimentally because of the very long time an atomic structure needs to reach thermodynamic equilibrium at very low temperature. DFT calculations provide the ground state energy of a structure of atoms from which some low temperature characteristics of materials can be deduced. DFT calculations based on crystalline structures are achieved by implementing periodic boundary conditions in order to guarantee the applicability of the Bloch's theorem. An important consequence of this approach is the fact that any system exhibits a periodicity equal to the size of the structure. This means that it is formally impossible to create a real random structure because periodic boundary conditions break the randomness. In order to study disordered alloy properties, the most intuitive approach consists in considering a large number of big structures where atoms are randomly distributed respecting a given solute concentration and to compute each quantity as the average on different configurations. The evident drawback of this method is the high computational cost. Two alternative ways exist for simulating disordered alloys by keeping reasonable the size of the system: the Coherent Potential Approximation (CPA)

[Gyorffy1972] and the Special Quasi-random Structures (SQS) method [Zunger1990] [Jiang2004]. The CPA consists in replacing the alloy components with one fictitious atomic species which reproduces some characteristics - such as scattering properties and cohesive energy - of the real structure, the properties of the fictitious atom are determined as concentration weighted averages of the properties of the real components of the alloy. CPA is a mean field approach, thus it cannot capture local properties of the alloy. The SQS method allows simulating disordered alloys by considering very small structures (a few tens of atoms) where atoms are arranged with particular care: the SQS are periodic structures generated by distributing the solute atoms to reproduce, as well as possible, the spatial correlation function of a random alloy (the spatial correlation function is computed by considering the relevant number of shells around each atom according to the physical property which is investigated). Even if numerically less efficient than the CPA approach, the SQS method allows alloys local properties to be taken into account.

In the case of Fe-Cr alloys a large amount of DFT results is available. Many of these results on the Fe-Cr alloy concern the still open issue of the phase diagram at low temperatures. In particular, in the past decade, a growing interest has been devoted to the problem of the solubility limit of chromium in iron. The relevant quantity related to this aspect is the chromium concentration dependence of Fe-Cr mixing enthalpy. The mixing enthalpy of a N-component alloy is given by:

$$H = E_{\text{alloy}} - \sum_i^N x_i E_i \quad (35)$$

where E_{alloy} is the total energy of the alloy, E_i and x_i are the reference total energy and the fraction of component i respectively. As was mentioned in the first chapter of this manuscript, one of the first DFT systematic studies of the evolution of the Fe-Cr alloy mixing enthalpy with chromium concentration has been achieved by Olsson *et al.* [Olsson2003]. Olsson and co-workers have simulated the random alloy in the framework of CPA, they performed spin polarised calculation within the Exact Muffin Tin Orbitals (EMTO) method for the representation of the wavefunctions [Andersen2000] by considering a magnetic ordered phase (ferromagnetic) and a magnetic disordered phase. The first corresponding to zero Kelvin condition, the latter partially accounting for high temperature effects. Indeed magnetic disorder corresponds to the paramagnetic phase which is the magnetic state of the system above its Curie temperature. The magnetic disordered calculations have been achieved within

the Disordered Local Moments (DLM) model. In the DLM picture the random paramagnetic alloy $\text{Fe}_c\text{-Cr}_{1-c}$ is modeled by the following random quaternary alloy: $(\text{Fe}\downarrow\text{-Fe}\uparrow)_c\text{-(Cr}\downarrow\text{-Cr}\uparrow)_{1-c}$, where an equal amount of spin up and spin down have been introduced. Olsson and co-workers showed that the Fe-Cr mixing enthalpy is strictly positive for the paramagnetic state. On the contrary, in the ferromagnetic state, the mixing enthalpy exhibits a sign change. It is negative in the range of chromium concentration below 10 at.% and positive for larger chromium contents. This observation clearly illustrates the crucial role magnetic interactions play in the physics of Fe-Cr system. Olsson *et al.* reproduced the Fe-Cr mixing enthalpy calculations for different chromium concentrations in the framework of DFT with the PAW method and constructing SQS super-cells to describe the random alloy [Olsson2006]. They qualitatively confirmed their previous EMTO-CPA results even if the width and the depth of the negative part of Fe-Cr mixing enthalpy obtained with PAW-SQS calculations has been found to be smaller compared to those obtained with the EMTO-CPA calculations. Olsson *et al.* results on chromium concentration dependence of Fe-Cr mixing enthalpy have been confirmed by further super-cell calculations [Klaver2006] [Lavrentiev2007]. In their 2006 paper Olsson *et al.* [Olsson2006] computed the averaged density of states of the Fe-Cr alloys for different chromium contents within the EMTO-CPA approach. They observed a lowering of the density of states at Fermi level in the chromium concentration region below 10at.% and identified this fact as being responsible of the stabilisation of the Fe-Cr alloy in the same region. This explanation was later confirmed by Korzhavyi *et al.* [Korzhavyi2009]. A more phenomenological explanation of the change of sign of Fe-Cr mixing enthalpy has been proposed by Klaver *et al.* [Klaver2006] with spin-polarised DFT calculations implemented within the PAW-GGA approach. On the one hand Klaver and co-workers showed that the chromium solubility for concentrations lower than about 10 at.% is due to repulsive chromium-chromium interaction. On the other hand, Klaver *et al.* computing the energy difference between an iron matrix containing dispersed chromium atoms and an iron matrix containing the same number of chromium atoms arranged in clusters, showed that, above a certain concentration, even if chromium-chromium interactions are repulsive, the configurations with clustered chromium atoms are energetically more stable than the ones with dispersed chromium atoms. It must be mentioned that in 2008 Paxton and Finnis provided a theoretical explanation of the connection between magnetic interactions and the concentration dependent Fe-Cr mixing enthalpy [Paxton2008]. Paxton and co-worker proposed a tight-binding Hamiltonian where magnetic interactions are described with a Stoner parameter; this model is able to explain the fact that, at low chromium concentration,

chromium atoms tend to repel each other and to orient their local magnetic moment anti-ferromagnetically with respect to the iron matrix atoms while as chromium concentration increases a cooperative effect takes place and chromium atoms tend to form clusters with anti-ferromagnetic configuration.

2.1.2 Embedded Atom Method based potentials for Fe-Cr alloys

DFT calculations are particularly suitable for the computation of static properties of materials. Even if first principle molecular dynamics can be implemented in a DFT framework, this method is very time-consuming. In most molecular dynamics or Monte Carlo simulations semi-empirical cohesive models are employed to obtain configurational energies. In the case of the Fe-Cr system, some semi-empirical interatomic potentials, based on the Embedded Atom Method (EAM), have been developed. In the following, the most frequently used Fe-Cr EAM potentials will be presented.

The EAM approach has been introduced by Daw and Baskes [Daw1984] for transition metals, it provides a many-body interatomic potential. In this context, the general expression of the cohesive energy of an atomic structure is given by the following equation:

$$E_{\text{tot}} = \sum_i F_i(\rho_i) + \frac{1}{2} \sum_i \sum_{j \neq i} \Phi_{ij}(R_{ij}) = \sum_i \left(E_i^{\text{embedding}} + E_i^{\text{pair}} \right). \quad (36)$$

The term $\sum_i F_i(\rho_i)$ in equation (36) is an embedding contribution at equilibrium conditions. ρ_i is the electron density at sites i due to the presence of all other atoms within the cut-off range while $F_i(\rho_i)$ is the energy needed to embed an atom at site i in the environmental electron density. ρ_i can be expressed as a sum of the atomic electron densities of all other atoms within the cut-off range:

$$\rho_i = \sum_{j \neq i} \rho_j(R_{ij}). \quad (36)$$

The term $\frac{1}{2} \sum_i \sum_{j \neq i} \Phi_{ij}(R_{ij})$ in equation (36) usually accounts for a short-range repulsive pair interaction. The functional form for the expressions of $\rho_j(R_{ij})$, $F_i(\rho_i)$, and $\Phi_{ij}(R_{ij})$ are not implicitly defined by EAM approach. Once such expressions are chosen, the

parameters are adjusted to fit experimental data or theoretical predictions about the physical properties of the particular materials which have to be modelled.

In order to describe the cohesive energy of a generic binary alloy A-B, an EAM potential must include the description of the pair interaction term for AA-like interactions, for BB-like interaction and for AB-like interactions. Concerning the Fe-Cr alloy, a few attempts have been made to develop such an interatomic many-body potential. In the 90's Fe-Cr potentials were developed and fit to the experimental data on the Fe-Cr mixing enthalpy for the paramagnetic state [Yifang1996, Konishi1999]. As a consequence, these potentials fail to capture the physically meaningful sign change of the Fe-Cr mixing enthalpy pointed out later by DFT calculations at 0 K [Olsson2003, Olsson2006]. More recently Wallenius *et al.* [Wallenius2004a, Wallenius2004b] derived an Fe-Cr potential constructed by considering the functional form proposed by Ackland *et al.* for the pair interactions terms [Ackland1997]. Wallenius and co-workers adjusted the Fe-Fe interaction term and the Cr-Cr interaction term to fit the cohesive energy, the lattice parameter, the vacancy formation energy, the elastic constants of ferromagnetic pure iron and paramagnetic pure chromium. Concerning the mixed pair interaction term (*i.e.* the Fe-Cr interaction term), different adjustments have been performed, each one for a different chromium concentration, in order to fit the concentration dependent Fe-Cr mixing enthalpy.

2.1.2.1 The Two Band Model

In 2005 Olsson *et al.* proposed an Fe-Cr potential [Olsson2005] based on an extension of the EAM approach previously proposed by Ackland and Reed [Ackland2003] called the Two Band Model (2BM). The 2BM approach consists in considering the s-electron contribution, as well as d-electron contribution (which is always taken into account), to the electron density and to write term $F_i(\rho_i)$ of equation (36) as follows:

$$F_i(\rho_i) = F_i^d(\rho_d) + F_i^s(\rho_s). \quad (37)$$

According to Ackland and Reed the expression for $F_i^b(\rho_b)$, where the index b stands for the s band or the d band, is:

$$F_i^b(\rho_b) = A_1^b \sqrt{\rho_b} + A_2^b \rho_b^2 + A_3^b \rho_b^4. \quad (38)$$

Following Wallenius *et al.*, Olsson *et al.* used cubic splines for the representation of the pair interaction terms ϕ_{ij} in equation (36). Coefficients A_i^b have been determined to fit the DFT results on concentration dependence of Fe-Cr mixing enthalpy at 0 K [Olsson2006], particularly the sign change (from negative to positive) observed for a 10at.% chromium concentration. Olsson and co-workers assumed that the s-electrons contribution to the electron density only affects the Fe-Cr interaction. The pair interaction terms for pure elements were adjusted to fit the cohesive energy, the lattice parameter, and the elastic constants of pure iron and pure chromium (in the case of pure chromium, the elastic constants of paramagnetic chromium extrapolated to 0 K have been considered as reference values).

The Fe-Cr mixing enthalpy obtained with the Olsson EAM-2BM potential predicts a sign change (from positive to negative) also in the chromium-rich part of the curve for a chromium concentration of 90 at.%, in disagreement with Olsson *et al.* DFT calculations [Olsson2006]. In order to overcome this disagreement Bonny *et al.* have recently proposed a new implementation based on the 2BM [Bonny2011a]. They used the potential developed by Mendeleev *et al.* for pure iron [Mendeleev2003]. For the pure chromium potential expression, they used cubic splines to fit the cohesive energy, the lattice parameter, the vacancy formation energy, the vacancy migration energy, the formation energy of self-interstitial defects of the ferromagnetic phase and the elastic constant of the paramagnetic phase. The Fe-Cr enthalpy of mixing obtained with the potential developed by Bonny *et al.* is not symmetric with respect to the 50 at.% chromium concentration and is strictly positive in the chromium rich part.

In the following of the manuscript we will refer to Olsson *et al.* Fe-Cr potential and to Bonny *et al.* Fe-Cr potential with the acronyms EAM-2BM-PO and EAM-2BM-GB respectively.

2.1.2.2 The concentration dependent model

A different approach - with respect to the 2BM - for the construction of an Fe-Cr many-body potential has been presented by Caro *et al.* [Caro2005]. Caro and co-workers developed an EAM potential which does not include any contribution of the s-electrons to the electron density but they introduced a chromium concentration dependence in the expression of the total cohesive energy. The general form of the total cohesive energy proposed is:

$$E = x_{\text{Fe}}^2 \sum \Phi_{\text{FeFe}}(r_{ij}) + x_{\text{Cr}}^2 \sum \Phi_{\text{CrCr}}(r_{ij}) + 2x_{\text{Cr}}x_{\text{Fe}} \sum \Phi_{\text{FeCr}}(r_{ij}) + x_{\text{Fe}}F_{\text{Fe}}(\tilde{\rho}) + x_{\text{Cr}}F_{\text{Cr}}(\tilde{\rho}),$$

(39)

where $\tilde{\rho} = x_{\text{Fe}} \sum \rho_{\text{Fe}}(r_{ij}) + x_{\text{Cr}} \sum \rho_{\text{Cr}}(r_{ij})$.

Caro *et al.* assumed that the functions depending on the electron density are slowly varying for small variation of ρ . Hence they considered the pair interactions as dominating the variations of the total cohesive energy. They used the same potential as Olsson *et al.* [Olsson2005] for the pure elements whereas they introduced a mixed Fe-Cr pair interaction depending not only on the distance between the atoms but also on the local chromium concentration. The Fe-Cr pair interaction then is written as:

$$\Phi_{\text{FeCr}}(x, r) = h(x) \frac{1}{2} [\Phi_{\text{FeFe}}(r) + \Phi_{\text{CrCr}}(r)] \quad (40)$$

where $h(x)$ has a polynomial form whose the parameters are obtained to fit the Fe-Cr mixing enthalpy obtained by Olsson *et al.* [Olsson2003]. In the following we will refer to the EAM potential parameterised by Caro *et al.* as the EAM-CDM where CDM stands for Concentration-Dependent Model.

2.1.2.3 Fe-Cr alloy phase diagram and mixing enthalpy obtained with the EAM Fe-Cr potentials

In order to choose the better potential for our investigations concerning the Fe-Cr system, we considered the comparative study that Bonny *et al.* [Bonny2011a, Bonny2011b] have performed to compare the capability of the three EAM potentials described in subsections 2.2.1 and 2.2.2 to reproduce the available thermodynamic data. Bonny *et al.* computed the Fe-Cr mixing enthalpy with the Fe-Cr EAM-2BM potentials and the EAM-CDM potential. In figure 1-Ch2 (taken from [Bonny2011a]) the Fe-Cr mixing enthalpy as a function of chromium concentration computed with the EAM potentials is compared with the DFT results obtained by Olsson *et al.* within the EMTO-CPA as well as the PAW-SQS methods.

Figure 1-Ch2 shows that both the EAM-2BM-GB potential and the EAM-CDM potential provide a very satisfactory agreement with the PAW-SQS [Olsson2006] and EMTO-

CPA calculations respectively [Olsson2003]. On the contrary, as stated before, the EAM-2BM-PO potential exhibits qualitative disagreements with the DFT results, as it predicts a negative mixing enthalpy in the chromium rich region. This latter circumstance would imply the existence of low iron content Cr-Fe solid solutions. Neither theoretical predictions nor experimental measurements indicate such scenario is realistic.

Bonny *et al.* also computed the Fe-Cr phase diagram using the EAM-2BM potentials and the EAM-CDM as cohesive models [Bonny2011a, Bonny2011b]. They used a mixed approach based on Monte Carlo simulations in the isobar semi-grand canonical ensemble ($N, P, T, \Delta\mu$) where $\Delta\mu = \mu_{\text{Cr}} - \mu_{\text{Fe}}$, on the one hand, and thermodynamic integration on the other hand.

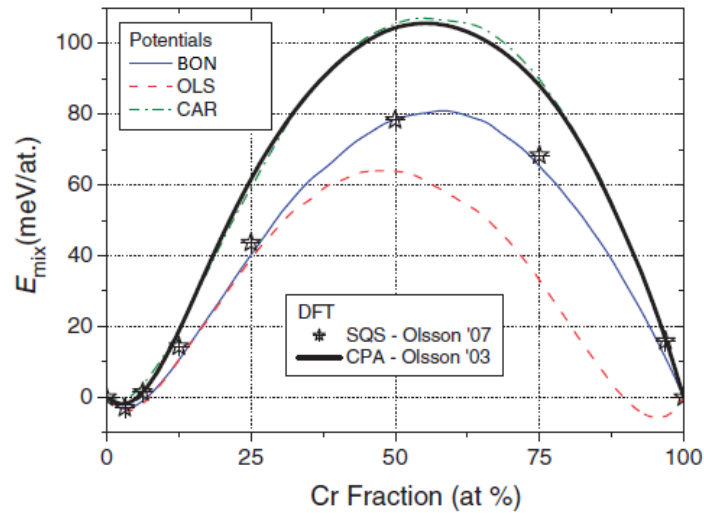


Figure 1-Ch2 Fe-Cr mixing enthalpy computed with the Fe-Cr potential developed by Bonny *et al.* (BON), Olsson *et al.* (OLS), and Caro *et al.* (CAR). The figure is from [Bonny2011a].

The Monte Carlo simulations - performed in structures containing 1024 atoms at 0 Pa for a temperature range going from 300 K to 1200 K and $\Delta\mu$ varying from -0.25 eV to 0.35 eV - were used to determine the equilibrium concentration for a given phase. At each Monte Carlo step the Metropolis algorithm was implemented for three different tests:

1. Random displacement of all atoms from their current position (to take into account the structure relaxation and the vibrational entropy).
2. Change of the atomic species of a randomly selected atom (sampling of the possible concentrations).

3. Variation of the simulation box volume (to keep the pressure constant).

Considering that $\Delta\mu(x_{\text{Cr}}) = \frac{\partial G}{\partial x_{\text{Cr}}}$, and the following expression for the free enthalpy of the Fe-Cr alloy:

$$G(\mathbf{x}) = x_{\text{Cr}}G_{\text{Cr}}(T) + x_{\text{Fe}}G_{\text{Fe}}(T) + k_{\text{B}}T(x_{\text{Cr}} \ln x_{\text{Cr}} + x_{\text{Fe}} \ln x_{\text{Fe}}) + x_{\text{Fe}}x_{\text{Cr}} \sum_{p=0}^M L_p(x_{\text{Cr}} - x_{\text{Fe}})^p, \quad (41)$$

the authors adjusted the free enthalpy derivative with respect to chromium concentration to the data obtained with the Monte Carlo simulations, hence they deduced the free enthalpy from which the solubility limits were computed with the common tangent construction. In the expression (41) for the free enthalpy, the free enthalpy of pure iron and pure chromium was obtained by thermodynamic integration, the third term accounts for the configurational entropy and the last term $-x_{\text{Fe}}x_{\text{Cr}} \sum_{p=0}^M L_p(x_{\text{Cr}} - x_{\text{Fe}})^p$ is a Redlich-Kister development that partially compensates for the discrepancy between the real system and the ideal solution.

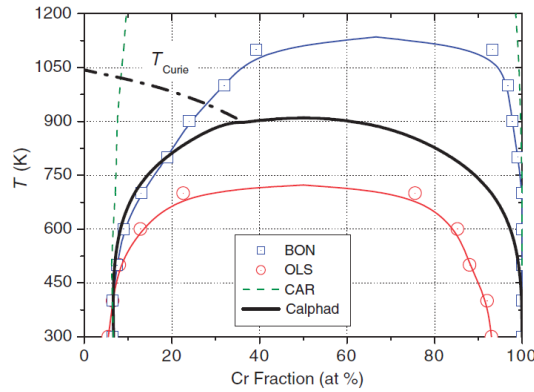


Figure 2-Ch2 Fe-Cr phase diagram computed with the Fe-Cr potential developed by Bonny *et al.* (BON), Olsson *et al.* (OLS), Caro *et al.* (CAR). The results obtained with the different Fe-Cr potentials are compared with the Fe-Cr phase diagram obtained within the CALPHAD method. The figure is from [Bonny2011a].

Bonny *et al.* compared (figure 2-Ch2) the phase diagrams obtained with the EAM potentials with the one they obtained with the CALPHAD method [Bonny2010]. The Bonny *et al.* computation of the phase diagram within the CALPHAD approach is based on Andersson *et al.* work [Andersson1987] except for the Fe-Cr bcc phase which they re-adjusted by introducing as reference data to fit the Olsson *et al.* Fe-Cr mixing enthalpy and the position of the solubility limit that they determined in a previous publication based on a

review of experimental data [Bonny2008]. The EAM-2BM potentials qualitatively reproduce the CALPHAD phase diagram even if the EAM-2BM-PO potential underestimates the critical temperature estimated by CALPHAD of about 200 K while the EAM-2BM-GB potential overestimates the critical temperature of the same amount. The most notable difference between the EAM-2BM-PO potential and the EAM-2BM-GB potential is the fact that the latter correctly predicts the non-solubility of iron in chromium. Finally, as it can be observed in figure 2-Ch2, the EAM-CDM captures the phase boundary predicted by the CALPHAD method up to 600 K but above this temperature it fails to close.

On the basis of Bonny *et al.* results which have been exposed above, we decided to use the EAM-2BM potentials in this work and, particularly the EAM-2BM-GB potential. Our choice was motivated by the better capability of the EAM-2BM-GB potential to reproduce the Fe-Cr phase diagram with respect to the EAM-CDM potential, and, the chromium concentration dependence of the Fe-Cr mixing enthalpy with respect to the EAM-2BM-PO potential. It should be noted that Bonny *et al.* calculations account for vibrational entropy, whereas we performed our atomistic kinetic Monte Carlo simulations of the Fe-Cr thermal ageing (see chapter 4) on a rigid lattice, thus neglecting vibrational effects. Nevertheless, we considered that the EAM-2BM-GB cohesive model allows a better description of the Fe-Cr alloy than the EAM-2BM-PO potential because it correctly reproduces the 0 K Fe-Cr mixing enthalpy dependence on the chromium content in the zone of high chromium concentrations. This is a very important issue because, as we previously discussed, the Fe-Cr mixing enthalpy dependence on chromium concentration is related to the magnetic properties of the alloy. Therefore, the EAM-2BM-GB potential appears to better account for magnetic interactions in Fe-Cr system than the EAM-2BM-PO potential. The Fe-Cr phase diagram computed with both the EAM-2BM-GB potential or the EAM-2BM-PO potential on a rigid lattice should lead to a wider miscibility gap. Consequently, in simulations on rigid lattice, one should expect to observe a lower solubility limit than the one computed by Bonny and co-workers (figure 2-Ch2).

2.2 Ground state energy calculation: the DFT and the EAM-2BM cohesive model

In this subsection, we will present some preliminary calculations that we performed in order to evaluate the capability of EAM-2BM Fe-Cr potentials to reproduce DFT estimations about some properties of Fe-Cr system which we consider as being relevant in the context of our study. Such quantities are the chromium-chromium and the chromium-vacancy binding energy (section 2.3), and the vacancy formation energy (section 2.4).

Moreover, in section 2.5, we will present our DFT results concerning the ground state magnetic configuration associated to iron structures containing two or more substitutional chromium atoms in different positions. Such calculations have been achieved *via* the computation of the local magnetic moments associated to each atom of the Fe-Cr structures.

2.2.1 Chromium-chromium and chromium-vacancy interaction

This work focuses on the modelling and the simulation of the thermal ageing of chromium rich Fe-Cr alloys. The microstructure evolution of Fe-Cr is considered as being driven by a vacancy diffusion mechanism (irradiation effects are not taken into account in the present work). The vacancy-atom exchange activation barrier depends on the chemical environment. We will assume that the local atomic environment (LAE) enclosing the first and second neighbour shells of the vacancy–migrating atom pair is mainly responsible for the environmental dependence of the migration energy. We then expect the chromium-chromium and the chromium-vacancy short-range interactions to have a remarkable effect on the vacancy migration barriers. Hence, we started by computing the chromium-chromium and the chromium-vacancy binding energy both with DFT and the EAM-2BM potentials. The formula we use to compute the binding energies can be written as follows:

$$E_b(A_1, A_2, \dots, A_n) = \sum_{i=1}^n E(A_i) - [E(A_1 + A_2 + \dots + A_n) + (n - 1)E_{\text{ref}}] \quad (41)$$

where $E(A_i)$ is the cohesive energy of a structure containing one entity A_i (*i.e.* a vacancy or a substitutional chromium atom), $E(A_1 + A_2 + \dots + A_n)$ is the cohesive energy of a structure containing all the n vacancies or substitutional chromium atoms which are considered ($n = 2$ in the case of the calculation of chromium-chromium or chromium-vacancy binding energy)

and E_{ref} is the cohesive energy of a defect-free structure (pure iron in our case). In this picture, a positive binding energy corresponds to an attractive interaction, while a negative binding energy indicates a repulsive interaction.

Calculations based on EAM-2BM cohesive models have been performed with the code DYMOKA [Becquart1997] considering a simulation box with dimensions $8a_0 \times 8a_0 \times 8a_0$, where $a_0 = 2.8553 \text{ \AA}$ is the equilibrium lattice parameter of pure iron obtained with both EAM-2BM-PO potential and EAM-2BM-GB potential.

Figure 3-Ch2 displays the chromium-chromium binding energy as a function of the chromium-chromium distance computed within DFT and with the EAM-2BM-PO and EAM-2BM-GB potentials. Regardless of the cohesive model, the chromium-chromium interaction is repulsive. When the two chromium atoms are first nearest neighbours the chromium-chromium interaction is strongly repulsive, and the estimations of the EAM-2BM potentials are in good agreement with DFT results. When the chromium-chromium distance increases, the binding energy computed within DFT rapidly varies from about -0.25 eV to -0.05 eV . On the contrary, the binding energy variation with the chromium-chromium distance is slower for the EAM-2BM potentials. EAM-2BM potentials describe thus a more long-ranged chromium-chromium interaction as compared to the DFT predictions. In particular, when the chromium-chromium distance varies from first nearest neighbour distance to second nearest neighbours distance, the DFT computed binding energy becomes about 50% less repulsive. In the same circumstances, almost no change in the binding energy obtained with the EAM-2BM potential is observed. Note that both potentials predict the same tendencies for the variation of the binding energy with the chromium-chromium distance, even if the chromium-chromium repulsion is slightly lower in the case of the EAM-2BM-GB potential.

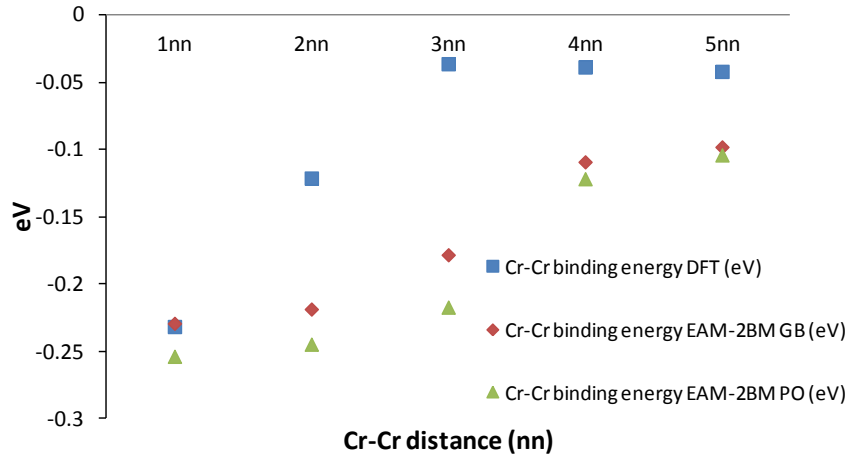


Figure 3-Ch2 Cr-Cr binding energy as a function of the relative position of the two chromium atoms.

DFT calculations: simulation box: $5a_0 \times 5a_0 \times 5a_0$, $a_0 = 2.831 \text{ \AA}$. K-points mesh: $2 \times 2 \times 2$.

EAM-2BM calculations: box $8a_0 \times 8a_0 \times 8a_0$, $a_0 = 2.8553 \text{ \AA}$.

The chromium-vacancy binding energy has been computed in the cases where chromium and vacancy are first or second nearest neighbours. Results are displayed in figure 4-Ch2. In both configurations, the DFT results show a very low positive chromium-vacancy binding energy; this corresponds to a weakly attractive interaction in agreement with experimental observation by muon spectroscopy performed by Möslang *et al.* [Möslang1983] which estimated the chromium-vacancy binding energy to be less than 105 meV.

whereas the EAM-2BM cohesive models predict a repulsive interaction. In the case of EAM-2BM-PO potential, the discrepancy with respect to the DFT results is much more pronounced than in the case of EAM-2BM-GB potential.

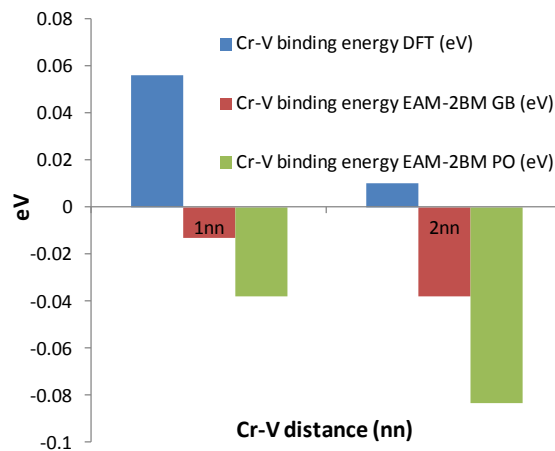


Figure 4-Ch2 Cr-V binding energy as a function of the distance between the chromium and the vacancy.

DFT calculations: simulation box size: $5a_0 \times 5a_0 \times 5a_0$, $a_0 = 2.831 \text{ \AA}$. K-points mesh: $2 \times 2 \times 2$.

EAM-2BM calculations: box $8a_0 \times 8a_0 \times 8a_0$, $a_0 = 2.8553 \text{ \AA}$.

Even if, for both DFT and the EAM-2BM potentials, the chromium-vacancy interaction is very weak, the fact that they predict opposite signs can lead to notable differences in the description of the physics of Fe-Cr alloy as we will see in chapter 3.

2.2.2 Vacancy formation energy

In order to further compare the semi-empirical models estimations with the DFT previsions, we computed the vacancy formation energy in pure iron and pure chromium. The vacancy formation energy for pure elements can be obtained as follows:

$$E_f^{\text{vac}} = E(N - 1) - \frac{E(N)}{N}(N - 1), \quad (41)$$

where N is the number of atoms constituting the structure, $E(N)$ is the cohesive energy of the structure containing all N atoms while $E(N - 1)$ is the cohesive energy of the structure where a vacancy has been introduced.

The DFT calculations have been performed in a simulation box containing 128 atoms, the first Brillouin zone has been sampled with a mesh of $3 \times 3 \times 3$ k-points in reciprocal space. The cut-off energy has been set to 300 eV. We considered the pure ferromagnetic iron and pure anti-ferromagnetic chromium equilibrium DFT lattice parameters which are $a_0 = 2.831 \text{ \AA}$ and $a_0 = 2.850 \text{ \AA}$ respectively [Olsson2007]. The atom positions have been relaxed by keeping constant the volume of the supercell. We performed the calculations based on EAM-2BM cohesive models in a simulation box with dimensions $8a_0 \times 8a_0 \times 8a_0$. For iron structures we considered $a_0 = 2.8553 \text{ \AA}$ both in the case of EAM-2BM-PO potential and EAM-2BM-GB potential. For chromium structures we considered $a_0 = 2.878 \text{ \AA}$ in the case of EAM-2BM-PO potential and $a_0 = 2.866 \text{ \AA}$ EAM-2BM-GB potential, these values are the pure chromium equilibrium lattice parameters obtained with the two potential respectively. Atoms positions relaxations within the EAM cohesive models have been achieved with the conjugate gradient algorithm.

Table 1-Ch2 collects the vacancy formation energies of pure iron and pure chromium. The EAM-2BM-PO potential and the EAM-2BM-GB potential provide very close values for the vacancy formation energy in pure iron and pure chromium. Both in the case of iron and chromium, the EAM-2BM potentials underestimate the vacancy formation energy with respect to DFT data, the discrepancy being larger in the case of the vacancy formation energy in iron.

	EAM-2BM- PO Relaxed structure (eV)	EAM-2BM- PO Unrelaxed structure (eV)	EAM-2BM- GB Relaxed structure (eV)	EAM-2BM- GB Unrelaxed structure (eV)	DFT (This work) (eV)	DFT (Olsson <i>et al.</i> [Olsson200] (eV)	Experimental observations (eV)
Iron	1.72	1.84	1.71	1.84	2.15	2.15	2.0±0.2 (a) 1.60±0.15 (b)
Chromium	2.56	2.88	2.52	2.68	2.72	2.71	2.0±0.2 (c)

Table 1-Ch2 Vacancy formation energy in pure iron and pure chromium.

(a) [DeSchepper1983], (b) [Schaefer1977], (c) [Loper1985]

If one considers the data on chromium-chromium binding energy, vacancy-chromium binding energy and vacancy formation energy presented above, there is no strong evidence from which to conclude that one of the two EAM-2BM potentials (namely the EAM-2BM-PO potential or the EAM-2BM-GB potential) is preferable over the other because of its better capability to reproduce DFT results. Nonetheless, EAM-2BM-GB potential, beside the fact that, compared to the EAM-2BM-PO potential, it provides a better thermodynamic description of the Fe-Cr alloy (see previous discussion in subsection 2.2.3), it is also slightly better in reproducing DFT results about chromium-chromium and chromium-vacancy interactions. In the following of this manuscript we will show that this latter aspect can lead to some observable consequences.

2.2.3 Substitutional chromium atoms local magnetic moments

Magnetism plays a fundamental role in the physics of the Fe-Cr system. Even if the Fe-Cr EAM potentials which have been presented in section 2.2 have been adjusted to reproduce data sets obtained with DFT spin-polarised calculations, they cannot treat explicitly the magnetic degrees of freedoms of the Fe-Cr system. On the contrary, in DFT ground state energy calculations the magnetic degrees of freedom are treated explicitly and are taken into account during the iterative relaxation of the system. According to DFT results obtained by Klaver *et al.* [Klaver2006], isolated substitutional chromium atoms in an iron matrix orient their local magnetic moment (LMM) μ anti-ferromagnetically with respect to the surrounding iron atoms. When the nearest neighbour sites of a substitutional chromium are progressively occupied with chromium atoms, the competition between the anti-ferromagnetic chromium

ground state (as predicted by GGA-PAW DFT calculations) and the tendency of chromium atoms' LMM to orient anti-ferromagnetically with respect to iron matrix atoms rises resulting in a magnetic frustration for the chromium atoms. As a consequence, the absolute values of the chromium atoms LMM decrease. In this subsection, we will illustrate some basic local magnetic properties of substitutional chromium atoms in an iron matrix. After DFT calculations of the ground state energy, the LMMs in relaxed Fe-Cr structures can be calculated by integrating the spin density expressed by equation (9) in the volume of a sphere centred on each atom and with a radius equal to the Wigner-Seitz radius corresponding to the atom type (1.323 Å for chromium and 1.302 Å for iron). We computed the LMM of two substitutional chromium atoms in an otherwise pure iron matrix as a function of the separation distance. Table 2-Ch2 gathers the results we obtained.

Cr-Cr distance (nn)	5nn	4nn	3nn	2nn	1nn
Cr magnetic moments (μ_B)	-1.73	-1.70	-1.67	-1.58	-1.38

Table 2-Ch2 Local magnetic moment of two substitutional chromium atoms in an iron matrix placed at different distances.

The iron atoms local magnetic moments in the relaxed structures are not affected by the presence of the chromium atoms, they have an absolute value of $2.2 \mu_B$ and are parallel, thus forming a ferromagnetic structure. The substitutional chromium atoms orient their LMM anti-ferromagnetically with respect to the iron atoms. As expected, the absolute value of the chromium atoms LMM decreases when the separation distance decreases (see table 2-Ch2). In order to illustrate on a quantitative point of view the rising of a frustrated magnetic configuration, we computed the LMM of all atoms in three different iron-based structures: the first containing one substitutional chromium, the second and the third obtained by filling with chromium atoms the (eight) first nearest neighbours and the (six) second nearest neighbours with chromium atoms (figure 5-Ch2). DFT calculations have been performed to relax the structures, 250 atoms were included in the simulation box. The cut-off energy has been set at 300 eV and the first Brillouin zone has been sampled with a mesh of $2 \times 2 \times 2$ k-points.

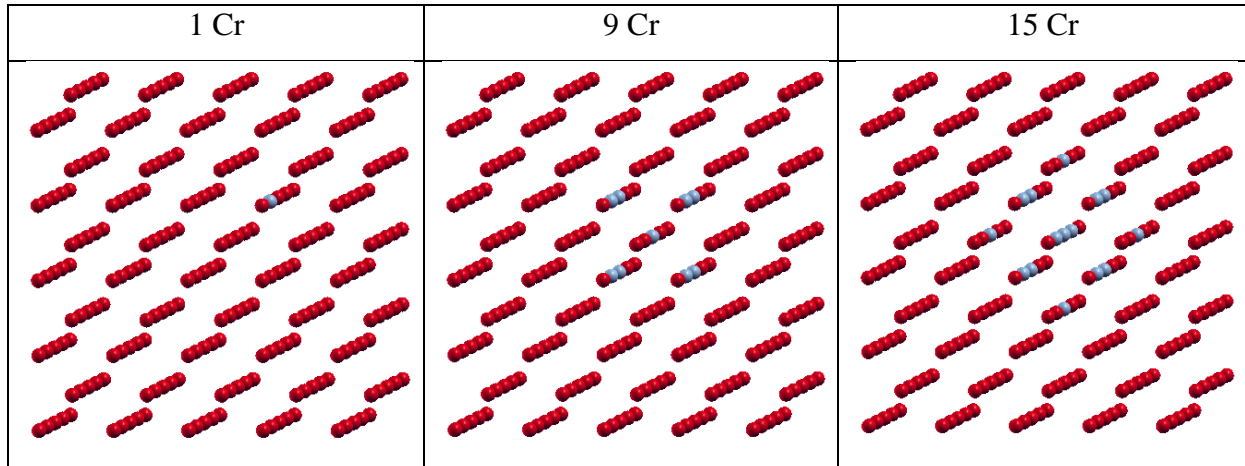


Figure 5-Ch2 From right to left : iron matrix containing one substitutional chromium, iron matrix containing a 9 substitutional chromium atoms cluster, iron matrix containing a 15 substitutional chromium atoms cluster. Red spheres: iron atoms. Blue spheres: chromium atoms. Simulation box size: $5a_0 \times 5a_0 \times 5a_0$, $a_0 = 2.831 \text{ \AA}$.

While all the iron atoms LMMs oscillate very close to the value of $2.2 \mu_B$ regardless of their environment, the situation for the chromium atoms is quite different. When a single chromium atom is introduced in the matrix, it orients its LMM anti-ferromagnetically with respect to iron atoms LMM. The single chromium LMM is $-1.71 \mu_B$. When additional chromium atoms are introduced in the first nearest neighbour shell, magnetic frustration takes place. It results from the cooperative tendency of the chromium atoms to arrange the nine Cr LMM in an anti-ferromagnetic configuration and the tendency of single chromium atoms to orient their LMM anti-ferromagnetically with respect to the surrounding iron atoms. The anti-ferromagnetic configuration is realised with the cost of a lowering of the absolute value of the chromium atoms LMM. In this case we found $0.79 \mu_B$ for the central chromium of the 9 Cr compound and $-1.09 \mu_B$ for its eight nearest neighbours. Finally, for the 15 Cr compound we found the following LMM: $0.10 \mu_B$ for the central chromium atom, $-0.30 \mu_B$ for chromium atoms in first nearest neighbours shell and $-0.24 \mu_B$ for chromium atoms in second nearest neighbours shell. A weak anti-ferromagnetic configuration stands for the central chromium atom and its first nearest neighbour shell but disappears at the boundary between the chromium compound and the iron matrix.

When a further chromium shell is added around the 15 Cr cluster (figure 6-Ch2), the trends are similar. As for the 15 Cr cluster, an anti-ferromagnetic configuration takes place in the core of the cluster while magnetic frustration persists at the boundary between the chromium cluster and the iron matrix as one would expect.

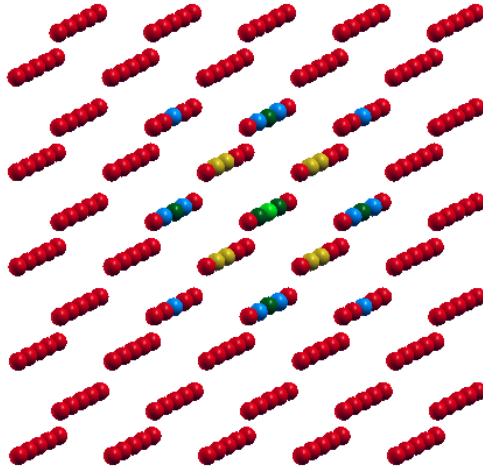


Figure 6-Ch2 Iron matrix containing a 27 substitutional chromium cluster. Red spheres: iron atoms. All other colours: chromium atoms. Simulation box size: $5a_0 \times 5a_0 \times 5a_0$, $a_0 = 2.831 \text{ \AA}$.

The LMM moment for the different chromium atoms are presented in table 3-Ch2.

Light green (central chromium atom)	$-0.19 \mu_B$
Yellow (1nn shell)	$0.38 \mu_B$
Dark green (2nn shell)	$-0.58 \mu_B$
Light blue (3nn shell)	$-0.85 \mu_B$

Table 3-Ch2 LMM for atoms occupying different position in the 27 Cr cluster.

It is interesting to notice that, in the case of the 27 Cr cluster, the central atom has a negative LMM whereas in the case of the 15 Cr cluster the central chromium LMM is positive. This is simply due to the fact that, in order to minimise the chromium-iron interfacial energy, chromium atoms at the boundary of the cluster orient their LMM anti-ferromagnetically with respect to the iron atoms belonging to the matrix. The sign of the LMM of the inner part of the chromium cluster are then consequently determined to set up the anti-ferromagnetic stable configuration.

2.3 Vacancy migration energy calculations

As was stated above, the vacancy diffusion in the bulk is considered as being the only mechanism driving the Fe-Cr microstructure evolution. The main problem concerning the theoretical investigation of the kinetics of transformation of a given system consists in identifying the lowest energy path for the evolution of the system from one configuration to

another. The potential energy maximum along the minimum energy path is the saddle point energy which corresponds to the activation energy barrier. Estimating the activation barrier associated to a given transition allows the modelling of the transition rate using, for example, the Vineyard harmonic transition state theory [Vineyard1957].

In order to compute the minimum energy path for the vacancy-atom jump, we used the Nudged Elastic Band method (NEB) [Jonsson1998], implemented in the VASP code, in the framework of DFT and the drag method, which we implemented within the DYMOKA code, in the framework of the EAM-2BM-GB cohesive model. The two methods will be presented in the next two sections.

2.3.1 The Nudged Elastic Band (NEB) method

The NEB approach consists in introducing M images of the system in which the migrating atom occupies M intermediary positions between the initial configuration (before the jump) and the final configuration (after the jump) of the system. Each image is relaxed and the migration barrier energy profile is obtained as the difference of the images' energy and the energy of the initial configuration of the system. In order to avoid the images to relax toward the initial migrating atom equilibrium position or the final migrating atom equilibrium position - leaving no images in the intermediate positions - elastic spring-like forces are introduced between the migrating atom images. During the relaxation procedure execution, the forces acting on each image are: the projection of the elastic forces on the local tangent to the migration trajectory and the force resulting from the interaction of the image with all other atoms in the super-cell projected in the orthogonal direction with respect to the local tangent to the migration trajectory. As a consequence, each image is relaxed under the action of a force which can be written as follows:

$$\vec{F}_i^0 = -\vec{\nabla}V(\vec{R}_i)_\perp + \vec{F}_i^S \cdot \hat{t}\hat{t} \quad (42)$$

where $-\vec{\nabla}V(\vec{R}_i)_\perp$ is the component of the force acting on the image at position R_i , projected on the direction orthogonal to the migration trajectory; $\vec{F}_i^S \cdot \hat{t}\hat{t}$ is the elastic force acting between each image and its two neighbouring images projected on the local tangent to the migration trajectory (\hat{t} is the unitary tangent vector to the migration trajectory). The accuracy of the NEB method depends both on the cohesive model which is used for the structure

relaxation and the number M of images which are considered. We have made a series of tests on the impact that the number of images has on the estimation of the saddle point of the vacancy-atom migration barrier. These tests have been implemented by considering three different ways to implement the NEB method. The first way consists in considering infinite spring constants for the elastic interaction acting between each image and its neighbouring images. The second way consists in considering the VASP default spring constant for the elastic interaction acting between each image and its neighbouring images, the third way corresponds to the previous method improved with the so called Climbing Image (CI) approach [Henkelman2000]. CI is designed to guarantee that one of the images will be located on the saddle point of the migration barrier profile. The CI technique consists in identifying - after the NEB procedure convergence - the higher energy image, to switch off the elastic interactions, and to relax this image again under the action of the force derived from the potential energy surface with opposite sign.

For all the three NEB techniques presented above, we performed different calculations of vacancy-atom energy barrier profiles for different numbers of images. The most important goal of this series of tests is to verify which of the three methods is the most appropriate for estimating vacancy-atom migration barriers in complicated cases such as an asymmetric double-hump barrier profile. For this reason, we decided to perform the tests on the barrier corresponding to the vacancy-chromium jump process in a chemical environment characterised by chromium occupation of the sites A, B1, B2, B3, C1, C2, C3, D1, D2, D3, E1, E2, E3, F, G1 (see figure 7-Ch2 for the atomic sites nomenclature).

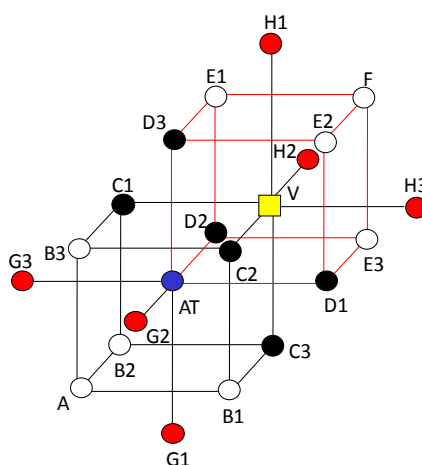


Figure 7-Ch2 Local chemical environment structure scheme and sites nomenclature.

AT: migrating atom,

V: vacancy.

Black spheres: atom windows the vacancy goes through along migration path (first window: C1, C2, C3. Second window: D1, D2, D3).

The first neighbours' shell of the vacancy-migrating atom pair is saturated with chromium atoms and an additional chromium atom is placed in a site of the second neighbours shell. This configuration of the LAE gives rise to an asymmetric double-hump barrier as can be seen in figures 8-Ch2, 9-Ch2, and 10-Ch2.

The barrier profiles obtained are presented in figure 8-Ch2 (NEB – infinite spring constants), figure 9-Ch2 (NEB – VASP default spring constants), figure 10-Ch2 (NEB – VASP default spring constants – Climbing Image algorithm). From the migration barrier profiles, we deduced the migration energies which are reported in table 4-Ch2 as a function of the number of images introduced in the system for the NEB calculation.

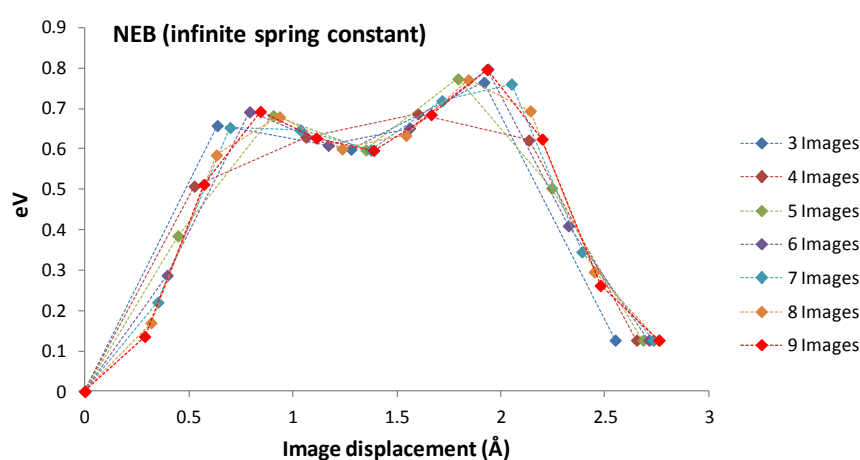


Figure 8-Ch2 NEB method calculations of chromium-vacancy migration energy profiles for different numbers of images. Each image is constrained to relax on a plane perpendicular to the local tangent of the migration trajectory.

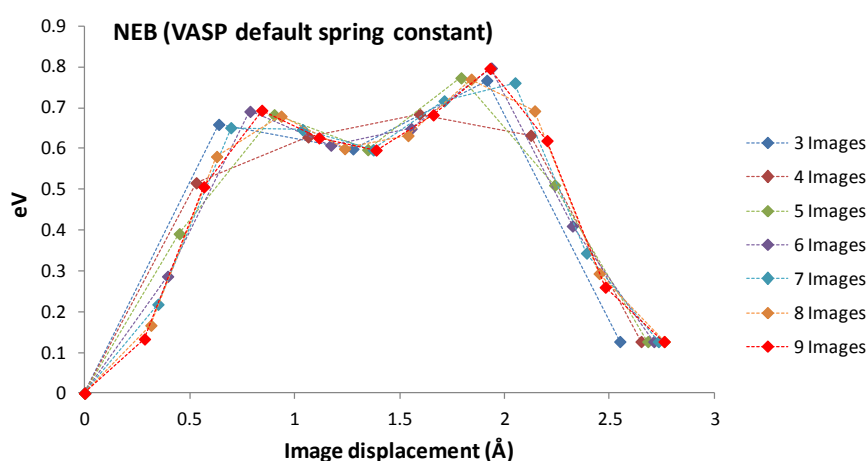


Figure 9-Ch2 NEB method calculations of chromium-vacancy migration energy profiles for different numbers of images. VASP default spring constants.

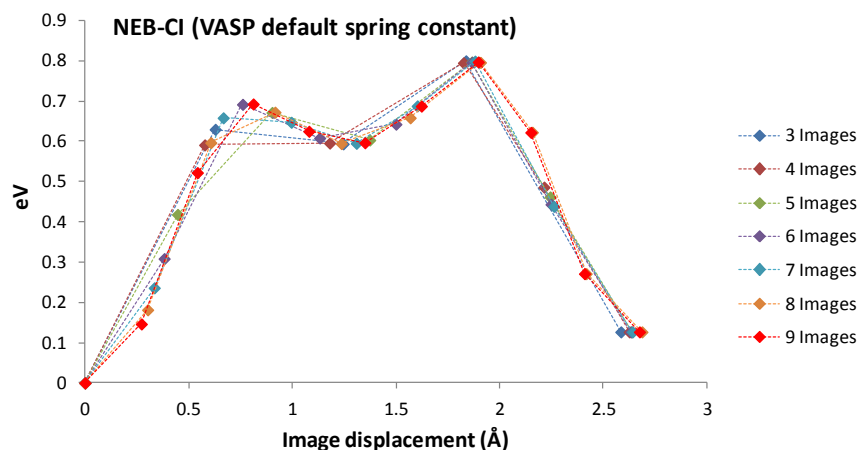


Figure 10-Ch2 NEB method calculations of chromium-vacancy migration energy profiles for different numbers of images. The climbing image algorithm is implemented. VASP default spring constants.

The data in table 4-Ch2 show that the NEB method implemented using the VASP default spring constant and the Climbing Image (CI) algorithm exhibits almost no-dependence of the estimated value of saddle point energy on the number of images. This means that all the saddle point energies obtained with the NEB-CI approach are very close or identical to the one obtained introducing 9 images (*i.e.* the most precise). We conclude thus that the NEB-CI technique is the optimal one to use in this particular case. Since the case was chosen explicitly for its complexity, we assume that all barriers will be well described by the NEB-CI method with the VASP default spring constant using three images, if not specified otherwise.

Number of images	NEB (Infinite spring constant) (eV)	NEB (VASP default spring constant) (eV)	NEB (VASP default spring constant- Climbing Image algorithm) (eV)
3	0.77	0.77	0.80
4	0.69	0.68	0.79
5	0.77	0.77	0.80
6	0.80	0.80	0.80
7	0.76	0.76	0.80
8	0.77	0.77	0.80
9	0.80	0.80	0.80

Table 4-Ch2 Migrating chromium saddle point energies. Sites A, B1, B2, B3, C1, C2, C3, D1, D2, D3, E1, E2, E3, F, G1 are occupied by chromium atoms (see figure 7-Ch2 for the atomic sites nomenclature), all other sites of the matrix are occupied by iron atoms.

2.3.2 The Drag Method (DM)

The computation of the minimum energy path for the vacancy-atom exchange with the EAM-2BM-GB cohesive model has been achieved within the so called Drag Method (DM).

Once the vacancy is introduced in the bcc Fe-Cr structure, the migration barrier profile is computed by the DM through the following procedure:

1. The migrating atom is displaced, step by step, from its initial position towards the vacancy initial position along the segment joining the initial vacancy position and the migrating atom initial position.
2. At each step, a specific constrained relaxation is performed.
3. At each step, the difference between the energy of the relaxed structure and the energy of the relaxed reference system is computed.

The energies differences computed at each step are plotted as a function of the reaction coordinate (*i.e.* the migrating atom position along the segment joining the initial vacancy position and the migrating atom initial position) to obtain the migration barrier profile. The migration energy is the maximum of the activation barrier profile. If the discretisation step used to increment the migrating atom position along the migration direction is sufficiently small, this point corresponds to the maximum of the minimum energy path (namely: the saddle point energy). During the structure relaxation procedure, two constraints are introduced. The first concerns the migrating atom which is allowed to move only on a plane orthogonal to the migrating direction. The second constraint is applied at the border of the simulation box: the positions of all the atoms located within a distance of 1 Å from the boundary of the simulation box are fixed. Constraining the migrating atom to relax in an orthogonal plane with respect to the migration trajectory avoids the migrating atom to move back to its initial equilibrium position during the relaxation. On the other hand, fixing the simulation box borders avoid the matrix to be dragged along migration direction when the migrating atom is displaced. A schematic representation of the DM is displayed in figure 11-Ch2 for a bcc structure.

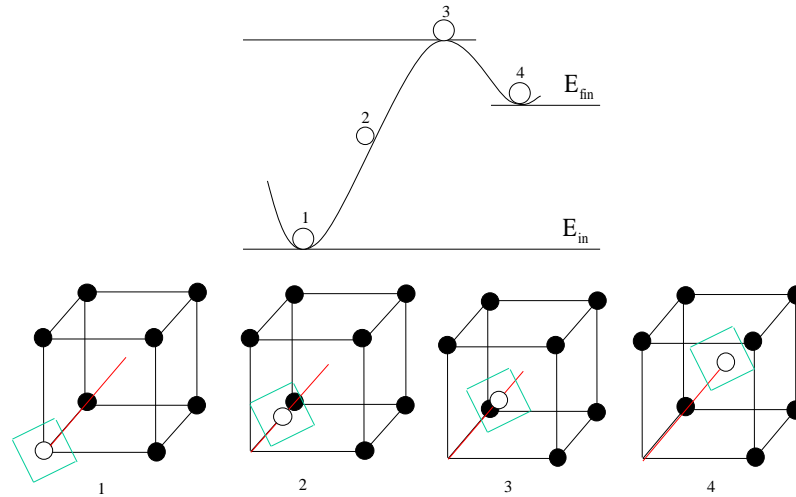


Figure 11-Ch2 Scheme of an atom (white sphere) dragged toward a vacancy placed in the centre of the cell and representation of the associated energy barrier profile.

Red line: migration trajectory

Green plane: plane orthogonal to the line joining the migrating atom initial and final position. At each dragging step, the atom is allowed to relax on the green plane.

The vacancy can jump towards one of its eight (in the case of a bcc structure) nearest neighbours so that the distance between the migrating atom initial position and the vacancy initial position equals the first nearest neighbours distance. For all DM calculations, we considered the equilibrium lattice parameter of a pure iron structure obtained with the EAM-2BM-GB potential: 2.8553 Å. The first nearest neighbours distance is then 2.47 Å. During the calculation of the migration barriers, the migrating atom has been moved by a total distance slightly bigger than the first nearest neighbour distance, namely 2.53 Å, in order to check the position of the final minimum from which the total energy change ΔE of the system associated to the vacancy-migrating atom exchange is computed.

We performed some tests on the effect of the size of the simulation box and on the influence of the discretisation step on the estimation of the migration energy. The first test was done by considering two cubic boxes: $6a_0 \times 6a_0 \times 6a_0$ and $8a_0 \times 8a_0 \times 8a_0$. For both simulation box sizes, the chromium and iron migration energy were computed for all possible chemical configurations of the first neighbour shell ($2^{14} = 16384$ configurations) of the vacancy-migrating atom pair in a first time, and for all possible chemical configurations of the two first neighbour shells ($2^{20} = 1048576$ configurations) of the vacancy-migrating atom pair in a second time. All other sites of the structure were occupied by iron atoms. In figure 12-Ch2, the migration energies computed in the two different sizes of the simulation box are compared.

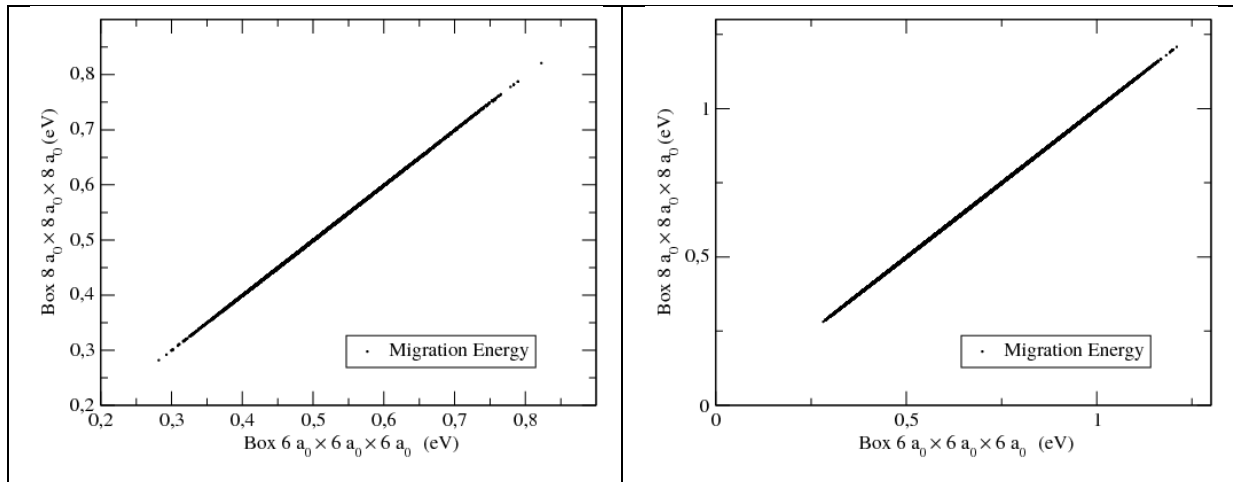


Figure 12-Ch2 Migration barrier computed in a $6a_0 \times 6a_0 \times 6a_0$ box versus migration barriers computed in a $8a_0 \times 8a_0 \times 8a_0$. $a_0 = 2.8553 \text{ \AA}$. Discretisation step: 0.04 \AA . Right hand side: the migration energy has been computed for all chemical configurations of the vacancy-migrating atom pair first nearest neighbours shell. Left hand side: the migration energy has been computed for all chemical configurations of the vacancy-migrating atom pair first and second nearest neighbours shell.

As figure 12-Ch2 displays, no box size effects have been observed: neither in the case where we explored all configurations of first nearest neighbour shell (right hand side of figure 12-Ch2), nor in the case we also considered the second nearest neighbour shell (left hand side of figure 12-Ch2).

The test on the effect of the discretisation step on the estimation of the saddle point energy has been performed for a particular LAE configuration in a $8a_0 \times 8a_0 \times 8a_0$ simulation box. We considered the migration of an iron atom in a LAE where sites A, B1, B2, B3, C1, C2, C3, D1, D2, D3 are occupied by chromium atoms (see figure 7-Ch2 for the atomic sites nomenclature) while all other sites of the structure are occupied by iron atoms. This configuration gives rise to an asymmetric double-hump barrier profile when the cohesive model is the EAM-2BM-GB potential. This configuration thus represents a non-trivial case where the effect of different choices of discretisation step can be efficiently compared. Four different discretisation steps were considered: 0.34 \AA , 0.16 \AA , 0.08 \AA , and 0.04 \AA . Figure 13-Ch2 shows the iron activation energy profile obtained with the four different choices for the discretisation step.

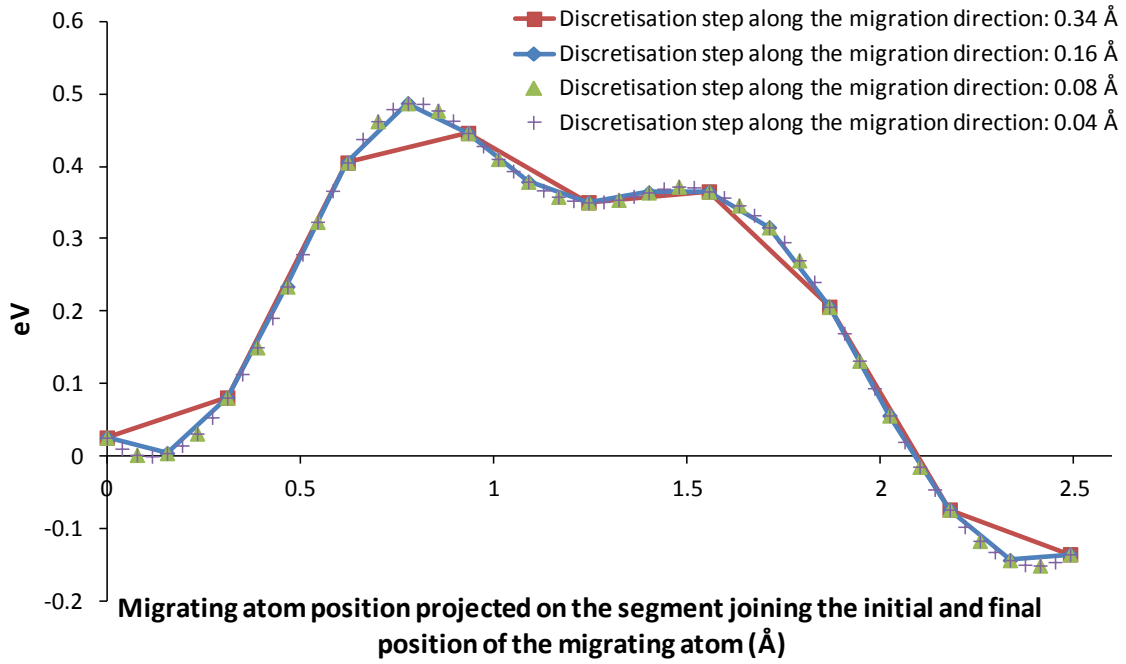


Figure 13-Ch2 Migration profile of a double hump barrier obtained by DM with different discretisation steps. Migrating atom: Fe. Sites A, B1, B2, B3, C1, C2, C3, D1, D2, D3 are occupied by chromium atoms (see figure 7-Ch2 for the atomic sites nomenclature), all other sites of the matrix are occupied by iron atoms. Simulation box size: $8a_0 \times 8a_0 \times 8a_0$. $a_0 = 2.8553 \text{ \AA}$.

As figure 13-Ch2 displays, the larger discretisation step leads to a bad estimation of the saddle point energy and misses the local energy minima associated to the initial and the final position of the migrating atom. The smaller the discretisation step, the better the migration energy barrier profile is reproduced. All the calculations of the vacancy migration energy which will be presented in this work have been performed in a $8a_0 \times 8a_0 \times 8a_0$ simulation box ($a_0 = 2.8553 \text{ \AA}$) and implemented by using the smallest discretisation step we considered in the previous test (*i.e.* 0.04 \AA).

In this chapter, we have characterised some basic properties related to the presence of chromium atoms in an iron matrix by DFT calculations. When possible (*i.e.* excepting for the local magnetic moments calculations), we compared DFT results with those obtained with the EAM-2BM-GB potential. On the other hand, we have defined the optimal parameters to implement the calculation of the vacancy migration energy both in the framework of DFT – with the NEB method – and in the framework of the EAM-2BM-GB potential – with the drag method –. In chapter 3, we will exploit these techniques to investigate the dependence of the vacancy migration energy on the local atomic environment. We will use both the DFT and the EAM-2BM-GB potential and compare their respective predictions. The aim of our approach will be to relate the vacancy migration energy dependence on the local environment to the chromium-chromium and chromium-vacancy interactions and to magnetic effects due to the presence of chromium in the iron matrix. We will show how the difference in the DFT and the EAM-2BM-GB potential estimates for the vacancy migration energy are related to the different estimations of the chromium-chromium and the chromium-vacancy binding energy that we obtained with the two approaches.

3. VACANCY MIGRATION ENERGY DEPENDENCE ON LOCAL CHEMICAL ENVIRONMENT

The first step towards understanding and modelling the Fe-Cr alloy kinetic properties consists in estimating the migration energies related to the processes which drive the microstructure evolution. The vacancy migration barrier is expected to depend on the vacancy-migrating atom pair atomic environment. In the case of Fe-Cu alloys the environmental dependence of the vacancy migration energy has been previously investigated by using an EAM Fe-Cu potential by Le Bouar and Soisson [LeBouar2002] or *via* a DFT approach by Soisson and Fu [Soisson2007]. To our knowledge, such an investigation misses in the case of the Fe-Cr system. The vacancy migration energy dependence on the local atomic environment has been previously studied by Nguyen-Manh *et al.* [Nguyen-Manh2008a, Nguyen-Manh2009] and by Bonny *et al.* [Bonny2011c]. Nguyen-Manh used a DFT approach, while Bonny *et al.* exploited the EAM-2BM-GB Fe-Cr potential as cohesive model. Both these studies only considered the effect of the chromium content in the first nearest neighbour shell of the migrating atom saddle point position without taking into account the effects due to the different positions chromium atoms can occupy within the saddle point local environment. In this chapter we will address the issue of the dependence on the vacancy local atomic environment (LAE) of both the vacancy migration energy and the configurational energy change ΔE which occurs when the vacancy jumps towards one of its nearest neighbour sites. The DFT as well as the EAM-2BM-GB potential will be used in order to determine the ground state energy associated to a given configuration of the system. Our DFT results on the LAE dependence of the vacancy migration energy will be interpreted in the light of the chromium-chromium and chromium-vacancy binding energies as well as the substitutional chromium atoms magnetic properties which we investigated in chapter 2. The DFT based study of the LAE dependence of the vacancy migration barriers and ΔE will be presented in section 3.1. In section 3.2, we will investigate the capability of EAM-2BM-GB potential to reproduce the DFT previsions and the impact that the difference between the DFT and the EAM-2BM-GB potential in the estimation of the chromium-chromium and chromium-vacancy binding energies has on the estimation of the vacancy migration barriers.

3.1 DFT study of the LAE dependence of the vacancy migration barriers

Our objective consists in achieving a better understanding of the influence of the LAE on the vacancy migration energies and the total energy change which occurs when the vacancy jump in an Fe-Cr structure. As we have shown in chapter 2, DFT computed chromium-chromium and chromium-vacancy interactions have been found to be repulsive and attractive respectively. In what follows, it will be shown that such considerations provide a rather simple explanation of the vacancy-atom migration barrier dependence on the LAE. We will also investigate the influence of the magnetic properties on the vacancy migration energy.

In a first step, we will examine how the vacancy migration energy and the total energy of the system evolve while progressively filling the neighbouring shells of the migrating atom with chromium atoms. We then evaluate the influence of the chromium content in different groups of atomic sites, namely B, C, D, and E sites (see figure 1-Ch3 for the atomic sites nomenclature) on the vacancy migration energy and ΔE .

Electronic structure calculations in the framework of DFT have been performed in order to relax all the different structures which have been considered. The vacancy migration energies have been computed with the NEB-CI method implemented by introducing three images between the initial and final position of the vacancy. We considered a simulation box containing 250 atoms. The initial absolute values of the iron and the chromium local magnetic moments have been set to $2.1 \mu_B$ and $0.6 \mu_B$ respectively. Following Klaver *et al.*'s DFT calculations [Klaver2006], isolated chromium atoms initial local magnetic moment (LMM) have been oriented anti-ferromagnetically with respect to the matrix iron atoms. When two or more chromium atoms are close to each other in the matrix, their LMM are oriented ferromagnetically if they are 2nn and anti-ferromagnetically if they are 1nn. The cut-off energy has been set at 300 eV. The first Brillouin zone has been sampled with a mesh of $2 \times 2 \times 2$ k-points in reciprocal space. The theoretical equilibrium lattice parameter of pure iron has been used ($a_0 = 2.831 \text{ \AA}$). One of the main advantages of DFT as compared to the empirical EAM-2BM-GB potential is the fact that, in the first case, the magnetic properties of the system are explicitly taken into account. This is an essential aspect as the magnetic contribution to the cohesive energy has a very strong influence on Fe-Cr alloy properties and, as it will be shown, particularly in the vacancy migration processes.

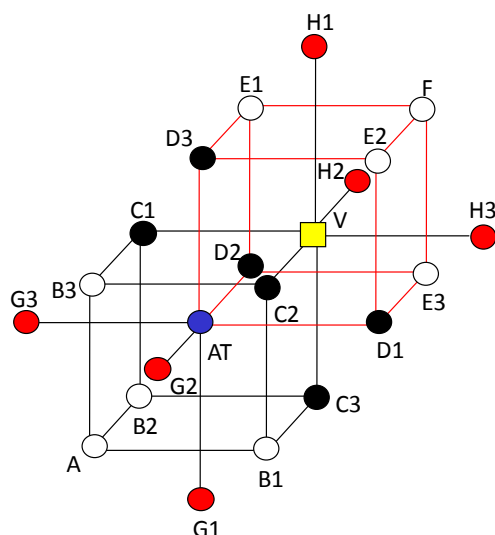


Figure 1-Ch3 Local chemical environment structure scheme and sites nomenclature.

AT: migrating atom

V: vacancy

Black spheres: atom windows the vacancy goes through along migration path (first window: C1, C2, C3. Second window: D1, D2, D3).

3.1.1 Migration barriers dependence on the chromium content in 1st and 2nd nearest neighbour sites of the migrating atom

As the closest atoms to the vacancy will very probably dominate the influence of the environment on the migration barriers, we computed the vacancy-iron and vacancy-chromium migration energies for different chromium contents in the first and the second nearest neighbour shells of the migrating atom and vacancy. The different LAE configurations have been obtained by progressively filling sites A, B1, B2, B3, C1, C2, C3, D1, D2, D3, E1, E2, E3, F, G1, G2, G3, H1, H2, H3 with chromium atoms (see ANNEX 1 for details on the atomic sites nomenclature). The iron and chromium migration energies for all the LAE configurations we explored are displayed in figure 2-Ch3. Figure 2-Ch3 also reports the difference in energy ΔE between the final and the initial configuration for each configuration of the LAE.

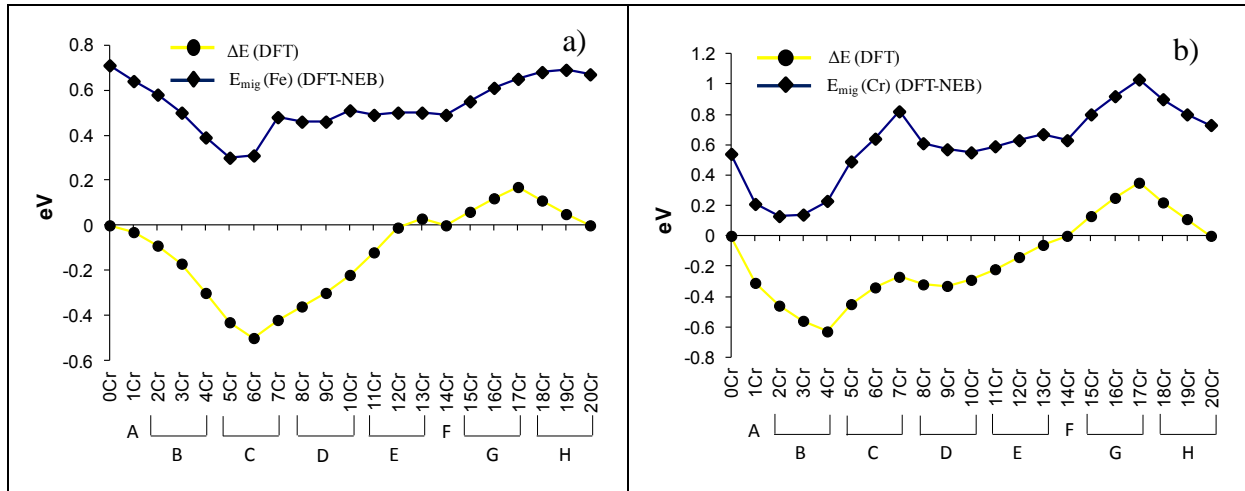


Figure 2-Ch3 Vacancy migration energy and total energy change ΔE for increasing chromium content in first and second nearest neighbour sites of the initial and final positions of the migrating atom. a) The migrating atom is an Fe atom, b) the migrating atom is a Cr atom.

The results presented in figure 1-Ch3 indicate that the vacancy-iron migration energy decreases from 0.64 eV to 0.3 eV when the chromium concentration around the migrating atom initial position increases. This fact is probably due to the chromium-vacancy attractive interaction. Indeed we have shown, in chapter 2, that the chromium interaction with a vacancy is attractive and equal to 0.056 eV when the chromium-vacancy separation corresponds to 1nn distance and 0.010 when the chromium-vacancy separation corresponds to 2nn distance. When sites A, B1, B2, B3, C1, C2, C3 are completely filled with chromium atoms (7 Cr in figure 1-Ch3 horizontal axis), the iron vacancy migration barrier rises from 0.3 eV to 0.5 eV. Then the migration energy remains constant with increasing Cr content until all the nearest neighbours of the migrating atom and vacancy are occupied with chromium atoms. When the second nearest neighbours (G and H sites) start to be occupied with chromium atoms, the vacancy-iron migration energy shows a slowly increasing tendency. As it will be shown in the following, the increase of iron migration energy occurring when the first nearest neighbour shell of iron initial position is saturated with chromium atoms (7 Cr in figure 1-Ch3 horizontal axis) probably has a magnetic origin.

When the migrating atom is a chromium atom, an increase (from 0.2 eV to 0.8 eV) of chromium migration energy can be observed when the C sites – which are first nearest neighbours of the migrating chromium initial position – are progressively filled with chromium atoms. A further increase (from 0.6 eV to 1 eV) of the chromium migration energy occurs when the G sites are occupied (15 to 17 Cr in figure 1-Ch3 b), one by one, by

chromium atoms. Finally the vacancy-chromium migration energy decreases (from 1 eV to 0.7 eV) while the H sites (18 to 20 Cr in figure 1-Ch3 b) are progressively occupied.

The results in figure 1-Ch3 indicate that the migration barriers do depend on the Cr content in the neighbourhood of the migrating atom as could be expected. This dependence is more pronounced when the migrating atom is a chromium atom as the changes in the barriers are larger.

As was shown in chapter 1 and chapter 2 the Fe-Cr system exhibits very peculiar magnetic properties. As a consequence, the Fe-Cr system kinetic behaviour is probably partially driven by magnetism. In order to investigate the role the magnetism plays in such a context, the average of the neighbouring atoms LMM (figure 3-Ch3 for a migrating iron atom and figure 4-Ch3 for a migrating chromium atom) and the migrating atom LMM (figure 5-Ch3 for a migrating iron atom and figure 6-Ch3 for a migrating chromium atom) has been computed for its initial position, saddle point and final position. This has been done for all the LAE configurations we considered here. According to what stated in chapter 2, the LMMs in relaxed Fe-Cr structures have been calculated by integrating the spin density (see equation (9) in chapter 2) in the volume of a sphere centred on each atom and with radius equal to the Wigner-Seitz radius corresponding to the atom type (1.323 Å for chromium and 1.302 Å for iron).

First of all it should be noted that, regardless of the migrating atom type and the chromium content in the LAE, the average LMM of the iron atoms in the super-cell (excluding the migrating atom) remains constant ($\sim 2.2 \mu_B$) whereas the average LMM of chromium atoms in the super-cell varies between $-2 \mu_B$ and $-0.4 \mu_B$ (see figure 3-Ch3 and figure 4-Ch3). Globally, the chromium magnetic moments tend to orient anti-ferromagnetically with respect to the iron matrix magnetic moments. The fact that the absolute value of the chromium atoms average LMM decreases with increasing chromium content in the migrating atom LAE is due to the rise of frustrated magnetic configurations for chromium atoms. This has been previously explained by Klaver *et al.* [Klaver2006] and is further confirmed by our DFT calculations. If one look more carefully to the reduction of the absolute value of the neighbouring chromium average LMM (figure 3-Ch3 and figure 4-Ch3), one can notice that it occurs by means of a three steps variation. This happens because magnetic frustration rises as a shell of chromium is added to a previous existing chromium shell: when sites A, B and C are occupied by chromium atoms, no magnetic frustration occurs; when the D, E and F sites are progressively filled with chromium atoms, magnetic frustration appears. Finally, it becomes more pronounced when the G and H sites are filled

with chromium. Looking at the variation of the migrating iron initial position magnetic moment with the chromium content in its nearest neighbour shell (figure 5-Ch3 horizontal axis), one can observe that the magnetic moment is anti-parallel ($-1.5 \mu_B$) with respect to the matrix when sites A, B1, B2, B3, C1, C2 are filled with chromium (6 Cr in figure 5-Ch3). For the same configuration of its LAE (namely: sites A, B1, B2, B3, C1, C2 occupied by chromium atoms), the migrating iron LMM is positive at the saddle point position. A certain amount of energy is required for this spin-flip to be realised during the displacement of the migrating atom from its initial position to the saddle point position. As a consequence of this spin-flip, a rise of the migration energy occurs starting from the configuration corresponding to the chromium filling of sites A, B1, B2, B3, C1, C2 (6 Cr in figure 1-Ch3 a). The spin flip effect described above occurs between the saddle point and final position of the migrating iron when sites A, B1, B2, B3, C1, C2, C3, D1, D2, D3, E1, E2 are all filled with chromium atoms (12 Cr in figure 5-Ch3 horizontal axis) and disappears when the first nearest neighbour shell of the final position is saturated with chromium atoms (14 Cr in figure 5-Ch3 horizontal axis).

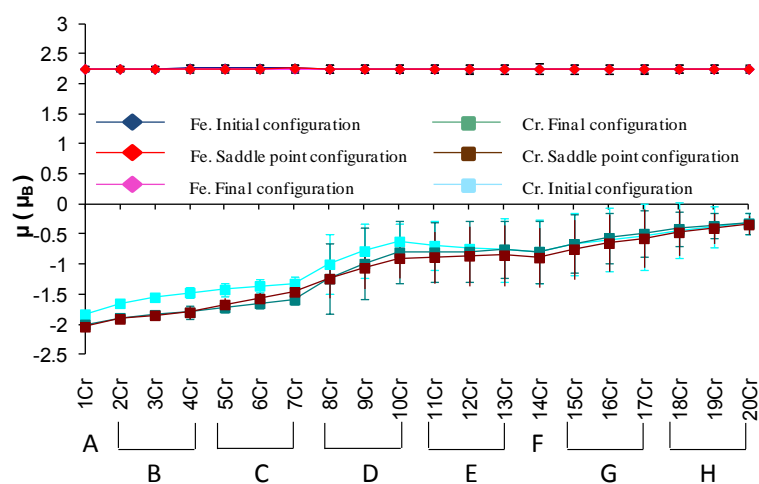


Figure 3-Ch3 Average magnetic moments of neighbouring iron and chromium atoms for the three different positions of a migrating iron atom (initial position, final position, saddle point position) and for different contents of chromium in first and second nearest neighbour sites of the migrating atom and the vacancy. The error bars correspond to the standard deviation.

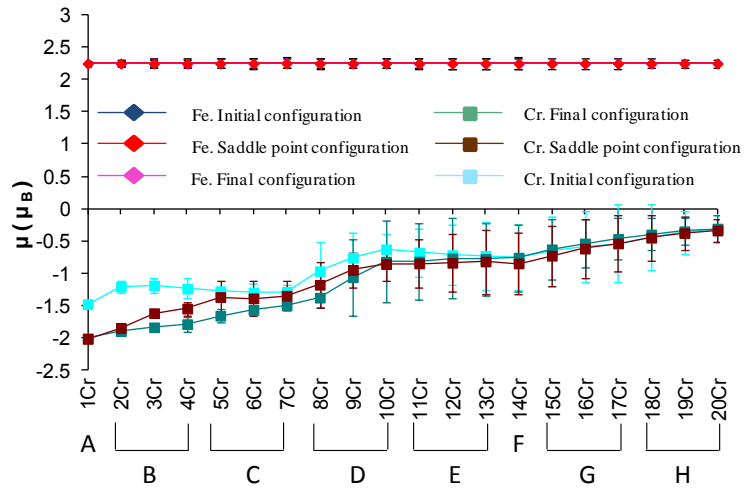


Figure 4-Ch3 Average magnetic moments of neighbouring iron and chromium atoms for the three different positions of a migrating chromium atom (initial position, final position, saddle point position) and for different contents of chromium in first and second nearest neighbour sites of the migrating atom and the vacancy. The error bars correspond to the standard deviation.

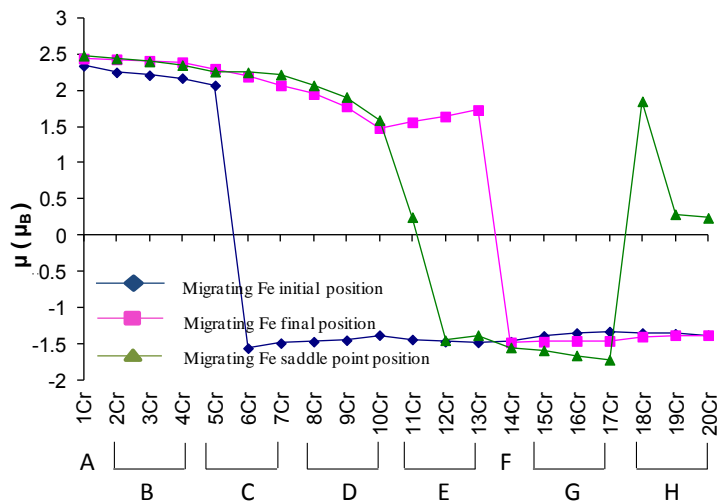


Figure 5-Ch3 Magnetic moments of a migrating iron atom in three different positions (initial position, final position, saddle point position) and for different contents of chromium in first and second nearest neighbour sites of the migrating atom and the vacancy. The error bars correspond to the standard deviation.

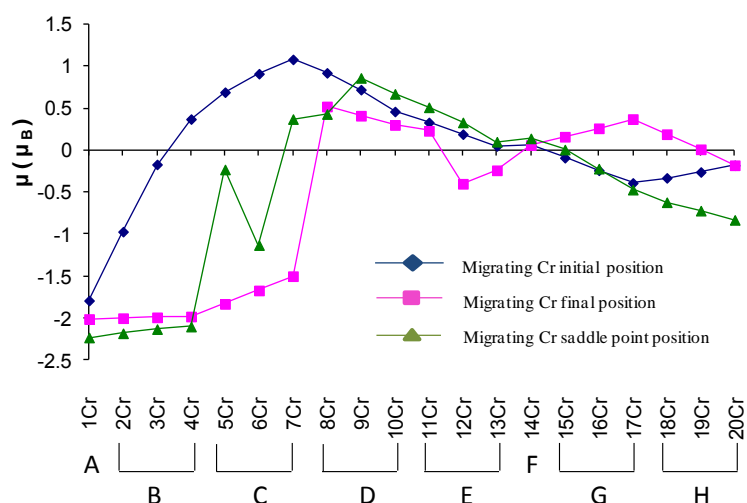


Figure 6-Ch3 Magnetic moments of a migrating chromium atom in three different positions (initial position, final position, saddle point position) and for different contents of chromium in first and second nearest neighbour sites of the migrating atom and the vacancy. The error bars correspond to the standard deviation.

The migrating chromium LMM undergoes a spin-flip when the chromium content in its first nearest neighbours passes from 4 to 7 Cr (figure 6-Ch3). As figure 6-Ch3 shows, the difference between the migrating chromium final and initial LMM increases during the filling of the A, B and C sites with chromium atoms (1 to 7 Cr in figure 6-Ch3). This fact should produce a monotonic increase of vacancy-chromium migration energy in the same region whereas, observing figure 1-Ch3 b, one realises that when sites A, B1, B2, B3 (from 1 Cr to 4 Cr in figure 1-Ch3 b horizontal axis) are progressively occupied with chromium atoms, the vacancy-chromium migration energy stays almost constant. This can be explained by the competition of two coexistent effects whose origins are magnetic in one case and chemical in the other case. On the one hand, the vacancy-chromium exchange requires more and more energy to be realised because of the LMM variation of the migrating atom during the jump, on the other hand the chromium-chromium repulsive interaction –which we have found to be – 0.232 eV (respectively –0.121 eV) when the chromium atoms separation equals first (respectively second) nearest neighbours distance (in good agreement with Olsson *et al.* DFT calculations [Olsson2007]) – lowers the migration barrier when sites A, B1, B2, B3 are filled with chromium atoms (from 1 to 4 Cr in figure 1-Ch3 b) because the neighbouring chromium atoms tend to push away the migrating chromium. These two opposite effects result in a weak variation of the vacancy-chromium migration barrier with the progressive filling of sites A, B1, B2, and B3. Above 7 Cr the figure 6-Ch3 then shows an overall tendency of the migrating chromium LMM to reduce its absolute value. This, we believe, is related to the attempt of the system to minimise its configurational energy excess due to the frustration phenomena.

Another interesting point to notice in figure 1-Ch3 is the fact that, regardless of the atomic species of the migrating atom, and for most of the configuration of the LAE we investigated, the trend observed in the migration energies follows the trend in the ΔE . The migration energy is the difference between the energy of the system when the migrating atom is at the saddle point position and when the migrating atom is at its initial position. In principle, there is no trivial relation between the value of the migration energy and ΔE for a given configuration of the LAE. However, when the ΔE is positive (*i.e.* the final state has higher energy than the initial state), it represents the lower limit of the energy the atom needs to jump towards the vacancy. The migration energy is generally higher than ΔE because the saddle point energy can be higher than the final state energy. As a consequence one can consider that, if ΔE is positive, the difference between the migration energy and ΔE , is the excess energy the atom needs to achieve the path towards the vacancy. Such energy can be supposed as being mainly dependent on the atomic environment near the saddle point position of the migrating atom. From this point of view, if one observes the zone where the second shell of the vacancy-migrating atom LAE starts to be filled with chromium atoms (from 15Cr in figure 1-Ch3 a and b), will note that ΔE is strictly positive and increases until the G sites are completely filled with chromium atoms and decreases when the H sites are progressively filled with chromium atoms. This tendency is a common feature of both chromium atom and iron atom migration energy. The positive ΔE corresponding to the progressive filling of the G1, G2, and G3 sites shows that for such LAE (15Cr, 16 Cr, and 17 Cr in figure 1-Ch3), the initial (before the vacancy jump) configuration of the system has lower energy than the final (after the vacancy jump) configuration of the system. This means that, regardless of the migrating atom type, the initial configuration where the migrating atom first neighbours shell (A, B1, B2, B3, C1, C2, and C3) and the migrating atom second neighbours shell (G1, G2, G3, D1, D2, and D3) are completely filled with chromium atoms is more stable than the final configuration where the vacancy has moved to the migrating atom initial position. From such consideration we deduce that, despite the fact that the chromium-vacancy interaction is attractive, the system is less stable when the vacancy is embedded by two chromium shells (this is not the case when the vacancy is embedded by only one chromium shell). This phenomenon has probably a magnetic origin. The LMMs of chromium atoms embedding the vacancy are slightly higher than LMMs of chromium atoms embedding a chromium atom or an iron atom so that magnetic frustration is enhanced in the former case than in the latter case. However it is very difficult to draw a definitive conclusion on this issue because the chromium compounds corresponding to the different configurations of the LAE that we are

considering here are too far from being large enough to orient their magnetic moment in the chromium antiferromagnetic stable configuration. Also, the spin density around each atom that we integrate to obtain the LMMs may correspond to local minima and not to the real ground state of the system. As a consequence the LMMs we obtain could be not fully reliable.

It is also interesting to note that the chromium atom migration energy variation with the chromium filling of the G sites and the H sites follow the variation of ΔE . The difference between the migration energy and ΔE remains almost constant during the filling of the G sites and the H sites with chromium atoms. This means that the excess energy which must be added to the ΔE to obtain the migration energy weakly depends on the vacancy-migrating atom pair second neighbour shell. Also it seems that the variation of the vacancy migration energy with the environment is driven by the variation of the ΔE when the G and H sites are progressively filled with chromium atoms. The situation is less clear in the case where the migrating atom is an iron atom (see figure 1-Ch3 a). Indeed, the ΔE variation with the increasing chromium content in the G sites and the H sites follows the tendency observed when the migrating atom is a chromium atom but the migration energy does not.

3.1.2 Migration barriers dependence on the position of the environmental chromium along the migration path

In order to better understand the influence of the specific positions of the chromium atoms on the vacancy-atom migration barriers, the vacancy-chromium and vacancy-iron migration energies have been calculated for different positions of a single chromium atom in the LAE.

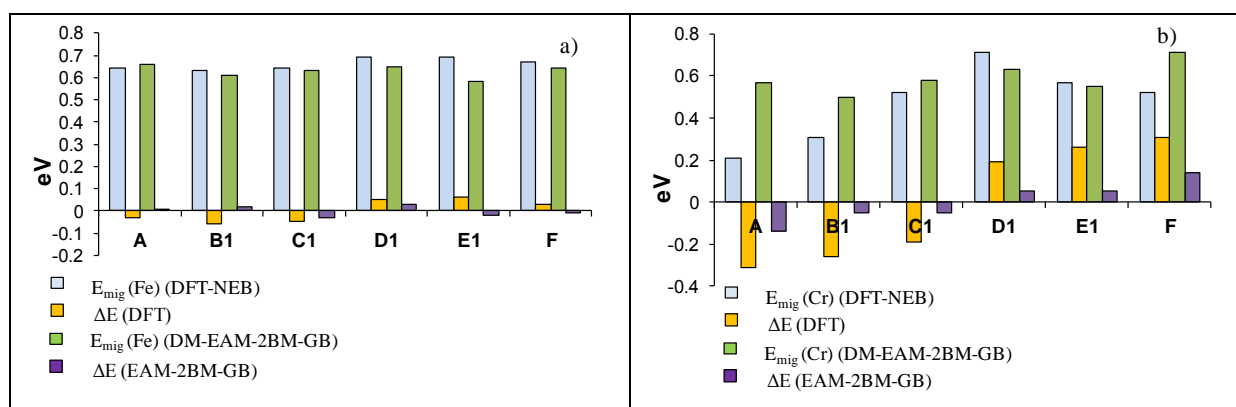


Figure 7-Ch3 Vacancy migration energy and difference (ΔE) between final (after the migration) and initial (before the migration) energy of the system for different positions of one chromium atom within the first nearest neighbour sites of initial and final position of migrating atom. a) The migrating atom is an Fe atom b) the migrating atom is a Cr atom.

Figure 7-Ch3 indicates that, as already observed in figure 3, the changes in the barrier are more pronounced when the migrating atom is a chromium atom. Indeed, the vacancy-iron migration energy and the ΔE depend very weakly on the presence of one chromium atom in the local environment whereas the vacancy-chromium migration is sensible to the presence and, in particular, to the relative position of the chromium atom. This fact can be easily explained as the consequence of the repulsive interaction existing between chromium atoms. When the system contains only two chromium atoms, their LMMs are both oriented antiferromagnetically with respect to the iron atoms LMMs and this regardless of their separation distance (see table 2-Ch2 in chapter 2). As a consequence, when the two chromium atoms are first nearest neighbours an intense repulsive force rise between them to increase their separation distance and avoid a frustrated magnetic configuration.

According to our results, the chromium-chromium repulsive interaction can either produce a rise of chromium migration energy or a reduction of chromium migration energy depending on the positions of the environmental chromium atoms. If a chromium atom is placed in site A or in site B1, the vacancy-chromium migration barrier is lower than in the

cases sites C1, D1, E1 or F are occupied. This is due to the fact that in the first cases the chromium-chromium repulsive force facilitates the jump of the migrating chromium atom towards the vacancy whereas in the latter cases chromium-chromium repulsive force represents an obstacle to the migrating chromium.

The migration barrier is also larger when the Cr atom is situated in the neighbourhood of the saddle point (C and D windows) or of the final position (E and F sites). In fact, the maximum value of the vacancy-atom migration energy results from the presence of a chromium atom in a D site (this fact is much more visible in the case where the migrating atom is chromium).

The dependence of ΔE on the LAE is related not only to the Cr-Cr binding energy but also to the Cr-V binding energy. According to our DFT calculations, the latter is equal to 0.056 eV when the chromium and the vacancy are 1st nearest neighbour and 0.01 eV when they are 2nd nearest neighbours. When the migrating atom is an iron atom, the main contribution to ΔE is the interaction of the vacancy with chromium atoms belonging to the LAE. The gain or the loss of stability for the system, which follows a vacancy-atom exchange, depends on the variation of the number of chromium atoms which are first or second nearest neighbours of the vacancy. As the chromium-vacancy interaction is attractive, the system tends to become more stable when the chromium occupancy of the sites surrounding the vacancy increases and *vice versa*. However, since the chromium-vacancy interaction is weak, this effect is quite small, as can be seen in figure 7-Ch3 a) for the migrating iron atom. On the other hand, the chromium-chromium interaction plays a more important role in the variation of the energy of the system, because of its magnitude with respect to the chromium-vacancy interaction. Chromium-chromium repulsion is strong and considerably dependent on the distance between the two chromium atoms (see figure 4-Ch2 in chapter 2). As a consequence, the ΔE can be very large and strongly affected by the LAE. When the vacancy jump leads to an increase of the distance between the migrating chromium and the chromium atoms in LAE, then the system becomes more stable. On the contrary, when the vacancy jump results in a reduction of the distance between the migrating chromium and environmental chromium atoms, then the total cohesive energy increases and the system becomes less stable (see in figure 7-Ch3 b).

3.1.3 Influence of the saddle point and the final configuration environment

Figure 1-Ch3 indicates that, especially in the case where the migrating atom is a chromium atom, the chromium content of the nearest neighbour sites of the migrating atom saddle point position (sites C1, C2, C3, D1, D2, and D3) has a notable influence on the variation of the migration energies. In particular figure 1-Ch3 shows that when the C sites and the D sites are progressively filled with chromium atom the dependence on the LAE of the vacancy migration energy differs from the variation of the ΔE . This can be noticed especially in the case where the migrating atom is a chromium atom for which the progressive filling sites C1, C2, and C3 corresponds to a monotonic growth of the vacancy-atom exchange migration energy. This latter aspect was previously pointed by Nguyen Manh *et al.* [Nguyen-Manh2008a, Nguyen-Manh2009] who investigated a few specific configurations. In order to study in a more precise way the influence of the neighbouring Cr atoms on the vacancy migration energy, we investigated all the possible configurations of the saddle point environment using the DFT-NEB-CI approach. All our results can be found in ANNEX 2, in what follows we will discuss the most significant cases.

Figure 8-Ch3 represents the evolution of the migration energy and the changes in total energy of the system when filling progressively the "saddle point windows" and the final configuration sites.

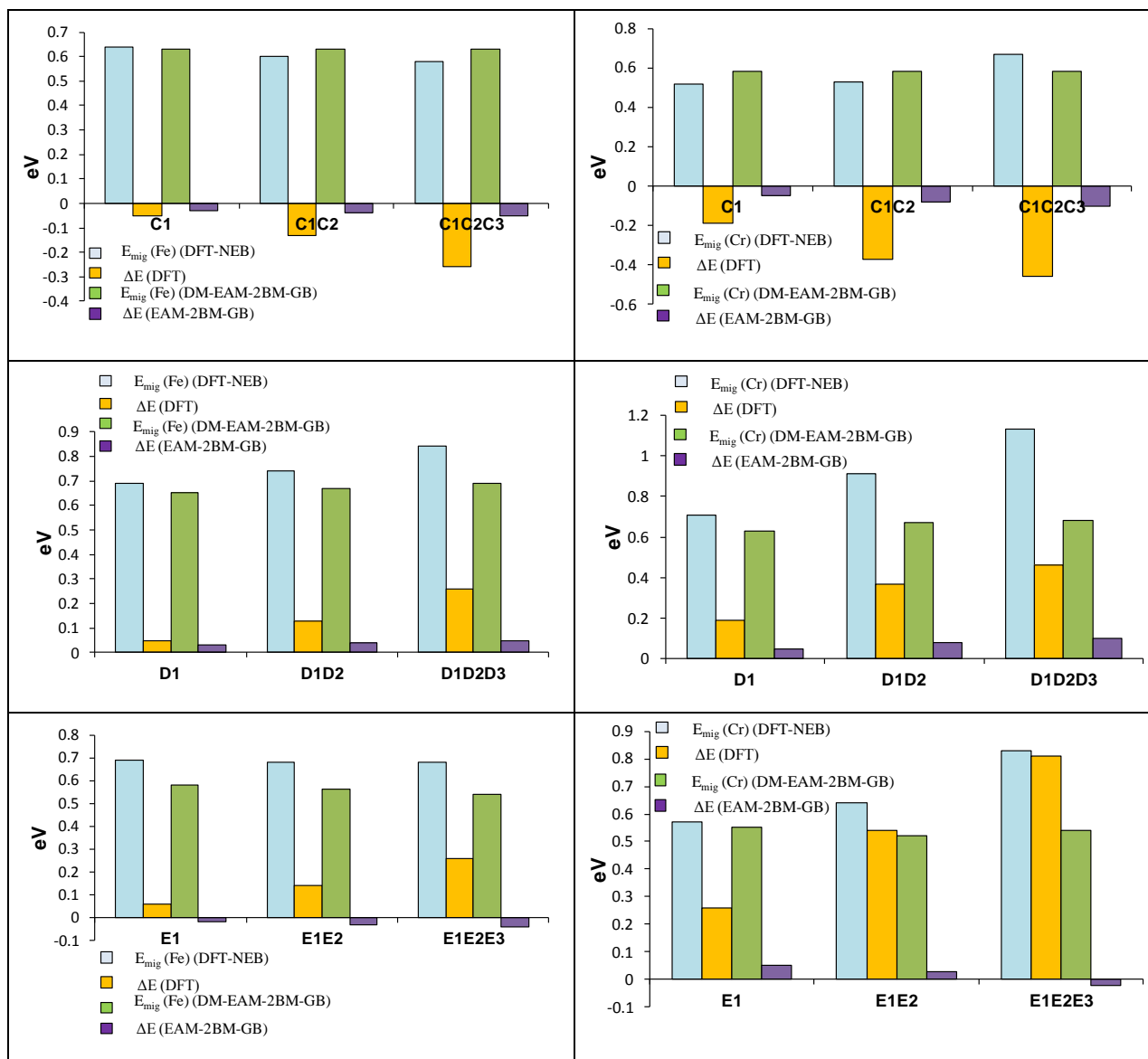


Figure 8-Ch3 Migration barriers and change in the total energy configuration ΔE as a function of the filling of the different sites (“saddle point window”: C and D and sites: E) with Cr atoms. Left: the migrating atom is an Fe atom; right: the migrating atom is a Cr atom.

Figure 8-Ch3 clearly shows that the filling of windows C and D and sites E has a strong impact on ΔE . The more Cr atoms located in the C window, the lower the final configuration energy, whereas the more Cr atoms located in the D and E sites the higher the final configuration energy. The fact that the trends are not as pronounced for the migration barrier, in particular for the E sites demonstrates the delicate balance between the contribution of the final and initial configurations and that of the local environment of the saddle point to the migration barrier.

The calculations of the vacancy-iron and vacancy-chromium migration energies show that the migration barriers exhibit a clear dependence on the saddle point nearest neighbour

shell chemical environment. In particular the most remarkable effect can be summarised as follows: when sites D1 D2 D3 are occupied by chromium atoms the vacancy migration energy is always higher than in the other cases. This tendency can be observed also for each configuration for which chromium occupancy of D sites is higher than chromium occupancy of C sites and is stronger when the migrating atom is chromium. The latter observation (in the extreme case corresponding to a complete chromium filling of the D sites and a complete iron filling of C sites) can be explained with a magnetic interaction argument. Chromium atoms in sites D are second nearest neighbours of the migrating chromium when the latter is at its initial position. When the migrating chromium reaches its final position by means of the exchange with the vacancy, the D sites become its nearest neighbours. This means that the migrating chromium atom at its initial position can orient its LMM in a parallel way with respect to the other chromium atoms in the structure (placed in sites D1, D2, and D3) and in anti-parallel way with respect to the iron atoms in the structure. The migrating chromium at its final position will tend to orient its LMM in order to create an anti-ferromagnetic compound with chromium atoms in D1, D2, D3 (now first nearest neighbours) and, at the same time, it will tend to orient its LMM in anti-ferromagnetic configuration with respect to the iron atoms in the matrix. This competition between two orientation states of the LMM associated to the migrating chromium at its final position leads to a frustrated configuration with higher energy than the one corresponding to the configuration before the chromium atom jump. Figure 9-Ch3 depicts the mechanism described above. In order to better illustrate this phenomenon, we computed the vacancy-chromium migration energy in an environment characterised by the chromium occupancy of sites D1, D2, and D3 (all other matrix sites being occupied by iron atoms) by introducing nine images between the initial and the final position of the vacancy. Figure 10-Ch3 displays the variation of migrating chromium LMM along the migration path (left hand side) and the migration barrier energy profile (right hand side). The left hand side of figure 10-Ch3 clearly shows that the migrating chromium LMM undergoes a spin-flip.

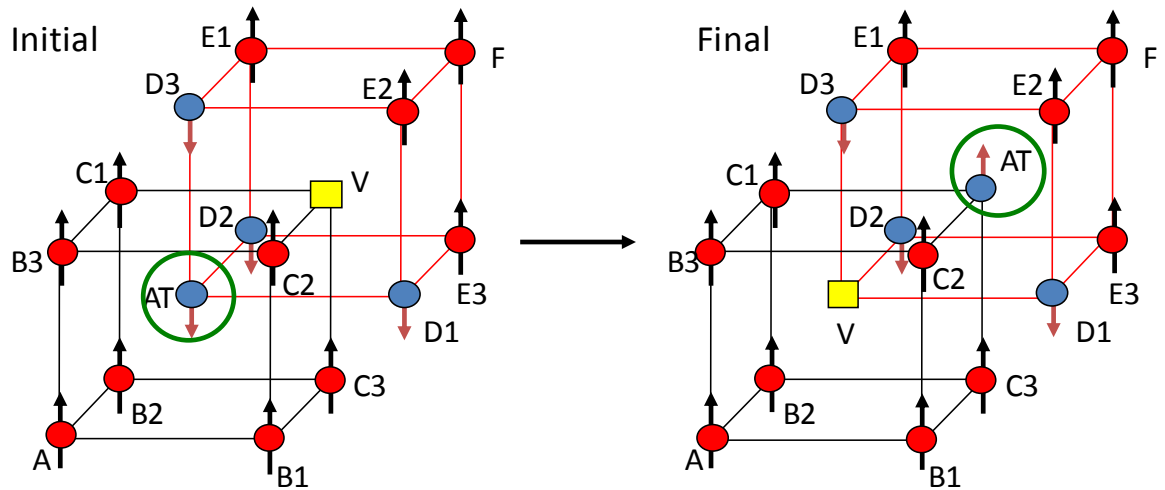


Figure 9-Ch3 Migrating chromium magnetic moment before (left side) and after (right side) the jump when sites D1, D2, D3 (see ANNEX 1) are occupied with chromium atoms.

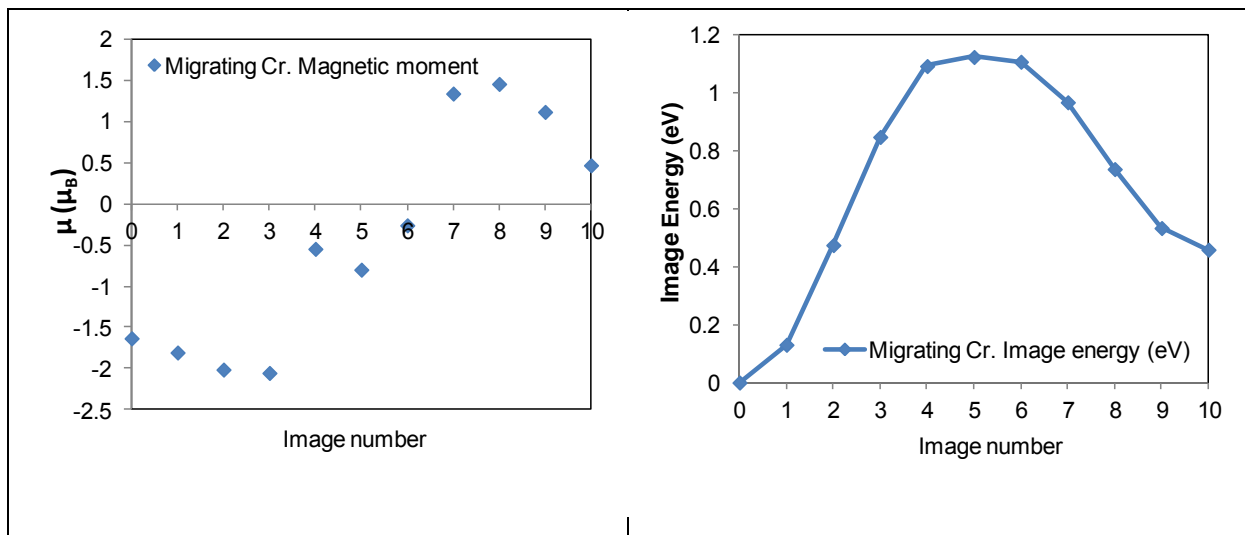


Figure 10-Ch3 Migrating chromium LMM (left) and migration barrier profile (right). Sites D1, D2, D3 (see ANNEX 1) are occupied by chromium atoms and all the other sites in the supercell are occupied by iron atoms.

A more general explanation of the fact that the vacancy-atom migration barrier is higher when the chromium content among the D sites is higher than the chromium content among the C sites can be formulated in terms of the chromium-chromium and the chromium-vacancy interaction.

A migration barrier profile associated to a vacancy-atom exchange provides both the migration energy of the forward jump and the migration energy of the backward jump. Let us consider, as an example, the case we dealt with above (figure 10-Ch3): the chromium migration in the environment characterised by the occupation of all D sites with chromium atoms and all C sites with iron atoms. The migration barrier represented in the right hand side

of figure 10-Ch3 provides the migration energy of the forward jump but also, by reversing the reaction coordinate, the migration energy of the backward jump. The backward jump path is equivalent, on a topological point of view, to the chromium migration in the environment characterised by full chromium occupancy of C sites and full iron occupancy of D sites. In the case represented in figure 10-Ch3, comparing the forward migration energy with the backward migration energy is equivalent to comparing chromium migration energy for the configuration represented by chromium saturation of D sites and iron saturation of C sites with the chromium migration energy for the symmetric configuration (*i.e.* chromium saturation of C sites and iron saturation of D sites). From this point of view, the difference of migration energy between a forward and backward vacancy-atom jump corresponds to the energy difference between the two reference equilibrium configurations (see figure 11-Ch3 for a schematic representation). This means that the difference between vacancy-atom migration energies computed for two symmetric configurations (by chromium occupancy exchange in sites D and C) corresponds to the energy difference between the initial and final state energy with a sign depending on the direction of the migration (from 1 to 2 or from 2 to 1, if one uses the nomenclature in figure 11-Ch3). It is clear that the energy the system needs for an atom to jump in a vacancy is at least the energy difference between the final state and the initial state energies, if the final state has a higher energy than the initial state. Inversely, the energy gain for the system corresponds to the energy difference between the initial state and the final state energies if the initial state has a higher energy than the final state. As a result the difference between the vacancy-atom migration energy in symmetric configurations simply corresponds to the energy difference of the final and the initial state energy. The reason why a higher chromium occupancy of the D sites leads to higher vacancy-atom migration energies can be then understood by simply thinking in terms of the final state (after the jump) and initial state (before the jump) energy difference:

- In the case the migrating atom is a chromium atom, a higher chromium occupancy of the D sites than the chromium occupancy of the C sites (all other sites of the matrix being occupied by iron atoms) will mean that the migrating chromium, at its final position, will have a larger number of chromium atoms within its nearest neighbours than at its initial position. This implies that the final configuration energy will be higher than the initial configuration energy because of the chromium-chromium repulsive interaction.

- In the case the migrating atom is an iron atom, a higher chromium occupancy of the D sites than the chromium occupancy of the C sites (all other sites of the matrix being occupied by iron atoms) will mean that the vacancy, at its final position, will have a lower number of chromium atoms within its nearest neighbour than at its initial position. This implies that the final configuration energy will be higher than the initial configuration energy because of the chromium-vacancy attractive interaction.

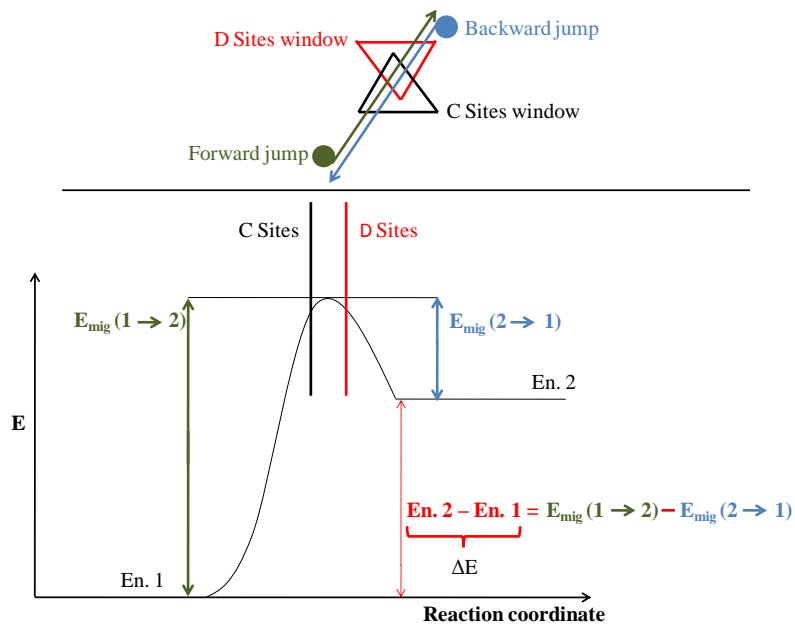


Figure 11-Ch3 Migration barrier for a forward and backward jump of the migrating atom through the C sites "window" and the D sites "window".

What has been stated above indicates that, in some cases, the variation of the vacancy migration barrier as a function of the LAE follows the variation of total energy of the whole system. In particular, this is true when one compares the vacancy migration energy for LAEs which are symmetric with respect to the inversion of the reaction coordinate.

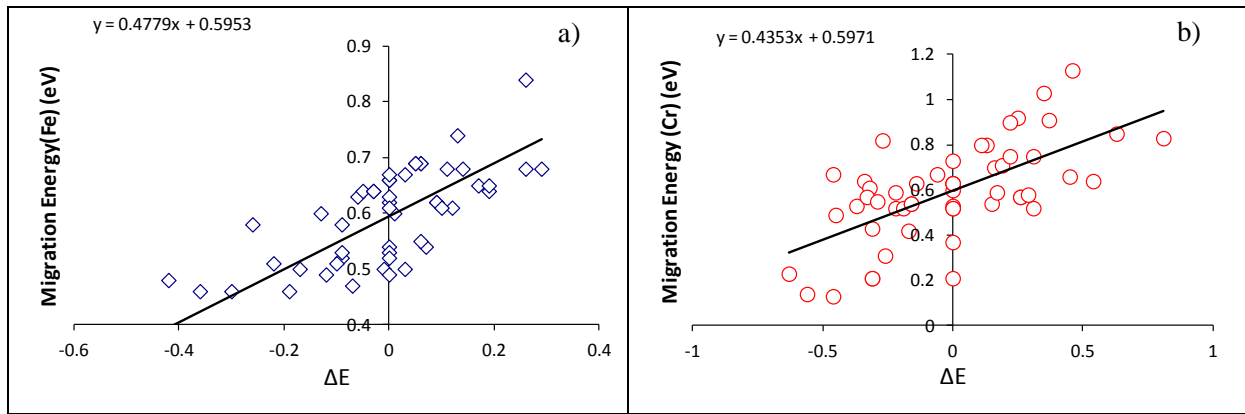


Figure 12-Ch3 Migration barrier as a function of the change in the total energy configuration (ΔE). a) The migrating atom is an Fe atom, b) the migrating atom is a Cr atom. The equations on the figure are the linear fits of the data points obtained by least square method. a) The square of the correlation coefficient is $R^2 = 0.6393$. b) The square of the correlation coefficient is $R^2 = 0.4176$.

However, a general relation between the vacancy migration energy and the energy change of the system due to the vacancy jump cannot be established. The reason for that is the fact that the migration energy is the difference between the saddle point energy (*i.e.* the energy of the system when the migrating atom is at the saddle point position) and the energy of the system before the vacancy jump. Thus, strictly speaking, the migration energy does not depend on the energy of the system after the vacancy jump. Figure 12-Ch3 – where all configurations which have been considered are represented – seems to indicate that there is indeed some correlation between the migration energy and the ΔE associated to a given vacancy migration process. However the dispersion of the data points also indicates that the migration energy depends also on the local environment at the saddle point as shown previously. Indeed most of the data points which lie far away from the "tendency line" can be understood by a careful examination of the saddle point windows.

All along this section we tried with some success to provide a physically consistent interpretation of the vacancy migration energy and ΔE dependence on the LAE based on magnetic arguments or considerations concerning the chromium-chromium and chromium-vacancy interaction. We can make the following conclusions:

1. In most cases the chromium-chromium and the chromium-vacancy interactions can explain the variation of the vacancy migration energy as a function of the LAE.
- 2.

3. In most configurations of the LAE, the trend we observed for the vacancy migration energy follows the trend of ΔE .
4. When chromium atoms occupy the nearest neighbour site of the migrating atom saddle point positions (C sites and D sites), the relationship between the migration energy and ΔE is not trivial.
5. A practical model of the migration barrier for the vacancy migration, such as the model introduced by Kang and Weinberg [Kang1988] and later referred as the final initial state energy (FISE) model [Vincent2008], in an Fe-Cr system has to take into account not only the total energies change of the system due to the vacancy jump but also a description of the saddle point chemistry and in particular the number of Cr atoms in the saddle point environment.

3.2 EAM-2BM-GB potential

In order to test the capability of the EAM-2BM-GB potential to reproduce the DFT trends regarding the influence of the LAE, we computed the vacancy migration energy and ΔE for different chromium contents using the Drag Method (DM) and the EAM-2BM-GB potential.

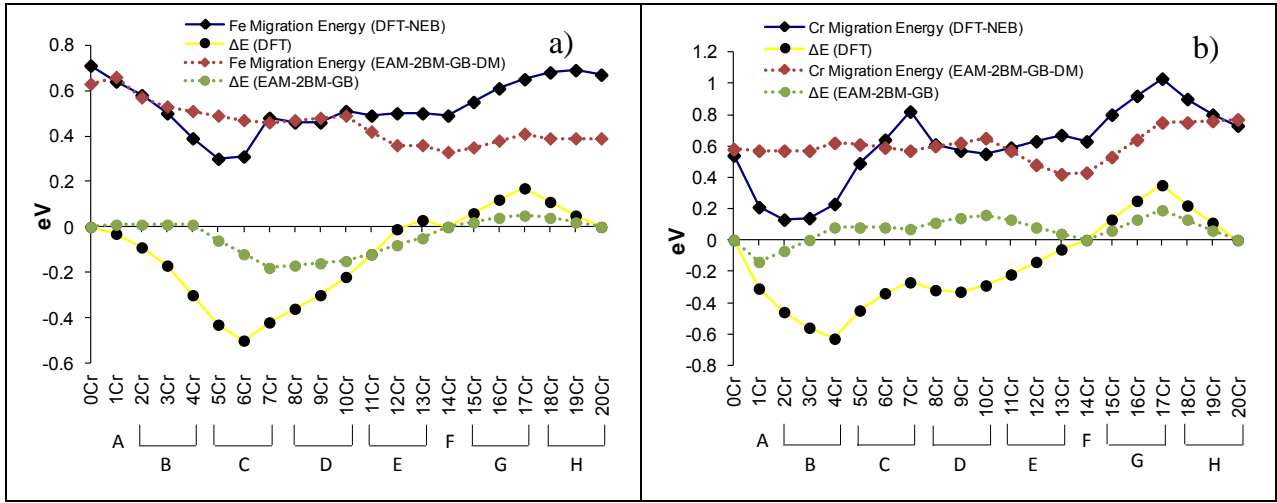


Figure 13-Ch3 Iron-vacancy migration energy and total energy change ΔE for increasing chromium content in first and second nearest neighbour sites of initial and final position of migrating atom. Comparison between DFT previsions and EAM-2BM-GB potential results. a) The migrating atom is an Fe atom, b) the migrating atom is a Cr atom.

Accordingly to our previous tests (see chapter 2), all the calculations of the vacancy migration energy with the EAM-2BM-GB potential have been performed within the DM in a $8a_0 \times 8a_0 \times 8a_0$ simulation box ($a_0 = 2.855 \text{ \AA}$) with a discretisation step corresponding to 0.04 \AA along the segment joining the initial and final position of the migrating atom. Our results are represented in figure 13-Ch3.

The first interesting feature of our results is that, as we observed for the DFT results, the EAM-2BM-GB calculations show some correlation between the dependence on the LAE of the migration energy and ΔE . Nevertheless, once again, no trivial relationship between the migration energy associated to a vacancy jump and the energy changes it leads to can be established. The largest disagreement between the EAM-2BM-GB potential and DFT results are observed when the migrating atom is a chromium atom. Furthermore, for both vacancy-iron exchanges and vacancy-chromium exchanges, a disagreement occurs when the C sites (which are first nearest neighbours of the saddle point position) are progressively filled with

chromium atoms. The disagreement is quite important also in the case of the vacancy-chromium exchange when one fills the A and B sites with chromium atoms. The latter observation is a consequence of the difference in the chromium-chromium binding energy predicted by DFT and the EAM-2BM-GB potential. Concerning the case of the vacancy-chromium exchange, figure 13-Ch3-(b) also reveals that, for a large range of chromium contents in the LAE, the cohesive energy change related to the vacancy jump computed by DFT or by the EAM-2BM-GB potential differs by the sign. An important point which should be emphasised is the fact that the EAM-2BM-GB potential correctly reproduces the variation of the migration energy due to the progressive filling of sites G and H.

Finally, figure 7-Ch3 and figure 8-Ch3 clearly show that the vacancy migration barriers and the ΔE computed with the EAM-2BM-GB potential are less sensitive to the LAE than the ones obtained by DFT. Nevertheless, it should be noticed that, from a qualitative point of view, the EAM-2BM-GB potential is able to reproduce some of the tendencies we observed. In particular, it correctly predicts the fact that both vacancy-chromium and vacancy-iron migration barriers are higher in the case where chromium atoms are located in the D sites than in the case where the chromium atoms of the LAE occupy the C sites.

Figure 14-Ch3 displays a comparison of the migration barriers computed with the EAM-2BM-GB potential and the DFT for different configurations of the LAE of the vacancy-migrating atom pair. The list of the configurations of the LAE which have been considered can be found in ANNEX 3.

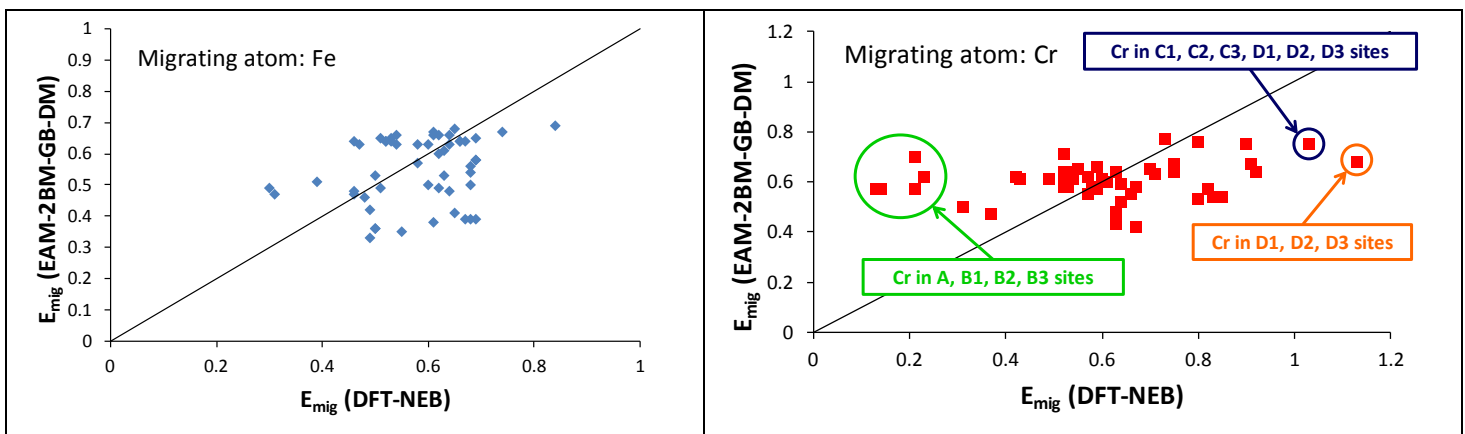


Figure 14-Ch3 DFT-NEB vs. DM-EAM-2BM-GB. Migration energy for different configurations of LAE. Left hand side: the migrating atom is an Fe atom, Right hand side: the migrating atom is a Cr atom.

Figure 14-Ch3 shows that the EAM-2BM-GB potential fails to reproduce the DFT estimations. Especially in the case where migrating atom is chromium, the migration energies

obtained with the EAM-2BM-GB potential exhibit a weak dependence on chemical environment compared to DFT results. The right hand side of figure 14-Ch3 shows that the variation domain of the migration energies is broader for DFT calculations than for the EAM-2BM-GB-DM ones. It is important to notice that some of the worst estimations of the chromium migration barriers obtained with the EAM-2BM-GB potential concern LAE configurations characterised by the presence of chromium atoms in the A, B1, B2, B3 sites (green circle in right hand side of figure 14-Ch3), in D1, D2, D3 sites (orange circle in right hand side of figure 14-Ch3) and in C1, C2, C3, D1, D2, D3 sites (blue circle in right hand side of figure 14-Ch3). This confirms our previous conclusions about the inability of the EAM-2BM-GB potential to correctly reproduce the DFT results for LAE containing chromium atoms in A, B or C sites (see figure 13-Ch3). A partial explanation is that the EAM-2BM-GB potential predicts that the chromium-chromium interactions decreases more slowly with distance than predicted by DFT (see figure 4-Ch2 in chapter 2) and is thus less sensible to the distance between chromium atoms. As a result, when a chromium atom migrates towards a vacancy and its position with respect to the chromium atoms in the LAE changes, a smaller variation of the total energy of the system occurs than predicted by DFT.

The same explanation holds regarding the dependence of ΔE on the LAE. It is stronger for the DFT results than for the EAM-2BM-GB potential calculations.

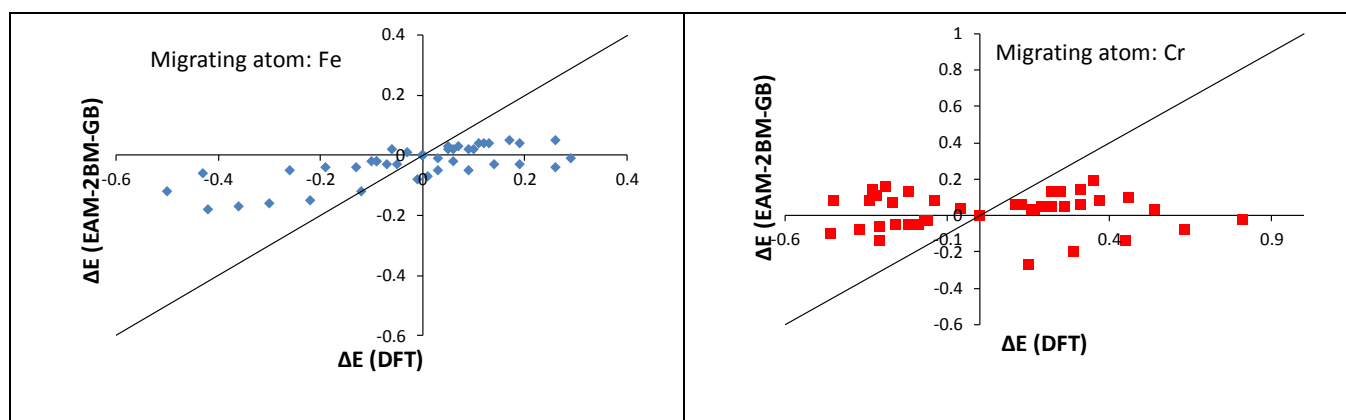


Figure 15-Ch3 DFT vs. EAM-2BM-GB. Total energy change of the system induced by a vacancy-atom exchange for different configurations of the LAE. Left: the migrating atom is an Fe atom, right: the migrating atom is a Cr atom.

Figure 15-Ch3 shows indeed that, for the configurations which we investigated, the variation range of ΔE is broader for DFT calculations than for EAM-2BM-GB potential based calculations.

The disagreement between the chromium-vacancy binding energy obtained with DFT or with the EAM-2BM-GB potential mainly affects the cohesive energy change ΔE induced by the vacancy-iron exchange (see left hand side of figure 15-Ch3). The reason of such a disagreement comes from the fact that, even if both the DFT and the EAM-2BM-GB potential predict very weak chromium-vacancy interactions, their estimations are qualitatively different: in the case of DFT the interaction is attractive whereas in the case of the EAM-2BM-GB potential the interaction is repulsive. This leads to the previously mentioned sign differences between the ΔE computed with the DFT or with the EAM-2BM-GB potential.

Considering what has been shown above, one could wonder why the EAM-2BM-GB potential is still capable of reproducing some of the DFT trends regarding the vacancy migration barriers dependence on the saddle point environment. In particular, the EAM-2BM-GB potential reproduces the fact that the vacancy migration energy is higher when the D sites chromium content is higher than the C sites chromium content, although their absolute values are far from DFT results. In section 3.1, we explained this tendency as being a consequence of the chromium-chromium interaction and the chromium-vacancy interaction. How can the EAM-2BM-GB potential reproduce such tendencies despite its disagreement with the DFT concerning the estimation of the chromium-chromium interaction and chromium-vacancy interaction (see chapter 2)? As we discussed above, the disagreement between the DFT and the EAM-2BM-GB potential is only quantitative for the chromium-chromium interaction: both the cohesive models predict a repulsive interaction. However, the EAM-2BM-GB potential predicts that the repulsive interaction decreases slower with chromium-chromium separation distance than in the case of DFT. As a consequence, the cohesive energies and migration barriers computed with the EAM-2BM-GB potential are less sensitive to the environmental chromium relative distances and, consequently, to the LAE configuration. Concerning the vacancy-chromium interaction, the EAM-2BM-GB potential predicts a repulsive interaction which increases when the vacancy-chromium separation increases from 1nn distance to 2nn distance whereas DFT predicts an attractive vacancy-chromium distance which decreases with vacancy-chromium separation. However, regardless of this striking qualitative disagreement, in both cases an increase of the distance between the vacancy and the chromium atoms in the LAE leads to an increase of the total cohesive energy of the system.

The comparison we made in this section between the DFT and the EAM-2BM-GB potential allows us to conclude that:

1. Because of the disagreement between the DFT and the EAM-2BM-GB potential results about the chromium-chromium and the chromium-vacancy interactions, the two approaches predicts ΔE which are sometimes in qualitative disagreement.
2. Even if the EAM-2BM-GB potential is able to reproduce some features of DFT results, its sensibility to the dependence of vacancy migration energy and ΔE on the LAE is smoothed by the fact that it predicts a too long-range chromium-chromium interaction.

In this chapter, we have investigated the dependence of the vacancy migration energy on the LAE. DFT calculations presented in section 3.1 allowed us to capture the vacancy migration dependence on the chromium content in the first and second nearest neighbour shells of the vacancy-migrating atom pair. We also investigated the specific influence of the presence of chromium atoms in localised zone of the LAE. In both cases, we partially interpreted the variation of the vacancy migration energy as driven by the chromium-chromium and the chromium-vacancy interactions as well as by the variation of the magnetic state of the system during the vacancy jump. Moreover, we investigated the relation between the vacancy migration energy and the variation of the cohesive energy ΔE of the system that follows a vacancy jump. We have shown that, even if in most configurations of the LAE, the trend we observed for the vacancy migration energy follows the trend of ΔE , this is not true in general. In particular, in the case of a migrating chromium atom, if chromium atoms are located among the nearest neighbour sites of the saddle point position (the C sites or the D sites), the relation between the migration energy and ΔE could be not trivial. As a consequence, a model based on the Kang and Weinberg approach [Kang1988] and providing an approximate estimation of the vacancy migration barrier in an Fe-Cr structure, has to take into account, not only the total energies change of the system due to the vacancy jump, but also a description of the saddle point chemistry.

Section 3.2 has been devoted to the investigation of the capability of the EAM-2BM-GB potential to reproduce DFT results. We observed that the disagreement between the DFT and the EAM-2BM-GB potential in the description of the chromium-chromium and the chromium-vacancy interactions sometimes leads to qualitative disagreement about the estimation of ΔE . Finally, from a general point of view, even if the EAM-2BM-GB potential is able to reproduce some features of DFT results, it is less sensible than the DFT to the dependence of the vacancy migration energy and ΔE on the LAE because it predicts a too long-range chromium-chromium interaction.

4. SIMULATION OF THE THERMAL AGEING OF Fe-Cr BINARY ALLOYS

Since experiments on materials thermal ageing are time-expensive, a reliable computer simulation approach, able to describe Fe-Cr alloys microstructure evolution, represents a useful tool which contributes to the understanding of the thermal ageing mechanism. The simulation of the microstructure evolution induced by thermal ageing in a crystalline structure can be described *via* the Atomistic Kinetic Monte Carlo (AKMC) approach. The AKMC allows, through the residence time algorithm, to estimate the physical time related to the microstructure evolution of the alloy. In this context, if one neglects relaxation effects and vibration entropy contributions to the free energy of the system, the bulk can be modelled by a rigid lattice. Moreover, if the existence of other kinds of defects such as interstitial atoms is not taken into account, the evolution of the configuration of the system can be simulated as being driven by a vacancy diffusion mechanism. In this work, the vacancy diffusion *via* a vacancy-atom exchange (*i.e.* the migration of an atom towards an unoccupied site among its eight nearest neighbours) will be considered as the only process leading to the Fe-Cr microstructure evolution. As we will not consider radiation damage situations, interstitial defects will not be introduced in the systems we will analyse.

The first step towards the understanding and modelling Fe-Cr alloy kinetic properties consists in computing the energy barriers related to the processes which drive the alloy microstructure evolution. The vacancy-atom diffusion is a thermally-activated mechanism. As shown in chapter 3, the migration energy associated to a vacancy jump depends not only on the migrating atom chemical type, but also on its local chemical environment. Several methods exist for including chemical environment effects on the transition energies computation in AKMC simulations, for a review paper on these methods one can refer, for example, to reference [Becquart2009]. A very popular choice for computing the energy required for a vacancy-atom exchange consists in introducing the so called Final Initial State Energy (FISE) approximation, according to the terminology adopted by Vincent *et al.* [Vincent2008] in the context of Fe-Cu alloys, which is based on Kang and Weinberg decomposition of migration energy barriers [Kang1988]. The FISE approximation have been widely used for the study of the Fe-Cr system [Pareige2009, Pareige2011, Wallenius2007,

Bonny2009c, Nguyen-Manh2008b, Nguyen-Manh2008a]. Within the approaches for computing atom-vacancy migration barriers, an alternative method proposed by Castin *et al.* must be mentioned. Castin and co-workers developed and trained an artificial neural network (ANN) to compute the energy barriers [Castin2010]. The ANN was trained on the basis of a set of 30000 atom-vacancy migration energy barriers computed for different chemical environment in a simulation box containing 615 atoms using the Nudged Elastic Band (NEB) method. They showed for instance, that their ANN-based AKMC was capable of reproducing the experimental Fe-Cr phase diagram in the range of concentration of 7 at.%Cr to 15 at.%Cr and between 0 and 1200 K. Finally, Martinez *et al.* [Martinez2011] used a recently introduced Fe-Cr concentration-dependent pair potential [Levesque2011] to parameterise AKMC simulation of the Fe-Cr thermal ageing. They computed the vacancy migration energy within the broken bond method (see, for example, [Becquart2009]). Martinez *et al.*'s results are in quite good agreement with Novy *et al.* TAP observations of the time evolution of the chromium concentration in the α -phase and the α' -phase in the Fe-20 at.%Cr alloy at 773 K [Novy2009a]. Their results also exhibit a very good agreement with Bley *et al.* [Bley1992] measurements by small angle neutron scattering of the time evolution of the position of the peak of the scattering intensity for Fe-20 at.%Cr, Fe-35 at.%Cr, and Fe-50 at.%Cr alloys at 773 K.

4.1 Atomistic Kinetic Monte Carlo (AKMC). The residence time algorithm

The first papers presenting a kinetic Monte Carlo approach have been published by Young and Elcock [Young1966] and by Bortz *et al.* [Bortz1975], the first dealing with the kinetic of the vacancy diffusion in ordered alloys, the latter dealing with the kinetic evolution of an Ising spin system. A full theoretical description and formalisation of the AKMC algorithm have been achieved quite recently by Fichtorn [Fichtorn1991]. The most important feature of the AKMC technique – as compared to Metropolis Monte Carlo (MMC) simulations [Metropolis1953] – is the fact that a time step can be related to each simulation step (jump of the vacancy). In the AKMC simulations, the configurations are not randomly generated and sampled respecting a given probability distribution (usually a thermodynamic equilibrium distribution) – as it is done in MMC approach –; the configuration at step i is obtained from configuration at step $i - 1$ by realising a vacancy jump. At each AKMC step,

the vacancy migrates toward one of its nearest neighbours, the probability associated to each possible jump corresponds to a transition frequency which depends on the energy barrier associated to the jump. As it will be shown below, this approach allows associating an average time increment to each simulation step. As a consequence, the AKMC simulations provide a physically realistic kinetic description of the micro-structural changes which occur in the system while it evolves toward the thermodynamic equilibrium. On a theoretical point of view, the AKMC algorithm describes the kinetic of the structure evolution as a stochastic process corresponding to a continuous-time Markov chain (each vacancy jump event does not depend on the previous jump but only on the current state). From this point of view, the AKMC simulation can be seen as a numerical solution of the master equation:

$$\frac{dP_a(t)}{dt} = \sum_b (w_{ba}P_b(t) - w_{ab}P_a(t)) \quad (1)$$

where w_{ba} and w_{ab} are, respectively, the transition rates from configuration b to configuration a and configuration a to configurations b, while $P_b(t)$ and $P_a(t)$ are the probabilities to find the system, respectively, in b and a state at time t. $P_b(t)$ and $P_a(t)$ do not depend on the previous state of the system but only on time t. The thermodynamic equilibrium of a system corresponds to the steady solution of the master equation. The condition $\frac{dP_a(t)}{dt} = 0$ leads to the equation:

$$\sum_b (w_{ba}P_b^{eq} - w_{ab}P_a^{eq}) = 0. \quad (2)$$

A possible solution of equation (2) is

$$w_{ba}P_b^{eq} = w_{ab}P_a^{eq}. \quad (3)$$

The latter condition is called detailed balance. By imposing the detailed balance condition for all possible vacancy-atom exchanges, one can define the transition probabilities w to guarantee that the system will reach thermal equilibrium.

In our case, the vacancy diffuses in a bcc structure in which each lattice site is surrounded by 8 nearest neighbours: at each AKMC step the system can evolve through one of 8 possible transitions. Vineyard's simplified transition state theory provides an expression

for the frequency associated to a given transition $a \rightarrow b$ which, in the case the process is a vacancy jump, can be written as [Vineyard1957]:

$$w_{ab} = \frac{\prod_{j=1}^{3N-3} v_j}{\prod_{j=1}^{3N-4} v_{j'}} \exp\left(-\frac{E_{\text{mig}}^{\text{ab}}}{k_B T}\right), \quad (4)$$

where $E_{\text{mig}}^{\text{ab}}$ is the energy barrier associated to the vacancy migration, it corresponds to the difference between the energy of the system with the migrating atom constrained at the saddle point position and the energy of the system with the migrating atom at its initial equilibrium position. The coefficient $\frac{\prod_{j=1}^{3N-3} v_j}{\prod_{j=1}^{3N-4} v_{j'}}$ is a term called attempt frequency in which v_j are the normal modes of the system at the starting point of the transition and $v_{j'}$ are the normal modes of the system when the atom exchanging its position with the vacancy is constrained at the saddle point of the migration barrier. T is the simulation temperature and k_B is Boltzmann's constant. Figure 1-Ch4 represents a scheme of the vacancy-atom exchange process. One of the 8 possible transitions is selected with a probability which corresponds to the transition frequency associated at each vacancy jump. This is schematically achieved at each AKMC step by means of the following procedure:

1. All possible transitions w_{ab} are listed and the probability rate w_i (jump frequency in the case of a vacancy-atom exchange) associated to each transition is computed.
2. The cumulative function $W_i = \sum_{j=1}^i w_j$, where $i = 1, \dots, N$ is an index on the possible transitions, is computed.
3. A random number $u \in]0,1]$ is generated.
4. The transition which is selected to be carried out is the event i which satisfies $W_{i-1} < uW_N \leq W_i$.

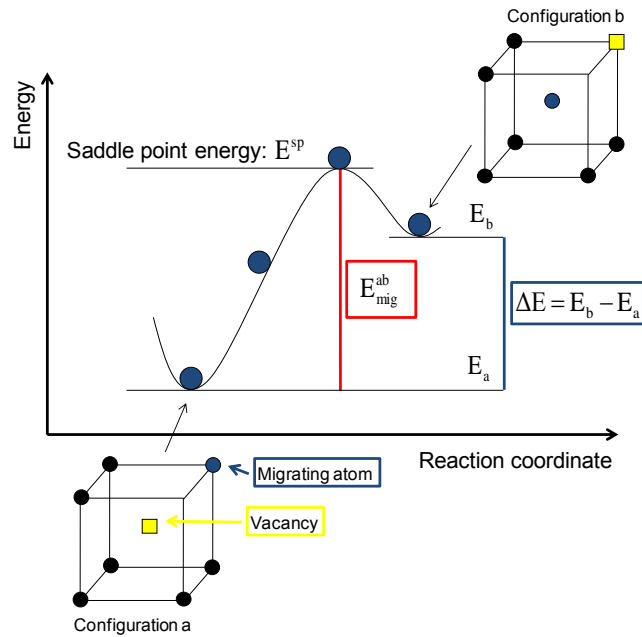


Figure 1-Ch4 Scheme of a Vacancy-atom exchange process.

A physical time step can be associated to each simulation step by implementing the residence time algorithm. The basic idea on which the algorithm relies is the fact that if the following conditions are fulfilled:

- a) the time step used to describe the process is sufficiently small so that it can enclose at most one transition (*i.e.* two events cannot occur simultaneously)
- b) the probability of a given transition to occur at time t is independent on the previous history

then the evolution of the system towards a series of transitions (vacancy jumps in the case we are considering here) is a Poisson process and the time distribution of transition events occurring during a sequence of time intervals will follow a Poisson's probability law [Fichtorn1991]:

$$P(n_e, t) = \frac{(W_N t)^{n_e}}{n_e!} e^{-W_N t} \quad (5)$$

where $P(n_e, t)$ is the probability that n_e events occur during time t and $W_N = \sum_{i=1}^N w_i$.

A very important feature of Poisson distributed events is the fact that the time interval τ separating two consecutive events is a stochastic variable exponentially distributed:

$$f(t) = W_N e^{-W_N t}, \quad (6)$$

where $f(t)$ is the probability that $t < \tau < t + dt$.

From equation (6) follows that the average time step separating two different transitions (two vacancy jumps in the case of vacancy diffusion simulation) is:

$$\langle t \rangle = \frac{1}{W_N}. \quad (7)$$

Equation (7) thus represents the time increment associated to each AKMC step.

4.2 Parameterisation of the AKMC simulations of the Fe-Cr thermal ageing

The most relevant quantity of AKMC simulations is the transition frequency. Following Pareige *et al.* [Pareige2011], in our AKMC simulations, the attempt frequency (factor $\frac{\prod_{j=1}^{3N-3} v_j}{\prod_{j=1}^{3N-4} v_j}$ in equation 4) has been considered as constant – as the atom in our system (iron and chromium) have similar masses and vibrational properties – and equal to $6 \cdot 10^{12} \text{ s}^{-1}$. The only quantity in equation (4) which varies in our simulations is the energy barrier of the transitions which drive the system evolution.

As discussed above, this work focuses on the bcc Fe-Cr microstructure evolution by means of a vacancy diffusion mechanism. The energy barrier associated to each transition is the migration energy E_{mig} the vacancy must overcome to jump toward one of its 8 nearest neighbours and to achieve the system's transition from a configuration to another. As shown in chapter 3, the vacancy migration energy strongly depends on the chemical environment of the migrating atom-vacancy pair. A realistic parameterisation of an AKMC simulation of Fe-Cr thermal ageing requires such a dependence to be taken into account. Since there is a low probability for the system to be found two times in the same configuration during the simulation, the vacancy migration energy should be – in principle – calculated at each step. In the subsections which follow, the different approaches which have been considered in this work to take into account the vacancy migration energy dependence on chemical environment

during the AKMC simulations will be presented. The AKMC simulation results which have been obtained with the different parameterisation will be exposed in the last section (section 4.3) of this chapter.

4.2.1 Final Initial State Energy approximation

A widely exploited approach for the computation of the vacancy migration energy for the simulation of the Fe-Cr microstructure evolution [Pareige2009, Pareige2011, Wallenius2007, Bonny2009c, Nguyen-Manh2008b, Nguyen-Manh2008a] is the so called final initial state energy (FISE) approach which consists in expressing the vacancy migration energy (associated to the transition from the configuration a to the configuration b) as the sum of two terms:

$$E_{\text{mig}}^{\text{ab}} = E_{\text{mig}0}^{\text{ab}} + \frac{(E_{\text{b}} - E_{\text{a}})}{2}. \quad (8)$$

$E_{\text{mig}0}^{\text{ab}}$ is often considered as being dependent on the migrating atom type but not on the chemical environment and all the effects of the environment on the migration barrier are carried by the term $(E_{\text{b}} - E_{\text{a}})$. In particular, in most of the FISE-based parameterisations of the AKMC simulations of the iron based alloys which can be found in the literature, $E_{\text{mig}0}^{\text{ab}}$ is simply the atom-vacancy exchange energy in a pure iron matrix. Equation (8) can then be written as follows:

$$E_{\text{mig}}^{\text{ab}} = E_{\text{mig}0}^{\text{ab}}(x_{\text{AT}}) + \frac{(E_{\text{b}} - E_{\text{a}})}{2}, \quad (9)$$

where x_{AT} indicates the migrating atom type.

To our knowledge, the only attempt to give a physical basis to this approximation is due to Kang and Weinberg [Kang1988]. Kang and Weinberg introduced what has been later called FISE approximation [Vincent2008] assuming that the migrating atom experiences a harmonic potential $\alpha_{\text{a}}(x)$ and $\alpha_{\text{b}}(x)$ when it is at its initial or final equilibrium position respectively and considering that the saddle point energy corresponds to the point where $\alpha_{\text{a}}(x)$ and $\alpha_{\text{b}}(x)$ cross each other (see figure 2-Ch4). The latter hypothesis implicitly corresponds to the questionable assumption that the harmonic approximation still holds quite

far from the equilibrium positions of the migrating atom and, particularly, at the saddle point position of the migrating atom, regardless of the chemical configuration of the local atomic environment.

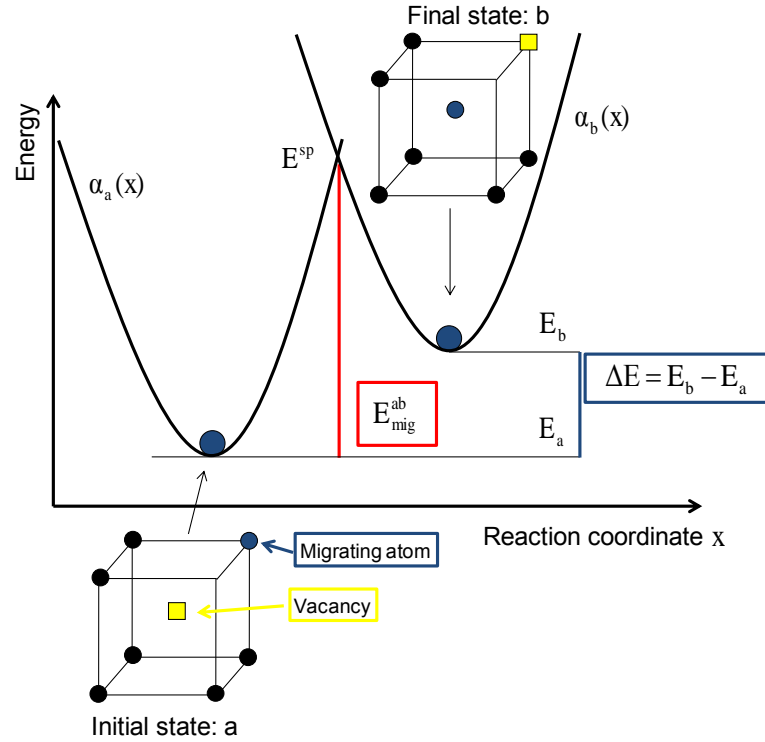


Figure 2-Ch4 FISE approximation scheme.

As stated in the previous section, the transition frequencies (equation 4), which represent the main ingredient of the AKMC parameterisation, must satisfy the detailed balance condition (equation 3) which can be written as:

$$e^{-\frac{E_{\text{mig}}^{ba}}{k_B T}} e^{-\frac{E_b}{k_B T}} \frac{1}{Z} = e^{-\frac{E_{\text{mig}}^{ab}}{k_B T}} e^{-\frac{E_a}{k_B T}} \frac{1}{Z} \quad (10)$$

where $\frac{e^{-\frac{E_b}{k_B T}}}{Z}$ et $\frac{e^{-\frac{E_a}{k_B T}}}{Z}$ are the probabilities to find the system in configuration a and in configuration b ($Z = \sum_i e^{-\frac{E_i}{k_B T}}$, where index i runs on all the possible configurations of the system, being the configurational partition function) while $e^{-\frac{E_{\text{mig}}^{ba}}{k_B T}}$ and $e^{-\frac{E_{\text{mig}}^{ab}}{k_B T}}$ are the transition rates associated to transition $b \rightarrow a$ and transition $a \rightarrow b$. If one considers a FISE-based expression for the approximation of the vacancy migration energy, equation (10) becomes:

$$e^{-\frac{E_{\text{mig}0}^{\text{ba}}(x_{\text{AT}}) + \frac{E_a - E_b}{2}}{k_B T}} e^{-\frac{E_b}{k_B T}} = e^{-\frac{E_{\text{mig}0}^{\text{ab}}(x_{\text{AT}}) + \frac{E_b - E_a}{2}}{k_B T}} e^{-\frac{E_a}{k_B T}}$$

$$\Leftrightarrow e^{E_{\text{mig}0}^{\text{ba}}(x_{\text{AT}})} e^{-\frac{E_a + E_b}{2}} = e^{E_{\text{mig}0}^{\text{ab}}(x_{\text{AT}})} e^{-\frac{E_a + E_b}{2}}. \quad (11)$$

Equation (11) is satisfied if $E_{\text{mig}0}^{\text{ba}}(x_{\text{AT}}) = E_{\text{mig}0}^{\text{ab}}(x_{\text{AT}})$. The latter condition is always fulfilled when $E_{\text{mig}0}(x_{\text{AT}})$ is considered to be independent of the vacancy atomic environment and corresponds to the migration energy of a vacancy-atom exchange in a pure iron matrix. The FISE approximation has been exploited with some success to compute the atom-vacancy exchange energy barrier in the context of the study of the Fe-Cr microstructural evolution [Pareige2009, Pareige2011, Wallenius2007, Bonny2009c, Nguyen-Manh2008a] because, even if it oversimplifies the migration energy dependence on the chemical environment, it is consistent with the detailed balance condition.

In most of the works using the FISE approach, $E_{\text{mig}0}^{\text{ab}}(x_{\text{AT}})$ is generally obtained by DFT calculation whereas $(E_b - E_a)$ is computed using an appropriate cohesive model. Some of the most frequently exploited approaches consist in using empirical many-body EAM potentials [Pareige2009, Pareige2011, Wallenius2007, Bonny2009c] or the cluster expansion (CE) method [Nguyen-Manh2008b, Nguyen-Manh2008a]. The term $(E_b - E_a)$ could be also obtained from DFT calculations but computing this quantity for each initial and final configuration encountered would require prohibitive numerical cost. Note that EAM potentials and CE cohesive models are nowadays often parameterised to fit some relevant *ab initio* data so, even if they take into account Fe-Cr magnetic properties indirectly, they do not explicitly treat magnetic interactions. One important exception is the magnetic cluster expansion (MCE) approach [Lavrentiev2009, Lavrentiev2010] which provides the Fe-Cr alloys cohesive energy by taking explicitly into account both the chemical interactions (up to second nearest neighbours) and the magnetic interactions (up to fifth nearest neighbours), the latter being introduced by assigning continuous (vector) spin variables to each atomic site. MCE seems to be a promising way to deal with Fe-Cr structures energetic and it was exploited to compute the $(E_b - E_a)$ term in a FISE parameterisation of AKMC simulation of Fe-Cr thermal annealing [Lavrentiev2009]. Nevertheless, according to its developers, this kind of AKMC parameterisation still presents some difficulties, such as large fluctuations of the magnetic contribution to the energy at elevated temperatures. Moreover, MCE is not

suitable to directly compute the atom-vacancy migration barriers since it is an on-lattice method.

Following our DFT results, we decided to introduce a dependence of the migration barrier ($E_{\text{mig}0}(x_{\text{AT}})$ in equation (9)) to the LAE. The second term in equation (9), namely $\frac{(E_b - E_a)}{2}$, being obtained, in our simulations, using an empirical potential, depends naturally on the chemical configuration. In chapter 3, it was shown that the chemical environment of the saddle point position of the migrating atom has a strong influence on the migration barriers, particularly when the migrating atom is chromium. As a result, it seems natural that an improvement of the model should start from taking into account, in a more explicit way, the saddle point environment effects on the energy barrier associated to the vacancy-atom exchange. For this purpose we introduced two possible expressions for $E_{\text{mig}0}(x_{\text{AT}})$:

- the first expression depends on the number $n_{\text{Cr}}^{\text{sp}}$ of chromium atoms which occupy the saddle point position nearest neighbour sites (namely C sites and D sites)
- the second expression depends on $n_{\text{Cr}}^{\text{sp}}$ as well as on the relative positions chromium atoms occupy within saddle point nearest neighbour sites.

In the first case, $E_{\text{mig}0}(x_{\text{AT}})$ will thus be a function $f(n_{\text{Cr}}^{\text{sp}})$ and in the second case $E_{\text{mig}0}(x_{\text{AT}})$ will be computed as a function $f(\vec{x}_{\text{Cr}}^{\text{sp}})$, $\vec{x}_{\text{Cr}}^{\text{sp}} \equiv (X_{\text{C}1}, X_{\text{C}2}, X_{\text{C}3}, X_{\text{D}1}, X_{\text{D}2}, X_{\text{D}3})$ being a vector whose components are the atomic species occupying sites C and D (see figure 3-Ch4 for the sites nomenclature). The functions $f(n_{\text{Cr}}^{\text{sp}})$ and $f(\vec{x}_{\text{Cr}}^{\text{sp}})$ have been defined as follows:

$$E_{\text{mig}0}^{\text{ab}}(x_{\text{AT}}, n_{\text{Cr}}^{\text{sp}}) = \langle E_{\text{mig}}^{\text{ab}}(x_{\text{AT}}, \vec{x}_{\text{Cr}}^{\text{sp}}) \rangle_{\text{sp configurations, fixed } n_{\text{Cr}}^{\text{sp}}} \quad (12)$$

$$E_{\text{mig}0}^{\text{ab}}(x_{\text{AT}}, \vec{x}_{\text{Cr}}^{\text{sp}}) = \frac{(E_{\text{mig}}^{\text{ab}}(x_{\text{AT}}, \vec{x}_{\text{Cr}}^{\text{sp}}) + E_{\text{mig}}^{\text{ba}}(x_{\text{AT}}, \vec{x}_{\text{Cr}}^{\text{sp}}))}{2}. \quad (13)$$

In the first case (equation 12), $E_{\text{mig}0}^{\text{ab}}(x_{\text{AT}}, n_{\text{Cr}}^{\text{sp}})$ is obtained as the average of the vacancy migration energies obtained for all the possible chemical configurations of the saddle point LAE for fixed chromium content ($n_{\text{Cr}}^{\text{sp}}$). Here, the LAE includes 1st nearest neighbours

only and all the other atoms in the structure are considered to be iron atoms. In the second case (equation 13), $E_{\text{mig}0}^{\text{ab}}(\mathbf{x}_{\text{AT}}, \vec{\mathbf{x}}_{\text{Cr}}^{\text{sp}})$ is obtained as the average of the forward (a \rightarrow b) and backward (b \rightarrow a) vacancy migration energy for a given chemical configuration of the saddle point LAE. In that case also, the LAE includes 1st nearest neighbours only and all the other atoms in the simulation box are considered to be iron atoms. In both cases it is clear that:

$$E_{\text{mig}0}^{\text{ab}} = E_{\text{mig}0}^{\text{ba}}. \quad (14)$$

Concerning equation (13), this follows directly from the invariance under a and b indexes exchange. Concerning equation (12), $\langle E_{\text{mig}}^{\text{ab}}(\mathbf{x}_{\text{AT}}, \vec{\mathbf{x}}_{\text{Cr}}^{\text{sp}}) \rangle_{\text{sp configurations, fixed } n_{\text{Cr}}^{\text{sp}}}$ is an average on all possible atomic configurations of the saddle point LAE hence, for each transition which is taken into account, the reverse transition is necessarily included in the average. For example, if one considers the atom AT migration in an environment where sites C1 and C2 are occupied by chromium atoms, the reverse migration will correspond, from a topological point of view, to the migration of atom AT in an environment where sites D1 and D2 are occupied by chromium atoms (see figure 3-Ch4 for the sites nomenclature), so that both forward and backward migration mechanisms contribute to the term $\langle E_{\text{mig}}^{\text{ab}}(\mathbf{x}_{\text{AT}}, \vec{\mathbf{x}}_{\text{Cr}}^{\text{sp}}) \rangle_{\text{sp configurations, fixed } n_{\text{Cr}}^{\text{sp}}}$. By applying the same consideration to all possible configurations of saddle point LAE, one concludes that for each configuration the forward and backward migration energy is taken into account in the estimation of $\langle E_{\text{mig}}^{\text{ab}}(\mathbf{x}_{\text{AT}}, \vec{\mathbf{x}}_{\text{Cr}}^{\text{sp}}) \rangle_{\text{sp configurations, fixed } n_{\text{Cr}}^{\text{sp}}}$ which is thus invariant under a and b index exchange.

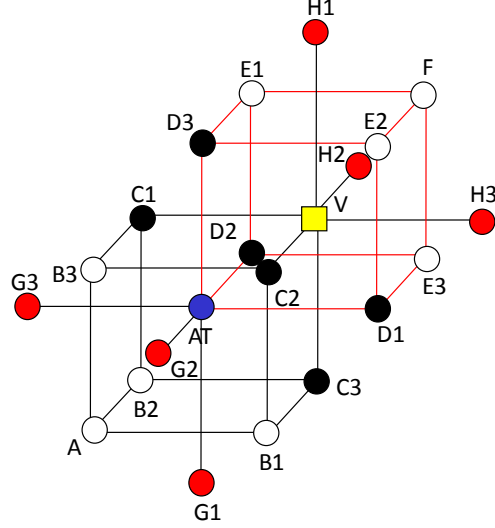


Figure 3-Ch4 Local chemical environment structure scheme and sites nomenclature. AT: migrating atom. V: vacancy. Black spheres: atom windows the vacancy goes through along migration path (first window: C1, C2, C3. Second window: D1, D2, D3).

Equations (12) and (13) lead, respectively, to two expressions of the activation barrier, in the FISE approximation:

$$E_{\text{mig}}^{\text{ab}} = E_{\text{mig}0}^{\text{ab}}(x_{\text{AT}}, n_{\text{Cr}}^{\text{sp}}) + \frac{(E_{\text{b}} - E_{\text{a}})}{2} = \langle E_{\text{mig}}^{\text{ab}}(x_{\text{AT}}, \vec{x}_{\text{Cr}}^{\text{sp}}) \rangle_{\text{sp configurations, fixed } n_{\text{Cr}}^{\text{sp}}} + \frac{\Delta E}{2} \quad (15)$$

$$E_{\text{mig}}^{\text{ab}} = E_{\text{mig}0}^{\text{ab}}(x_{\text{AT}}, \vec{x}_{\text{Cr}}^{\text{sp}}) + \frac{(E_{\text{b}} - E_{\text{a}})}{2} = \frac{(E_{\text{mig}}^{\text{ab}}(x_{\text{AT}}, \vec{x}_{\text{Cr}}^{\text{sp}}) + E_{\text{mig}}^{\text{ba}}(x_{\text{AT}}, \vec{x}_{\text{Cr}}^{\text{sp}}))}{2} + \frac{\Delta E}{2}. \quad (16)$$

Since both $E_{\text{mig}0}^{\text{ab}}(x_{\text{AT}}, n_{\text{Cr}}^{\text{sp}})$ and $E_{\text{mig}0}^{\text{ab}}(x_{\text{AT}}, \vec{x}_{\text{Cr}}^{\text{sp}})$ fulfil condition (14), it follows that expressions (15) and (16) for the approximation of the migration barriers satisfy the detailed balance condition (equation 10). They may be thus suitable for the parameterisation of AKMC simulations of the evolution of the system toward thermodynamic equilibrium.

It should be noticed that equation (16), reduces to the exact migration energy when the system does not contain chromium atoms other than those which are included in the saddle point LAE (1st nearest neighbours). Indeed, in this case, equation (16) becomes (see figure 2-Ch4 for the notation):

$$E_{\text{mig}}^{\text{ab}} = \frac{(E^{\text{sp}} - E_{\text{a}} + E^{\text{sp}} - E_{\text{b}})}{2} + \frac{E_{\text{b}} - E_{\text{a}}}{2} = E^{\text{sp}} - E_{\text{a}}. \quad (17)$$

In the following of this manuscript we will refer to standard FISE approximation – equation 9 – with the denomination "FISE 1" and to the improved FISE approximations – equation 15 and 16 – with denominations "FISE 2" and "FISE 3" respectively. The table below (table 1-Ch4) summarises this nomenclature:

FISE 1	$E_{\text{mig}}^{\text{ab}} = E_{\text{mig } 0}^{\text{ab}}(x_{\text{AT}}) + \frac{\Delta E}{2}$
FISE 2	$E_{\text{mig}}^{\text{ab}} = \langle E_{\text{mig}}^{\text{ab}}(x_{\text{AT}}, \vec{x}_{\text{Cr}}^{\text{sp}}) \rangle_{\text{sp configurations, fixed } n_{\text{Cr}}^{\text{sp}}} + \frac{\Delta E}{2}$
FISE 3	$E_{\text{mig}}^{\text{ab}} = \frac{(E_{\text{mig}}^{\text{ab}}(x_{\text{AT}}, \vec{x}_{\text{Cr}}^{\text{sp}}) + E_{\text{mig}}^{\text{ba}}(x_{\text{AT}}, \vec{x}_{\text{Cr}}^{\text{sp}}))}{2} + \frac{\Delta E}{2}$

Table 1-Ch4 FISE approximations.

For all our FISE parameterisations, we computed the first term, namely $E_{\text{mig } 0}$, with a full DFT approach and the second term, namely $\frac{\Delta E}{2}$, using the EAM-2BM potential parameterised by Bonny *et al.* [Bonny2011] which was described in chapter 2. The EAM-2BM-GB potential parameterised by Bonny *et al.* has been chosen, over other potentials such as the potential derived by Olsson *et al.* (EAM-2BM-PO) [Olsson2005] and the one proposed by Caro *et al.* (EAM-CDM) [Caro2005], because of its better consistency with the thermodynamics (considering, in particular, the fact that it provides a Fe-Cr phase diagram in better agreement with the recently recalculated CALPHAD Fe-Cr phase diagram [Xiong2011]) [Bonny2011a].

During our AKMC simulations, depending on the parameterisation used, either the migrating atom species or both the migrating atom species and the saddle point LAE configuration (depending on whether FISE 1 or FISE 2 and 3 are used) are read at each step. A migration energy is then assigned to each one of the possible transitions (the eight possible jump of the vacancy) to compute the transition frequencies. It is clear that, because of the high numerical cost required, the DFT computed quantities involved in the AKMC parameterisation must be obtained and tabulated before the simulations. In particular, the implementation of FISE 2 and FISE 3 parameterisations requires the vacancy migration barriers for all possible configurations of the saddle point LAE (and for the two possible kinds of migrating atom) to be computed. All the DFT results obtained are reported in ANNEX 2.

Before focusing on AKMC simulations results of thermal ageing, we first present a study of the efficiency of the different FISE parameterisations for computing the vacancy migration barriers, and compare them with full DFT calculations. To this event, we used the FISE approximations to compute the migration barriers in a LAE progressively filled with chromium atoms and compared the FISE estimations with the DFT-NEB results. In order to better assess the quality of our model, we also computed the ΔE term in the framework of DFT as well as with the EAM-2BM-GB potential. As previously stated, since ΔE is computed on the fly during our AKMC simulations, it was done using the EAM-2BM-GB potential to keep a reasonable numerical cost. It is also important to notice that the different FISE approaches that we have considered in this work are partially based on polarized DFT calculations. This is reasonable since, for the chromium concentrations and the temperature that we considered in our AKMC simulations, the Fe-Cr alloy is in the ferromagnetic domain [Xiong2010]. Furthermore, the choice of the EAM-2BM-GB cohesive model is also consistent with this fact because, as stated in chapter 2, this potential has been parameterised to reproduce polarised DFT calculations.

Figures 4-Ch4 and 5-Ch4 show, respectively, the migration energies of the vacancy-iron and vacancy-chromium exchange for different chromium contents of the LAE. The configurations have been obtained by progressively replacing iron atoms in the LAE with chromium atoms. The filling order of the LAE with chromium atoms is: A, B1, B2, B3, C1, C2, C3, D1, D2, D3, E1, E2, E3, F, G1, G2, G3, H1, H2, and H3. We remind that, following the nomenclature which has been employed in this work, the saddle point nearest neighbour sites correspond to the C and D sites. FISE 2 and FISE 3 are identical when one, five or six chromium atoms are found in the saddle point LAE (1st nearest neighbours). This is due to the fact that $E_{\text{mig}0}^{\text{ab}}(x_{\text{AT}}, n_{\text{Cr}}^{\text{sp}})$ and $E_{\text{mig}0}^{\text{ab}}(x_{\text{AT}}, \vec{x}_{\text{Cr}}^{\text{sp}})$ are computed in a simulation box where the only chromium atoms are in the saddle point LAE, all other sites of the structure being occupied by iron atoms. As a consequence, for $n_{\text{Cr}}^{\text{sp}} = 6$, only one configuration of the system exists (which corresponds to $\vec{x}_{\text{Cr}}^{\text{sp}} \equiv (X_{\text{C}1} = \text{Cr}, X_{\text{C}2} = \text{Cr}, X_{\text{C}3} = \text{Cr}, X_{\text{D}1} = \text{Cr}, X_{\text{D}2} = \text{Cr}, X_{\text{D}3} = \text{Cr})$) and the forward migration energy equals the backward migration energy for this configuration so that:

$$\frac{(E_{\text{mig}}^{\text{ab}}(x_{\text{AT}}, \vec{x}_{\text{Cr}}^{\text{sp}}) + E_{\text{mig}}^{\text{ba}}(x_{\text{AT}}, \vec{x}_{\text{Cr}}^{\text{sp}}))}{2} = \langle E_{\text{mig}}^{\text{ab}}(x_{\text{AT}}, \vec{x}_{\text{Cr}}^{\text{sp}}) \rangle_{\text{sp configurations}, n_{\text{Cr}}^{\text{sp}}=6}. \quad (18)$$

On the other hand, when $n_{\text{Cr}}^{\text{sp}} = 1$ or $n_{\text{Cr}}^{\text{sp}} = 5$, even if there are six possible configurations $\vec{x}_{\text{Cr}}^{\text{sp}} \equiv (X_{\text{C}1}, X_{\text{C}2}, X_{\text{C}3}, X_{\text{D}1}, X_{\text{D}2}, X_{\text{D}3})$ of the saddle point LAE which satisfy $n_{\text{Cr}}^{\text{sp}} = 1$ or $n_{\text{Cr}}^{\text{sp}} = 5$, only two different configurations are distinguishable from a topological point of view in each of the two cases:

- a) $n_{\text{Cr}}^{\text{sp}} = 1$: the only chromium atom is placed either on one of the C sites or on one of the D sites
- b) $n_{\text{Cr}}^{\text{sp}} = 5$: the only iron atom is placed either on one of the C sites or on one of the D sites.

One can easily verify that:

$$\frac{(E_{\text{mig}}^{\text{ab}}(x_{\text{AT}}, \vec{x}_{\text{Cr}}^{\text{sp}}) + E_{\text{mig}}^{\text{ba}}(x_{\text{AT}}, \vec{x}_{\text{Cr}}^{\text{sp}}))}{2} = \langle E_{\text{mig}}^{\text{ab}}(x_{\text{AT}}, \vec{x}_{\text{Cr}}^{\text{sp}}) \rangle_{\text{sp configurations, } n_{\text{Cr}}^{\text{sp}}=1,5} \quad (19)$$

for all $\vec{x}_{\text{Cr}}^{\text{sp}} \equiv (X_{\text{C}1}, X_{\text{C}2}, X_{\text{C}3}, X_{\text{D}1}, X_{\text{D}2}, X_{\text{D}3})$ satisfying the constraint $n_{\text{Cr}}^{\text{sp}} = 1$ or $n_{\text{Cr}}^{\text{sp}} = 5$.

Thus, observing figures 4-Ch4, 5-Ch4 and considering the filling order of saddle point LAE sites with chromium atoms, one should keep in mind that:

- a) FISE 1, FISE 2 and FISE 3 approximations for the vacancy migration energy overlap from 0 Cr to 4 Cr (because for these configurations $E_{\text{mig}0}^{\text{ab}}$ is the same for the three approximations).
- b) FISE 2 and FISE 3 approximations for the vacancy migration energy overlap from 0 Cr to 5 Cr and from 9 Cr to 20 Cr (because for these configurations $E_{\text{mig}0}^{\text{ab}}$ is the same for the both the approximations).

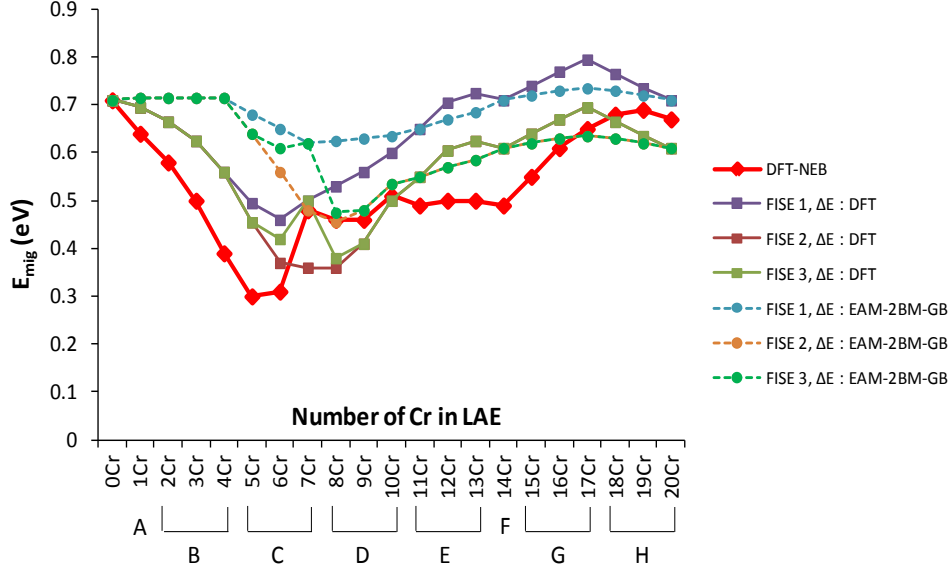


Figure 4-Ch4 Fe migration energy for increasing number of chromium atom in the LAE. Comparison between DFT-NEB results and different FISE approximations. Filling order of the LAE with Cr atoms: A, B1, B2, B3, C1, C2, C3, D1, D2, D3, E1, E2, E3, F, G1, G2, G3, H1, H2, and H3.

Figures 4-Ch4 and 5-Ch4 show that in the region where the saddle point LAE is progressively filled with chromium atoms, FISE 1 approximation is weakly dependent on chemical environment whereas FISE 2 and FISE 3 predict a variation of both the iron and chromium migration energy in qualitatively good agreement with the DFT-NEB predictions (especially when the migrating atom is a chromium atom). Furthermore, it holds true, both in the case where ΔE has been computed with the EAM-2BM-GB potential or in DFT framework.

It is important to notice that the most remarkable disagreement, both qualitatively and quantitatively, between the estimations of the migration energies obtained with the FISE approximations by computing ΔE with the EAM-2BM-GB potential or by DFT can be observed in the zone where no chromium atoms are present in the saddle point LAE (*i. e.* when sites A, B1, B2, B3 are occupied with chromium atoms). This suggests that FISE estimations are dominated by the ΔE term when no chromium atoms are placed in the saddle point LAE and by $E_{\text{mig}0}$ term when, on the contrary, the saddle point LAE is populated with chromium atoms. Not surprisingly, this effect is particularly visible when the migrating atom is a chromium atom: in this case the Cr-Cr interaction has a strong effect on the saddle point energy when the migrating atom goes through C window or D window. When the saddle point LAE is saturated with iron atoms, the dependence of ΔE on the LAE seems to be responsible for most of the migration barrier dependence on the LAE. A large difference can

be observed between the migration barrier using ΔE computed with the EAM-2BM-GB potential or by DFT. The reason for this effect is the partial failure of EAM-2BM-GB to estimate properly ΔE as compared to the DFT results which is due to the fact that the EAM-2BM-GB potential fails to reproduce DFT-computed Cr-Cr and Cr-V interactions (see discussions in chapters 2 and 3).

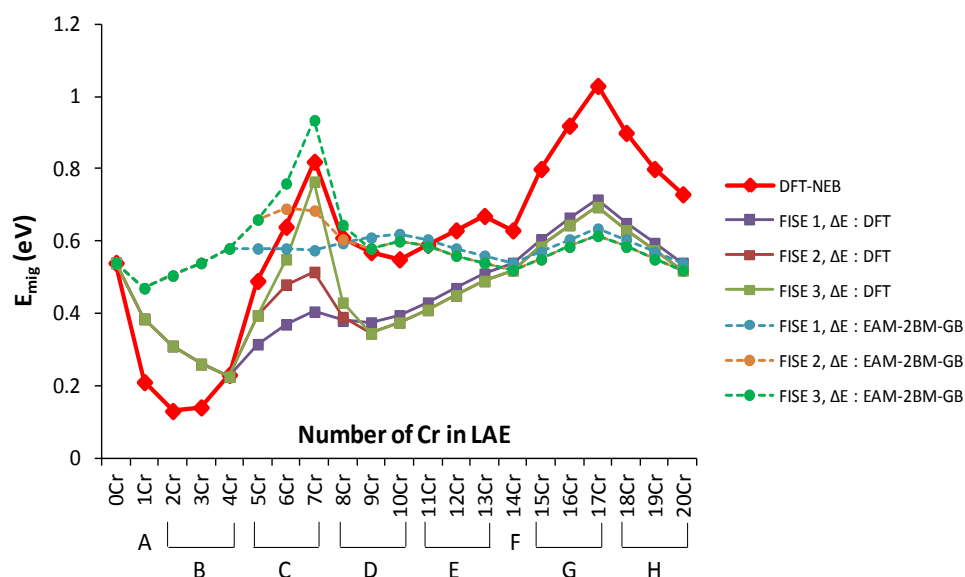


Figure 5-Ch4 Cr migration energy for increasing number of chromium atoms in the LAE. Comparison between DFT-NEB results and different FISE approximations. Filling order of the LAE with Cr atoms: A, B1, B2, B3, C1, C2, C3, D1, D2, D3, E1, E2, E3, F, G1, G2, G3, H1, H2, and H3.

In order to further investigate the capability of different FISE approximations to account for the migration barrier dependence on the saddle point LAE, we traced the DFT-NEB computed migration barriers versus the FISE approximation estimations for some configurations containing chromium atoms among saddle point nearest neighbour sites (figure 6-Ch4). The list of the chemical environment configurations which have been considered can be found in ANNEX 3. In principle, FISE approximations should be more accurate as the dependence of $E_{\text{mig}0}$ on saddle local chemical environment is better taken into account. Thus, FISE 1, for which no dependence of $E_{\text{mig}0}$ on the local chemical environment is taken into account, should provide the roughest estimation of the migration barriers whereas FISE 3 should provide the best estimation of the migration barriers since, in this latter case, $E_{\text{mig}0}$ depends both on the number and the position of chromium atoms among the saddle point nearest neighbours sites. Figure 6-Ch4 shows that both in the case the migrating atom is an iron or a chromium atom, the more detailed the FISE description of the saddle point, the better reproduced the DFT-NEB migration energies.

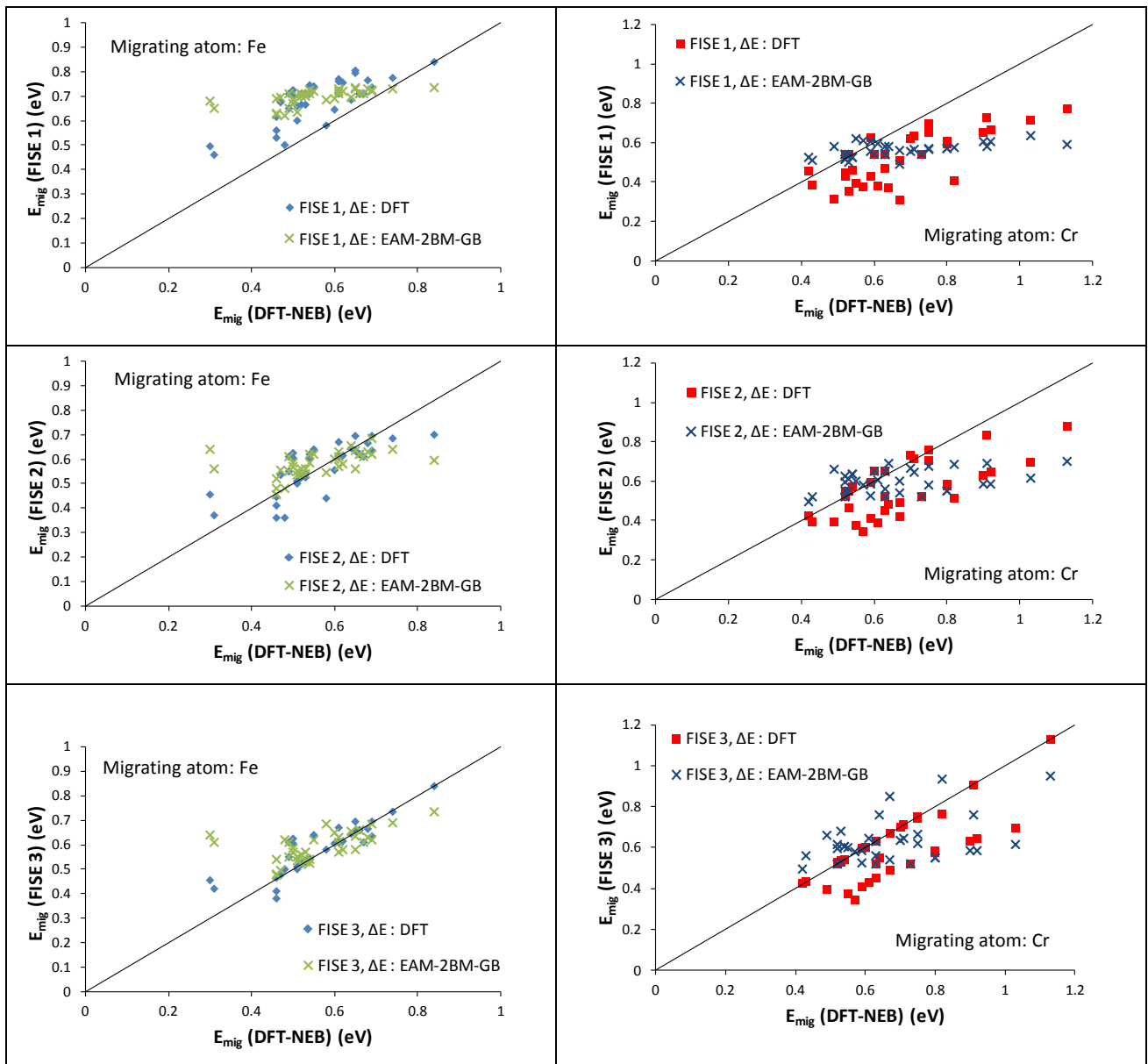


Figure 6-Ch4 DFT-NEB vs. FISE approximations. Migration energy for different configurations of the LAE containing chromium atoms among saddle point nearest neighbour sites. Left: the migrating atom is an Fe atom, right: the migrating atom is a Cr atom.

In the case where the migrating atom is an iron atom (left hand side of figure 6-Ch4), regardless of the way the ΔE term is computed, the agreement between FISE approximation and DFT-NEB previsions becomes more and more satisfying as the $E_{\text{mig}0}$ dependence on saddle point LAE is described in more details. This is not however the case when the migrating atom is a chromium atom (right hand side of figure 6-Ch4) for which the accuracy of FISE approximation seems to increase significantly with the accuracy of $E_{\text{mig}0}$ only if the ΔE term is obtained from DFT. This is due to the fact that EAM-2BM-GB potential does not

describe the Cr-Cr and Cr-V interactions (see discussion in chapter 3) correctly. Of course, the Cr-V interaction also intervenes in the change of the total energy of the system whatever the migrating atom, as the chromium vacancy distance will also change when the migrating atom is an iron atom, but this effect is small compared to the change of the total energy of the system due to the variation of the distances separating chromium atoms. This is due to the fact that, regardless of the cohesive model, the absolute value of the Cr-V binding energy is one order of magnitude lower than the absolute value of the Cr-Cr binding energy. Table 2-Ch4 and table 3-Ch4 gather the linear fit associated to DFT-NEB vs. FISE approximations plots represented in figure 6-Ch4 for a migrating iron atom and a migrating chromium atom respectively.

	Linear fit	Square of the correlation coefficient
FISE 1	$y = 0.65x + 0.32$ (ΔE : DFT)	0.65 (ΔE : DFT)
	$y = 0.20x + 0.59$ (ΔE : EAM)	0.44 (ΔE : EAM)
FISE 2	$y = 0.68x + 0.19$ (ΔE : DFT)	0.59 (ΔE : DFT)
	$y = 0.23x + 0.45$ (ΔE : EAM)	0.24 (ΔE : EAM)
FISE 3	$y = 0.78x + 0.14$ (ΔE : DFT)	0.77 (ΔE : DFT)
	$y = 0.33x + 0.41$ (ΔE : EAM)	0.33 (ΔE : EAM)

Table 2-Ch4 DFT-NEB vs. FISE approximations : linear fit and correlation coefficient. The migrating atom is an iron atom.

	Linear fit	Square of the correlation coefficient
FISE 1	$y = 0.54x + 0.16$ (ΔE : DFT)	0.52 (ΔE : DFT)
	$y = 0.12x + 0.48$ (ΔE : EAM)	0.31 (ΔE : EAM)
FISE 2	$y = 0.55x + 0.20$ (ΔE : DFT)	0.47 (ΔE : DFT)
	$y = 0.13x + 0.52$ (ΔE : EAM)	0.13 (ΔE : EAM)
FISE 3	$y = 0.73x + 0.10$ (ΔE : DFT)	0.60 (ΔE : DFT)
	$y = 0.31x + 0.42$ (ΔE : EAM)	0.22 (ΔE : EAM)

Table 3-Ch4 DFT-NEB vs. FISE approximations: linear fit and correlation coefficient. The migrating atom is a chromium atom.

4.2.2 Parameterisation *via* the EAM-2BM-GB potential. Vacancy migration energy dependence on the LAE configuration (up to second nearest neighbour shell)

Another approach for the parameterisation of the AKMC consists in computing the vacancy-atom migration energy for all possible LAE configurations of the migrating atom-vacancy pair. In this case, during an AKMC run, the LAE of the migrating atom-vacancy pair is read, the appropriate migration energy is assigned to each one of the eight possible jumps of the vacancy and the transition rate corresponding to each diffusion event computed. This approach has been implemented using the EAM-2BM-GB potential. To compute the migration barriers, we used the Drag Method which has been described in chapter 2.

We computed the vacancy-atom exchange energy barriers in a first step considering the 1nn shell of the migrating atom-vacancy pair in the LAE. In a second step, the barriers were calculated including also the second nearest neighbours (2nn) contributions. The number of possible configurations is 2^{14} for each possible type of migrating atom (*i. e.* iron or chromium) in the first case and 2^{20} in the second case. The migration barriers were computed in a bcc structure where only the migrating atom-vacancy LAE (either 1nn or 1nn and 2nn shell) was progressively changed to generate all possible chemical configurations, all other sites of the matrix being occupied by iron atoms. Following our usual site nomenclature (see figure 3-Ch4) the 1nn LAE includes sites A, B1, B2, B3, C1, C2, C3, D1, D2, D3, E1, E2, E3, F, whereas the 2nn LAE corresponds to sites G1, G2, G3, H1, H2, H3. As stated in chapter 2 we used the DYMOKA code to relax the structures and determine the barriers. The size of the simulation box ($8a_0 \times 8a_0 \times 8a_0$) and the discretisation step 0.04 \AA along the migration trajectory were chosen according to the tests we performed and presented in chapter 2.

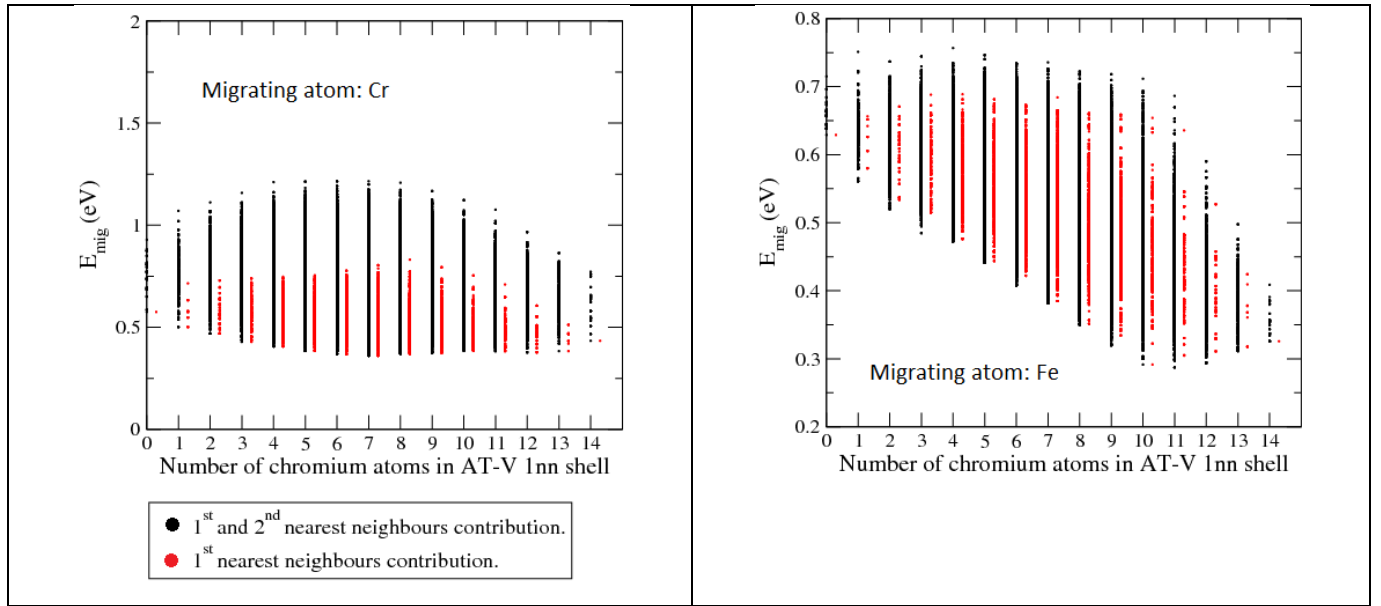


Figure 7-Ch4 Migration barriers for different chromium contents in the vacancy and migrating atom 1nn shell. In the case where the barriers are computed for all the configurations of the first and the second neighbour shells of the migrating atom–vacancy pair, the barriers have been ordered according to the vacancy 1nn shell chromium content. AT and V stands for the migrating atom and the vacancy respectively. Left hand side: the migrating atom is a chromium atom. Right hand side: the migrating atom is an iron atom. Simulation box size: $8a_0 \times 8a_0 \times 8a_0$. Discretisation step along the migration direction: 0.04 \AA .

Figure 7-Ch4 displays the migration barriers for increasing chromium contents in the migrating atom-vacancy pair 1nn shell. It shows that the 2nn shell has quite an important effect on the migration energy, especially when the migrating atom is a chromium atom. In order to assess the extent of this effect, we performed some AKMC runs with both sets of migration barriers. The simulations were performed in a simulation box with size $32a_0 \times 32a_0 \times 32a_0$ ($a_0 = 2.8553 \text{ \AA}$) at a temperature of 773 K for two different composition of the Fe-Cr alloy *i.e.* Fe-20 at.%Cr and Fe-25 at.%Cr. In such conditions, according to the Fe-Cr phase diagram, the alloy is inside the miscibility gap, hence the α - α' phase separation is expected to occur.

Figures 8-Ch4 and 9-Ch4 show the final AKMC configurations for the Fe-20 at.%Cr and Fe-25 at.%Cr alloys respectively. When the vacancy migration barriers have been determined considering both the 1nn and 2nn LAE, both in the case of Fe-20 at.%Cr or Fe-25 at.%Cr alloy, chromium clustering is observed after 1×10^8 AKMC steps for both alloys. On the contrary, when the 2nn LAE dependence of vacancy migration barrier is neglected – left hand side of figures 8-Ch4 and 9-Ch4 – chromium precipitation has not occurred after 1.6×10^9 AKMC steps, for neither alloys. These latter results seem to be not consistent with the Fe-Cr phase diagram but they could also be the consequence of a slower phase separation

kinetics. The 2nn LAE contribution to the migration barriers has been included in all further AKMC simulations.

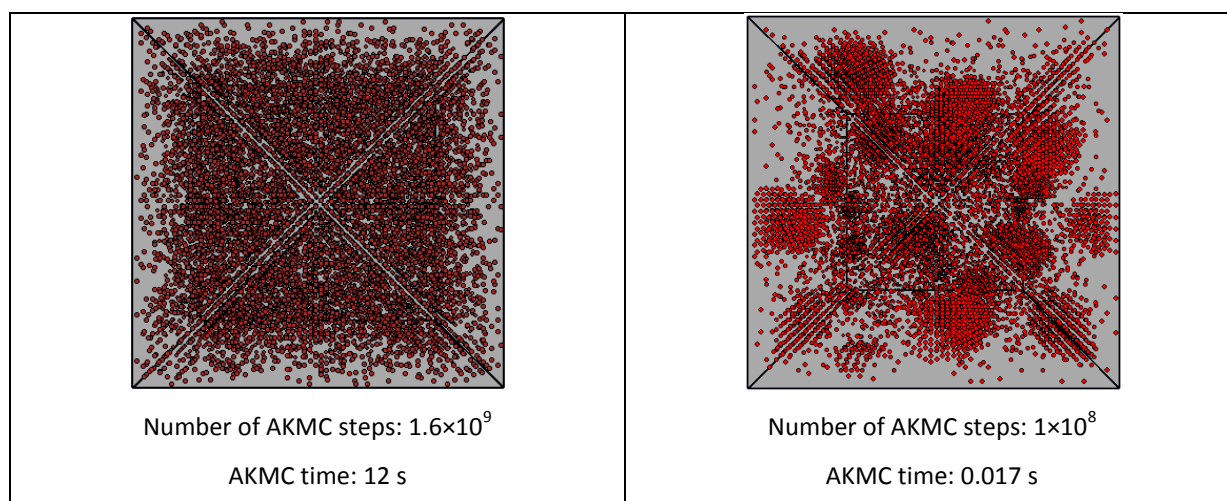


Figure 8-Ch4 Fe-20 at.%Cr structures after AKMC simulated thermal ageing at 773 K. Red spheres are chromium atoms, iron atom have not been represented. Simulation box size: $32a_0 \times 32a_0 \times 32a_0$ ($a_0 = 2.8553 \text{ \AA}$). Left hand side: the migration barriers have been determined for the 1nn migrating atom-vacancy pair chemical environments. Right hand side: the migration barriers have been determined for 1nn end 2nn migrating atom-vacancy pair chemical environments.

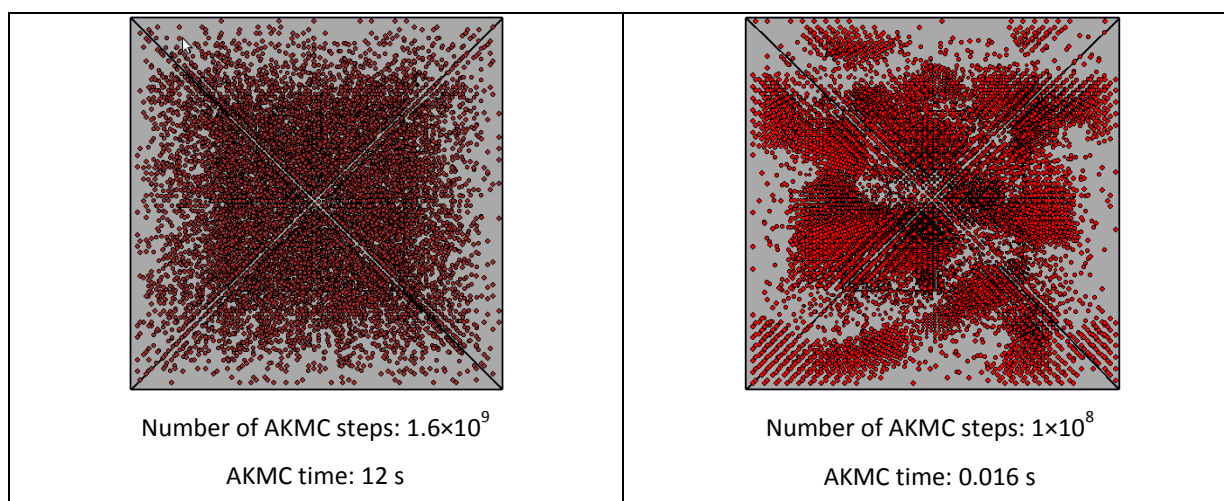


Figure 9-Ch4 Fe-25 at.%Cr structures after AKMC simulated thermal ageing at 773 K. Red spheres are chromium atoms, iron atom have not been represented. Simulation box size: $32a_0 \times 32a_0 \times 32a_0$ ($a_0 = 2.8553 \text{ \AA}$). Left hand side: the migration barriers have been determined for the 1nn migrating atom-vacancy pair chemical environments. Right hand side: the migration barriers have been determined for 1nn end 2nn migrating atom-vacancy pair chemical environments.

4.3 AKMC simulations of Fe-20 at.%Cr and Fe-25 at.%Cr thermal ageing

The kinetics of the Fe-Cr microstructure evolution has been studied by AKMC simulations on a rigid bcc lattice. Our study focused on bcc Fe-Cr alloys with 20 at.% and 25 at.% chromium content at 773 K, for such compositions very recent experimental observations are available in the literature [Novy2009a, Pareige2011]. In order to include the vacancy migration barrier dependence on the LAE, the AKMC simulations have been parameterised with the different FISE approaches (namely FISE 1, FISE 2, and FISE 3) or by exploiting the migration barriers computed with the EAM-2BM-GB potential for all possible configurations of 1nn and 2nn shell of the migrating atom-vacancy pair.

In order to characterise the phase separation mechanism which occurs during our simulations, we represented different slabs of the structure corresponding to different AKMC steps. In figure 10-Ch4 and 11-Ch4, we represented the Fe-20 at.%Cr and the Fe-25 at.%Cr alloys respectively. We considered two different thicknesses for the slabs: 1.2 nm (*e.g.* 8 atomic layers) and 2.4 nm (*e.g.* 17 atomic layers). Comparing the structure of the Fe-20 at.%Cr alloy (figure 10-Ch4) with the structure of the Fe-25 at.%Cr alloy (figure 11-Ch4), one can notice that in the case of Fe-25 at.%Cr there is a larger number of connected chromium-rich clusters than in the Fe-20 at.%Cr structure and that, as the simulation advances, an interconnected structure seems to further develop in Fe-25 at.%Cr.

A difference in the microstructure morphologies between the Fe-20 at.%Cr and the Fe-25at.%Cr can also be observed in figure 12-Ch4 where we only represented the chromium-rich precipitates containing more than fifty atoms of a structure obtained after 10^8 AKMC steps. We identified the chromium rich clusters with the same method as the one discussed in subsection 4.3.3.

In figure 12-Ch4, one can clearly see that most of the chromium clusters are isolated in the case of the Fe-20 at.%Cr system, whereas in the case of the Fe-25 at.%Cr most of them are interconnected.

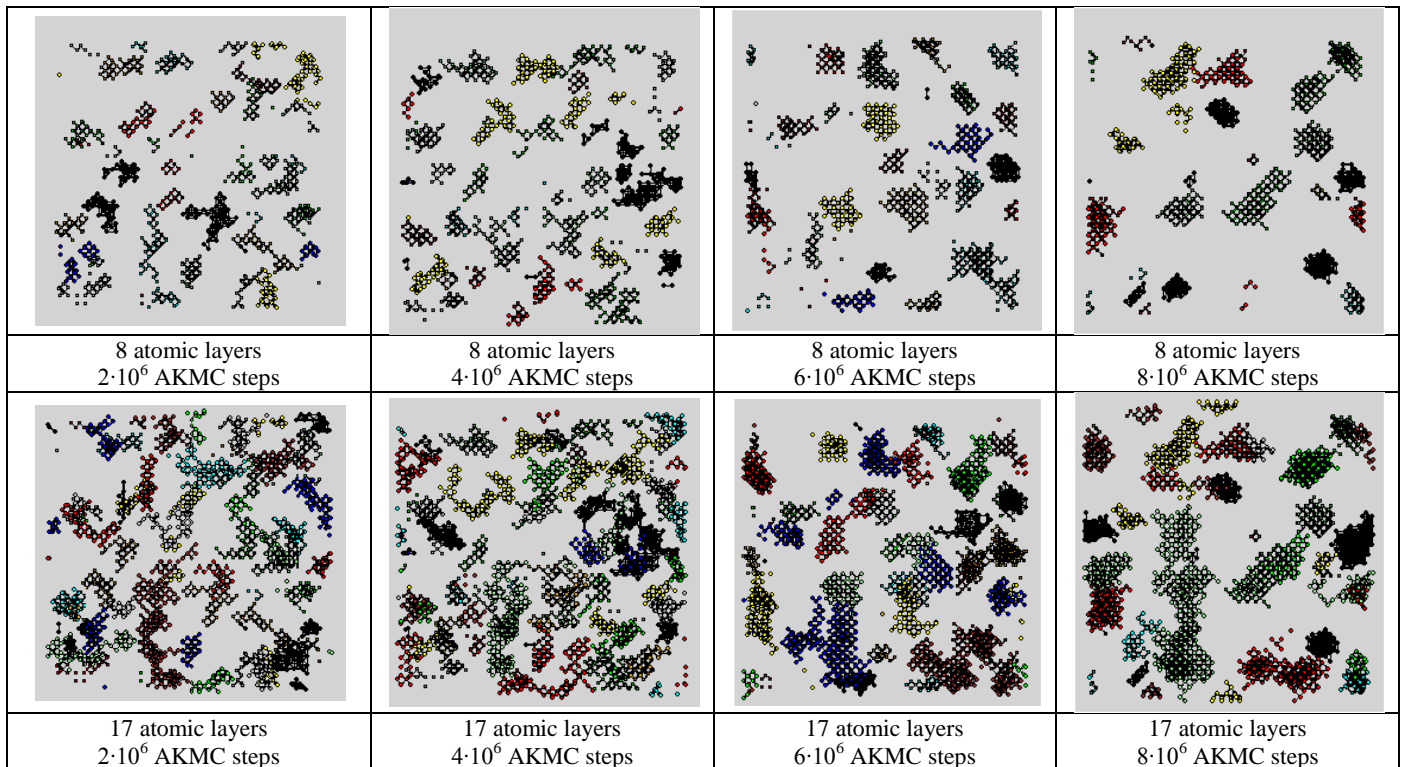


Figure 10-Ch4 Fe-20 at.%Cr microstructure corresponding to 8 atomic layers (1.2 nm thickness, higher row) or 17 atomic layers (2.4 nm thickness, lower row) at different AKMC steps. Only chromium atoms in clusters larger than 50 atoms have been represented. For visualisation, clusters have different colours, but some different clusters have the same colour, thus all atoms with the same colour do not necessarily belong to the same cluster. Isolated chromium atoms are not represented. FISE 3 parameterisation.

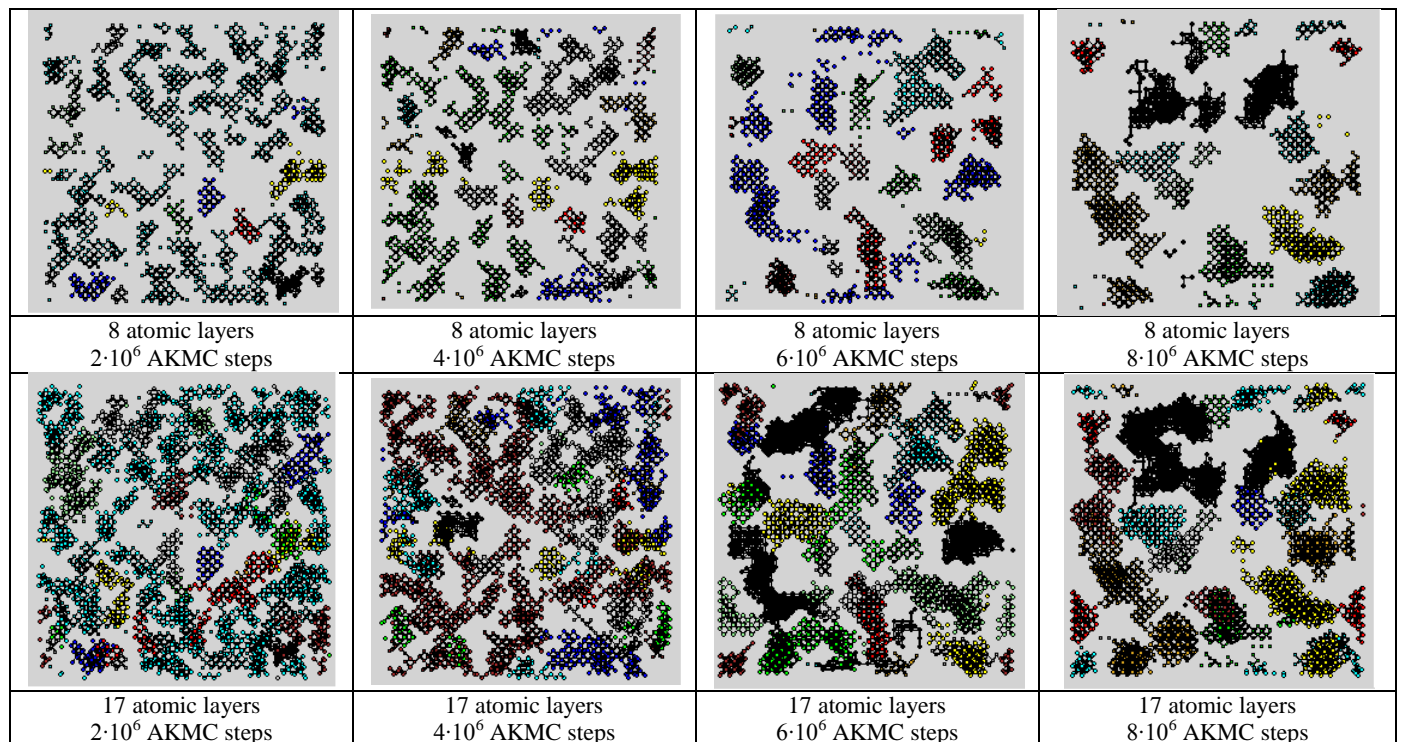


Figure 11-Ch4 Fe-25 at.%Cr microstructure corresponding to 8 atomic layers (1.2 nm thickness, higher row) or 17 atomic layers (2.4 nm thickness, lower row) at different AKMC steps. Only chromium atoms in clusters larger than 50 atoms have been represented. For visualisation, clusters have different colours, but some different clusters have the same colour, thus all atoms with the same colour do not necessarily belong to the same cluster. Isolated chromium atoms are not represented. FISE 3 parameterisation.

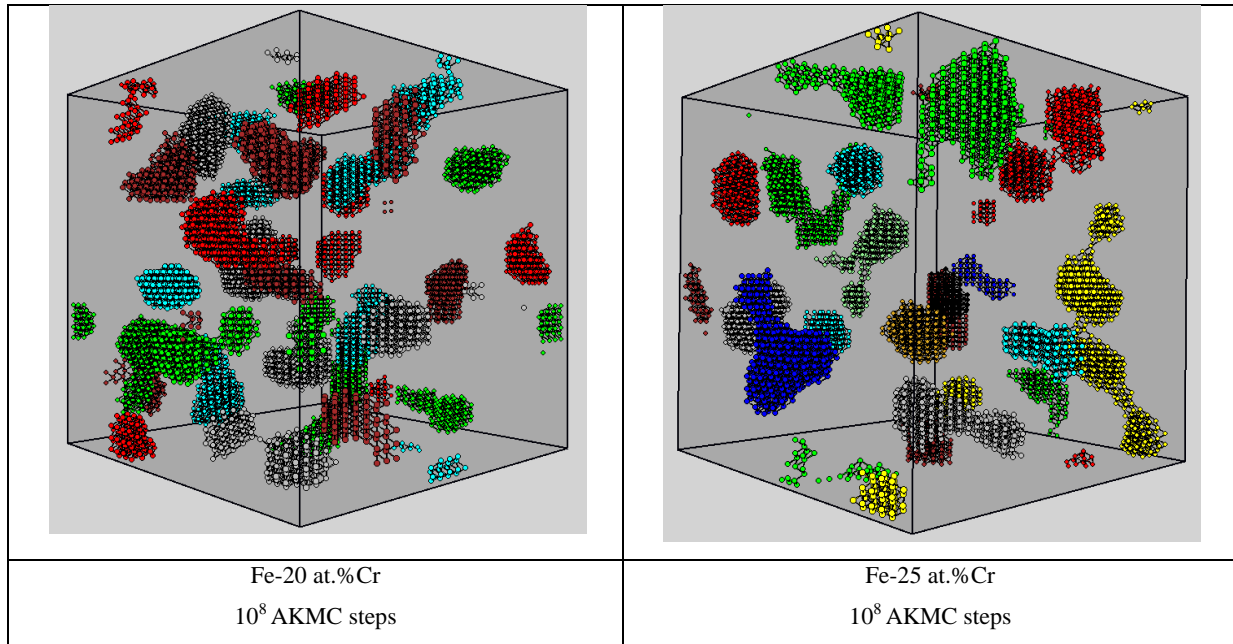


Figure 12-Ch4 Fe-20 at.%Cr (left) and Fe-25 at.%Cr (right) microstructures after 10⁸ AKMC steps. Only chromium-rich clusters with size larger than 50 atoms are represented. The chromium clusters have been identified using the method described in subsection 4.3.3 ($\mathbf{R}_{\text{samp}} = 3.5 a_0$, $\mathbf{x}_{\text{th}} = 40$ at.%). For visualisation, clusters have different colours, but some different clusters have the same colour, thus all atoms with the same colour do not necessarily belong to the same cluster. FISE 3 parameterisation.

4.3.1 Local vacancy environment evolution during thermal ageing

As a first step in the characterisation of the thermal ageing kinetics, we computed the fraction of time the vacancy diffuses in the α or α' phase during the AKMC simulations. The main difficulty consists in defining a systematic criterion allowing to distinguish the iron rich phase (α -phase) from the chromium rich phase (α' -phase). In order to introduce such a criterion, we computed the probability for the vacancy nearest neighbour sites to be occupied by chromium atoms when the vacancy is in the iron rich phase. In the initial configuration of the Fe-Cr structure, chromium atoms are randomly distributed. Under the hypothesis that the solute atoms are randomly distributed in the α -phase, such probability can be computed with a binomial distribution [Novy2009b]:

$$P(n, x_{\text{Cr}}) = \frac{8!}{(8-n)!n!} x_{\text{Cr}}^n (1 - x_{\text{Cr}})^{8-n}, \quad (20)$$

where 8 is the number of the vacancy nearest neighbours, x_{Cr} is the chromium concentration in the alloy, and n is the number of chromium atoms which occupy the vacancy nearest neighbour sites. We computed the probability expressed by equation (20) for different

chromium contents (namely 9at.%, 14at.%, 20at.%, and 25at.%) and for a chromium occupancy of the vacancy first nearest neighbours (1nn) shell going from zero to eight. Our results are presented in figure 13-Ch4.

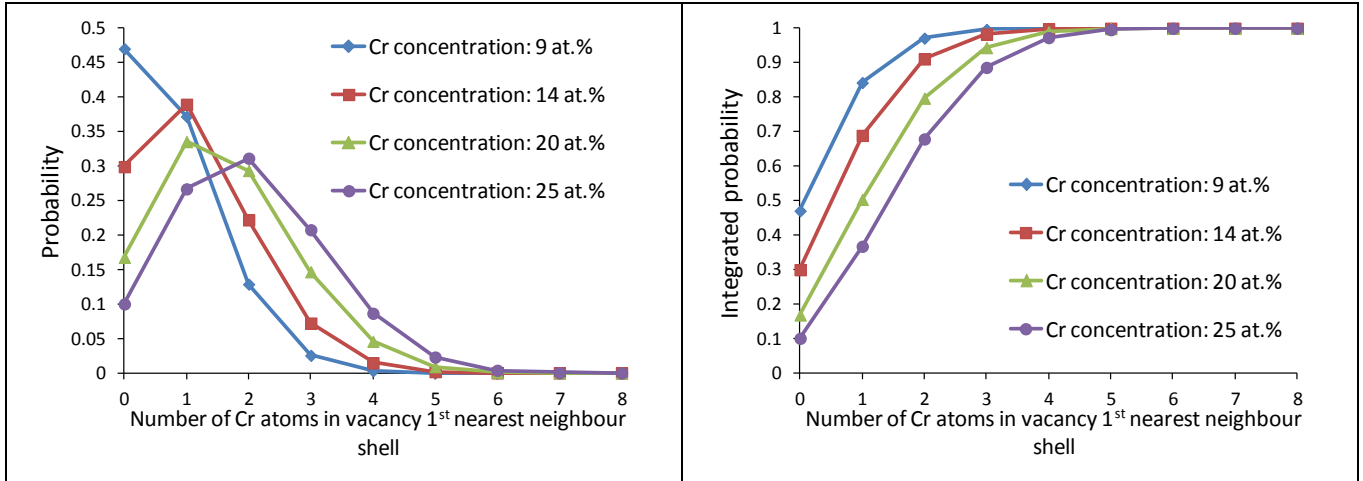


Figure 13-Ch4 Probability (left) and integrated probability (right) of different chromium occupancies (from 0 to 8) of vacancy 1nn sites for different chromium concentrations in the Fe-Cr structure (9at.%, 14 at.%, 20 at.%, and 25 at. %).

Figure 13-Ch4 shows that, for chromium concentrations between 9 at.% and 25 at.%, there is a non negligible probability to find up to four chromium atoms in the vacancy 1nn shell. Hence, in our AKMC simulations, we considered that the vacancy is in the α -phase when the number of chromium atoms located among its eight nearest neighbours sites is lower than five. In order to verify the robustness of the method, we also considered a more restrictive condition by limiting to three the maximum number of chromium atoms which are expected to be found in vacancy 1nn shell when the latter is moving in α -phase. For all the AKMC simulations done in this work, the fraction of time the vacancy spends in α -phase has been measured and plotted every 2×10^4 AKMC steps. Figures 14-Ch4 and 15-Ch4 display our results for Fe-20 at.%Cr alloy and Fe-25 at.%Cr alloy, respectively.

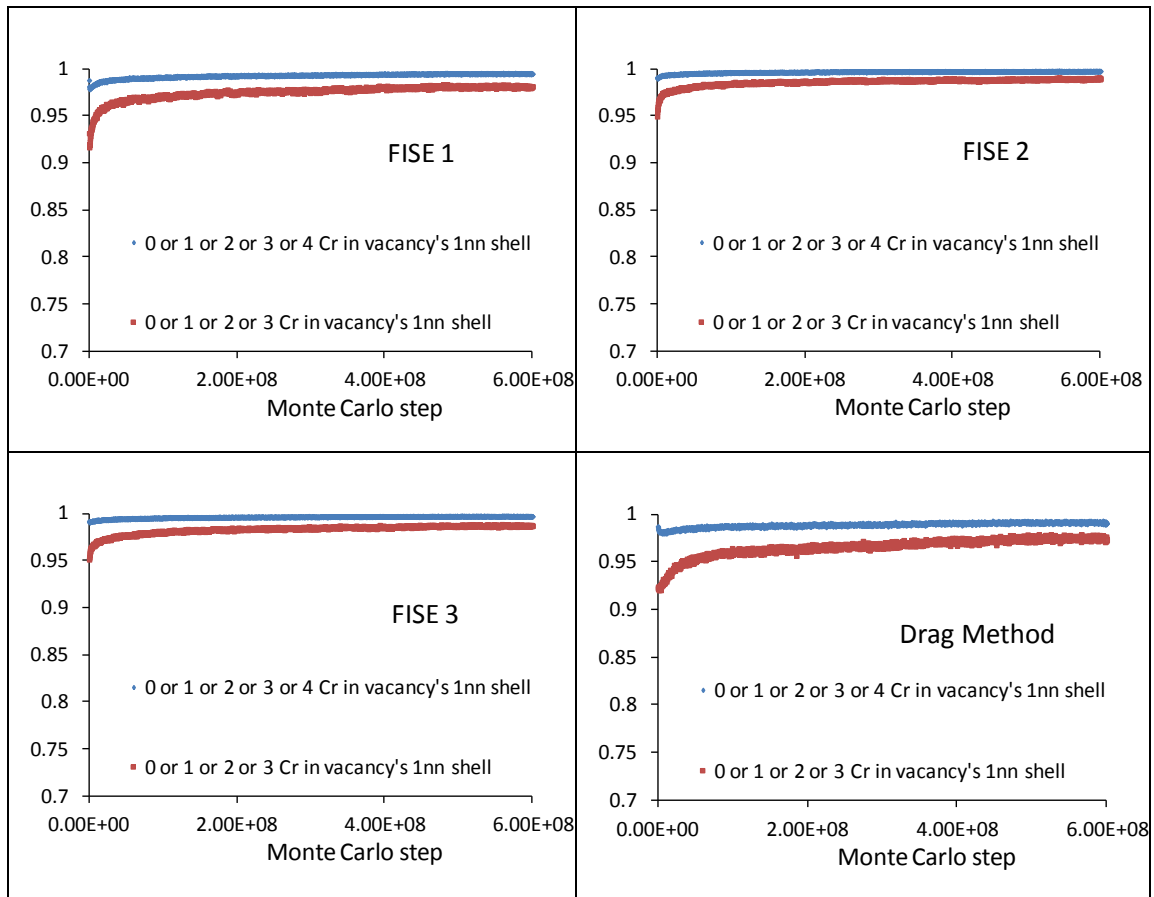


Figure 14-Ch4 Fraction of time the vacancy diffuses in the α phase for different parameterisations of our AKMC simulations of Fe-20 at.%Cr. T=773 K. Simulation box size: $32a_0 \times 32a_0 \times 32a_0$ ($a_0=2.8553 \text{ \AA}$).

Despite a small difference between the results obtained with the two different criteria used to determine whether the vacancy is located in the α -phase or outside (*i.e.* at the interface or in the α' -phase), the vacancy seems to spend almost all its time in the α -phase for both alloys. The results show that the vacancy does not diffuse into the α' -phase, as could be expected because of the higher vacancy formation energy (see chapter 2). Based on figures 14-Ch4 and 15-Ch4, the time spent by the vacancy at the α/α' interface is not significantly enhanced. Indeed, figures 14-Ch4 and 15-Ch4 indicate that the fraction of time the vacancy spends in a local environment characterised by the presence of up to three or four chromium atoms in its first neighbour shell is consistent with the integrated probability of finding up to three or four chromium atoms in the vacancy nearest neighbour shell (figure 13-Ch4) obtained for an ideal solid solution with different solute concentrations. This is due to the fact that the migration energy is higher when the vacancy migrates towards a chromium-rich environment compared to a case where the vacancy jumps towards an iron-rich environment. These results confirm those previously obtained by Pareige *et al.* for Fe-25 at.%Cr alloy [Pareige2011].

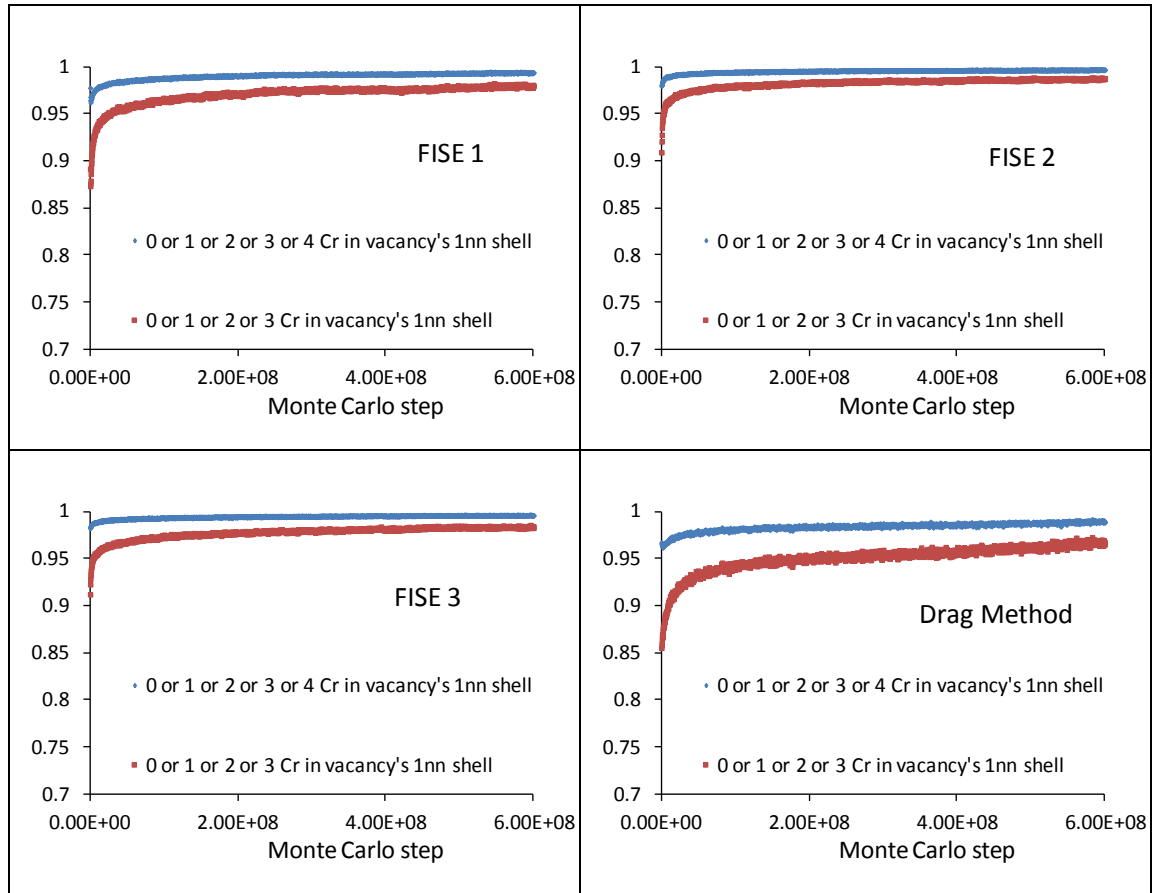


Figure 15-Ch4 Fraction of time the vacancy diffuses in the α phase for different parameterisations of our AKMC simulations of Fe-25 at.%Cr. $T=773$ K. Simulation box size: $32a_0 \times 32a_0 \times 32a_0$ ($a_0=2.8553$ Å).

Concerning the different parameterisations of the AKMC, all FISE approaches provide similar results. When the barriers have been fully computed with the EAM-2BM-GB potential, the fraction of time the vacancy spends in the iron rich phase (α -phase) is slightly smaller than in simulations based on FISE parameterisations. This latter observation can be probably explained by the fact that, as shown in chapter 3, the migration barriers associated to vacancy jumps towards chromium rich zones are predicted by the EAM potential to be lower than the ones obtained with DFT.

4.3.2 Time scaling

One of the most important issues related with the AKMC simulations concerns the simulated time, and more precisely how it scales with real experimental time. Since the vacancy concentration in the simulation box is some orders of magnitude larger than the real equilibrium vacancy concentration in the alloy, AKMC simulated time must be rescaled in order to compare simulations results with experimental observations. For this purpose,

different approaches can be considered. The real time can be obtained from Monte Carlo time with the following relation:

$$t_{\text{phys}} = t_{\text{MC}} \frac{C_v^{\text{MC}}}{C_v^{\text{eq}}}, \quad (21)$$

where C_v^{eq} is the equilibrium vacancy concentration in the real alloy and C_v^{MC} is the vacancy concentration in the simulation box. In the context of thermal ageing simulations of binary alloys, equation (21) is often applied considering that the term C_v^{eq} is constant during the phase separation [Pareige2011, Wallenius2007, Bonny2009c, Nguyen-Manh2008a, Castin2010, Castin2011, Bonny2009c]. Another way to obtain the time scaling factor consists in comparing the composition evolution of one of the two phases or the evolution of the chromium rich precipitate size computed during the simulations with experimental observations of the same quantities. In the first case, one has just to compute the appropriate scaling factor for which the equilibrium composition is reached at the same time in experiments and simulations. In the second case, one has to compute the time scaling factor for which the simulations provide the same precipitates size as experiences for identical ageing times. Another method, less frequently used than the previous ones, consists in computing the time scaling factor progressively, during the microstructure evolution of the alloy and more precisely by following the evolution of the chromium concentration in the α phase. The basic idea is to consider the vacancy concentration in the α phase rather than in the entire simulation box. This technique has been introduced in the context of the simulation of the thermal ageing of Fe-Cu very dilute alloys [Soisson2007, LeBouar2002], as in such alloys, one can assume that the vacancy diffuses either in pure iron phase or pure chromium phase. The case of highly concentrated Fe-Cr alloy is more complicated since none of the two phases can be assumed as being pure. Nevertheless, equation (21) can be applied in a more realistic way by considering that the relevant ratio between the vacancy concentration in the simulation box and the vacancy concentration in the real alloy – which determines the ratio between the simulated time and the real time – should be computed in a given phase (α or α') of the alloy. This means that, when the vacancy diffuses into the α phase, one should compare the vacancy concentration in the α phase of the simulation box and the equilibrium vacancy concentration in an Fe-Cr structure characterised by a chromium concentration equal to the one of the phase where the vacancy is diffusing. In the previous subsection, we have shown

that the vacancy spends almost all the time in the iron rich α -phase (see figures 14-Ch4 and 15-Ch4). As a consequence, the simulated local vacancy concentration can be written as:

$$C_v^{MC} = \frac{1}{V_\alpha}, \quad (22)$$

where V_α is the volume of the α phase. Since the volume of the α phase changes during the microstructure evolution, the time scaling factor in equation (21) must be progressively computed during the simulation. Moreover, it is necessary to follow the chromium concentration evolution in the α phase in the simulation box in order to compute, progressively, the equilibrium vacancy concentration in a real Fe-Cr structure with the same chromium concentration. Neglecting entropic contributions and considering the volume of the structure as being constant, the equilibrium vacancy concentration in a real alloy can be estimated as follows [Vincent2008]:

$$C_v^{eq} = \exp\left(-\frac{\Delta S}{k_B}\right) \exp\left(-\frac{E_v^f(Fe)}{k_B T}\right) \left[1 - 8x_{Cr} - 6x_{Cr} + 8x_{Cr} \exp\left(\frac{E_b^{1nn}(Cr-V)}{k_B T}\right) + 6x_{Cr} \exp\left(\frac{E_b^{2nn}(Cr-V)}{k_B T}\right)\right], \quad (23)$$

where x_{Cr} is the chromium concentration $E_v^f(Fe)$ is the vacancy formation energy in pure iron, $E_b^{1nn}(Cr - V)$ and $E_b^{2nn}(Cr - V)$ are the binding energies of first nearest neighbour and second nearest neighbour chromium-vacancy pair in a pure iron structure. The factor $\exp\left(-\frac{\Delta S}{k_B}\right)$ accounts for vibrational entropy contribution and equals 3 [Porter1996] Equation (23) allows the vacancy concentration in an Fe-Cr structure to be computed by taking into account the vacancy interaction with first and second nearest neighbour solutes.

In the case where Monte Carlo time is progressively rescaled to obtain a real time with the procedure described above or by comparison of the simulated composition evolution and the experimentally observed one, the chromium concentration in iron rich α phase must be measured. This can be achieved by identifying the chromium rich α' precipitates and by computing the chromium concentration in the remaining volume (*i.e.* in the structure resulting from the exclusion of the α' precipitates).

4.3.3 Identification of the chromium rich precipitates

One possible way to characterise the α - α' phase separation mechanism during the Fe-Cr thermal ageing consists in observing the time evolution of the chromium rich precipitates

size. This can provide some indications on the precipitation regime that characterise the phase separation. In order to understand whether the models we considered for the parameterisation of the AKMC simulations are consistent or not with phase separation thermodynamics and kinetics, we will compare our AKMC simulation results with existing experimental data on the one side, and with theoretical models and previous AKMC simulations on the other side.

Two approaches have been considered for the estimation of the α' precipitate size. The first approach consists in computing the position of the first zero L of the spherical average of the spatial autocorrelation function. This quantity provides the characteristic length scale of the microstructure. For our system it corresponds to the mean width of the α and α' domains [Huse1986, Rautiainen1999, Pareige2011] (see figure 16-Ch4) and is exploited for the analysis of interconnected structures characterised by diffuse interfaces. The spherical average of the autocorrelation function can be written as:

$$g(r) = \left\langle \frac{1}{N(r)} \sum_{j=1}^{N(r)} [\sigma(\mathbf{r}_i) - \bar{\sigma}] [\sigma(\mathbf{r}_i - \mathbf{r}_j) - \bar{\sigma}] \right\rangle, \quad (24)$$

where \mathbf{r}_i are the positions of the atoms, $\sigma(\mathbf{r}_i)$ is the \mathbf{r}_i site occupancy ($\sigma(\mathbf{r}_i)$ equals 1 if the atom in \mathbf{r}_i is chromium and -1 if the atom in \mathbf{r}_i is iron), $\bar{\sigma}$ is the average of the site occupancy over the whole structure, $N(r)$ is the number of possible \mathbf{r}_j vectors for a given distance r from the i site. $\langle \rangle$ denotes the average over all the sites of the matrix. The autocorrelation function is normalised so that $g(0) = 1$.

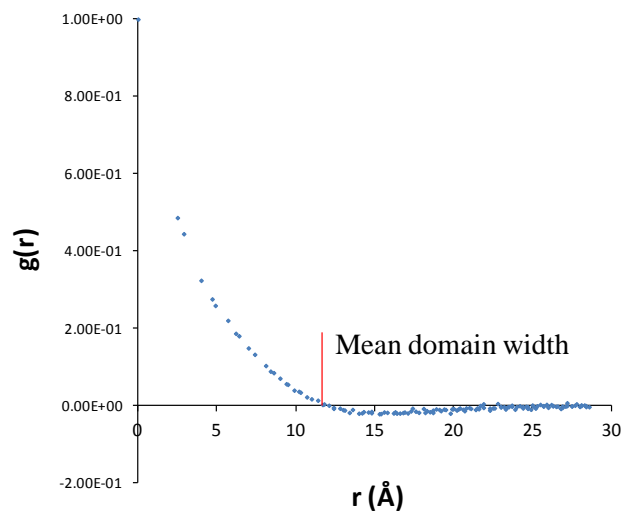


Figure 16-Ch4 Example of spherical averaged spatial autocorrelation function. The position where the autocorrelation function crosses the horizontal axis corresponds to the mean domain width.

The second approach consists in considering that chromium rich precipitates have a spherical shape so that their radius can be obtained from their volume as follows:

$$R = \sqrt[3]{\frac{3nV_{at}}{4\pi}}, \quad (25)$$

where n is the number of lattice sites included in the precipitate and V_{at} is the atomic volume obtained as the half of the bcc cell volume. This second approach requires the chromium rich precipitates to be identified in order to count the number of lattice sites they embed. To identify the chromium rich precipitates, we exploited a procedure similar to that used by Novy *et al.* [Novy2009a]. The method consists in introducing the concept of local chromium concentration: chromium content is measured inside a sampling sphere of given radius R_{samp} centred on a lattice site. In practice, the sampling sphere is displaced within all the volume of the simulation box and centred on each atomic site of the Fe-Cr structure, the chromium concentration in the sampling sphere is measured, if it is higher than a given threshold x_{th} then the site is included in α' -phase otherwise it is considered as belonging to α -phase.

The length associated to the zero of the autocorrelation function cannot be strictly identified with the size of the α' precipitate. The relation between L and the precipitate size is not direct and not trivial, and it depends for instance if the α' rich zone consists in isolated precipitates or interconnected domains.

Despite these difficulties, the evolution of L with time is similar to the evolution of the α' rich zone (precipitate) and it is a good descriptor of the evolution of the microstructure that has been used in this work, as already used in the literature.

4.3.4 Box size effects

In order to assess the influence of the simulation box size on the results, we compared the time evolution of the position of the first zero of the spherical average of the autocorrelation function obtained in a $32a_0 \times 32a_0 \times 32a_0$ simulation box and in a $72a_0 \times 72a_0 \times 72a_0$ simulation box. This has been done for both the Fe-20 at.%Cr and the Fe-25 at.%Cr with one vacancy in the simulation box. In order to represent and compare the results obtained for the two different size of the simulation box on the same time scale, the AKMC

time of the simulations performed in the $72a_0 \times 72a_0 \times 72a_0$ simulation box was rescaled by a factor corresponding to the ratio between the vacancy concentrations in each box.

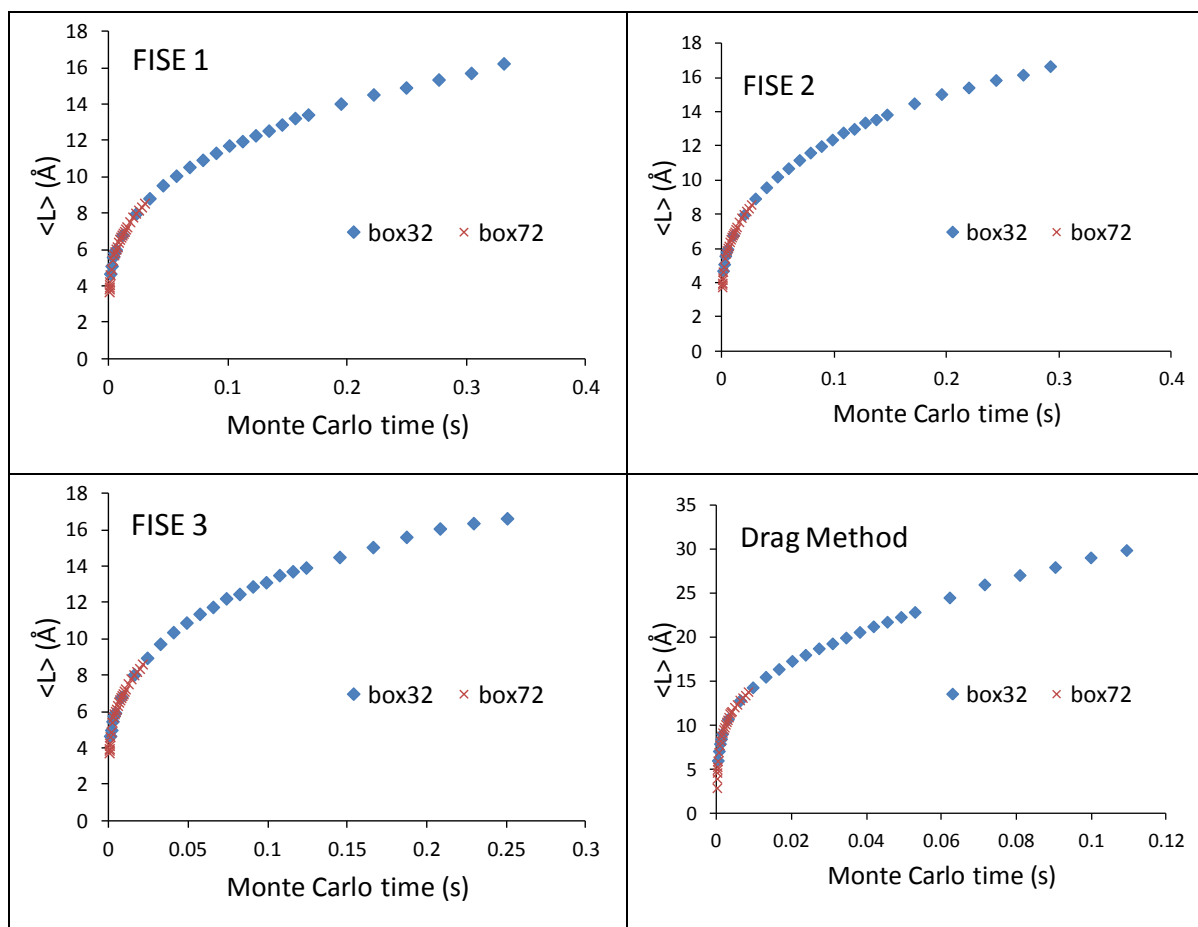


Figure 17-Ch4 First zero of the spherical average of the spatial autocorrelation function. $T=773$ K. The data have been averaged on ten AKMC runs. box32 stands for $32a_0 \times 32a_0 \times 32a_0$ simulation box size whereas box72 stands for $72a_0 \times 72a_0 \times 72a_0$ simulation box size ($a_0=2.8553$ Å). Fe-20 at.%Cr.

Figure 17-Ch4 and figure 18-Ch4 indicate that, regardless of the parameterisation considered for implementing the AKMC simulations, no box size effect is observed for both alloys.

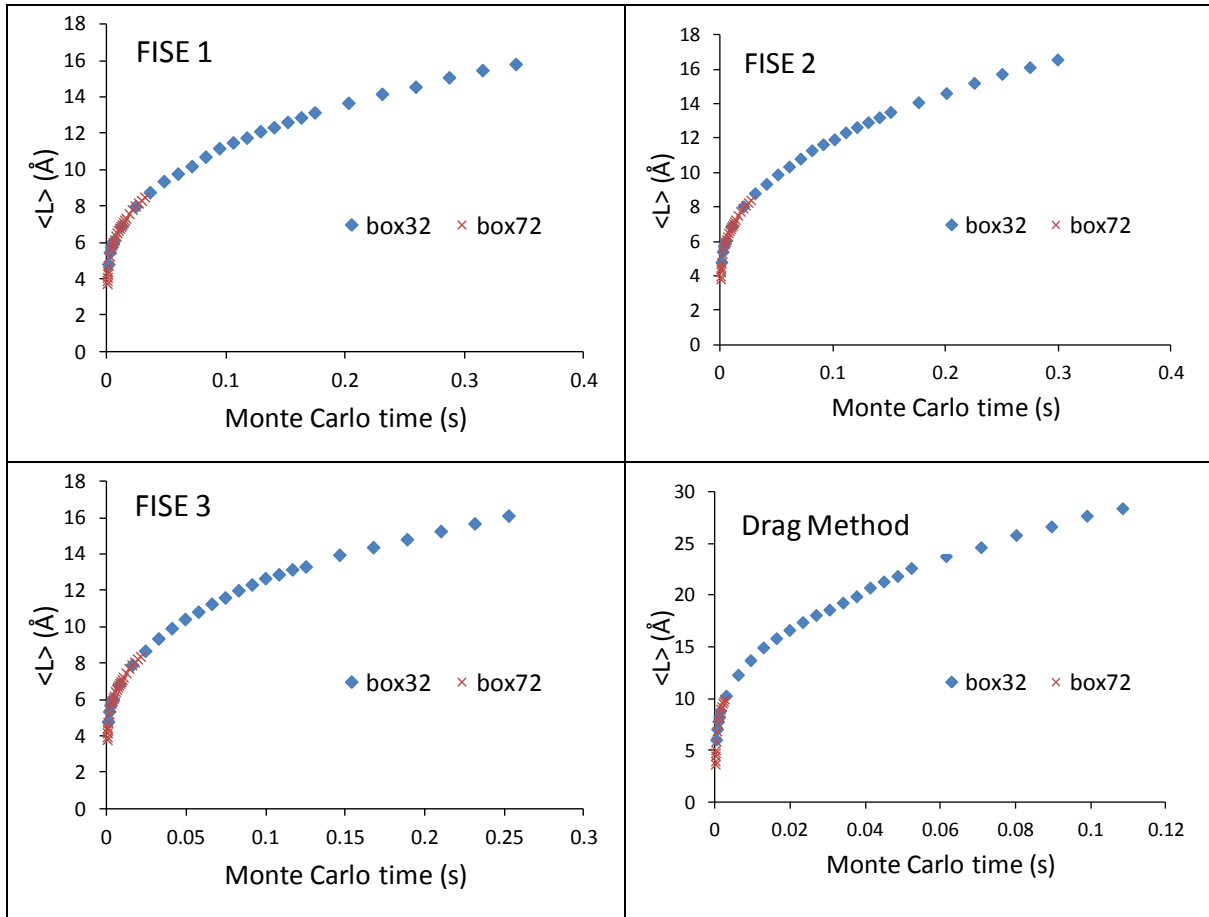


Figure 18-Ch4 First zero of the spherical average of the spatial autocorrelation function. $T=773$ K. The data have been averaged on ten AKMC runs. box32 stands for $32a_0 \times 32a_0 \times 32a_0$ simulation box size whereas box72 stands for $72a_0 \times 72a_0 \times 72a_0$ simulation box size ($a_0=2.8553$ Å). Fe-25 at.%Cr.

4.3.5 Time evolution of the precipitate size in Fe-20 at.%Cr and Fe-25 at.%Cr alloys

To pursue the analysis, we computed the time evolution of the characteristic thickness L of the α' -phase in the case of Fe-25 at.%Cr alloy and the time evolution of the mean precipitate radius R in the case of Fe-20 at.%Cr alloy.

The AKMC time has been rescaled to obtain the real time by implementing the progressive scaling that we illustrated in subsection 4.3.2. This allows to compare the simulated precipitates radius or α' -phase thickness time evolution with experimental observations without introducing the bias which would consist in computing the time scaling factor by adjusting the simulated precipitate size or α' -phase thickness time evolution to match with the observed ones. On the other hand, the progressive time scaling is more realistic than simply computing a unique time scale factor from the ratio of the vacancy

concentration in the simulation box to the equilibrium vacancy concentration computed for a pure iron structure. The progressive time scaling approach requires the chromium concentration in the matrix to be estimated at each intermediate configuration in order to compute the vacancy concentration in the matrix with equation (23). This has been done by identifying the chromium-rich precipitates and by computing the chromium concentration in the volume obtained by subtracting the α' precipitates from the simulation box. In order to identify the α' phase, we used the procedure described in subsection 4.3.3.

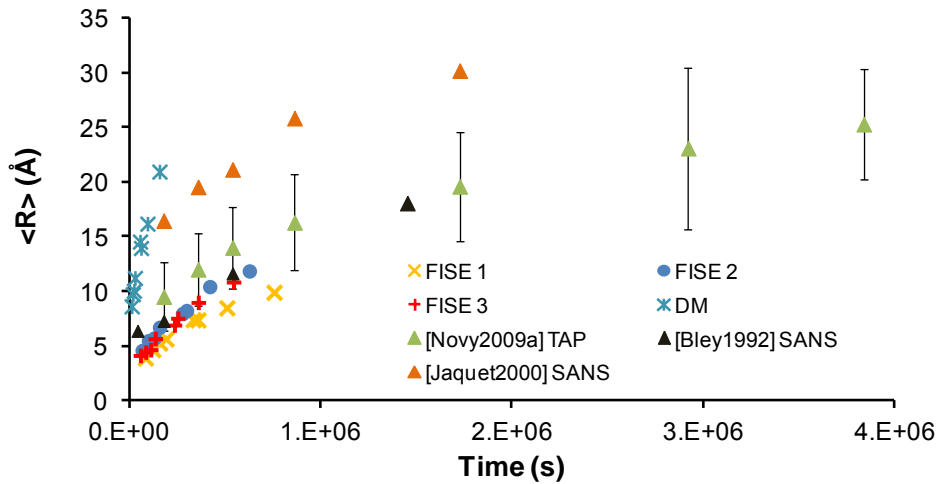


Figure 19-Ch4 Precipitate radius time evolution obtained by AKMC simulation of the thermal ageing of Fe-20 at.%Cr compared with experimental observations by tomographic atom probe from [Novy2009a]. $T=773$ K. Simulation box size: $32a_0 \times 32a_0 \times 32a_0$ ($a_0=2.8553$ Å). The Monte Carlo time has been rescaled to real time with the progressive time scaling described in subsection 4.3.2. AKMC simulation results are also compared with observations by small angle neutron scattering from [Bley1992] and [Jaquet2000].

In order to be consistent with Novy *et al.*'s [Novy2009a] and Pareige *et al.*'s [Pareige2011] analysis we considered the following parameters for the chromium cluster identification: $R_{\text{samp}} = 10$ Å, $x_{\text{th}} = 40$ at.% and $R_{\text{samp}} = 6.2$ Å, $x_{\text{th}} = 30\%$ respectively. Bonny *et al.* have used an analogous criterion for the identification of the chromium rich precipitates in the case of AKMC simulation of the Fe-Cr thermal annealing [Bonny2007]. Bonny and co-workers used a higher chromium concentration threshold (namely 90 at.%) and the 5th nearest neighbours distance for the radius of the sampling sphere. Chromium concentration in the core of α' -phase precipitates is higher than 40 at.%, but the α - α' interfaces in highly concentrated Fe-Cr alloy have a diffuse character so that, if one considers a too high concentration threshold for the identification of chromium rich precipitates, the interfaces could be completely or partially excluded from the α' -phase.

Following Pareige *et al.*'s, in the case of Fe-25 at.%Cr alloy, we estimated the characteristic length of the α' phase L by locating the first zero of the spherical average of the autocorrelation function computed in each Fe-Cr intermediate structure, as obtained during the simulations, and without applying any post-processing treatment (see discussion in subsection 4.3.3). In the case of Fe-20 at.%Cr alloy, we computed the precipitate radius R by counting the average number of atomic sites included in the solute-rich clusters and deducing the radius from equation (25) according to Novy *et al.* analysis. The results for the Fe-25 at.%Cr have been obtained as the average over ten AKMC runs whereas those for the Fe-20 at.%Cr have been computed considering one AKMC run.

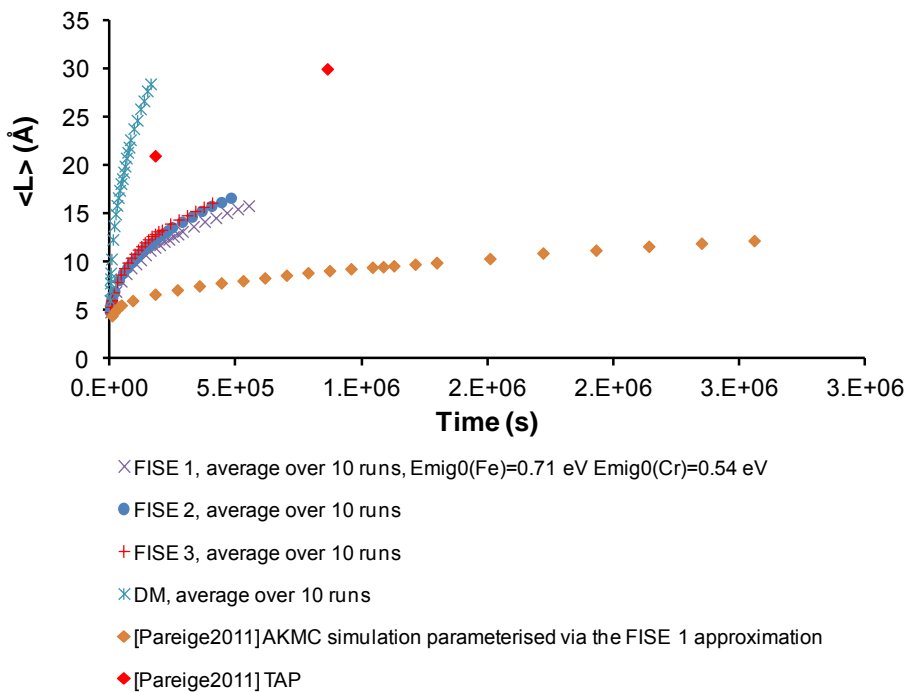


Figure 20-Ch4 Time evolution of typical thickness of the α' phases in the AKMC simulations of the thermal ageing of Fe-25 at.%Cr. They are compared with experimental observations and AKMC simulations from [Pareige2011] at the same temperature $T=773$ K. The data have been averaged on ten AKMC runs. Simulation box size: $32a_0 \times 32a_0 \times 32a_0$ ($a_0=2.8553$ Å). The Monte Carlo time has been rescaled to real time with the progressive time scaling described in subsection 4.3.2.

The results of our simulations parameterised with the FISE approximations are in good agreement with Novy *et al.*'s [Novy2009a] and Bley's experimental observations in the case of the Fe-20 at.%Cr alloy (figure 19-Ch4) whereas they underestimate the experimentally measured precipitate size in the case of the Fe-25 at.%Cr alloy (figure 20-Ch4). The results obtained from the AKMC simulations parameterised with the vacancy migration energies computed with the EAM-2BM-GB potential overestimate experimental data in both the case of the Fe-20 at.%Cr alloy and the Fe-25 at.%Cr alloy. This is probably due to the fact that, on

the one hand, the chromium-chromium interaction computed with the EAM-2BM-GB potential remains almost constant when the chromium separation increases from the first nearest neighbours to the second nearest neighbours distance and, on the other hand, the first nearest neighbour chromium-vacancy interaction is very weak.

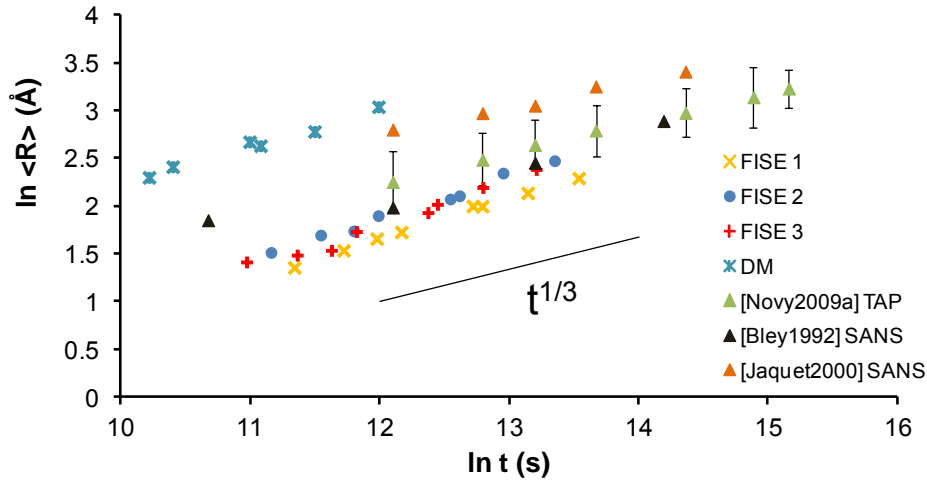


Figure 21-Ch4 Logarithm of the precipitate mean radius as a function of the logarithm of the time obtained by AKMC simulation of the thermal ageing of Fe-20 at.%Cr. $T=773$ K. Simulation box size: $32a_0 \times 32a_0 \times 32a_0$ ($a_0=2.8553$ Å). The Monte Carlo time has been rescaled with the progressive time scaling described in subsection 4.3.2. AKMC simulation results are also compared with observations by small angle neutron scattering from [Bley1992] and [Jaquet2000].

In the case of Fe-25 at.%Cr alloy (figure 20-Ch4), it should be noticed that our results are closer to the experimental data than the AKMC results of Pareige *et al.* Their AKMC simulations were performed by implementing the FISE 1 parameterisation and using the EAM-2BM-PO potential to compute the ΔE term and $E_{\text{mig } 0}(\text{Fe}) = 0.65$ eV and $E_{\text{mig } 0}(\text{Cr}) = 0.52$ eV. In our case, the FISE 1 approximation has been implemented considering $E_{\text{mig } 0}(\text{Fe}) = 0.71$ eV and $E_{\text{mig } 0}(\text{Cr}) = 0.54$ eV (as obtained by DFT calculation) and the EAM-2BM-GB potential to compute ΔE . Our results obtained with the three different FISE approximations are very close to each other, so one can suppose that the effect of the choice of the $E_{\text{mig } 0}$ on the estimation of the vacancy migration barrier is quite small in the case of the chromium concentrations that we considered here. Therefore, the difference between our simulations and those from Pareige *et al.* [Pareige2011] is probably mainly due to the different choice of the EAM-2BM potential.

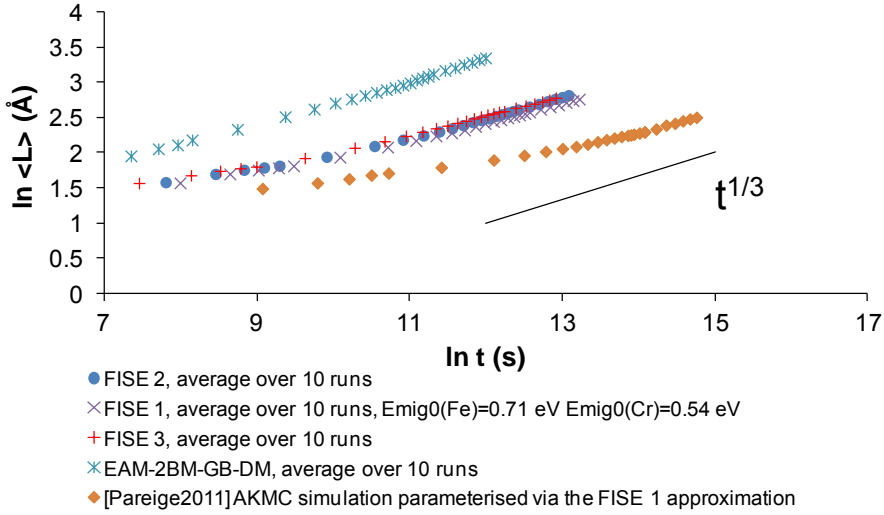


Figure 22-Ch4 Logarithm of the typical thickness of the α' phases as a function of the logarithm of the time obtained by AKMC simulations of the thermal ageing of Fe-25 at.%Cr compared with AKMC simulations from [Pareige2011]. $T=773$ K. The data have been averaged on ten AKMC runs. Simulation box size: $32a_0 \times 32a_0 \times 32a_0$ ($a_0=2.8553$ Å). The Monte Carlo time has been rescaled to real time with the progressive time scaling described in subsection 4.3.2.

In order to characterise the unmixing regime which drives the α/α' phase separation in our simulations, we plotted the logarithm of the precipitate mean radius R (in the case of the Fe-20 at.% alloy) and the α' -phase characteristic thickness L (in the case of the Fe-25 at.% alloy) as a function of the logarithm of the time. If one considers a time evolution relation with the following form:

$$\langle R \rangle^n (t) = At \text{ (or } \langle L \rangle^n (t) = At), \quad (30)$$

$\frac{1}{n}$ can be obtained as:

$$\frac{1}{n} = \frac{d \ln \langle R \rangle (t)}{d \ln t} \text{ (or } \frac{1}{n} = \frac{d \ln \langle L \rangle (t)}{d \ln t}). \quad (31)$$

Thus, the time exponent $\frac{1}{n}$ can be obtained as the slope of the $\ln \langle R \rangle$ vs. $\ln t$ (or $\ln \langle L \rangle$ vs. $\ln t$) plot. Figures 21-Ch4 and 22-Ch4 show our results for both alloys. In the case of the Fe-25 at.% alloy and regardless of the parameterisation of the AKMC simulations, we obtained a time exponent, which asymptotically tends towards $\frac{1}{3}$. This value corresponds to the one predicted by the LSW description of the coarsening regime. The values of the

precipitate size that we computed for the Fe-20 at.%Cr alloy were obtained in one AKMC run only, so it is difficult to draw a conclusion about the time-exponent; the tendency that these values exhibit seems to be close to what would be expected from the LSW law again. However, LSW theory is based on the hypothesis that the precipitate volume fraction is close to zero (see chapter 1), and this hypothesis is not verified in our case. Nevertheless, Huse introduced a model describing the time evolution of the α' -phase thickness in the very late stages of the phase separation in highly concentrated binary systems by taking into account the contribution of the diffusion of the vacancy along the interfaces between domains [Huse1986] (in his work, Huse obtained the precipitate thickness by locating the first zero of the spherical average of the spatial autocorrelation function). Huse computed the time exponent and found that it tends to $\frac{1}{3}$ in the late stages of the phase separation. Recently, Pareige *et al.* [Pareige2011] have shown that the LSW law and the model introduced by Huse converge towards the same asymptotic behaviour. The same result was experimentally obtained by Novy *et al.* for the time evolution of precipitate mean radius in Fe-20 at.%Cr alloy.

In order to further evaluate the AKMC simulation parameterisations, we compared our results with some very recent predictions obtained by L'vov *et al.* [Lvov2011] with a thermodynamic model describing the phase equilibrium of binary alloys containing solute rich nanometric precipitates. The model introduced by L'vov *et al.* is based on the estimation of the free energy of the system *via* the regular solution approach and takes into account the solute concentration dependence near the α/α' interfaces on the precipitate radius due to the Gibbs-Thomson effect. L'vov and co-workers plotted the chromium concentration in the matrix and in the chromium-rich precipitates as a function of the precipitates radius at 773 K. Their results are illustrated in figure 23-Ch4 where they can be compared with our AKMC simulations. Our predictions seem to be in qualitative rather good agreement with both L'vov's model and Novy *et al.*'s observations.

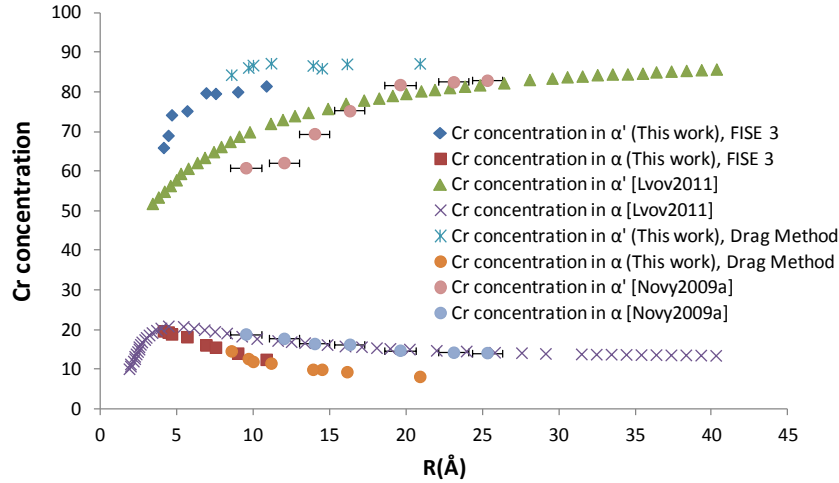


Figure 23-Ch4 Evolution of the chromium concentration in the chromium-rich precipitates and in the matrix as a function of the precipitate size in Fe-20 at.%Cr. T=773 K. Results from this work are compared with observations from [Novy2009a] and theoretical predictions from [Lvov2011]. Simulation box size: $32a_0 \times 32a_0 \times 32a_0$ ($a_0=2.8553 \text{ \AA}$).

A very important issue is the fact that the AKMC simulations performed with the FISE 3 parameterisation and computing the vacancy migration energies obtained with the EAM-2BM-GB (by drag method) exhibit similar tendencies. This means that the two parameterisations are compatible from the thermodynamic point of view, as it is expected since, in both cases, the energy variation of the system due to a vacancy jump is described by the EAM-2BM-GB potential. Thus, the disagreement between the two parameterisations has probably a kinetic origin and is related to the difference between the estimations of the saddle point energy associated to the vacancy migration process obtained with the two different approaches.

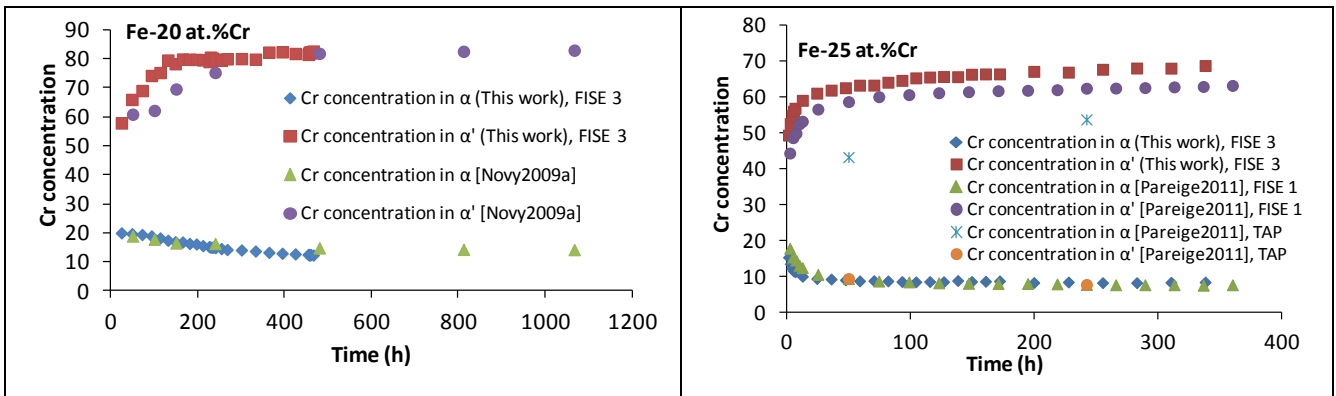


Figure 24-Ch4 Time evolution of the chromium concentration in the chromium-rich precipitates and in the matrix. Left: our AKMC simulation results for the Fe-20 at.%Cr alloy (T=773 K) are compared with Novy *et al.*'s experimental observations [Novy2009a]. Right: our AKMC simulation results for the Fe-25 at.%Cr alloy (T=773 K) are compared with both Pareige *et al.*'s AKMC simulation and experimental observations [Pareige2011].

We also compared the time evolution of the chromium concentration in the α -phase and in the α' -phase estimated with the AKMC simulation parameterised with the FISE 3 approximation with Novy *et al.*'s experimental results for the Fe-20 at.%Cr alloy and with Pareige *et al.*'s AKMC simulation and experimental results for the Fe-25 at.%Cr alloy. We identified the α' -phase with the method described in subsection 4.3.3 and using the same parameters as Novy *et al.* and Pareige *et al.* ($R_{\text{samp}} = 10 \text{ \AA}$, $x_{\text{th}} = 40 \text{ at.}\%$ and $R_{\text{samp}} = 6.2 \text{ \AA}$, $x_{\text{th}} = 30\%$ respectively). Our results are presented in figure 24-Ch4. They are in quite good agreement with both the Novy *et al.*'s observations and Pareige *et al.* simulation, whereas they overestimate the experimentally observed chromium concentration in the α' -phase in the case of the Fe-25 at.%Cr alloy. The composition of the chromium-rich precipitating phase evolves with the time, thus indicating that the decomposition mechanism should be either the non-classical nucleation or the spinodal decomposition. Our simulation results show that the evolution of the chromium concentration in the α -phase during the thermal ageing evolves towards a lower value than the solubility limit obtained by Bonny *et al.* [Bonny2011a] at 773 K with the EAM-2BM-GB potential (figure 2-Ch2). This is due to the fact that Bonny and co-workers included the vibrational entropy contribution in their calculations whereas our AKMC simulations are performed on a rigid lattice.

It should be noted that Martinez *et al.* AKMC simulation of the Fe-20 at.%Cr alloy thermal ageing [Martinez2011], parameterised with the concentration-dependent Fe-Cr pair potential introduced by Levesque *et al.* [Levesque2011], also exhibits a good agreement with Novy *et al.* TAP observations of the Fe-20 at.%Cr alloy. Furthermore, Martinez *et al.* AKMC simulation better reproduce the chromium-rich precipitate size time evolution with respect to our simulations.

The results presented in this chapter indicate that our FISE parameterisation for the AKMC simulations seems to be able to capture the difference in the phase separation mechanism that occurs in Fe-Cr alloys with different chromium concentrations. In particular, spinodal decomposition seems to occur in the case of the Fe-25 at.%Cr alloy but this remains to be confirmed by further analysis.

The fact that the precipitate size and α' -phase characteristic thickness that we observed in our simulations follows the asymptotic behaviour described by the LSW theory suggests also that most of the structures we have investigated could correspond to the late stages of the α/α' phase separation. In principle, it should be possible to characterise the spinodal decomposition regime by studying the time dependence of the wavelength of the concentration fluctuations in the early stage of the phase separation. According to Rautiainen

and Sutton [Rautiainen1999], in the case of isotropic spinodal decomposition, the time dependence of the chromium rich domain thickness and the wavelength follow similar time dependence characterised by a power law. The time exponent is expected to be between 0.15 and 0.2 in this regime [Binder2001]. Both the domain thickness and the wavelength can be estimated *via* the spatial autocorrelation function (the wavelength can be obtained as the position of the first maximum of the normalised spherical average of the autocorrelation function [Rautiainen1999]). Consequently, one could, in principle, show whether or not the spinodal decomposition occurs in the first stage of the thermal ageing by analysing the time dependence of the chromium-rich domain thickness. Unfortunately, we do not have a sufficient amount of data concerning the early stages of the thermal ageing simulations to draw any conclusion in that matter.

Globally, we observed very little differences in the results obtained with the three FISE parameterisations even though, especially in the case where the migrating atom is an iron atom, the FISE 2 and FISE 3 approximations exhibit a small but visible improvement compared to FISE 1 in their capability to reproduce full DFT-NEB calculations of the vacancy migration barriers (see figure 6-Ch4). FISE 2 and FISE 3 provide a better description of the effect that the chromium content in the saddle point environment has on the vacancy migration energies. Therefore, a difference between FISE 1 approximation and the FISE 2 and FISE 3 approximations should be more visible in highly concentrated alloys where one would expect the LAE of the vacancy-migrating atom pair to be richer in chromium. Even if the alloys we simulated in this work contain a large amount of chromium, that is probably not enough to see a difference between simulations parameterised with the different FISE approximations. However, there is an even more important aspect which could explain the apparent equivalence between the simulations based on the different FISE parameterisations: the α/α' phase separation occurs faster than we expected and, as we have shown, the vacancy spends almost all the time in the iron rich α -phase (see figures 14-Ch4 and 15-Ch4). Hence, the difference between FISE 1 approximation and FISE 2 and FISE 3 does not affect the vacancy diffusion significantly. In order to understand whether or not the description we proposed, by means of the FISE 2 and FISE 3 parameterisations, of the migration barriers dependence on the saddle point environment has an effect on the simulations of the thermal ageing, the very early stages of the structure evolution will have to be carefully observed.

Concerning the parameterisation fully based on the EAM-2BM-GB potential, we considered, in a first step, only the contribution of the first nearest neighbour shell of the vacancy-migrating atom pair for the calculation of the migration barriers. In this case, we did

not observe the α/α' phase separation after $1.6 \cdot 10^9$ AKMC steps, whereas two separated phases were clearly visible after 10^8 AKMC steps when we included the second nearest neighbours effect in the calculation of the vacancy migration barriers. This means that, in the first case, the kinetics of the phase separation is at least considerably slower with respect to the second case.

It is still not completely clear why the parameterisation fully based on the EAM-2BM-GB potential leads to a precipitate phase characterised by higher mean precipitate radius in the case of Fe-20 at.% Cr alloy, and higher α' -phase thickness in the case of Fe-25 at.% Cr alloy compared to results obtained with the FISE parameterisations. Nevertheless, the comparison of the simulations of the Fe-20 at.%Cr alloy performed within the FISE 3 parameterisation or within the parameterisation fully based on the EAM-2BM-GB potential with the L'vov model and with Novy *et al.*'s experimental observations, makes us think that the reason for this disagreement could rely on kinetic rather than thermodynamic reasons (figure 20-Ch4).

It should be emphasised that, concerning the time dependence of the evolution of the mean precipitate radius R or the chromium α' -phase typical thickness, all the parameterisations that we considered here predict a microstructure late stage evolution kinetics which is consistent with both the experimental observations and the LSW theory of coarsening.

Finally, in the case of the AKMC simulations parameterised with the FISE 3 approximation, we observed the evolution of the Fe-Cr microstructure in order to try to understand if a difference can be noticed between the phase separation mechanism that occurs in Fe-20 at.%Cr and Fe-25 at.%Cr alloys. We concluded that, in the Fe-25 at.%Cr alloy, interconnected chromium-rich clusters are more likely to develop than in the Fe-20 at.%Cr alloy. Nevertheless, Novy *et al.* have shown that non-classical nucleation occurs in Fe-20 at.%Cr. The change in phase separation mechanism from classical nucleation to non-classical nucleation and spinodal decomposition occurs progressively and continuously with the increase of the solute concentration (see chapter 1). Hence, the characterisation of the difference between the phase separation mechanism in Fe-20 at.%Cr and Fe-25 at.%Cr alloys is a hard task that requires a detailed analysis of the early stages of the unmixing kinetics.

In this chapter, we illustrated the parameterisation that we have implemented to employ the AKMC for the simulation of the Fe-Cr thermal annealing. We considered two types of parameterisations. The first type is a parameterisation fully based on the calculation of the vacancy migration barriers with the EAM-2BM-GB potential for all the configurations of the vacancy-migrating atom pair first and second nearest neighbour shells. The second type is a parameterisation based on the FISE approximation which has been implemented by progressively introducing the dependence of the $E_{\text{mig } 0}^{\text{ab}}$ term on the migrating atom saddle point position nearest neighbour environment. In order to compare our simulations with recent experimental observations, we focused on Fe-20 at.%Cr and Fe-25 at.%Cr alloys. Concerning the time evolution of the precipitate mean radius R (in the case of the Fe-20 at.%Cr alloy) or the α' -phase thickness L (in the case of the Fe-25 at.%Cr alloy), the FISE parameterisations results are in good agreement with experimental data in the case of the Fe-20 at.%Cr alloy whereas they underestimate the experimental observations in the case of the Fe-25 at.%Cr alloy. The parameterisation fully based on the EAM-2BM-GB potential overestimate both the experimental results and those obtained with the FISE parameterisations. Nevertheless, all the parameterisations are consistent with the time dependence of the chromium-rich precipitates described by the LSW theory. The observation of the Fe-Cr microstructure at different AKMC steps and for the two chromium contents that we considered here seems to indicate that the unmixing mechanism occurring in the Fe-25 at.%Cr is the spinodal decomposition but further analysis are necessary to confirm this hypothesis.

CONCLUSIONS

This work is a contribution to the materials research for nuclear industry, both in the framework of the European project GETMAT (GEneration IV and Transmutational MATerials) concerning the future generation nuclear power plants, and in the context of EDF R&D research activity on french operating reactors. This contribution addressed the study of chromium-rich ferritic/martensitic stainless steels in the first case, and chromium-rich austenitic/ferritic stainless steels in the second case. The main goal of this thesis consisted in the study of the thermal ageing of the ferritic phase in the absence of radiation effects.

We chose the Fe-Cr binary alloy as a model system for the investigation of the ferritic stainless steels. The first part of this work has been devoted to the description of some important physical properties of the Fe-Cr system. We discussed the fact that even if the Fe-Cr binary alloy represents a simplified system with respect to ferritic stainless steels, particularly for the study of the time evolution of the microstructure at a given temperature, it still carries some difficulties mainly related to its peculiar magnetic properties.

We then presented the theoretical framework and computational methods which have been the basis of our investigation. These are the cohesive models we used to determine the energy associated to a given Fe-Cr structure (*i.e.* the density functional theory and an embedded atom method potential) as well as the method we chose to compute the vacancy migration energy (*i.e.* the nudged elastic band method and the drag method). Concerning the empirical potential, our literature review made us choose the parameterisation achieved by Bonny *et al.* within the two band model [Bonny2011a].

One of our main objectives consisted in achieving a better understanding of the influence that the vacancy chemical environment has on the vacancy diffusion and, in particular, on the activation barrier of such a process. Thus, in a first time, we computed, both in the framework of the density functional theory (DFT) and using the empirical potential, some properties of the Fe-Cr binary alloy which are likely to have an influence on the vacancy migration energy (*i.e.* the interaction between a solute chromium atom and another chromium atom or a vacancy). Furthermore, we investigated, within the DFT, the magnetic properties of an iron matrix containing substitutional chromium atoms in different configurations and we showed that magnetism can have an influence on the energy barriers that oppose the microstructural changes.

In a second step, we used the nudged elastic band method and the density functional theory (DFT-NEB), as well as the drag method and the EAM potential to investigate the vacancy migration energy dependence on the local atomic environment. We observed, on the one side, the variation of the vacancy migration energy as a function of the chromium content in the first and second neighbour shells of the vacancy-migrating atom pair and, on the other side, the specific influence that the presence of chromium atoms in specific sites of the vacancy environment has on the migration barriers. The DFT-NEB calculations of the vacancy migration energy revealed the particular influence that the atomic configuration of the migrating atom saddle point position nearest neighbour shell has on the migration barriers. We have been able to partially relate the dependence of the vacancy migration energy on the local atomic environment to the chromium-chromium and the chromium-vacancy interactions properties (*i.e.* the attractive or repulsive character and the dependence of the binding energy on the chromium-chromium or the chromium-vacancy separation distance) that we previously characterised.

In general, we observed a clear disagreement between DFT-NEB results and the EAM estimations about the vacancy migration barriers. When the migrating atom is a chromium atom, the differences between the DFT and the EAM potential provisions about the migration energy are consequences of the disagreement between the two methods concerning the estimation of the chromium-chromium and the chromium-vacancy binding energy. In particular, the EAM potential predicts a chromium-chromium repulsive interaction which decreases more slowly with the chromium atoms separation distance than predicted by DFT. In the case of DFT calculations, the chromium-chromium binding energy is reduced by almost a factor 1/2 when the chromium-chromium separation passes from the first nearest neighbours' distance to the second nearest neighbours' distance. On the other hand, in the case of the EAM calculations, the chromium-chromium binding energy is almost unchanged when the chromium-chromium separation passes from the first nearest neighbours' distance to the second nearest neighbours' distance. As a result, the EAM potential predicts a considerably weaker dependence on the local atomic environment of the energy barrier associated to the vacancy-chromium exchange than DFT.

When the migrating atom is an iron atom, the difference between the DFT provisions and the EAM provisions about the vacancy migration energy is due to the disagreement in the estimation of the chromium-vacancy interaction. In this case, the difference between DFT calculations and EAM calculations is also qualitative. Indeed, the DFT predicts an attractive interaction whereas the EAM potential predicts a repulsive interaction.

We also investigated the relation between the vacancy migration energy and the total energy change ΔE the system undergoes when the vacancy migration occurs. The DFT calculations have shown that, in most of the configurations of the vacancy environment we considered, the ΔE trend follows the migration barriers one. The EAM calculations of ΔE disagree with the DFT data both in the case where the migrating atom is a chromium atom or an iron atom. In some cases even, the methods disagree on the sign of the energy change. We showed that the origin of such disagreement is, once again, a consequence of the difference between DFT and EAM descriptions of the chromium-chromium and the chromium-vacancy interactions.

On the basis of these results we developed a series of possible approaches for the parameterisation of the atomistic kinetic Monte Carlo simulations of the thermal ageing of the Fe-Cr binary alloy. We considered two different options: a parameterisation fully based on the EAM potential and a parameterisation partially based on DFT and the EAM potential.

In the first case, we computed the migration barriers corresponding to all possible chemical configurations of the first and second neighbour shells of the vacancy-migrating atom pair with the EAM potential using the drag method.

In the second case, we used the final initial state energy (FISE) approximation for the computation of the vacancy migration energy. According to this model, the vacancy migration energy can be written as the sum of two terms: one corresponding to the vacancy-migration energy, and the other being the energy variation of the system ΔE produced by the vacancy jump. In this work, we computed the first term within the DFT-NEB method and the second term with the EAM potential. In the standard FISE approximation – referred to as FISE 1 in this manuscript – , the only term accounting for the chemical environment effect on the vacancy migration energy is ΔE , whereas the migration energy depends only on the migrating atom species in an otherwise perfect iron matrix. We proposed two possible ways to improve this description and to introduce a richer description of the dependence of the vacancy migration energy on the local environment. In the first case (FISE 2), we introduced a dependence of the migration energy with the number of chromium atoms located among the saddle point position nearest neighbour sites. In the second case (FISE 3), we also took into account the detailed local configuration of the saddle point position nearest neighbour atoms. For a set of chemical configurations of the vacancy environment, we compared the vacancy migration energy obtained using the three FISE approximations, with full DFT-NEB previsions. We showed that a more precise way of describing the saddle point chemical environment leads to a better estimation of the migration barriers.

Finally, we simulated the thermal ageing of two alloys: a Fe-20 at.%Cr and a Fe-25 at.%Cr with AKMC and our different parameterisations. The results were compared with the experimental results of Novy *et al.* [Novy2009a] for the Fe-20 at.%Cr alloy, and those of Pareige *et al.* [Pareige2011] for the Fe-25 at.%Cr alloy.

To compare AKMC simulations and experimental observations, it has been necessary to find a method allowing to transform the Monte Carlo time into a real experimental time. This approach, described in chapter 4, is based on the computation of a scaling factor, as the ratio of the vacancy concentration in the α -phase of the simulation box to the real vacancy concentration in an Fe-Cr alloy with the chromium concentration of the simulated α -phase. We compared the time evolution of the mean radius of the chromium-rich precipitate (in the case of the Fe-20 at.%Cr alloy) or the typical thickness of the α' -phase (in the case of the Fe-25 at.%Cr alloy) which formed during the simulation of the thermal ageing with the experimentally observed ones.

In the case of the Fe-25 at.%Cr alloy, we found that the results of the AKMC simulations based on the FISE parameterisations underestimate the α' -phase size of about a factor 1/2 with respect to the experimental observations whereas a good agreement with experimental data has been found for the Fe-20 at.%Cr alloy. On the contrary, in the AKMC simulations fully based on the EAM potential, the chromium-rich precipitate mean radius is overestimated as compared to experimental data for both the Fe-20 at.%Cr and the Fe-25 at.%Cr alloys. We are not able yet to explain the different behaviour of the FISE parameterisations and the EAM potential parameterisation.

For both the Fe-20 at.%Cr alloy and the Fe-25 at.%Cr alloy, we observed the time exponent describing the time evolution of the precipitate size and the α' -phase thickness. In both cases, regardless of the parameterisation used, we found that the exponent asymptotically tends towards 1/3 which is the value predicted by the LSW theory of coarsening. The same conclusion was drawn by Novy *et al.* about the time evolution of the precipitates size observed in Fe-20 at.%Cr alloy and by Pareige *et al.* about the time evolution of α' -phase thickness obtained with AKMC simulations parameterised with the FISE 1 approximation.

Concerning the Fe-20 at.%Cr, we compared our results with theoretical previsions of L'vov *et al.* [Lvov2011] based on the regular solution approximation and taking into account the Gibbs-Thomson effect. We found a rather good agreement with both the FISE 3 and full EAM parameterisations. This suggests that, from a thermodynamic point of view, the two parameterisations are consistent with each other.

Since we observed the coarsening regime, which occurs in late stages of phase separation, we cannot draw any firm conclusion about the decomposition regime in early stages for the moment. In particular, we cannot distinguish between non-classical nucleation and spinodal decomposition. We can only argue that, since the chromium rich precipitates composition varies during our simulations, the classical nucleation mechanism can be excluded. Nevertheless, our observations of the microstructure evolution in both the alloys we studied show that interconnected chromium-rich precipitates are more likely to form in the Fe-25 at.%Cr alloy thus suggesting that spinodal decomposition could occur in this case.

A further exploitation of our AKMC simulations can focus on the early stages of the phase separation, the goal being the characterisation of the phase decomposition regime by the calculation of the time exponent describing the evolution of both the chromium-rich domain thickness and the wavelength. The characteristic wavelength can be obtained by computing both the first maximum of the spatial autocorrelation function or the position of the pick of the structure factor.

Moreover, in this work we only considered two alloys and one temperature. A study of the temperature dependence and the chromium concentration dependence of the phase separation kinetics must be planned. In order to observe a nucleation regime, systems with lower chromium concentration will be more appropriate.

Concerning the vacancy migration energy dependence on the local atomic environment, we have shown that the EAM potential is not able to fully reproduce the DFT previsions and in particular the chromium-chromium interaction. The strong chromium-chromium long range repulsion obtained with the EAM potential is probably a consequence of the fact that this potential was parameterised to reproduce Olsson *et al.* [Olsson2006] DFT results on the mixing enthalpy. Indeed, a strong chromium-chromium repulsion is necessary to obtain a low solubility of chromium in iron at low chromium concentrations. A better potential could probably be obtained if one takes care of reproduce both the DFT data regarding the Fe-Cr mixing enthalpy and the chromium-chromium and the chromium-vacancy binding energies. It will be also very interesting to implement AKMC simulations using the FISE 2 or FISE 3 parameterisations and to compute the ΔE term with another cohesive model such as cluster expansion, and to compare these simulations with available experimental observations. This would allow to have a better insight on the effect that the choice of the cohesive model has in the AKMC description of the Fe-Cr thermal ageing kinetics.

Since we performed our AKMC simulations considering internal energies, temperature effect is only partially included in the computation of the transition frequencies. A further modelling effort will consist, for example, in including vibrational contribution to the total energy of the system by means of the frozen phonons approximation, for instance.

Finally, in order to achieve a more realistic description of the ferritic stainless steels, the study of the effect of other alloying elements, such as molybdenum and silicon, can be addressed. In this context, a particular attention will be devoted to the molybdenum whose a known effect consists in accelerating the precipitation kinetics of the chromium-rich phase in the ferritic phase of austenitic-ferritic stainless steels [LeDellou1994].

ANNEX 1: LOCAL ATOMIC ENVIRONMENT SITES NOMENCLATURE

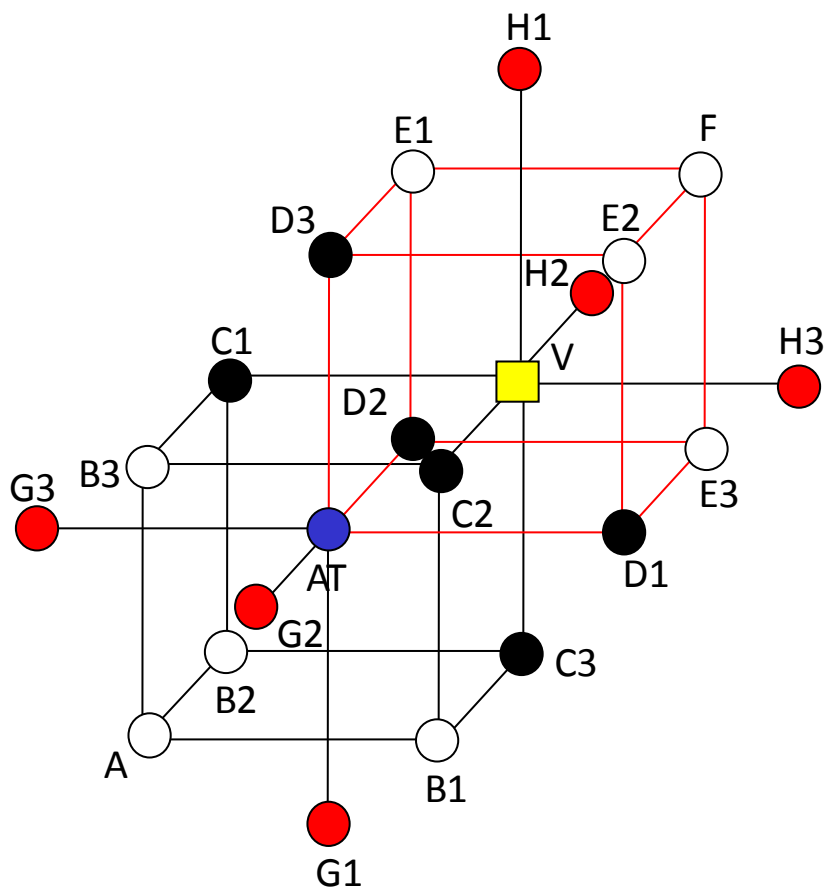


Figure 1-A1 Local chemical environment structure scheme and sites nomenclature.

AT: migrating atom

V: vacancy

Black spheres: atom windows the vacancy goes through along migration path (first window: C1, C2, C3. Second window: D1, D2, D3).

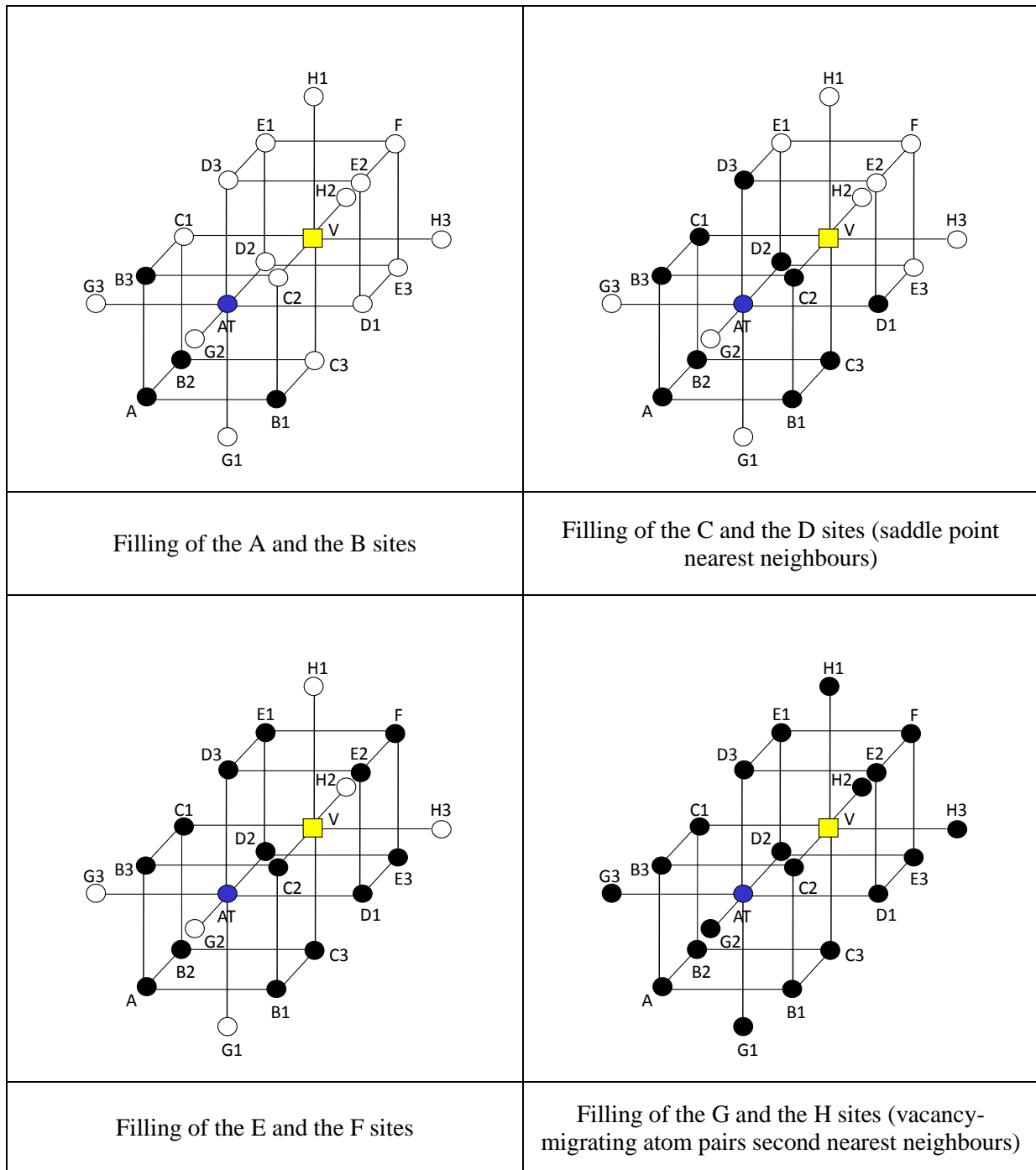


Figure 2-A 1 Scheme of the progressive filling of the vacancy-migrating atom pair local atomic environment with chromium atoms.

ANNEX 2: VACANCY MIGRATION ENERGIES FOR ALL SADDLE POINT CONFIGURATIONS

Tables 1-A2, 3-A2, 5-A2, 7-A2, 9-A2, and 11-A2 contain the vacancy migration energies computed for all possible atomic configurations of saddle point nearest neighbour shell (*i.e.* all possible atomic configurations for the sites C1, C2, C3, D1, D2, D3). All the other sites of the matrix are occupied by iron atoms.

Tables 2-A2, 4-A2, 6-A2, 8-A2, and 10-A2 contains the average between the forward and backward vacancy migration energy for each atomic configuration of saddle point nearest neighbour shell.

All calculations have been performed in the framework of DFT with the NEB approach by implementing the climbing image algorithm (NEB-CI).

Simulation box size: $5a_0 \times 5a_0 \times 5a_0$ ($a_0 = 2.831 \text{ \AA}$)

$E_{\text{cut-off}} = 300 \text{ eV}$

k-points mesh: $2 \times 2 \times 2$

Number of images: 3

1 Cr ATOM AMONG THE MIGRATING ATOM SADDLE POINT POSITION NEAREST NEIGHBOUR SITES:

Lattice sites occupied by a chromium atom	Fe –V migration energy NEB-CI (eV)	Cr –V migration energy NEB-CI (eV)
C1	0.64	0.52
C2	0.64	0.52
C3	0.64	0.52
D1	0.69	0.71
D2	0.69	0.71
D3	0.69	0.71

Table 1-A2 Vacancy-iron and vacancy chromium migration energy for configurations containing one chromium atom among the migrating atom saddle point position first nearest neighbour sites.

Configuration averages of vacancy-iron and vacancy-chromium (1 Cr atom among the migrating atom saddle point position first nearest neighbour sites):

Migration Fe-V: 0.67 eV

Migration Cr-V: 0.62 eV

Average between the forward and backward path of the vacancy-iron and the vacancy-chromium migration energies (1 Cr atom among the migrating atom saddle point position first nearest neighbour sites):

Lattice sites occupied by a chromium atom	Fe –V migration energy NEB-CI (eV)	Cr –V migration energy NEB-CI (eV)
C1	0.67	0.62
C2	0.67	0.62
C3	0.67	0.62
D1	0.67	0.62
D2	0.67	0.62
D3	0.67	0.62

Table 2-A2 Average between the forward and backward vacancy-iron and vacancy-chromium migration energies for each configuration containing one chromium atom among the migrating atom saddle point position first nearest neighbour sites.

2 Cr ATOMS AMONG THE MIGRATING ATOM SADDLE POINT POSITION NEAREST NEIGHBOUR SITES:

Lattice sites occupied by a chromium atom	Fe –V migration energy NEB-CI (eV)	Cr –V migration energy NEB-CI (eV)
C1 C2	0.60	0.53
C1 C3	0.60	0.53
C1 D1	0.66	0.63
C1 D2	0.54	0.60
C1 D3	0.54	0.60
C2 C3	0.60	0.53
C2 D1	0.54	0.60

C2 D2	0.66	0.63
C2 D3	0.54	0.60
C3 D1	0.54	0.60
C3 D2	0.54	0.60
C3 D3	0.66	0.63
D1 D2	0.74	0.91
D1 D3	0.74	0.91
D2 D3	0.74	0.91

Table 3-A2 Vacancy-iron and vacancy chromium migration energy for configurations containing two chromium atoms among the migrating atom saddle point position first nearest neighbour sites.

Configuration averages of vacancy-iron and vacancy-chromium (2 Cr atoms among the migrating atom saddle point position first nearest neighbour sites):

Migration Fe-V: 0.62 eV

Migration Cr-V: 0.65 eV

Average between the forward and backward path of the vacancy-iron and the vacancy-chromium migration energies (2 Cr atoms among the migrating atom saddle point position first nearest neighbour sites):

Lattice sites occupied by a chromium atom	Fe –V migration energy NEB-CI (eV)	Cr –V migration energy NEB-CI (eV)
C1 C2	0.67	0.72
C1 C3	0.67	0.72
C1 D1	0.66	0.63
C1 D2	0.54	0.60
C1 D3	0.54	0.60

C2 C3	0.67	0.72
C2 D1	0.54	0.60
C2 D2	0.66	0.63
C2 D3	0.54	0.60
C3 D1	0.54	0.60
C3 D2	0.54	0.60
C3 D3	0.66	0.63
D1 D2	0.67	0.72
D1 D3	0.67	0.72
D2 D3	0.67	0.72

Table 4-A2 Average between the forward and backward vacancy-iron and vacancy-chromium migration energies for each configuration containing two chromium atoms among the migrating atom saddle point position first nearest neighbour sites.

3 Cr ATOMS AMONG THE MIGRATING ATOM SADDLE POINT POSITION NEAREST NEIGHBOUR SITES:

Lattice sites occupied by a chromium atom	Fe -V migration energy NEB-CI (eV)	Cr -V migration energy NEB-CI (eV)
C1 C2 C3	0.58	0.67
D1 D2 D3	0.84	1.13
C1 C2 D1	0.52	0.54
C1 C2 D2	0.52	0.54
C1 C2 D3	0.47	0.52
C1 C3 D1	0.53	0.54
C1 C3 D2	0.47	0.52
C1 C3 D3	0.53	0.54
C2 C3 D1	0.47	0.52

C2 C3 D2	0.53	0.54
C2 C3 D3	0.53	0.54
D1 D2 C1	0.62	0.70
D1 D2 C2	0.62	0.70
D1 D2 C3	0.54	0.75
D1 D3 C1	0.62	0.70
D1 D3 C2	0.54	0.75
D1 D3 C3	0.62	0.70
D2 D3 C1	0.54	0.75
D2 D3 C2	0.62	0.70
D2 D3 C3	0.62	0.70

Table 5-A2 Vacancy-iron and vacancy chromium migration energy for configurations containing three chromium atoms among the migrating atom saddle point position first nearest neighbour sites.

Configuration averages of vacancy-iron and vacancy-chromium (3 Cr atoms among the migrating atom saddle point position first nearest neighbour sites):

Migration Fe-V: 0.57 eV

Migration Cr-V: 0.65 eV

Average between the forward and backward path of the vacancy-iron and the vacancy-chromium migration energies (3 Cr atoms among the migrating atom saddle point position first nearest neighbour sites):

Lattice sites occupied by a chromium atom	Fe –V migration energy NEB-CI (eV)	Cr –V migration energy NEB-CI (eV)
C1 C2 C3	0.71	0.90
D1 D2 D3	0.71	0.90

C1 C2 D1	0.57	0.62
C1 C2 D2	0.57	0.62
C1 C2 D3	0.51	0.64
C1 C3 D1	0.58	0.62
C1 C3 D2	0.51	0.64
C1 C3 D3	0.58	0.62
C2 C3 D1	0.51	0.65
C2 C3 D2	0.58	0.62
C2 C3 D3	0.58	0.62
D1 D2 C1	0.57	0.62
D1 D2 C2	0.57	0.62
D1 D2 C3	0.51	0.64
D1 D3 C1	0.58	0.62
D1 D3 C2	0.51	0.64
D1 D3 C3	0.58	0.62
D2 D3 C1	0.51	0.65
D2 D3 C2	0.58	0.62
D2 D3 C3	0.58	0.62

Table 6-A2 Average between the forward and backward vacancy-iron and vacancy-chromium migration energies for each configuration containing three chromium atoms among the migrating atom saddle point position first nearest neighbour sites.

**4 Cr ATOMS AMONG THE MIGRATING ATOM SADDLE POINT POSITION
NEAREST NEIGHBOUR SITES:**

Lattice sites occupied by a chromium atom	Fe –V migration energy NEB-CI (eV)	Cr –V migration energy NEB-CI (eV)
C3 D1 D2 D3	0.65	0.75
C2 D1 D2 D3	0.65	0.75
C2 C3 D2 D3	0.53	0.53
C2 C3 D1 D3	0.52	0.52
C2 C3 D1 D2	0.52	0.52
C1 D1 D2 D3	0.65	0.75
C1 C3 D2 D3	0.52	0.52
C1 C3 D1 D3	0.53	0.53
C1 C3 D1 D2	0.52	0.52
C1 C2 D2 D3	0.52	0.52
C1 C2 D1 D3	0.52	0.52
C1 C2 D1 D2	0.53	0.53
C1 C2 C3 D3	0.46	0.43
C1 C2 C3 D2	0.46	0.43
C1 C2 C3 D1	0.46	0.43

Table 7-A2 Vacancy-iron and vacancy chromium migration energy for configurations containing four chromium atoms among the migrating atom saddle point position first nearest neighbour sites.

Configuration averages of vacancy-iron and vacancy-chromium (4 Cr atoms among the migrating atom saddle point position first nearest neighbour sites):

Migration Fe-V: 0.54 eV

Migration Cr-V: 0.55 eV

Average between the forward and backward path of the vacancy-iron and the vacancy-chromium migration energies (4 Cr atoms among the migrating atom saddle point position first nearest neighbour sites):

Lattice sites occupied by a chromium atom	Fe –V migration energy NEB-CI (eV)	Cr –V migration energy NEB-CI (eV)
C3 D1 D2 D3	0.56	0.59
C2 D1 D2 D3	0.56	0.59
C2 C3 D2 D3	0.53	0.53
C2 C3 D1 D3	0.52	0.52
C2 C3 D1 D2	0.52	0.52
C1 D1 D2 D3	0.56	0.59
C1 C3 D2 D3	0.52	0.52
C1 C3 D1 D3	0.53	0.53
C1 C3 D1 D2	0.52	0.52
C1 C2 D2 D3	0.52	0.52
C1 C2 D1 D3	0.52	0.52
C1 C2 D1 D2	0.53	0.53
C1 C2 C3 D3	0.56	0.59
C1 C2 C3 D2	0.56	0.59
C1 C2 C3 D1	0.56	0.59

Table 8-A2 Average between the forward and backward vacancy-iron and vacancy-chromium migration energies for each configuration containing four chromium atoms among the migrating atom saddle point position first nearest neighbour sites.

**5 Cr ATOMS AMONG THE MIGRATING ATOM SADDLE POINT POSITION
NEAREST NEIGHBOUR SITES:**

Lattice sites occupied by a chromium atom	Fe –V migration energy NEB-CI (eV)	Cr –V migration energy NEB-CI (eV)
C2C3D1D2D3	0.61	0.59
C1C3D1D2D3	0.61	0.59
C1C2D1D2D3	0.61	0.59
C1C2C3D2D3	0.51	0.42
C1C2C3D1D3	0.51	0.42
C1C2C3D1D2	0.51	0.42

Table 9-A2 Vacancy-iron and vacancy chromium migration energy for configurations containing five chromium atoms among the migrating atom saddle point position first nearest neighbour sites.

Configuration averages of vacancy-iron and vacancy-chromium (5 Cr atoms among the migrating atom saddle point position first nearest neighbour sites):

Migration Fe-V: 0.56 eV

Migration Cr-V: 0.51 eV

Average between the forward and backward path of the vacancy-iron and the vacancy-chromium migration energies (5 Cr atoms among the migrating atom saddle point position first nearest neighbour sites):

Lattice sites occupied by a chromium atom	Fe –V migration energy NEB-CI (eV)	Cr –V migration energy NEB-CI (eV)
C2C3D1D2D3	0.56	0.51
C1C3D1D2D3	0.56	0.51
C1C2D1D2D3	0.56	0.51
C1C2C3D2D3	0.56	0.51

C1C2C3D1D3	0.56	0.51
C1C2C3D1D2	0.56	0.51

Table 10-A2 Average between the forward and backward vacancy-iron and vacancy-chromium migration energies for each configuration containing five chromium atoms among the migrating atom saddle point position first nearest neighbour sites.

6 Cr ATOMS AMONG THE MIGRATING ATOM SADDLE POINT POSITION NEAREST NEIGHBOUR SITES:

Lattice sites occupied by a chromium atom	Fe –V migration energy NEB-CI (eV)	Cr –V migration energy NEB-CI (eV)
C1C2C3D1D2D3	0.61	0.52

Table 11-A2 Vacancy-iron and vacancy chromium migration energy for configurations containing six chromium atoms among the migrating atom saddle point position first nearest neighbour sites.

ANNEX 3: VACANCY MIGRATION ENERGIES FOR DIFFERENT CONFIGURATIONS OF THE LOCAL ATOMIC ENVIRONMENT

Table 1-A3 and table 2-A3 contain the vacancy migration energies as well as ΔE for all configurations of the local atomic environment that we considered in this work. Table 1-A3 concerns the vacancy-iron exchange, whereas table 2-A3 concerns the vacancy-chromium exchange. Configurations in yellow are those for which at least a chromium atom is located in the saddle point local atomic environment (*i.e.* in the C or D sites). The calculations have been performed within the DFT using the NEB method, within the EAM potential using the drag method (DM), and using our different implementations of the FISE approximation.

DFT-NEB calculations:

Simulation box size: $5a_0 \times 5a_0 \times 5a_0$ ($a_0 = 2.831 \text{ \AA}$)

$E_{\text{cut-off}} = 300 \text{ eV}$

k-points mesh: $2 \times 2 \times 2$

Number of images: 3

EAM-DM calculations:

Simulation box size: $8a_0 \times 8a_0 \times 8a_0$ ($a_0 = 2.8553 \text{ \AA}$)

Discretisation step: 0.04 \AA

VACANCY-IRON MIGRATION ENERGIES:

Lattice sites occupied by a chromium atom	DFT-NEB (eV)	EAM-DM (eV)	ΔE (DFT) (eV)	ΔE (EAM) (eV)	FISE 1 (ΔE : DFT) (eV)	FISE 2 (ΔE : DFT) (eV)	FISE 3 (ΔE : DFT) (eV)	FISE 1 (ΔE : EAM) (eV)	FISE 2 (ΔE : EAM) (eV)	FISE 3 (ΔE : EAM) (eV)
C1, C2	0.60	0.63	-0.13	-0.04	0.65	0.56	0.61	0.69	0.60	0.65
D1, D2	0.74	0.67	0.13	0.04	0.78	0.69	0.74	0.73	0.64	0.69
C1, D2	0.54	0.63	0.00	0.00	0.71	0.62	0.54	0.71	0.62	0.54
C1, D1	0.66	0.64	0.00	0.00	0.71	0.62	0.66	0.71	0.62	0.66
D1, D2, D3	0.84	0.69	0.26	0.05	0.84	0.70	0.84	0.74	0.60	0.74
C1, C2, C3	0.58	0.63	-0.26	-0.05	0.58	0.44	0.58	0.69	0.55	0.69
C1, C2, D1	0.52	0.64	-0.09	-0.02	0.67	0.53	0.53	0.70	0.56	0.56
C1, C2, D3	0.47	0.63	-0.07	-0.03	0.68	0.54	0.48	0.70	0.56	0.50
C1, C3, D1	0.53	0.64	-0.09	-0.02	0.67	0.53	0.54	0.70	0.56	0.57
D1, D2, C1	0.62	0.66	0.09	0.02	0.76	0.62	0.62	0.72	0.58	0.58
D1, D2, C3	0.54	0.66	0.07	0.03	0.75	0.61	0.55	0.73	0.59	0.53
E1	0.69	0.58	0.06	-0.02	0.74	0.74	0.74	0.70	0.70	0.70

E1, E2	0.68	0.56	0.14	-0.03	0.78	0.78	0.78	0.70	0.70	0.70
E1, E2, E3	0.68	0.54	0.26	-0.04	0.84	0.84	0.84	0.69	0.69	0.69
E1, E2, E3, F	0.68	0.50	0.29	-0.01	0.86	0.86	0.86	0.71	0.71	0.71
E1, E2, E3, F, H1	0.64	0.48	0.19	-0.03	0.81	0.81	0.81	0.70	0.70	0.70
E1, E2, E3, F, H1, H2	0.62	0.49	0.09	-0.05	0.76	0.76	0.76	0.69	0.69	0.69
E1, E2, E3, F, H1, H2, H3	0.60	0.50	0.01	-0.07	0.72	0.72	0.72	0.68	0.68	0.68
B1	0.63	0.61	-0.06	0.02	0.68	0.68	0.68	0.72	0.72	0.72
C1	0.64	0.63	-0.05	-0.03	0.69	0.65	0.65	0.70	0.66	0.66
D1	0.69	0.65	0.05	0.03	0.74	0.70	0.70	0.73	0.69	0.69
F	0.67	0.64	0.03	-0.01	0.73	0.73	0.73	0.71	0.71	0.71
A, F	0.62	0.60	0.00	0.00	0.71	0.71	0.71	0.71	0.71	0.71
C3, D3	0.66	0.64	0.00	0.00	0.71	0.62	0.66	0.71	0.62	0.66
A	0.64	0.66	-0.03	0.01	0.70	0.70	0.70	0.72	0.72	0.72
A, B1	0.58	0.57	-0.09	0.01	0.67	0.67	0.67	0.72	0.72	0.72
A, B1, B2	0.50	0.53	-0.17	0.01	0.63	0.63	0.63	0.72	0.72	0.72

A, B1, B2, B3	0.39	0.51	-0.30	0.01	0.56	0.56	0.56	0.72	0.72	0.72
A, B1, B2, B3, C1	0.30	0.49	-0.43	-0.06	0.50	0.46	0.46	0.68	0.64	0.64
A, B1, B2, B3, C1, C2	0.31	0.47	-0.50	-0.12	0.46	0.37	0.42	0.65	0.56	0.61
A, B1, B2, B3, C1, C2, C3	0.48	0.46	-0.42	-0.18	0.50	0.36	0.50	0.62	0.48	0.62
A, B1, B2, B3, C1, C2, C3, D1	0.46	0.47	-0.36	-0.17	0.53	0.36	0.38	0.63	0.46	0.48
A, B1, B2, B3, C1, C2, C3, D1, D2	0.46	0.48	-0.30	-0.16	0.56	0.41	0.41	0.63	0.48	0.48
A, B1, B2, B3, C1, C2, C3, D1, D2, D3	0.51	0.49	-0.22	-0.15	0.60	0.50	0.50	0.64	0.54	0.54
A, B1, B2, B3, C1, C2, C3, D1, D2, D3, E1	0.49	0.42	-0.12	-0.12	0.65	0.55	0.55	0.65	0.55	0.55
A, B1, B2, B3, C1, C2, C3, D1, D2, D3, E1, E2	0.50	0.36	-0.01	-0.08	0.71	0.61	0.61	0.67	0.57	0.57
A, B1, B2, B3, C1, C2, C3, D1, D2, D3, E1, E2, E3	0.50	0.36	0.03	-0.05	0.73	0.63	0.63	0.69	0.59	0.59

A, B1, B2, B3, C1, C2, C3, D1, D2, D3, E1, E2, E3, F	0.49	0.33	0.00	0.00	0.71	0.61	0.61	0.71	0.61	0.61
A, B1, B2, B3, C1, C2, C3, D1, D2, D3, E1, E2, E3, F, G1	0.55	0.35	0.06	0.02	0.74	0.64	0.64	0.72	0.62	0.62
A, B1, B2, B3, C1, C2, C3, D1, D2, D3, E1, E2, E3, F, G1, G2	0.61	0.38	0.12	0.04	0.77	0.67	0.67	0.73	0.63	0.63
A, B1, B2, B3, C1, C2, C3, D1, D2, D3, E1, E2, E3, F, G1, G2, G3	0.65	0.41	0.17	0.05	0.80	0.70	0.70	0.74	0.64	0.64
A, B1, B2, B3, C1, C2, C3, D1, D2, D3, E1, E2, E3, F, G1, G2, G3, H1	0.68	0.39	0.11	0.04	0.77	0.67	0.67	0.73	0.63	0.63
A, B1, B2, B3, C1, C2, C3, D1, D2, D3, E1, E2, E3, F, G1, G2, G3, H1, H2	0.69	0.39	0.05	0.02	0.74	0.64	0.64	0.72	0.62	0.62

A, B1, B2, B3, C1, C2, C3, D1, D2, D3, E1, E2, E3, F, G1, G2, G3, H1, H2, H3	0.67	0.39	0.00	0.00	0.71	0.61	0.61	0.71	0.61	0.61
C1, C2, C3, D1	0.46	0.64	-0.19	-0.04	0.62	0.45	0.47	0.69	0.52	0.54
C1, D1, D2, D3	0.65	0.68	0.19	0.04	0.81	0.64	0.66	0.73	0.56	0.58
C1, C2, D1, D2	0.53	0.65	0.00	0.00	0.71	0.54	0.53	0.71	0.54	0.53
C2, C3, D1, D3	0.52	0.64	0.00	0.00	0.71	0.54	0.52	0.71	0.54	0.52
C1, C2, C3, D1, D2	0.51	0.65	-0.10	-0.02	0.66	0.51	0.51	0.70	0.55	0.55
D1, D2, D3, C1, C2	0.61	0.67	0.10	0.02	0.76	0.61	0.61	0.72	0.57	0.57
C1, C2, C3, D1, D2, D3	0.61	0.66	0.00	0.00	0.71	0.61	0.61	0.71	0.61	0.61

Table 1-A3 Vacancy-iron migration energies and ΔE for different configurations of the local atomic environment. Configurations in yellow are those for which at least a chromium atom is located in the saddle point local atomic environment (*i.e.* in the C or D sites).

VACANCY-CHROMIUM MIGRATION ENERGIES:

Lattice sites occupied by a chromium atom	DFT-NEB (eV)	EAM-DM (eV)	ΔE (DFT) (eV)	ΔE (EAM) (eV)	FISE 1 (ΔE : DFT) (eV)	FISE 2 (ΔE : DFT) (eV)	FISE 3 (ΔE : DFT) (eV)	FISE 2 (ΔE : EAM) (eV)	FISE 3 (ΔE : EAM) (eV)	FISE 1 (ΔE : EAM) (eV)
C1, C2	0.53	0.58	-0.37	-0.08	0.36	0.47	0.54	0.61	0.68	0.50
D1, D2	0.91	0.67	0.37	0.08	0.73	0.84	0.91	0.69	0.76	0.58
C1, D2	0.60	0.61	0.00	0.00	0.54	0.65	0.60	0.65	0.60	0.54
C1, D1	0.63	0.64	0.00	0.00	0.54	0.65	0.63	0.65	0.63	0.54
D1, D2, D3	1.13	0.68	0.46	0.10	0.77	0.88	1.13	0.70	0.95	0.59
C1, C2, C3	0.67	0.58	-0.46	-0.10	0.31	0.42	0.67	0.60	0.85	0.49
C1, C2, D1	0.54	0.62	-0.16	-0.03	0.46	0.57	0.54	0.64	0.61	0.53
C1, C2, D3	0.52	0.59	-0.22	-0.05	0.43	0.54	0.53	0.63	0.62	0.52
C1, C3, D1	0.54	0.62	-0.16	-0.03	0.46	0.57	0.54	0.64	0.61	0.53
D1, D2, C1	0.70	0.65	0.16	0.03	0.62	0.73	0.70	0.67	0.64	0.56
D1, D2, C3	0.75	0.64	0.22	0.05	0.65	0.76	0.75	0.68	0.67	0.57
E1	0.57	0.55	0.26	0.05	0.67	0.67	0.67	0.57	0.57	0.57

E1, E2	0.64	0.52	0.54	0.03	0.81	0.81	0.81	0.56	0.56	0.56
E1, E2, E3	0.83	0.54	0.81	-0.02	0.95	0.95	0.95	0.53	0.53	0.53
E1, E2, E3, F	0.85	0.54	0.63	-0.08	0.86	0.86	0.86	0.50	0.50	0.50
E1, E2, E3, F, H1	0.66	0.55	0.45	-0.14	0.77	0.77	0.77	0.47	0.47	0.47
E1, E2, E3, F, H1, H2	0.58	0.58	0.29	-0.20	0.69	0.69	0.69	0.44	0.44	0.44
E1, E2, E3, F, H1, H2, H3	0.54	0.61	0.15	-0.27	0.62	0.62	0.62	0.41	0.41	0.41
B1	0.31	0.50	-0.26	-0.05	0.41	0.41	0.41	0.52	0.52	0.52
C1	0.52	0.58	-0.19	-0.05	0.45	0.53	0.53	0.60	0.60	0.52
D1	0.71	0.63	0.19	0.05	0.64	0.72	0.72	0.65	0.65	0.57
F	0.52	0.71	0.31	0.14	0.70	0.70	0.70	0.61	0.61	0.61
A, F	0.21	0.70	0.00	0.00	0.54	0.54	0.54	0.54	0.54	0.54
A	0.21	0.57	-0.31	-0.14	0.39	0.39	0.39	0.47	0.47	0.47
A, B1	0.13	0.57	-0.46	-0.07	0.31	0.31	0.31	0.51	0.51	0.51
A, B1, B2	0.14	0.57	-0.56	0.00	0.26	0.26	0.26	0.54	0.54	0.54

A, B1, B2, B3	0.23	0.62	-0.63	0.08	0.23	0.23	0.23	0.58	0.58	0.58
A, B1, B2, B3, C1	0.49	0.61	-0.45	0.08	0.32	0.40	0.40	0.66	0.66	0.58
A, B1, B2, B3, C1, C2	0.64	0.59	-0.34	0.08	0.37	0.48	0.55	0.69	0.76	0.58
A, B1, B2, B3, C1, C2, C3	0.82	0.57	-0.27	0.07	0.41	0.52	0.77	0.69	0.94	0.58
A, B1, B2, B3, C1, C2, C3, D1	0.61	0.60	-0.32	0.11	0.38	0.39	0.43	0.61	0.65	0.60
A, B1, B2, B3, C1, C2, C3, D1, D2	0.57	0.62	-0.33	0.14	0.38	0.35	0.35	0.58	0.58	0.61
A, B1, B2, B3, C1, C2, C3, D1, D2, D3	0.55	0.65	-0.29	0.16	0.40	0.38	0.38	0.60	0.60	0.62
A, B1, B2, B3, C1, C2, C3, D1, D2, D3, E1	0.59	0.57	-0.22	0.13	0.43	0.41	0.41	0.59	0.59	0.61
A, B1, B2, B3, C1, C2, C3, D1, D2, D3, E1, E2	0.63	0.48	-0.14	0.08	0.47	0.45	0.45	0.56	0.56	0.58
A, B1, B2, B3, C1, C2, C3, D1, D2, D3, E1, E2, E3	0.67	0.42	-0.06	0.04	0.51	0.49	0.49	0.54	0.54	0.56

A, B1, B2, B3, C1, C2, C3, D1, D2, D3, E1, E2, E3, F	0.63	0.43	0.00	0.00	0.54	0.52	0.52	0.52	0.52	0.54
A, B1, B2, B3, C1, C2, C3, D1, D2, D3, E1, E2, E3, F, G1	0.80	0.53	0.13	0.06	0.61	0.59	0.59	0.55	0.55	0.57
A, B1, B2, B3, C1, C2, C3, D1, D2, D3, E1, E2, E3, F, G1, G2	0.92	0.64	0.25	0.13	0.67	0.65	0.65	0.59	0.59	0.61
A, B1, B2, B3, C1, C2, C3, D1, D2, D3, E1, E2, E3, F, G1, G2, G3	1.03	0.75	0.35	0.19	0.72	0.70	0.70	0.62	0.62	0.64
A, B1, B2, B3, C1, C2, C3, D1, D2, D3, E1, E2, E3, F, G1, G2, G3, H1	0.90	0.75	0.22	0.13	0.65	0.63	0.63	0.59	0.59	0.61
A, B1, B2, B3, C1, C2, C3, D1, D2, D3, E1, E2, E3, F, G1, G2, G3, H1, H2	0.80	0.76	0.11	0.06	0.60	0.58	0.58	0.55	0.55	0.57

A, B1, B2, B3, C1, C2, C3, D1, D2, D3, E1, E2, E3, F, G1, G2, G3, H1, H2, H3	0.73	0.77	0.00	0.00	0.54	0.52	0.52	0.52	0.52	0.54
C1, C2, C3, D1	0.43	0.61	-0.31	-0.06	0.39	0.40	0.44	0.52	0.56	0.51
C1, D1, D2, D3	0.75	0.67	0.31	0.06	0.70	0.71	0.75	0.58	0.62	0.57
C1, C2, D1, D2	0.53	0.64	0.00	0.00	0.54	0.55	0.53	0.55	0.53	0.54
C2, C3, D1, D3	0.52	0.63	0.00	0.00	0.54	0.55	0.52	0.55	0.52	0.54
C1, C2, C3, D1, D2	0.42	0.62	-0.17	-0.03	0.46	0.43	0.43	0.50	0.50	0.53
D1, D2, D3, C1, C2	0.59	0.66	0.17	0.03	0.63	0.60	0.60	0.53	0.53	0.56
C1, C2, C3, D1, D2, D3	0.52	0.64	0.00	0.00	0.54	0.52	0.52	0.52	0.52	0.54

Table 2-A3 Vacancy-chromium migration energies and ΔE for different configurations of the local atomic environment. Configurations in yellow are those for which at least a chromium atom is located in the saddle point local atomic environment (*i.e.* in the C or D sites).

BIBLIOGRAPHY

[Abromeit2000] C. Abromeit, H. Wollenberg, S. Matsumura, C. Kinoshita, *Stability of ordered phases under irradiation*, Journal of Nuclear Materials, **276**, 104 (2000).

[Ackland1997] G. J. Ackland, D. J. Bacon, A. F. Calder, T. Harry, *Computer simulation of point defect properties in Fe-Cu alloy using a many-body interatomic potential*, Philosophical Magazine A, **75**, 713 (1997).

[Ackland2003] G. J. Ackland, S. K. Reed, “*Two-band second moment mode land an interatomic potential for caesium*”, Physical Review B, **67**, 174108 (2003).

[Aldred1976a] A. T. Aldred, *Ferromagnetism in iron-chromium alloys. I. Bulk magnetisation measurements*, Physical Review B, **14**, 219 (1976).

[Aldred1976b] A. T. Aldred, B. D. Rainford, J. S. Kouvel, T. J. Hicks, *Ferromagnetism in iron-chromium alloys. II. Neutron scattering studies*, Physical Review B, **14**, 228 (1976).

[Andersen2000] O. K. Andersen, T. Saha-Dasgupta, *Muffin-tin orbitals of arbitrary order*, Physical Review B, **62**, 16219 (2000).

[Andersson1987] J. O. Anderson, B. Sundman, *Thermodynamic properties of the Fe-Cr system*, CALPHAD, **11**, 83 (1987).

[Arakawa2004] K. Arakawa, M. Hatanaka, H. Mori, K. Ono, *Effects of chromium on the one-dimensional motion of interstitial-type dislocation loops in iron*, Journal of Nuclear Materials, **329**, 1194 (2004).

[Ashcroft1976] N. W. Ashcroft, N. D. Mermin, *Solid State Physics*, Saunders College Publishing (New York, 1976) , chapter 8.

- [Auger2011] M. A. Auger, T. Leguey, A. Muñoz, M. A. Monge, V. de Castro, P. Fernández, G. Garcés, R. Pareja, *Microstructure and mechanical properties of ultrafine-grained Fe-14Cr and ODS Fe-14Cr model alloys*, Journal of Nuclear Materials (2011).
- [Baïlon2007] J.-P. Baïlon, Jean-Marie Dorlot, *Des Matériaux*, Presses Internationales Polytechnique, troisième édition (2007).
- [Barbu2008] A. Barbu, *Modelling of long term kinetic evolution: a fruitful relationship between experiment and theoretical development*, Comptes Rendus Physique, **9**, 353 (2008).
- [Becquart1997] C. S. Becquart, K. M. Decker, C. Domain, J. Ruste, Y. Souffez, J. C. Turbatte, J. C. van Duysen, *Massively parallel molecular dynamics simulations with EAM potentials*, Radiation Effects and Defects in Solids, **142**, 9 (1997).
- [Becquart2009] C. S. Becquart, and C. Domain, *Introducing chemistry in atomistic kinetic Monte Carlo simulations of Fe alloys under irradiation*, Physica Status Solidi B, 1 (2009).
- [Bergner2009] F. Bergner, A. Ulbricht, C. Heintze, *Estimation of the solubility limit of Cr in Fe at 300°C from small-angle neutron scattering in neutron-irradiated Fe-Cr alloys*, Scripta Materialia, **61**, 1060 (2009).
- [Binder2001] *Phase Transformations in Materials*, Gernot Kostorz (editor), chapter 6, K. Binder and P. Fratzl, *Spinodal Decomposition* (Weinheim 2001).
- [Bley1992] F. Bley, *Neutron small-angle scattering study of unmixing in Fe-Cr alloys*, Acta Metallurgica et Materialia, **40**, 1505 (1992).
- [Bloch1928] F. Bloch, *Über die Quantenmechaniken der Elektronen in Kristallgittern*, Zeitschrift für Physik, **52**, 555 (1928).
- [Blöchl1994] P. E. Blöchl, *Projector augmented-wave method*, Physical Review B, **50**, 17953 (1994).

[Bonnet1990] S. Bonnet, J. Bourgoïn, J. Champredonde, D. Guttman, M. Guttman, *Relationship between evolution of mechanical properties of various cast duplex stainless steels and metallurgical and aging parameters: outline of current EDF programs*, Materials Science and Technology, **6**, 221 (1990).

[Bonny2007] G. Bonny, D. Terentyev, L. Malerba, *Identification and characterization of Cr-rich precipitates in FeCr alloys: An atomistic study*, Computational Materials Science, **42**, 107 (2007).

[Bonny2008] G. Bonny, D. Terentyev and L. Malerba, *On the α - α' miscibility gap of Fe-Cr alloys*, Scripta Materialia, **59**, 1193 (2008).

[Bonny2009a] G. Bonny, D. Terentyev, L. Malerba, *The hardening of iron-chromium alloys under thermal ageing: An atomistic study*, Journal of Nuclear Materials, **385**, 278 (2009).

[Bonny2009b] G. Bonny, R. C. Pasianot, L. Malerba, A. Caro, P. Olsson, M. Yu. Lavrentiev, *Numerical prediction of thermodynamic properties of iron-chromium alloys using semi-empirical cohesive models: The state of the art*, Journal of Nuclear Materials, **385**, 268 (2009).

[Bonny2009c] G. Bonny, D. Terentyev, L. Malerba, D. Van Neck, *Early stages of α - α' phase separation in Fe-Cr alloys: An atomistic study*, Physical Review B, **79**, 10407 (2009).

[Bonny2010] G. Bonny, D. Terentyev, L. Malerba, *New Contribution to the Thermodynamics of Fe-Cr Alloys as Base for Ferritic Steels*, Journal of Phase Equilibria and Diffusion, **31**, 439 (2010).

[Bonny2011a] G. Bonny, R.C. Pasianot, D. Terentyev, L. Malerba, *Iron chromium potential to model high-chromium ferritic steels*, Philosophical Magazine, **91**, 1724 (2011).

[Bonny2011b] G. Bonny, R. C. Pasianot, E. E. Zhurkin, M. Hou, *Determination of the phase diagram from interatomic potentials: The iron-chromium case*, Computational Material Science, **50**, 2216 (2011).

[Bonny2011c] G. Bonny, R.C. Pasianot, D. Terentyev, and L. Malerba, *Interatomic Potential to Simulate Radiation Damage in Fe-Cr Alloys*, Open Report SCK-CEN-BLG-1077 (2011).

[Bortz1975] A. B. Bortz, M. H. Kalos, and J. L. Lebowitz, *A New algorithm for Monte Carlo Simulation of Ising Spin Systems*, Journal of Computational Physics, **17**, 10 (1975).

[Burke2007] K. Burke, *The ABC of DFT* (University of California, Irvine, 2007).

[Cahn1958] J. W. Cahn, J. E. Hilliard, *Free Energy of Nonuniform System. I. Interfacial Free Energy*, The Journal of Chemical Physics, **28**, 258 (1958).

[Cahn1959a] J. W. Cahn, *Free Energy of Nonuniform System. II. Thermodynamic Basis*, The Journal of Chemical Physics, **30**, 1121 (1959).

[Cahn1959b] J. W. Cahn, J. E. Hilliard, *Free Energy of Nonuniform System. III. Nucleation in a Two-Component Incompressible Fluid*, The Journal of Chemical Physics, **31**, 688 (1959).

[Cahn1961] J. W. Cahn, *On Spinodal Decomposition*, Acta Metallurgica, **9**, 795 (1961).

[Cahn1965] J. W. Cahn, *Phase Separation by Spinodal Decomposition in Isotropic Systems*, The Journal of Chemical Physics, **42**, 93 (1965).

[Caro2005] A. Caro, D. A. Crowson, and M. Caro, *Classical Many-Body Potential for Concentrated Alloys and the Inversion of Order in Iron-Chromium Alloys*, Physical Review Letters, **95**, 075702 (2005).

[Castin2010] N. Castin, L. Malerba, *Calculation of proper energy barriers for atomistic kinetic Monte Carlo simulations on rigid lattice with chemical and strain field long-range effects using artificial neural networks*, The Journal of Chemical Physics, **132**, 074507 (2010).

[Castin2011] N. Castin, G. Bonny, D. Terentyev, M. Yu Lavrentiev, D. Nguyen-Manh, *Modelling phase separation in Fe-Cr system using different atomistic kinetic Monte Carlo techniques*, Journal of Nuclear Materials, 417, 1086 (2011).

[Chen2001] Q. Chen, B. Sundman, *Modeling of thermodynamic properties for BCC, FCC, liquid, and amorphous iron*, J. Phase Equilib. **22**, 631 (2001).

[Clouet2010] E. Clouet, F. Soisson, *Atomic simulations of diffusional phase transformations*, Comptes Rendus Physique, **11**, 226 (2010).

[Cook1970] H. E. Cook, *Brownian Motion in Spinodal Decomposition*, Acta Metallurgica, **18**, 297 (1970).

[Corliss1959] L. M. Corliss, J. M. Hastings, R. J. Weiss, *Antiphase antiferromagnetic structure of chromium*, Physical Review Letters, **3**, 211 (1959).

[Cowley1950] J. M. Cowley, *An Approximate Theory of Order in Alloys*, Physical Review, **77**, 669 (1950).

[Danoix2000] F. Danoix, P. Auger, *Atom probe studies of the Fe-Cr system and stainless steels aged at intermediate temperatures*, Materials Characterization, **44**, 177 (2000).

[Daw1984] M. S. Daw, M. I. Baskes, *Embedded-atom method : Derivation and application to impurities, surfaces and other defects in metals*, Physical Review B, **29**, 6443 (1984).

[DeNault2007] K. J. De Nault, *The 230 Space Groups*, Department of Earth Science, University of Northern Iowa (2007).

[DeSchepper1983] L. De Schepper, D. Segers, L. Dorikens-Vanpraet, M. Dorikens, G. Knuyt, L. M. Stals, P. Moser, *Positron annihilation on pure and carbon-doped α -iron in thermal equilibrium*, Physical Review B, **27**, 5257 (1983).

[Domain2001] C. Domain, C. S. Becquart, *Ab initio calculations of defects in Fe and dilute Fe-Cu alloys*, Physical Review B, **65**, 024103 (2001).

[Dubiel1987] S. M. Dubiel, G. Inden, *On the miscibility gap in the Fe-Cr system: A Mössbauer study on long term annealed alloys*, Zeitschrift für Metallkunde, **78**, 544 (1987).

[Dubiel2011] S. M. Dubiel, J. Cieslak, *Short-range order in iron-rich Fe-Cr alloys as revealed by Mössbauer spectroscopy*, Physical Review B, 83, 180202 (2011).

[Dudarev2009] S. L. Dudarev, J. L. Boutard, R. Lässer, M. J. Caturla, P. M. Derlet, M. Fivel, C. C. Fu, M. Y. Lavrentiev, L. Malerba, M. Mrovec, D. Nguyen-Manh, K. Nordlund, M. Perlado, R. Schäublin, H. Van Swygenhoven, D. Terentyev, J. Wallenius, D. Weygand, F. Willaime, *The EU programme for modeling radiation effects in fusion reactor materials: An overview of recent advances and future goals*, Journal of Nuclear Materials, **386**, 1 (2009).

[Erhart2008] P. Erhart, A. Caro, M. Serrano de Caro, B. Sadigh, *Short-range order and precipitation in Fe-rich Fe-Cr alloys: Atomistic off-lattice Monte Carlo simulations*, Physical Review B, **77**, 134206 (2008).

[Fawcett1988] E. Fawcett, *Spin-density-wave antiferromagnetism in chromium*, Reviews of Modern Physics, **60**, 209 (1988).

[Fichtorn1991] K. A. Fichtorn, W. H. Weinberg, *Theoretical foundations of dynamical Monte Carlo simulations*, Journal of Chemical Physics, **95**, 1090 (1991).

[Filippova2000] N. P. Filippova, V. A. Shabashov, and A. L. Nikolaev, *Mössbauer study of irradiation-accelerated short-range ordering in binary Fe-Cr alloys*, Phys. Met. Metallogr. **90**, 140 (2000).

[Fry2002] A. Fry, S. Osgerby, M. Wright, *Oxidation of alloys in steam environment – a review*, National Physics Laboratory Report, NPL MATC(A)90 (2002).

[Garner2000] F. A. Garner, M. B. Toloczko, B. H. Sencer, *Comparison of swelling and irradiation creep behavior of fcc-austenitic and bcc-ferritic/martensitic alloys at high neutron exposure*, Journal of Nuclear Materials, **276**, 123 (2000).

[Gelles1982] D. S. Gelles, *Microstructural examination of neutron-irradiated simple ferritic alloys*, Journal of Nuclear Materials, **108 & 109**, 515 (1982).

[Gelles2000] D. S. Gelles, *On quantification of helium embrittlement in ferritic/martensitic steels*, Journal of Nuclear Materials, **283**, 838 (2000).

[Gendrot1999] G. Benzdikian Gendrot, J.-P. Massoud, S. Jayet, H. Churier-Bossennec, C. Faïdy, P. Le Delliou, *Life evaluation of cast duplex stainless steel elbows in french PWR NPP*, 7th International Conference on Nuclear Engineering, Tokyo, Japan, April 19-23 (1999), ICONE – 7320.

[Geng2003] W. T. Geng, *Cr segregation at the fe-Cr surface: A first-principles GGA investigation*, Physical Review B, **68**, 233402 (2003).

[Grobner1973] P. J. Grobner, *The 885°F (475°C) embrittlement of ferritic stainless steels*, Metallurgical and Materials Transactions B, **4**, 251 (1973).

[Gyorffy1972] B. L. Gyorffy, *Coherent-Potential Approximation for a Nonoverlapping-Muffin-Tin-Potential Model of Random Substitutional Alloys*, Physical Review B, **5**, 2382 (1972).

[Hafner2001] R. Hafner, D. Spišák, R. Lorenz, J. Hafner, *Does density-functional theory predict a spin-density-wave ground state for Cr?*, Journal of Physics: Condensed Matter, **13**, 239 (2001).

[Hafner2002] R. Hafner, D. Spišák, R. Lorenz, J. Hafner, *Magnetic ground state of Cr in density-functional theory*, Physical Review B, **65**, 184432 (2002).

[Hamann1979] D. R. Hamann, M. Schlüter, C. Chiang, *Norm-conserving pseudopotentials*, Physical Review Letters, **43**, 1494 (1979).

[Hättestrand2009] M. Hättestrand, P. Larsson, G. Chai, J.-O. Nilsson, J. Odqvist, *Study of decomposition of ferrite in a duplex stainless steel cold worked and aged at 450-500° C*, Materials Science and Engineering A, **499**, 489 (2009).

[Heintze2011] C. Heintze, F. Bergner, A. Ulbricht, H. Eckerlebe, *The microstructure of neutron-irradiated Fe-Cr alloys: A small-angle neutron scattering study*, **409**, 106 (2011).

[Henkelman2000] G. Henkelman, B. P. Uberuaga, H. Jonsson, *A climbing image nudged elastic band method for finding saddle points and minimum energy paths*, Journal of Chemical Physics, **113**, 9901 (2000).

[Hennion1983] M. Hennion, Chemical SRO effects in ferromagnetic Fe alloys in relation to electronic band structure. Journal of Physics F: Metal Physics, **13**, 2351 (1983).

[Hishinuma1998] A. Hishinuma, A. Kohyama, R. L. Klueh, D. S. Gelles, W. Dietz, K. Ehrlich, *Current Status and future R&D for reduced-activation ferritic/martensitic steels*, Journal of Nuclear Materials, **258**, 193 (1998).

[Hohenberg1964] P. Hohenberg, W. Kohn, *Inhomogeneous electron gas*, Physical Review B, **136** (1964).

[Huse1986] D. A. Huse, *Corrections to late-stage behaviour in spinodal decomposition: Lifshitz-Slyozov scaling and Monte Carlo simulations*, Physical Review B, **34**, 7845 (1986).

[Hyde1995a] J. M. Hyde, M. K. Miller, M. G. Hetherington, A. Cerezo, G. D. W. Smith, C. M. Elliot, *Spinodal decomposition in Fe-Cr alloys: experimental study at the atomic level and comparison with computer models – II. Development of domain size and composition amplitude*, Acta Metallurgica, 43, 3403-3413 (1995).

[Hyde1995b] J. M. Hyde, M. K. Miller, M. G. Hetherington, A. Cerezo, G. D. W. Smith, C. M. Elliot, *Spinodal decomposition in Fe-Cr alloys: experimental study at the atomic level and comparison with computer models – III. Development of morphology*, Acta Metallurgica, 43, 3415-3426 (1995).

[IAEA2010] *Nuclear Power Reactors in the world*, International Atomic Energy Agency, Reference Data Series No. 2 (2010).

[IEA2010] *Key World Energy Statistics*, International Energy Agency (IEA) (2010).

[Jaquet2000] V. Jaquet, PhD thesis, Ecole Polytechnique, Palaiseau (2000).

[Jiang2004] C. Jiang, C. Wolverton, J. Sofo, L.-Q. Chen, Z.-K. Liu, *First-principles study of binary bcc alloys using special quasirandom structures*, Physical Review B, **69**, 214202 (2004).

[Jonsson1998] H. Jonsson, G. Mills, K. W. Jacobsen, *Nudged Elastic Band Method for Finding Minimum energy Paths of Transitions*, Classical and Quantum Dynamics in Condensed Phase Simulation, Ed. B. J. Berne, G. Ciccotti and D. F. Coker, 385 (Proceedings of the International School of Physics “Computer Simulation of Rare Events and the Dynamics of Classical and Quantum Condensed-Phase Systems, Lerici, Italy, World Scientific, 1998).

[Joubert2008] J.-M. Joubert, *Crystal chemistry and Calphad modeling of the σ phase*, Progress in Materials Science, **53**, 528 (2008).

[Kajzar1980] F. Kajzar, G. Parette, *Magnetic-Moment distribution and environmental effects in dilute iron-based alloy with V, Cr, and Mn impurities*, Physical Review B, **22**, 5471 (1980).

[Kang1988] H. C. Kang and W. H. Weinberg, *Dynamical Monte Carlo with a proper energy barrier: Surface diffusion and two-dimensional domain ordering*, Journal of Chemical Physics, **90**, 2824 (1989).

[Kittel1996] C. Kittel, *Introduction to Solid State Physics*, 7th edition (Wiley, New York, 1996).

[Klaver2006] T. P. C. Klaver, R. Drautz, M. W. Finnis, *Magnetism and thermodynamics of defect free Fe-Cr alloys*, Physical Review B, **74**, 094435 (2006).

[Klueh207] R. L. Klueh, A. T. Nelson, *Ferritic/martensitic steels for next-generation reactors*, Journal of Nuclear Materials, **371**, 37 (2007).

[Kohn1965] W. Kohn, L. J. Sham, *Self-consistent equations including exchange and correlation effects*, Physical Review A, **140** (1965).

[Kohyama1996] A. Kohyama, A. Hishinuma, D. S. Gelles, R. L. Klueh, W. Dietz, K. Ehrlich, *Low activation ferritic and martensitic steels for fusion application*, Journal of Nuclear Materials, **233**, 138 (1996).

[Konishi1999] T. Konishi, K. Ohsawa, H. Abe, E. Kuramoto, *Determination of N-body potential for Fe-Cr alloy system and its application to defect study*, Computational Materials Science, **14**, 108 (1999).

[Konobeev2006] Yu. V. Konobeev, A. M. Dvoriashim, S. I. Porollo, F. A. Garner, *Swelling and microstructure of pure Fe and Fe-Cr alloys after neutron irradiation to ~26 dpa at 40°C*, Journal of Nuclear Materials, **355**, 124 (2006).

[Korzavyi2009] P. A. Korzhavyi, A. V. Ruban, J. Odqvist, J. O. Nilsson, B. Johansson, *Electronic structure and effective chemical and magnetic exchange interactions in bcc Fe-Cr alloys*, Physical Review B, **79**, 054202 (2009).

[Kresse1996a] G. Kresse, J. Furthmüller, *Efficient iterative schemes for ab initio total-energy calculations using plane-wave basis set*, Physical Review B **54**, 11169 (1996).

[Kresse1996b] G. Kresse, J. Furthmüller, *Efficiency of ab-initio total energy calculations for metals and semiconductors using a plane-wave basis set*, Computational Materials Science, **6**, 15 (1996).

[Kresse1999] G. Kresse, D. Joubert, *From ultrasoft pseudopotentials to the projector augmented-wave method*, Physical Review B, **59**, 1758 (1999).

[Kuвано1985] H. Kuвано, *Mössbauer effect study on the miscibility gap of the iron-chromium binary system*, Transaction of the Japan Institute of Metals, **26**, 473 (1985).

[Kuвано1988] H. Kuвано, Y. Hamaguchi, *Mössbauer study of iron-chromium alloys irradiated by energetic protons*, Journal of Nuclear Materials, **155-157**, 1071 (1988).

- [Lavrentiev2007] M. Yu. Lavrentiev, R. Drautz, D. Nguyen-Manh, T. P. C. Klaver, and S. L. Dudarev, *Monte Carlo study of thermodynamic properties and clustering in the bcc Fe-Cr system*, Physical Review B **75**, 014208 (2007).
- [Lavrentiev2009] M. Yu. Lavrentiev, S. L. Dudarev, D. Nguyen-Manh, *Magnetic cluster expansion simulation of FeCr alloys*, Journal of Nuclear Materials, **386**, 22-25 (2009).
- [Lavrentiev2010] M. Yu. Lavrentiev, D. Nguyen-Manh, S. L. Dudarev, *Cluster expansion models for Fe-Cr alloys, the prototype materials for a fusion power plant*, Computational Materials Science, **49**, 199-203 (2010).
- [LeBouar2002] Y. Le Bouar, F. Soisson, *Kinetic pathways from embedded-atom-method potentials: Influence of the activation barriers*, Physical Review B, **65**, 094103 (2002).
- [LeDelliou1994] P. Le Delliou, S. Jayet-Gendrot, J.-P. Massoud, J.-C. Van Duysen, *Vieillessement thermique des coudes moulés du circuit primaire*, Epure (ISSN 0758-489X), **44**, 55 (1994).
- [Levesque2011] M. Levesque, E. Martinez, C.-C. Fu, M. Nastar, F. Soisson, *Simple concentration-dependent pair interaction model for large-scale simulations of Fe-Cr alloys*, Physical Review B, **84**, 184205 (2011).
- [Lifshitz1959] I. M. Lifshitz, V. V. Slyozov, *The Kinetics of Precipitation from Supersaturated Solid Solutions*, Journal of Physics and Chemistry of Solids, **19**, 35 (1959).
- [Little1979] E. A. Little and D. A. Stow, *Void-swelling in irons and ferritic steels. II. An experiment survey of materials irradiated in a faster reactor*, Journal of Nuclear Materials, **87**, 25 (1979).
- [Lo2009] K. H. Lo, C. H. Shek, J. K. L. Lai, *Recent developments in stainless steels*, Materials Science and Engineering R, **65**, 39 (2009).

[Loper1985] G. Loper, L. Smedskjaer, M. Chason, R. Siegel, *Positron Annihilation*, edited by P. Jain, R. Singru, K. Gopinathan (World Scientific, Singapore, 1985), p. 461.

[Lvov2011] P. E. L'vov, V. V. Svetukhin, A. O. Obukhov, Thermodynamic of Phase Equilibrium of Binary Alloys Containing Nanoprecipitates, *Physics of the Solid State*, **53**, 421 (2011).

[Malerba2008] L. Malerba, A. Caro, J. Wallenius, *Multiscale modelling of radiation damage and phase transformations: The challenge of FeCr alloys*, *Journal of Nuclear Materials*, **382**, 112 (2008).

[Mansur2004] L. K. Mansur, A. F. Rowcliffe, R. K. Nanstand, S. J. Zinkle, W. R. Corwin, R. E. Stoller, *Materials needs for fusion, Generation IV fission reactors and spallation neutron sources – similarities and differences*, *Journal of Nuclear Materials*, **329**, 166 (2004).

[Martin1984] G. Martin, *Phase stability under irradiation: Ballistic effect*, *Physical Review B*, **30**, 1424 (1984).

[Martin2004] R. M. Martin, *Electronic Structure: Basic Theory and Practical Methods*, Cambridge University Press (Cambridge, 2004).

[Martinez2011] E. Martinez, C.-C. Fu, M. Levesque, M. Nastar, F. Soisson, *Simulations of decomposition kinetics of Fe-Cr solid solutions during thermal ageing*, *Solid State Phenomena*, **172-174**, 1016 (2011).

[Matijasevic2008] M. Matijasevic, A. Almazouzi, *Effect of Cr on the mechanical properties and microstructure of Fe-Cr model alloys after n-irradiation*, *Journal of Nuclear Materials*, **377**, 147 (2008).

[Mendelev2003] M. I. Mendelev, S. Han, D. J. Srolovitz, G. J. Ackland, D. Y. Sun, M. Asta, *Development of new interatomic potentials appropriate for crystalline and liquid iron*, *Philosophical Magazine*, **83**, 3977 (2003).

[Metropolis1953] N. Metropolis, A. W. Rosenbluth, M. N. Rosenbluth, A. H. Teller, E. Teller, *Equation of State Calculations by fast Computing Machines*, Journal of Chemical Physics, **21**, 1087 (1953).

[Miller1995] M. K. Miller, J. M. Hyde, M. G. Hetherington, A. Cerezo, G. D. W. Smith, C. M. Elliot, *Spinodal decomposition in Fe-Cr alloys: experimental study at the atomic level and comparison with computer models – I. Introduction and methodology*, Acta Metallurgica, **43**, 3385-3401 (1995).

[Miller1996] M. K. Miller, I. M. Anderson, J. Bentley, K. F. Russel, *Phase separation in the Fe-Cr-Ni system*, Applied Surface Science, **94**, 391 (1996).

[Mirebeau1984] I. Mirebeau, M. Hennion, and G. Parette, *First Measurement of Short-Range-Order Inversion as a Function of Concentration in a Transition Alloy*, Physical Review Letters, **53**, 687 (1984).

[Mirebeau2010] I. Mirebeau and G. Parette, *Neutron study of the short range order inversion in $Fe_{1-x}Cr_x$* , Physical Review B, **82**, 104203 (2010).

[Monkhorst1976] H. J. Monkhorst, J. D. Pack, *Special points for Brillouin-zone integration*, Physical Review B, **13**, 5188 (1976).

[Möslang1983] A. Möslang, H. Graf, G. Balzer, E. Recknagel, A. Weidinger, Th. Wichert, R. I. Grynszpan, *Muon trapping at monovacancies in iron*, Physical Review B, **27**, 2674 (1983).

[Murty2008] K. L. Murty, I. Charit, *Structural materials for Gen-IV nuclear reactors: Challenges and opportunities*, Journal of Nuclear Materials, **383**, 189 (2008).

[Nguyen-Manh2007] D. Nguyen-Manh, M. Yu Lavrentiev, S. L. Dudarev, *Magnetic origin of nano-clustering and point defect interaction in Fe-Cr alloys: an ab-initio study*, Journal of Computer-Aided Materials Design, **14**, 159 (2007).

[Nguyen-Manh2008a] D. Nguyen-Manh, M. Yu Lavrentiev, S. L. Dudarev, *The Fe-Cr system: atomistic modelling of thermodynamics and kinetics of phase transformations*, Comptes Rendus de Physique, **9**, 379 (2008).

[Nguyen-Manh2008b] D. Nguyen-Manh, M. Yu. Lavrentiev, S. L. Dudarev, *Ab initio and Monte Carlo modeling in Fe-Cr system: Magnetic origin of anomalous thermodynamic and kinetic properties*, Computational Material Science, **44**, 1 (2008).

[Nguyen-Manh2009] D. Nguyen-Manh, M. Yu. Lavrentiev, S. L. Dudarev, *Magnetic properties of point defect interaction with impurity atoms in Fe-Cr alloys*, Journal of Nuclear Materials, **386**, 60 (2009).

[Novy2009a] S. Novy, P. Pareige, C. Pareige, *Atomic scale analysis and phase separation understanding in a thermally aged Fe-20at.% Cr alloy*, Journal of Nuclear Materials, **384**, 96-102 (2009).

[Novy2009b] S. Novy, *Mécanismes de vieillissement à très longue échéance des aciers inoxydables austénoferritiques*, Ph D Thesis (2009).

[Okada1999] A. Okada, H. Maeda, K. Hamada, I. Ishida, *Defect structure development in a pure iron and dilute iron alloys irradiated with neutron and electrons*, Journal of Nuclear Materials, **271**, 133 (1999).

[Olsson2003] P. Olsson, I. A. Abrikosov, L. Vitos, J. Wallenius, *Ab initio formation energies of Fe-Cr alloys*, Journal of Nuclear Materials, **321**, 84 (2003).

[Olsson2005a] P. Olsson, J. Wallenius, C. Domain, K. Nordlund, and L. Malerba, *Two-band modeling of α -prime phase formation in Fe-Cr*, Physical Review B, **72**, 214119 (2005).

[Olsson2005b] P. Olsson, *Modelling of Formation and Evolution of Defects and Precipitates in Fe-Cr Alloys of Reactor Relevance*, Ph D Thesis (2005).

[Olsson2006] P. Olsson, I. A. Abrikosov, J. Wallenius, *Electronic origin of the anomalous stability of Fe-rich bcc Fe-Cr alloys*, Physical Review B **73**, 104416 (2006).

- [Olsson2007] P. Olsson, C. Domain, J. Wallenius, *Ab initio study of Cr interactions with point defects in bcc Fe*, Physical Review B, **75**, 014110 (2007).
- [Overhauser1962] A. W. Overhauser, *Spin Density Waves in an Electron Gas*, Physical Review, **128**, 1437 (1962).
- [Pareige2009] C. Pareige, C. Domain, and P. Olsson, *Short- and long-range orders in Fe-Cr: A Monte Carlo study*, Journal of Applied Physics, **106**, 104906 (2009).
- [Pareige2011] C. Pareige, M. Roussel, S. Novy, V. Kuksenko, P. Olsson, C. Domain, P. Pareige, *Kinetic study of phase transformation in a highly concentrated Fe-Cr alloy: Monte Carlo simulation versus experiments*, Acta Materialia, **59**, 2404 (2011).
- [Parr1989] R. G. Parr, W. Yang, *Density-Functional Theory of Atoms and Molecules*, Oxford University Press (Oxford, 1989), chapters 1-2-3.
- [Paxton2008] A. Paxton, M. W. Finnis, *Magnetic tight binding and the iron-chromium enthalpy anomaly*, Physical Review B, **77**, 24428 (2008).
- [Perdew1991] J. P. Perdew, *Electronic Structure of Solids*, Akademie Verlag, Berlin (1991).
- [Perdew1992] J. P. Perdew, Y. Wang, *Accurate and simple analytic representation of the electron-gas correlation energy*, Physical Review B, **45**, 13244 (1992).
- [Perdew1996] J. P. Perdew, K. Burke, M. Ernzerhof, *Generalized Gradient Approximation Made Simple*, Physical Review Letters, **77**, 3865 (1996).
- [Perez2003] M. Perez, A. Deschamps, *Microscopic modelling of simultaneous two-phase precipitation: application to carbide precipitation in low-carbon steels*, Materials Science and Engineering A, **360**, 214 (2003).
- [Porollo1998] S. I. Porollo, A. M. Dvoriashim, A. N. Vorobyev, Yu. V. Konobeev, *The microstructure and tensile properties of Fe-Cr alloys after neutron irradiation at 400°C to 5.5-7.1 dpa*, Journal of Nuclear Materials, **256**, 247 (1998).

- [Porter1996] D. A. Porter, K. E. Easterling, *Phase Transformations in Metals and Alloys*, Chapman & Hall (London, 1996), chapter 1.
- [Postnikov2003] A. V. Postnikov, P. Entel, J. M. Soler, *Density functional simulation of small Fe nanoparticles*, The European Physical Journal D **25**, 261, (2003).
- [Rautiainen1999] T. T. Rautiainen, A. P. Sutton, *Influence of the atomic diffusion mechanism on morphologies, kinetics, and the mechanisms of coarsening during phase separation*, Physical Review B, **59**, 13681 (1999).
- [Ruban2008] A. V. Ruban, P. A. Korzhavyi, B. Johansson, *First-principles theory of magnetically driven anomalous ordering in bcc Fe-Cr alloys*, Physical Review B, **77**, 094436 (2008).
- [Sanchez1984] J. M. Sanchez, F. Ducastelle and D. Gratias, *Generalized cluster description of multicomponent systems*, Physica A, **128**, 334 (1984).
- [Schaefer1977] H. E. Schaefer, K. Maier, M. Weller, D. Herlach, A. Seeger, J. Diehl, *Vacancy formation in iron investigated by positron annihilation in thermal equilibrium*, Scripta Metallurgica, **11**, 803 (1977).
- [Soisson2007] F. Soisson, C.-C. Fu, *Cu-precipitation kinetics in α -Fe from atomistic simulations: Vacancy-trapping effects and Cu-cluster mobility*, Physical Review B, **76**, 214102 (2007).
- [Soriano-Vargas2010] O. Soriano-Vargas, E. O. Avila-Davila, V. M. Lopez-Hirata, N. Cayetano-Castro, Jorge L. Gonzalez-Velazquez, *Effect on spinodal decomposition on the mechanical behavior of Fe-Cr alloys*, Material Science and Engineering A, **527**, 2910 (2010).
- [Soulariol2010] R. Soulariol, Chu-Chun Fu, C. Barreateau, *Structure and magnetism of bulk Fe and Cr: from plane waves to LCAO methods*, 22, Journal of Physics: Condensed Matter, **22**, 295502 (2010).

- [Terentyev2011] D. Terentyev, G. Bonny, N. Castin, C. Domain, L. Malerba, P. Olsson, V. Molodtsov, R. C. Pasianot, *Further development of large-scale atomistic modeling techniques for Fe-Cr alloys*, Journal of Nuclear Materials, **409**, 167 (2011).
- [Tisinai1957] G. F. Tisinai, C. H. Samans, Some observations on 885°F embrittlement, transactions AIME, Journal of Metals, 1221 (October 1957).
- [Tsunoda1994] Y. Tsunoda, *The commensurate-incommensurate SDW phase boundary of CrFe alloys*, Journal of Physics: Condensed Matter, **6**, 8513 (1994).
- [Vanderbilt1990] D. Vanderbilt, *Soft self-consistent pseudopotentials in a generalized eigenvalue formalism*, Physical Review B, **41**, 7892 (1990).
- [Vincent2008] E. Vincent, C. S. Becquart, C. Pareige, P. Pareige, C. Domain, *Precipitation of the FeCu system: A critical review of atomic kinetic Monte Carlo simulations*, Journal of Nuclear Materials, **373**, 387 (2008).
- [Vineyard1957] G. H. Vineyard, Frequency factors and isotope effects in solid state rate processes, Journal of Physics and Chemistry of Solids, **3**, 121 (1957).
- [Vosko1980] S. H. Vosko, L. Wilk, M. Nusair, *Accurate spin-dependent electron liquid correlation energies for local spin density calculations: a critical analysis*, Canadian Journal of Physics, **58**, 1200 (1980).
- [Wagner2001] *Phase Transformations in Materials*, Gernot Kostorz (editor), chapter 5, R. Wagner, R. Kampmann, P. W. Voorhees, *Homogeneous Second-Phase Precipitation* (Weinheim 2001).
- [Wallenius2004a] J. Wallenius, P. Olsson, C. Lagerstedt, N. Sandberg, R. Chakarova, V. Pontikis, *Modeling of chromium precipitation in Fe-Cr alloys*, Physical review B, **69**, 094103 (2004).
- [Wallenius2004b] J. Wallenius, I. A. Abrikosov, R. Chakarova, C. Lagerstedt, L. Malerba, P. Olsson, V. Pontikis, N. Sandberg, D. Terentyev, *Development of an EAM potential for*

simulation of radiation damage in Fe-Cr alloys, Journal of Nuclear Materials, **329**, 1175 (2004).

[Wallenius2007] J. Wallenius, Pär Olsson, Lorenzo Malerba, Dimitry Terentyev, *Simulation of thermal ageing and radiation damage in Fe-Cr*, Nuclear Instruments and Methods in Physics Research B, **255**, 68-74 (2007).

[Was2007] G. S. Was, *Materials in fission reactors: Lesson learned of relevance to fusion reactor systems*, Journal of Nuclear Materials, **367**, 11 (2007).

[Xiong2010] W. Xiong, M. Selleby, Q. Chen, J. Odqvist, Y. Du, *Phase Equilibria and Thermodynamic Properties in the Fe-Cr System*, Critical Reviews in Solid State and Materials Sciences, **35**, 125 (2010).

[Xiong2011] W. Xiong, P. Hedström, M. Selleby, J. Odqvist, M. Thuvander, Q. Chen, *An improved thermodynamic modeling of the Fe-Cr system down to zero Kelvin coupled with key experiments*, CALPHAD, **35**, 355 (2011).

[Yifang1996] O. Yifang, Z. Bangwei, L. Shuzhi, J. Zhanpeng, *A simple analytical EAM model for bcc metals including Cr and its application*, Zeitschrift Für Physik B, **101**, 161 (1996).

[Yvon2009] P. Yvon, F. Carré, *Structural materials challenges for advanced reactor systems*, Journal of Nuclear Materials, **385**, 217 (2009).

[Zener1949] C. Zener, *Theory of Growth of Spherical Precipitates from Solid Solution*, Journal of Applied Physics, **20**, 950 (1949).

[Zinkle2009] J. Zinkle, J. T. Busby, *Structural materials for fission & fusion energy*, Materials today, **12**, 11 (2009).

[Zunger1990] A. Zunger, S.-H. Wei, L. G. Ferreira, J. E. Bernard, *Special Quasirandom Structures*, Physical Review Letters, **65**, 353 (1990).